ABSTRACT

Title of Document:	STRUCTURE-PROPERTY RELATIONSHIPS IN CRYSTALLINE-AMORPHOUS BLOCK COPOLYMERS: SYNTHESIS, PHASE BEHAVIOR AND MECHANICAL PROPERTIES
	Wonseok Hwang, Doctor of Philosophy, 2017
Directed By:	Professor Robert M. Briber Department of Materials Science and Engineering
	Professor Lawrence R. Sita Department of Chemistry and Biochemistry

Block copolymers are composed of two or more polymer chains that are chemically distinctive and covalently bonded at the single point. Due to the incompatibility between blocks, the block copolymers undergo microphase separation generating long-range ordered microdomains. Considerable effort has been put on the understanding of the microdomain structure-mechanical properties relationships in block copolymers where both blocks are amorphous. Less research has been done on structure-property relationships in crystalline-amorphous block copolymers.

In this thesis, the structure-property relationships in crystalline-amorphous block copolymers have been explored using two polymer systems, 1) well-defined isotactic-atactic-isotactic stereoblock (sbPP) and stereoirregular (irPP) polypropylene materials, 2) poly(1-hexene)-poly(methyl-1,3-cyclopentane) (PH-PMCP) block copolymers.

The structure-property relationships in sbPP and irPP materials have been characterized using tensile testing, dynamic mechanical analysis (DMA) and rheology. The sbPP materials demonstrated higher tensile modulus exhibiting elongation ratios of more than 2,000 % while irPP materials showed lower tensile modulus with elongation of less than 100 %. Furthermore, sbPP materials exhibited more than 90 % of tensile recovery in contrast to 60-70 % tensile recovery for irPP materials. The discrete crystalline-amorphous-crystalline structure in sbPP materials provides both rigidity and flexibility.

The morphologies of PH-PMCP materials have been investigated using *in-situ* small and wide angle X-ray scattering (SAXS/WAXS), rheology, atomic force microscopy (AFM), and transmission electron microscopy (TEM). The melting of the crystalline PMCP followed by the microphase separation in PH-PMCP results in a modulus transition after the PMCP melting. In particular, sphere-forming PH-PMCP block copolymers exhibit a drop of 2 orders of magnitude in the storage modulus at the PMCP melting temperature. The recovery in storage modulus within 2 min results from the low molecular weight and the incompatibility between PH and PMCP blocks. By tuning PMCP content, this modulus transition has been demonstrated in sphere, cylinder, double gyroid, and lamellae forming block copolymers. The viscoelastic response in sphere-forming PH-PMCP block copolymers indicate that after the PMCP crystal melt

the molten PMCP blocks participate the formation of block copolymer microdomains and improve the microdomain ordering.

STRUCTURE-PROPERTY RELATIONSHIPS IN CRYSTALLINE-AMORPHOUS BLOCK COPOLYMERS: SYNTHESIS, PHASE BEHAVIOR AND MECHANICAL PROPERTIES

By

Wonseok Hwang

Dissertation submitted to the Faculty of the Graduate School of the
University of Maryland, College Park, in partial fulfillment
of the requirements for the degree of
Doctor of Philosophy
2017

Advisory Committee:

Professor Robert M. Briber, Chair and Co-Advisor

Professor Lawrence R. Sita, Co-Advisor

Professor Isabel Lloyd

Professor Peter Kofinas

Professor Srinivasa R. Raghavan

Acknowledgements

It is hard to believe that it has been so long ago since I joined the PhD program at the University of Maryland. Nine years have passed by with many experiences and lots of challenges and full of joy as well. It was only possible because of those individuals who made nine years so short and memorable.

First and foremost, I would like to thank my two advisors, Professor Robert M. Briber and Professor Lawrence R. Sita for their invaluable guidance and endless patience throughout my PhD. They are willing to share their time with me to discuss about science. Their passion and unparalleled intelligence for science have inspired me to accomplish my researches in both polymer physics and chemistry. Including discussions and support, Professor Briber and Professor Sita provided tremendous opportunities for me to envision the fundamental understanding of the phase behavior and the properties in polymers.

I would like to thank Professor Peter Kofinas for helping me to broaden my research scope. He is always supportive and open to discuss about my research. I am also thankful to Professor Isabel Lloyd for her help. She encourages me to how to approach and solve the mechanical properties of the materials. Without Professor Srinivasa R. Raghavan's help, I would not be able to get involved the viscoelastic behavior of polymers. He is always willing to share his lab facilities and believes in my skills.

Throughout graduate school, there have been many colleagues who have spent their time with me in both classes and labs. My classmates, Gary Paradee, Adam Katz, Seungyong Lee, always encourage me to keep my sanity. Former and current Professor Briber's lab members, Dr. Joon Ho Roh, Sang Hak Shin, Wonjoo Lee, Doug Henderson,

Rui Lu, Eddy Salgado, and Xin Zhang, help me to finish my researches. Especially, Xin gives helpful comments based on his experiences. I would like to give many thanks to former and current Professor Sita's lab members, Dr. Jonathan Reeds, Brendan Yonke, Jia Wei, Rennisha Wickham, Andrew Keane, Wesley Farrell, Gail Blakley, Kaitlyn Crawford, Tessy Thomas, Leila Duman, Samantha Nowak, Rick Thompson, Mark Wallace, Kätchen Lachmayr, and two awesome undergrads, Kyle Augustine and Jocelyn Baer. I would like to thank a former Professor Kofinas lab member, Adam Behrens. He is a great collaborator and willing to help my writings as well as researches. Former Professor Raghavan's lab members, Bani Cipriano and Hyuntaek Oh, trained me how to use their rheometers.

In addition my classmates, lab members, and colleagues, I would like to thank Dr. Howard Wang, Dr. Peter Zavalij, Dr. Wen-An Chiou, Dr. Sz-Chian Liou, and Dr. Karen Gaskell. They are willing to support me with sharing their facilities and discuss about my researches.

Of course, I appreciate Korean graduate students at the University of Maryland who keep me sane, especially, Sungwon Han, Moon Soo Lee, In Hak Baick, Sangyool Lee, Jungyeon Han, and David Yang. In addition, I would like to thank my former and current housemates, Arthur, Tristin, Elisabeth, Gareth, Liz, Wrick and Troy.

Lastly, I can never thank my parents and brother's family enough for their love and support.

Table of Contents

List of Tables

List of Figures

Chapter 1. Introduction

1.1. Introduction to Block Copolymers

1.1.1. Block copolymer and random copolymer structure

Polymers are macromolecules that are composed of many covalently bonded repeating monomers. A polymer consisting of a single monomer type is called a homopolymer. If the monomers composing the polymer chain are from two or more different chemical species and connected in a random fashion, it is called a random copolymer. Random copolymers typically have the averaged properties of the homopolymers of each constituent monomer species. Block copolymers are composed of two or more polymer chains that are chemically distinct and covalently bonded at a single point between blocks.[1]

The number of monomer units in the polymer chain determines a degree of polymerization. There are two important quantities to represent a set of polymer chains: average molecular weight (M) and polydispersity (PDI). The average molecular weight is generally described with number-averaged molecular weight (M_n) and weight-averaged molecular weight (M_w). Following equations determine M_n and M_w,

$$M_n = \frac{\sum_i N_i M_i}{\sum_i N_i} \quad (1)$$

$$M_w = \frac{\sum_i N_i M_i^2}{\sum_i N_i} \quad (2)$$

where N_i is the number of polymer chains with molecular weight M_i. The ratio of the two averaged values is used to represent the width of the molecular weight distribution, polydispersity index (PDI),

$$\text{polydispersity index, PDI} = \frac{M_w}{M_n} \tag{3}$$

The physical and chemical properties of block copolymers along with their unique phase behavior have been studied extensively. In general, the two chemically distinct polymer chains are incompatible and would macroscopically phase separate if not linked together. Tethering the two polymer chains result in microphase separation in the form of periodic microstructures. The length scale of the microstructures is typically between 10-100 nm. These self-assembled nanoscale structures have led to interest in the use of block copolymers in applications such as membranes, adhesives, elastomers, and nanopatterning. The schematic diagram of random and block copolymer chains are shown in Figure 1.1.

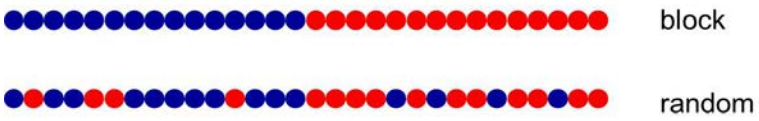

Figure 1.1 Schematic of block and random copolymers.

1.1.2. Synthetic methods for block copolymers

Due to their ability to self-assemble into ordered structures, block copolymers have been extensively studied by theoreticians and experimentalists for decades. Studies have focused on the generation of microstructures and on expanding the range of

monomers for synthesizing block copolymers. Synthetic routes have also been developed and applied to address basic scientific questions and to aid in mass production. The two most commonly used methods for synthesizing block copolymers are either the sequential addition of monomers termed “living” polymerization or the coupling two polymer chains through functional end groups. The first method is more widely used to synthesize block copolymers at scale, however, there are several requirements that need to be satisfied to attain the desired product. These requirements for living polymerization are:

1. The polymerization initiation should be much faster than the chain propagation rate, such that all the polymers start growing at the same time when the initiator is added to the reaction mixture.

2. The chain propagation rate should be much faster than the chain termination rate. If chain termination is present or faster than propagation, it is generally not possible to polymerize the monomers to high molecular weight.

3. It is desirable that the growth rate of the polymer chain is linear. This offers the ability to predict the molecular weight from the molar ratio of monomer to initiator.

The polydispersity index (PDI) of the molecular weight of polymers from a living polymerization is generally very small (PDI<1.1). A small PDI is necessary for well-defined microphase separation in block copolymer systems.

Among a wide variety of synthetic routes, living polymerization has been known as the best way to control both the chain architecture and molecular weight with narrow

molecular weight distribution. Particularly, living coordination polymerization, which was discovered in the mid-1950s by Karl Ziegler and Giulio Natta, has been utilized for olefin monomers.[2] Organometallic compounds are considered as counter cations for the anionic alkyl chain end (π-bond). Through metal-alkyl coordination, chain propagation is initiated and can be controlled in a precise manner. Coupling the living polymerization with the sequential monomer addition, it is possible to tailor the chain architecture and length as well as the material properties.

1.1.3. Microphase separation in block copolymers

The simplest and most well-defined block copolymer structure is a linear diblock copolymer. Flory and Huggins developed a method to quantify phase separation in a coil-coil binary polymer mixture.[3] Based on the properties of a polymer mixture using a lattice model, the Flory-Huggins theory provides a theoretical framework for the thermodynamics of mixing using the Flory-Huggins interaction parameter χ, the degree of polymerization N, and temperature T. The parameter, χN, is inversely related to temperature, $\chi N \sim 1/\mathrm{T}$, and is the measure of the phase separation strength in the two phase region at a given temperature.

The phase behavior of *A*-*B* diblock copolymer is considered as a mixture of *A* and *B* homopolymer chains. Using Gibbs free energy of polymer-polymer mixing (Eq. 4), the phase behavior of the binary mixture can be written with the degree of polymerization (N_A and N_B), the volume fraction (f_A and f_B), and Flory-Huggins interaction parameter χ.

$$\frac{\Delta G_{mixing}}{k_B T} = \frac{f_A}{N_A} \ln f_A + \frac{f_B}{N_B} \ln f_B + f_A f_B \chi \qquad (4)$$

where k_B is the Boltzmann constant and T is absolute temperature.

The phase behavior of a block copolymer in molten state can be distinguished from the binary mixing of homopolymers with the key difference being the block copolymer generates microphases with on the order of the molecular dimensions. As such, the simple Flory-Huggins free energy for binary mixing is not valid to predict the order-disorder transition in block copolymers. Helfand and Wasserman pioneered phase separation theory (strong segregation limit, SSL) that describes a spatial distribution of a block composition based on the probability of finding a segment in different position.[4] Leibler introduced the order-disorder transition using random phase approximation and the phase behavior near the boundary.[5] Leibler's theory describes the composition fluctuations near the transition, weak segregation limit (WSL). Using scattering function based on the composition fluctuations, Leibler predicted the critical value for the microphase separation in block copolymers, χN=10.495 when the block ratio is $f_A = f_B = 0.5$.

To understand the order-disorder transition, Leibler introduced the order parameter $\psi(\vec{r})$ to investigate the local density fluctuations and the free energy density in block copolymers. The approach of this theory is based on the random-phase approximation (RPA). The RPA equation provides the general functions for the phase transition and that leads to the relationship between the density correlation function and the free energy of the molten state block copolymer.

In order to characterize the phase behavior in single phase region before the order-disorder transition, the order parameter used was,

$$\psi(\vec{r}) = < (1-f)\rho_A(\vec{r}) - f\rho_B(\vec{r}) > = < \rho_A(\vec{r}) - f > \qquad (5)$$

where $\rho_A(\vec{r})$ and $\rho_B(\vec{r})$ are the local density fluctuations of monomer A and monomer B at the point r satisfying $\rho_A(\vec{r}) + \rho_B(\vec{r}) = 1$ and $\delta\rho_A(\vec{r}) + \delta\rho_B(\vec{r}) = 0$. In the disordered phase, $\psi(\vec{r})$ disappears at all points. In the ordered phase, $\psi(\vec{r})$ does not vanish and $\psi(\vec{r})$ becomes a periodic function. The local density fluctuation results from the amount of excess density distribution at different two points because one segment motion induces motion of another segment. Thus, the probability of the chain conformation contributes to the density-density correlation. The scattering intensity measured by small angle scattering experiments is proportional to the Fourier transformation of the two-point correlation function (i.e., density-density correlation function). The density-density correlation function is defined as,

$$\tilde{S}(\vec{r} - \vec{r}\,') = \frac{1}{k_B T} < \delta\rho_A(\vec{r})\delta\rho_A(\vec{r}\,') > \qquad (6)$$

The scattering function is the Fourier transformation of the density correlation function at position $\vec{r}$. Therefore, the scattering intensity is proportional to the Fourier transformation of the correlation function,

$$I(\vec{q}) = \int d\vec{r}\ < \delta\rho_A(\vec{r})\delta\rho_A(\vec{r}\,') > e^{-i\vec{q}\cdot\vec{r}} \qquad (7)$$

The free energy of the system is a function of the external potential which is generated by the surrounding monomer *A* and *B* where,

$$\int U_A(\vec{r})\,\delta\rho_A(\vec{r})d\vec{r} + \int U_B(\vec{r})\,\delta\rho_B(\vec{r})d\vec{r} = \int U(\vec{r})\rho_A(\vec{r})d\vec{r} \qquad (8)$$

Using the Legendre transformation, the free energy can be written as a function of $\psi(\vec{r})$,

$$F(\psi) = F'(U) - \int U(\vec{r})\psi(\vec{r})d\vec{r} \qquad (9)$$

The free energy density $F'([U])$ induced by the external field U is,

$$F'(U) = -k_B T \ln Z[U(\vec{r})] \qquad (10)$$

where $Z([U])$ is the partition functional of the system to the external field U.

$$Z = Z_0 < \exp\left(-\frac{1}{k_B T}\int U(\vec{r})\delta\rho_A\, d\vec{r}\right) > \qquad (11)$$

Z_0 is the partition function at the uniform state (i.e., no external field U=0). The free energy functional F' can be expressed using Taylor expansion series,

$$F' = F_1 + \sum_{n=1}^{\infty} \frac{(-\beta)^{n-1}}{n!}\int \tilde{G}^{(n)}(\vec{r}_1, \ldots, \vec{r}_n)U(\vec{r}_1)\ldots U(\vec{r}_n)d\vec{r}_1 \ldots d\vec{r}_n \qquad (12)$$

where $\beta=1/k_BT$, k_B is Boltzmann constant and T is temperature. The expansion coefficients are the monomer density correlation functions defined by

$$\tilde{G}^{(n)}(\vec{r}_1, \dots, \vec{r}_n) \equiv -(k_B T) \frac{\delta^n}{\delta U(\vec{r}_1) \dots \delta U(\vec{r}_n)} \ln\left(\frac{Z}{Z_0}\right)\Big|_{U=0} \tag{13}$$

The order parameter, now, can be a function of a potential at point $\vec{r}$.

$$\psi(\vec{r}) = \sum_{n=0}^{\infty} \frac{(-\beta)^n}{n!} \int \tilde{G}^{(n+1)}(\vec{r}, \vec{r}_1, \dots, \vec{r}_n) U(\vec{r}_1) \dots U(\vec{r}_n) d\vec{r}_1 \dots d\vec{r}_n \tag{14}$$

The Fourier transformation of the order parameter $\psi(\vec{r})$ is

$$\psi(\vec{q}_1) = \sum_{n=1}^{\infty} \frac{(-\beta)^{n-1}}{(n-1)!} V^{n-1} \sum_{q_2, \dots q_n} \delta(\vec{q}_1 + \dots + \vec{q}_n) \times \tilde{G}^{(n)}(\vec{q}_1, \dots, \vec{q}_n) U(\vec{q}_1) \dots U(\vec{q}_n) \tag{15}$$

Using Eq. 13 and 15, the free energy expansion is obtained as a function of Fourier transformation of the order parameter $\psi(\vec{q})$,

$$F = F_0 + k_B T \sum_{n=2}^{\infty} \frac{V^{-n}}{n!} \sum_{q_1, \dots q_n} \Gamma^{(n)}(\vec{q}_1, \dots, \vec{q}_n) \psi(\vec{q}_1) \dots \psi(\vec{q}_n) \tag{16}$$

where $\psi(\vec{q}) = \int \psi(r) e^{i\vec{q}\cdot\vec{r}} d\vec{r}$ and $\psi(\vec{r}) = < \rho_A(\vec{r}) - f >$. The second-order term (n=2) in the free energy expansion is represented as,

$$F = F_0 + \frac{k_B T}{2NV} \sum_q \{F(x) - 2\chi N\} \psi^2(\vec{q}) \tag{17}$$

where $F(x)$ is,

$$F(x) = \frac{g_D(1,x)}{g_D(f,x)g_D(1-f,x) - \frac{1}{4}[g_D(1,x) - g_D(f,x) - g_D(1-f,x)]^2} \tag{18}$$

where Debye function is,

$$g_D(f,x) = \frac{2}{x^2}(fx + e^{-fx} - 1) \tag{19}$$

Based on the ideal Gaussian chain assumption, the radius of gyration of a polymer with *N* monomers and segment length *b* can be written as,

$$x = \frac{1}{6} N b^2 q^2 = q^2 {R_g}^2 \tag{20}$$

When the $F(x)$ has a minimum value of 20.99 at $x = q^2 {R_g}^2 = 3.78$, the correlation function $\tilde{S}(\vec{q})$ diverges and the scattering intensity will have a maximum value.[6] Since the block copolymer microdomain periodicity, *L*, is inverse proportional to the scattering vector, $L = 2\pi/q$, the minimum ratio of $L/R_g = 3.23$. The critical microphase separation value is, therefore,

$$F\left(q^2{R_g}^2 = 3.78\right)_{min} = 20.99 = 2xN \qquad f_A = f_B = 0.5$$

$$xN = \frac{20.99}{2} = 10.495 \tag{21}$$

From Eq. 15, the correlation function $\tilde{S}(\vec{q})$ can be represented,

$$\tilde{S}(\vec{q}) = \tilde{S}_{AA}(\vec{q}) = \frac{W(\vec{q})}{S(\vec{q}) - 2\chi W(\vec{q})} \tag{22}$$

where

$$S_{AA}(\vec{q}) = N g_D(f, x)$$

$$S_{BB}(\vec{q}) = N g_D(1 - f, x)$$

$$S_{AB}(\vec{q}) = S_{BA}(\vec{q}) = \frac{1}{2} N[g_D(1, x) - g_D(f, x) - g_D(1 - f, x)] \tag{23}$$

$$W(\vec{q}) = S_{AA}(\vec{q}) S_{BB}(\vec{q}) - {S_{AB}}^2(\vec{q})$$

$$S(\vec{q}) = S_{AA}(\vec{q}) + S_{BB}(\vec{q}) + 2S_{AB}(\vec{q})$$

Therefore, the inverse form of the correlation function $\tilde{S}(\vec{q})$ is,

$$S(\vec{q}) = \frac{N}{F(x) - 2\chi N} \tag{24}$$

$$\frac{1}{S(\vec{q})} = \frac{1}{N}\left[\frac{S_{AA}(\vec{q}) + S_{BB}(\vec{q}) + 2S_{AB}(\vec{q})}{S_{AA}(\vec{q})S_{BB}(\vec{q}) - {S_{AB}}^2(\vec{q})}\right] - 2\chi$$

From Eq. 24, the scattering function in both large $\vec{q}$ and small $\vec{q}$ shows an independent behavior of the interaction parameter χ.

$$S(\vec{q}) \approx \frac{2Nf(1-f)}{\left(qR_g\right)^2}, \qquad qR_g \gg 1\ (large\ \vec{q})$$

$$S(\vec{q}) \cong \frac{2Nf^2(1-f)^2\left(qR_g\right)^2}{3}, \qquad qR_g \ll 1\ (small\ \vec{q}) \tag{25}$$

Based on Eq. 24 and 25, the constructed plots are represented in Figure 1.2. As the scattering intensity $I(q)$ is proportional to the scattering function $S(q)$, the maximum $I(q)$ occurs at $q=q^*$ when a symmetric diblock copolymer in disordered state and $q^*=1.944$.[7,8]

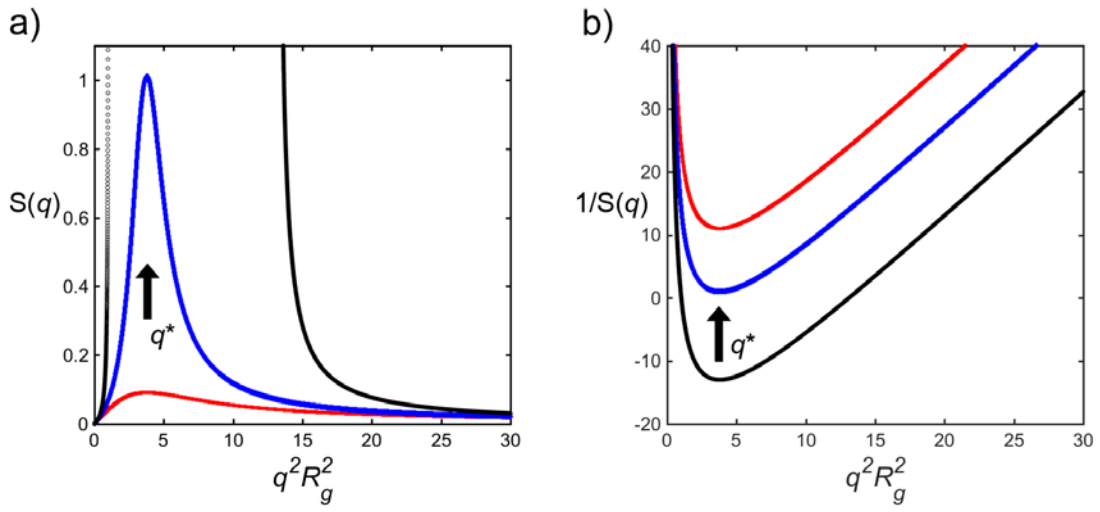

Figure 1.2 Schematic plots of a) inverse scattering function $S(q)$ and b) scattering function $1/S(q)$ as a function of $x=q^2R^2$ when χN=5 (red), χN=10 (blue), and χN=17 (black). The maximum $S(q)$ occurs at $q=q^*$ when a symmetric diblock copolymer (f=0.5) in disordered state. When χN >10.495, the microphase separation state becomes unstable and $S(q)$ diverges.

In the microphase separated region of the phase diagram, the *A* block segregates with other *A* blocks to minimize contact with *B* blocks. Using Helfand and Leibler's theories, the phase separation behavior in block copolymers has been studied using a wide variety of chemistries for the different blocks. In addition, it is possible to predict the phase behavior, domain size, and even the interfacial width between microphase separated domains.[9]

Depending on the volume ratio of the *A* block, the occupied volume of *A* can rearrange and undergo microphase separation. A block copolymer phase diagram based on Eq. 16 is shown in Figure 1.3. When the volume fraction of the *A* block is small, the *A* block forms spherical block copolymer domains on a body-centered cubic (BCC) lattice surrounded by the *B* block matrix. As the fraction of *A* block increases, A domains order as hexagonally packed cylinders (HEX) and then a lamellar (LAM) morphology. Figure 1.4 represents the schematic microdomain morphologies for a linear diblock copolymer

as a function of volume fraction of A block.[9] The basic phase diagram which was established by Leibler's theory has been improved by Fredrickson. Still, Leibler's theory is sufficient to understand the phase behavior of block copolymers for this discussion.

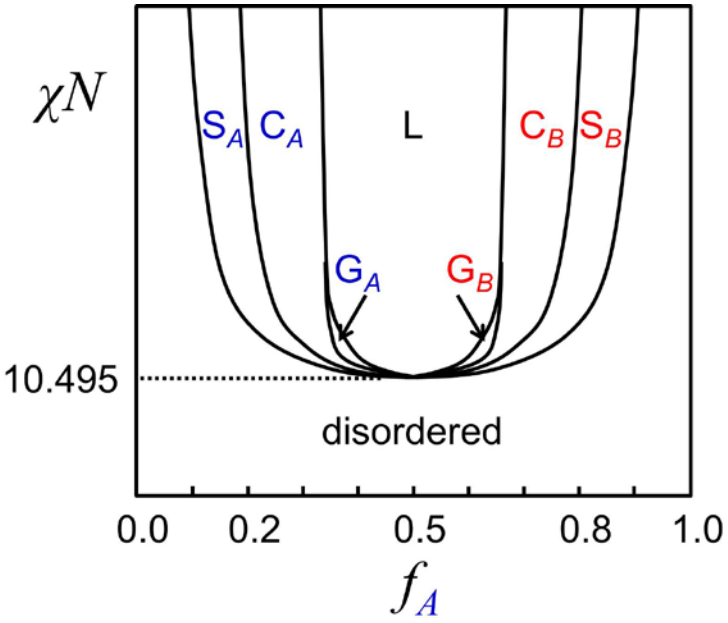

Figure 1.3 Phase diagram of A-B diblock copolymers. f_A is volume fraction of the A block in A-B diblock copolymer. S, C, G, and L are spherical (body-centered cubic, BCC), cylinder (hexagonally packed cylinder, HEX), double gyroid (GYR), and lamellar (LAM) structure, respectively.

Recent experiments and calculations have classified three regimes in the microphase separated region (χN>10.495); weak segregation (10.495≤ χN≤12.5), intermediate segregation (12.5< χN≤95), and strong segregation (100< χN) (WSL, ISR, and SSL, respectively) based on the product of the overall degree of polymerization, N and the interaction parameter, χ.[10]

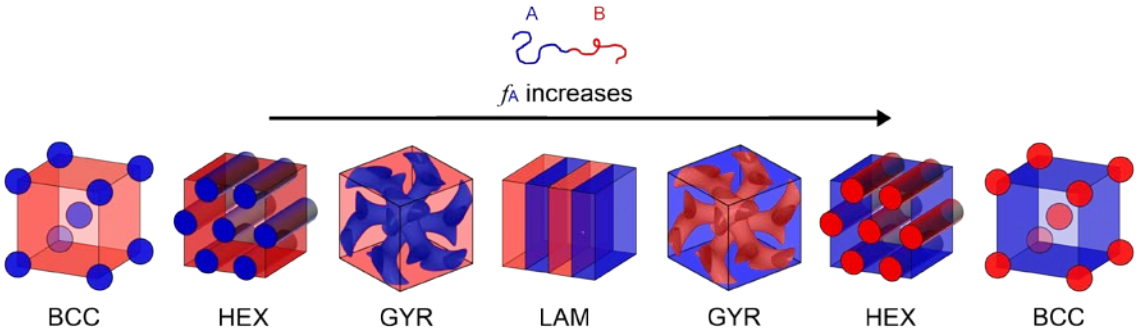

Figure 1.4 Schematic microdomain structures in A-B diblock copolymer as a function of volume fraction.

In the microphase separated region from $10.495 \leq \chi N \leq 12$, the block copolymer is in the WSL region.[5] In this regime, a compositional fluctuations occur and the system displays an order-disorder transition temperature (ODT) at $T=T_{ODT}$. The theoretical limit for the order-disorder transition is $\chi N=10.495$. The boundary between the domains is not sharp and the composition profile across the boundary changes gradually. In a symmetric block copolymer ($f_A = f_B = 0.5$) which generates lamellar morphology below T_{ODT}, the domain spacing D shows a molecular weight dependence with $D \sim N^{0.5}$.

When χN is very large ($\gg 10^3$), the phase separation falls into SSL. In this regime, the phase boundary is sharp and the composition profile between blocks shows a very sharp profile.[4] In addition to narrow interface between domains, the molecular weight N dependence of the domain spacing D is $D \sim N^{0.67}$.

In between SSL and WSL where $12.5< \chi N \leq 95$, termed the ISR region, the domain spacing D is proportional to $N^{0.72}$ suggesting that there are concentration fluctuations resulting in a delocalized interface.[10]

Researchers have been able to tune the chemical stability, polarity, stiffness, and the order-disorder transition temperature of block copolymers using different monomers and different synthetic routes. Furthermore, numerous studies of diblock copolymer phase behavior have been carried over with a wide range of block ratios, polymer types,

and molecular weights, allowing for the exploration and development of new materials for a variety of applications.

1.1.4. Coil-Coil vs. Crystalline-Coil block copolymer

As previously discussed, the phase diagram of an *A*-*B* block copolymer can be predicted as a function of volume fraction *f*, degree of polymerization *N*, Flory-Huggins interaction parameter χ, and temperature T. This calculation is based on the assumption that both blocks are coils (i.e., in the amorphous state). With new synthetic methodologies, chain architecture of block copolymers has been extended to comb-like shapes, miktoarm (star-like), and hyper-branched including multiple linear structures.

Much like new chain architectures, block copolymers that contain crystallizable blocks have complicated phase diagrams that are more challenging to predict than that of a coil-coil system.[11,12] One of the challenges originates from the effect of the glass transition of amorphous block (T_g^A) and the melting temperature of crystallizable block (T_c^C). When the crystallization temperature is higher than the glass transition of amorphous block (weak confinement, i.e., $T_c^C > T_g^A$), the crystallization is preferred to microphase separation and the effect of microdomain constraints is weak. Generally, randomly distributed crystalline lamellar phases or spherulites are observed.[13,14] In opposite case (strong confinement, i.e., $T_g^A > T_c^C$), where the glassy amorphous regions are sufficiently stiff to restrict the crystallization and the crystalline domains are confined within the block copolymer microdomains e.g. sphere, cylinder, double gyroid, or lamellae.[15,16] Figure 1.5 schematically summarizes the phase separation mechanism in crystalline-amorphous block copolymer systems. The interplay between crystallization

and microphase separation can also generate complex microstructures, such as arrowhead lamellar, wavy patterns, and zig-zag lamellar phases.[17,18]

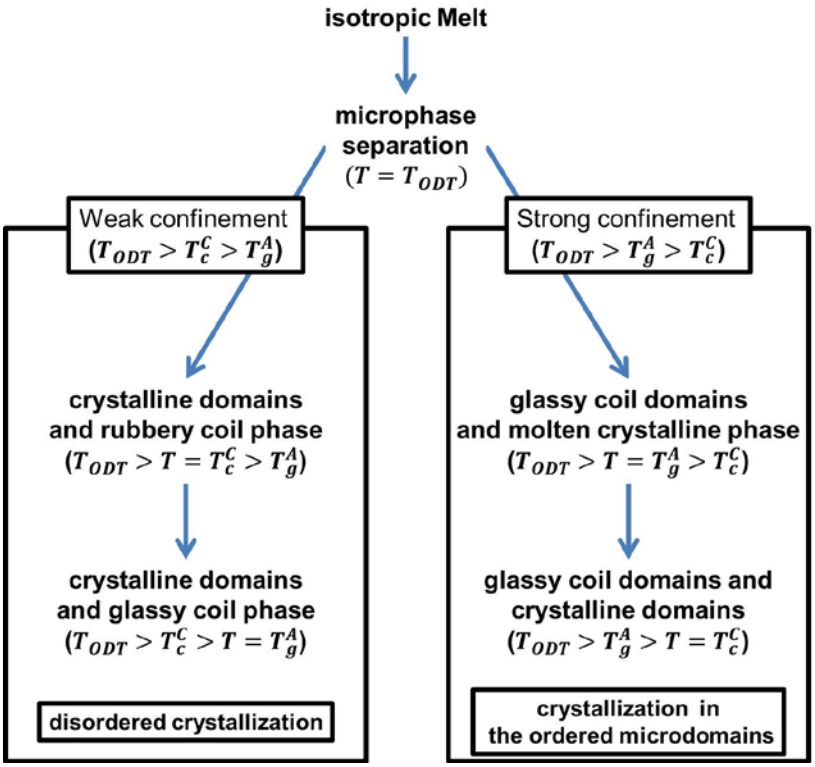

Figure 1.5 The phase separation pathways of crystalline-amorphous block copolymers.

1.1.5. Mechanical properties of block copolymers

The key factors to determine the physical properties of polymers are the chemical composition, chain architecture, molecular weight, and the glass transition temperature. For semicrystalline polymers, the melting point of the polymer also plays a critical role in the mechanical properties.

Block copolymers which consist of two or more chemically distinctive homopolymers display combined mechanical properties based on the key factors as mentioned. Figure 1.6 displays schematic plots of the mechanical properties for homopolymer blends and copolymers.[19] For example, when monomer A and monomer B

generate a random copolymer, the glass transition temperature of the random copolymer lies in between each glass transition of A and B and the polymer generally displays single T_g. When homopolymer A and B are miscible and generate a single phase blend, the blend has single T_g. By contrast, when the mixture of polymer A and B is immiscible, the blend shows two phases and has two T_g values. Likewise, an immiscible A-B block copolymer shows two T_g values resulting from each homopolymer A and B.

Considering that the mechanical properties of polymers have a strong dependency on temperature, both a random copolymer and a mixture of miscible polymers A and B have an averaged modulus behavior as a function of temperature. For a block copolymer or an immiscible blend A and B, it is generally possible to distinguish the modulus of each chain as a function of temperature.

Therefore, a block copolymer composed of immiscible two or more polymer chains retains the physical properties of each homopolymer and can have advantages over random copolymers in terms of tensile strength, bulk modulus, and viscosity as a function of temperature.

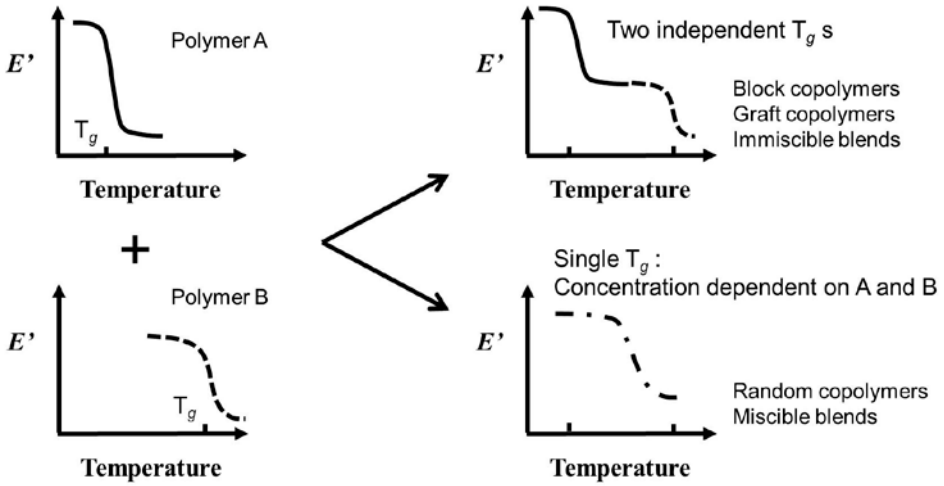

Figure 1.6 The relationship of the mechanical properties of homo- and block copolymers.

The effect of microdomain structures on viscoelastic properties in block copolymers will be discussed in Chapter 2.

1.1.6. Stereoregularity in polyolefins

The control of the stereoregularity (or tacticity) has emerged as a tool for synthesizing polymers with new properties. The original work of Natta demonstrated the different properties of polypropylene and the dependence on tacticity.[2] He discovered that the detailed synthetic conditions and catalyst can change the details of monomer insertion to the growing chain, leading to different tacticity and resultant changes in crystallinity, mechanical properties, and solubility. A schematic of the three basic forms of configuration of chain tacticity is shown in Figure 1.7.

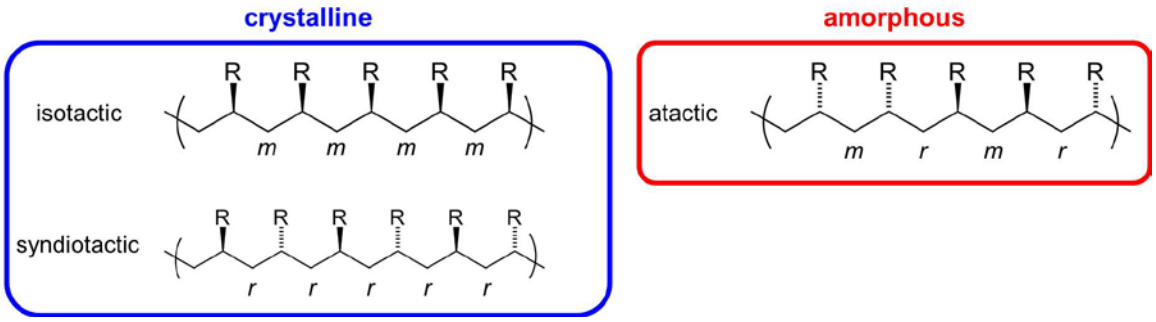

Figure 1.7 Representative stereochemical structure of polyolefin.

With the availability of stereochemical analysis[20,21] and the modification of ligands and activators, the ability to synthesize tailored olefin polymers has been greatly improved. In particular, polypropylenes have been extensively studied for decades as a model system.

Many attempts have been made to improve the mechanical properties of block structured polypropylene materials by varying chain architectures and ligand systems.[22,23] Yet, one of the key challenges, synthesizing discrete crystalline-amorphous block structures, has remained largely untouched.[24,25]

1.2. Motivation and Proposed Researches

The majority of the phase behavior in diblock copolymers has been studied using styrenic block copolymers and diene based polyolefin block copolymers.[26,27] In addition, the molecular weight range of those diblock copolymers is generally well above the order-disorder transition, i.e., where χN is large. While much of the recent work have been focused on finding systems that have a sub-10 nm domain size and exploring new hierarchical structures from coil-coil di- and triblock copolymers, relatively little effort has been dedicated to understanding the fundamental phase behavior near the phase boundary and the mechanical properties in crystalline-coil (i.e., crystalline-amorphous)

block copolymers.[28-30] Particularly, the structure-property relationships between two thermodynamically stable states, i.e., crystallization-driven phase separation and block incompatibility-driven microphase separation, remains relatively unexamined in polyolefin block copolymers.

It is important to explore the structure-property relationships in crystalline-amorphous diblock copolymers. Particularly, polyolefin diblock copolymer systems with crystalline-amorphous structure are desirable for the following reasons. First, polyolefin materials have been commercialized for decades and the fundamental understanding of the crystalline-amorphous system in homopolymers provides background for this class of materials. Polypropylenes, the second largest synthetic polymer in production, have been studied for decades. However, the material properties of well-defined crystalline-amorphous block polypropylene materials have remained relatively unknown in comparison with commercialized polypropylenes.[31] Secondly, unlike the phase behavior of amorphous-amorphous block copolymers, the phase behavior of low molecular weight crystalline-amorphous block copolymers has not been thoroughly addressed. Polyolefin materials that have simple chemical structures can be used as model systems to understand the phase behavior as well as materials properties.

To accomplish this project, several analysis techniques are required to assess the structure-property relationship in crystalline-amorphous olefin block copolymers. The basic concept of each technique will be discussed in a subsequent chapter.

Chapter 2. Experimental Techniques

2.1. Mechanical Properties of Materials

2.1.1. Stress-Strain relation

One of the most important physical properties in solid materials is tensile stress-strain behavior. The general stress-strain relations results from the uniaxial mechanical deformation. The external load causes a dimensional change of the material in both parallel and perpendicular to the applied load direction. By definition, the tensile stress (σ) and the tensile strain (ε) are given as

$$\varepsilon = \frac{L' - L}{L} = \frac{\Delta L}{L} \tag{5}$$

$$\sigma = \frac{F}{A} \tag{6}$$

where L and L' is the initial and final length of the specimen, respectively, F is the applied load to the specimen and A is the cross-sectional area of the specimen. The slope in the linear regime represents Young's modulus (E) (Figure 2.1).

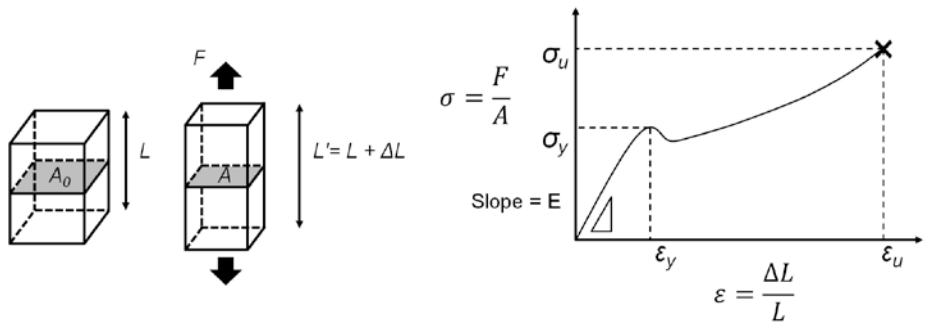

Figure 2.1 A schematic for uniaxial deformation and a generalized stress-strain plot.

As the external force increases, the stress increases linearly as a function of the strain. The linear region shows elastic behavior of a specimen. After the linear region, the material displays a non-linear stress-strain curve implying that the specimen undergoes plastic deformation. The transition point which is denoted by σ_y is the yield stress at the yield strain, ε_y. As the deformation continues, the specimen eventually breaks. This point determines the fracture tensile strength (σ_f) at the fracture tensile strain (ε_f).

When a polymer is subjected to a tensile load with a small deformation ($< \varepsilon_y$), the material tends to recover to initial length as soon as the external force is removed. For some applications require elastomers to exhibit no dimensional change after unloading a large deformation. The parameter, recovery after deformation, is generally used to evaluate the ability to return to the initial dimensions of the material. The recovery of the material is measured as a function of time. The usual testing method for recovery (ASTM D412) is that the specimen is under a specified deformation for a given period at a given temperature. After the deformation, the specimen is allowed to relax for 10 min. and the final displacement is measured. For the recovery after break, the recovery ratio is calculated as

$$Recovery\ at\ break, C = \frac{L_{break} - L_{final}}{L_{break} - L_{initial}} \times 100 \quad (7)$$

where L_{break} is the fracture elongation, L_{final} is the relaxed length for 10 min. after break, $L_{initial}$ is the initial length of the specimen.

2.1.2. Dynamic mechanical analysis (DMA) and rheology

Accurately determining material properties is important to characterize new materials for specific applications. Dynamic mechanical analysis (DMA) is one well-known method used to characterize the small strain mechanical properties.[32] Most polymers show distinctive characteristics such as glassy, rubbery, and viscous states. By changing the measurement time scale, the materials behavior can be discriminated in terms of the storage and loss modulus at a given temperature.

Briefly, the basis of the simple mechanics in elastic materials, the modulus for either tensile or shear force can be described as,

$$\sigma = E\varepsilon \quad \text{for tensile force} \quad (8)$$

$$\tau = G\gamma \quad \text{for shear force} \quad (9)$$

where σ and ε represent the stress (i.e., applied force per unit area, *F/A*) and strain (i.e., the displacement in relative to a given length, *ΔL/L*) for tensile force and τ and γ represent the shear stress (i.e., applied shear force per unit area, *F/A*) and shear strain (i.e., the angle relative to a given length, *tan* (*d/L*)), respectively.

The storage modulus is a measure of the elasticity of the material, whereas the loss modulus is a measure of the viscosity of the material. The general strain and stress as a function of time *t* and frequency ω can be expressed in Figure 2.2.

$$\varepsilon(t) = \omega\varepsilon_0 \sin(\omega t + \frac{\pi}{2}) \tag{10}$$

$$E' = \frac{\sigma_0}{\varepsilon_0}\cos(\delta) \ \ and \ E'' = \frac{\sigma_0}{\varepsilon_0}\sin(\delta) \tag{11}$$

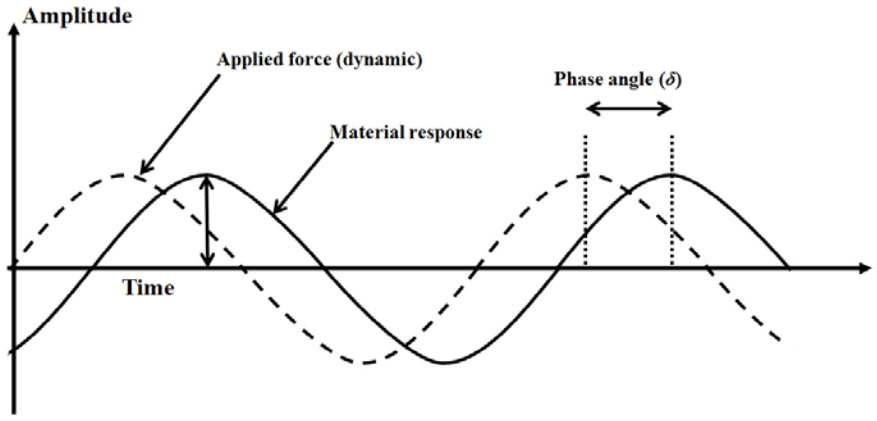

Figure 2.2 The schematic diagram of the relationship of the materials under the oscillating external force. The response time between the external force and the material is the phase lag (δ).

$$tan\ \delta = \frac{E''}{E'} \tag{12}$$

The ratio of the loss modulus to stored modulus is defined as a phase lag (tan δ), tan δ goes through a maximum at the glass transition temperature, T_g.

Block copolymers often exhibit distinct viscoelastic behaviors depending on their microstructure (spherical, cylindrical, or lamellar). Moreover, DMA has been applied to identify order-disorder transitions as well as order-order transitions in block copolymers. Figure 2.3 shows the distinct viscoelastic behavior of block copolymers having different

microphase separation morphologies. The shear elastic modulus (*G'*) is strongly influenced by the block copolymer microdomain structure and molecular weight. Additionally, the *G'* and frequency (ω) show a different power laws depending on the morphology.[33] When a block copolymer has spherical domains, the power law between *G'* and ω is α=0, which corresponds to solid-like behavior. As the volume ratio of one block increases, the microdomain morphology becomes hexagonally-packed cylinders and the viscoelastic response displays a power law of α=1/3. When the two blocks are of approximately equal volume fraction, the lamellar phase is dominant. At this stage, the mechanical response shows power law behavior with α=1/2. At high the frequency region, the viscoelastic behaviors of block copolymers having different microphase separations are similar to the homopolymers and the mechanical response is less distinguishable and shows frequency independent behavior (i.e., solid-like behavior).

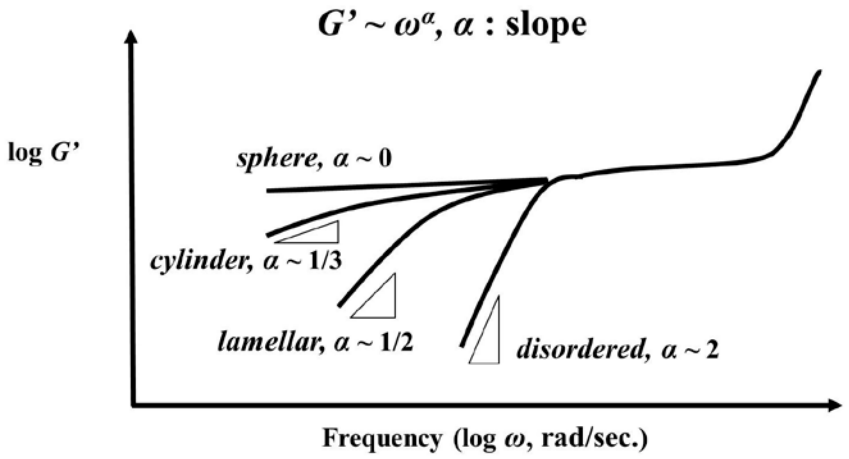

Figure 2.3 Viscoelastic behavior of block copolymers having different microphase separations.

In contrast to amorphous-amorphous block copolymer systems, crystalline-amorphous block copolymer systems have a more complicated phase separation behavior. For crystalline-amorphous block copolymer systems, either the crystallization-induced microphase or incompatibility-induced microphase separation governs the overall domain

morphology. The crystalline block length and the glass transition of the amorphous block both play a significant role in determining the microphase separation mechanism. Hence, viscoelastic properties for crystalline-amorphous block copolymers are more complicated in regard to the domain morphologies.[34-37]

2.2. Scattering Methods: Small and Wide Angle X-ray Scattering (SAXS / WAXS)

One powerful method to confirm the presence and type microdomains in block copolymers is X-ray scattering.[38-40] When scattering occurs from the atoms and crystal lattice and the detector is close to the sample, it is called Wide Angle X-ray Scattering (WAXS). When the scattering occurs from the larger domain such as particles and polymer domain structures, the detector should be located further away from the sample to collect the information at small scattering angles (i.e., Small Angle X-ray Scattering, SAXS). The instrument layout for X-ray scattering is shown in Figure 2.4.

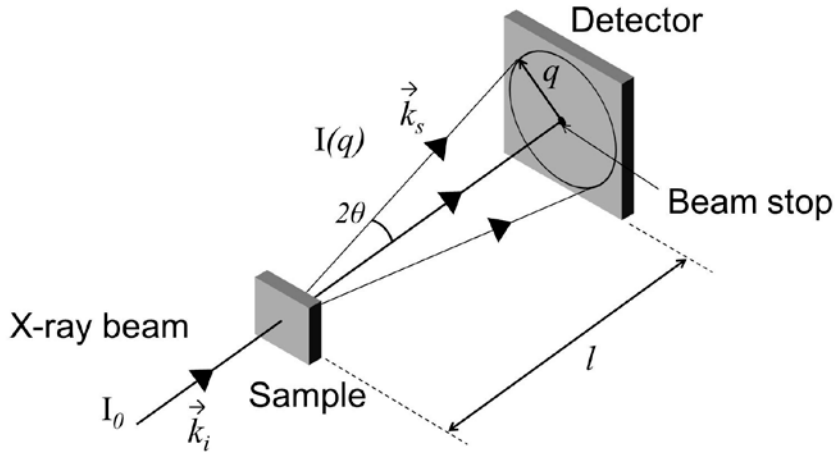

Figure 2.4 Schematic layout Wide/Small Angle X-ray Scattering (WAXS/SAXS). The incident beam (I_0) passes through the sample and the scattered beam (I_q) with scattering vector q is detected at distance l. The majority of the transmitted beam is blocked with beam stop. The scattering angle θ can be converted with scattering vector q.

The photons in the incident beam (I_0) are scattered from the sample as a function of scattering angle (2θ). The scattered beam from the sample is assumed to be elastic because the incident beam has high energy and the excitation in the sample is relatively low. Therefore, the magnitudes of the incident beam and the scattered beam can be written as,

$$|\overrightarrow{k_i}| = |\overrightarrow{k_s}| = \frac{2\pi}{\lambda} \tag{13}$$

In addition, the scattering vector q is defined as ,

$$q = \overrightarrow{k_s} - \overrightarrow{k_i} \tag{14}$$

The magnitude of q is given as,

$$q = \frac{4\pi}{\lambda} sin\theta \tag{15}$$

Small Angle X-ray Scattering (SAXS) is widely used for studying microphase separation of block copolymers, as the microdomain spacing is in the range of 1-100 nm. Wide Angle X-ray Scattering (WAXS) can detect crystalline structure in semicrystalline polymers. SAXS and WAXS are able to provide the average information on the microdomain spacing as well as the crystalline structure in crystalline-amorphous block copolymer systems by averaging over a relatively large volume due to the beam spot size and the sample thickness (>100 μm^3). The scattering technique can be combined with

temperature control, *in-situ* wide and small angle X-ray scattering (WAXS/SAXS) and is useful to identify self-assembly in crystalline-amorphous block copolymers.

For determining microphase separation and the dimensions of block copolymer domains, microphase structures give rise to scattering peaks that are characteristic of the structures. The primary scattering peak is generally related to the domain spacing of the microstructure. Based on Bragg's law for the periodic crystal system, the microphase structures are considered as macrocrystal systems due to the ordered spacing of the microdomains. The ratio of the scattering peaks in ordered phases of microdomains can be analyzed to identify the crystalline symmetry[41,42];

1. Lamellar phase (LAM) 1: 2: 3: 4: 5 : …
2. Double gyroid structure (GYR) $\sqrt{3}$: $\sqrt{4}$: $\sqrt{7}$: $\sqrt{8}$: $\sqrt{10}$: …
3. Hexagonally packed cylinders (HEX) 1: $\sqrt{3}$: 2 :$\sqrt{7}$:3: …
4. Body centered cubic spheres (BCC) 1: $\sqrt{2}$: $\sqrt{3}$: 2: $\sqrt{5}$: …

For the periodicity in the block copolymer can be obtained by Bragg's law and the scattering equation. Consequently, the domain spacing *d* can be expressed as,

$$d = \frac{2\pi}{q} \times n, (n = integer) \qquad (16)$$

2.3. Imaging Techniques: Atomic Force Microscopy (AFM) and Transmission Electron Microscopy (TEM)

Dynamic mechanical analysis and scattering characterization can be used to characterize the morphologies and properties in bulk state, while atomic force

microscopy (AFM) and transmission electron microscopy (TEM) are techniques to locally characterize the microdomain structures in block copolymers.[43]

AFM is generally used to measure the surface morphology of materials. A sharp tip is located on a cantilever of length 100-300 μm. A detector measures the deflection as the tip scans the sample surface. The measured deflection signal generates an image as a function of sample height and stiffness. Figure 2.5 is a schematic of an AFM instrument.

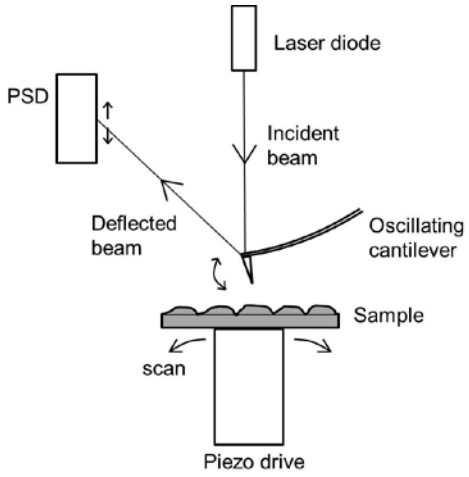

Figure 2.5 Schematic diagram of AFM.

While AFM displays the surface morphology and stiffness of materials with non-destructive mode, TEM images the internal structure of materials using an electron beam transmitted through the sample. The TEM resolution can be at the atomic level but is generally limited by radiation damage in soft materials. TEM can be used to characterize block copolymer domain morphology, orientation, and degree of ordering. For soft materials, especially polymeric materials, the image contrast results from sample thickness, electron absorption, and composition. Most polymer samples are prepared as thin films by casting, spin coating or ultramicrotoming, the main contribution to the contrast is the electron density of the components. For crystalline polymers, the

crystalline regions generally have higher density than the amorphous regions. Figure 2.6 is a schematic for a TEM and the bright field imaging mode.

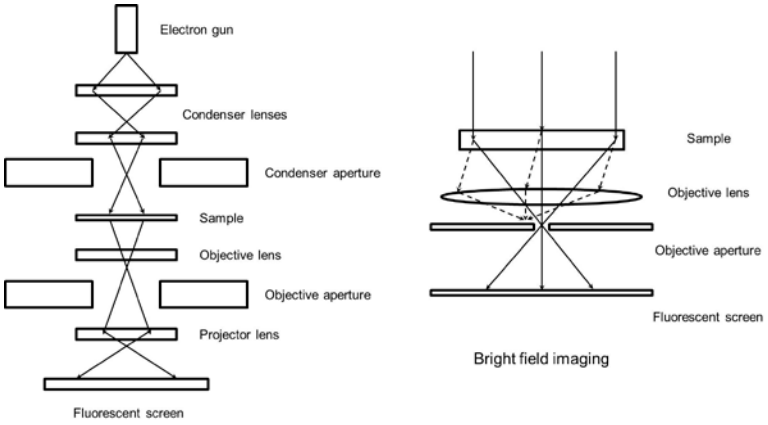

Figure 2.6 Schematic diagram of TEM and bright field imaging modes.

Chapter 3. Structure-Property Relationship of Stereoblock and Stereoirregular Polypropylenes

3.1. Background

Thermoplastic elastomers (TPEs) are materials that combine the thermoplastics and rubbers to obtain both rigidity and flexibility.[44] Polyurethane based TPEs are one of the commercialized TPEs since polyurethanes have introduced in 1950, followed by styrene-based TPEs. Generally, TPEs are composed of hard segments (high T_g or semicrystalline) and soft segments (low T_g and amorphous). Hard segments serve as physical cross-linking domains and soft segments provide the elasticity of the materials.

Among the number of TPEs, olefin based TPEs have major advantages over others due to the chemical stability, low density and cost effectiveness.[45] Taking advantages of the readily available olefin monomers, the considerable effort has been put on the new synthetic routes and catalytic systems in both scientific and technological areas. The structure-property relationship of the TPEs is the crucial aim for commercialization.

Ethylene and 1-alkene copolymers are representative olefin-based TPEs, utilizing crystalline-amorphous motif.[46] Depending on the concentration of 1-alkene monomer, ethylene-based copolymers can be either stiff or soft TPEs. Randomly distributed crystalline and amorphous structure, however, becomes a major huddle for the high temperature applications.[45]

Polypropylene based elastomers have great advantages over ethylene due to the higher melting than polyethylene.[47,48] Furthermore, polypropylene can have a crystalline as well as an amorphous structures based on the tacticity (stereoregularity).[2,49-52]

In 1953, Natta first discovered the different physical properties of polypropylenes, through controlling the chain microstructures.[2] A regular arrangement of methyl groups leads to high crystalline polypropylene (isotactic polypropylene). On the contrary, atactic polypropylenes have a random arrangement propylene sequences, resulting in amorphous chains. For decades, a variety of polypropylenes containing different level of stereoregularity and chain architecture have been synthesized such that polypropylenes can cover the wide range of applications.[31] To improve the mechanical properties, especially elastomeric properties, one of the challenges in polypropylenes is the synthesis of crystalline-amorphous block structures, ideally crystalline-amorphous-crystalline or consecutive multiblock structures.[53-61]

For this purpose, the crystalline blocks provide physical cross-linking domains while the amorphous blocks aid elastic deformation. Chien *et al.* reported on a series of crystalline-amorphous polypropylenes via controlling stereochemistry using coordination polymerization.[62,63] The proposed idea was that the alternating atactic and isotactic polymerization yields elastomeric polypropylenes using metallocene catalysts. Changing the reaction temperature produced polypropylenes with broad PDI (~2.0) and the materials showed an elastomeric behavior. The melting points of the materials, however, were below 100 °C indicating that the produced polypropylenes had lower content of crystalline isotatic PP.

Subsequently, Coates *et al.* introduced a strategy for stereocontrol using unbridged metallocene catalysts where the chiral / achiral isomerization generated isotactic-atactic block polypropylene elastomers.[23] Oscillation between isotactic and atactic polymerization rate was sensitive to the temperature and monomer pressure, altering the polymerization kinetics. By changing reaction temperature and propene pressure, the synthesized polypropylenes showed elastomeric properties having isotatic pentad content ranging from 6.3 to 28.1 %. The statistical modeling of the system also provided insight into the distribution of isotactic and atactic polypropylene sequences.[20,21,64-68] Still, the broad PDI (~2.0) and the broad range of the melting point of the materials remained major huddles to manipulate the elastomeric properties.

Even with the discovery of an oscillating catalyst for stereoblock polypropylenes, the precise control of the molecular weight, stereochemistry and block length remains challenging through single-site metallocene catalysts.[69,70] De Rosa and coworkers developed a series of metallocene catalysts having different architectures to control the stereoregularity and molecular weight.[24,71-75] The catalysts they used isotactic content of polypropylenes from the set of catalysts provided from 50 to 98 %. The mechanical properties as well as the thermal properties of polypropylenes were tailored as a function of the isotactic propene content. Moreover, the chain microstructure characterized from NMR was responsible for the crystal structures that might affect the thermal and the mechanical properties.

Although those progresses enable to obtain both elastomeric polypropylenes, both oscillating metallocene catalysts and a variety of metallocene catalysts are still limited. The non-living polymerization character of the catalysts causes broad PDI (>2.0) and the

random distribution of isotactc and atactic PP blocks does not result in precise control of chain architecture, which impedes the prediction of the structure-based mechanical properties in polypropylenes.

To overcome these limitations, Sita and coworkers demonstrated the discrete block architecture polypropylenes using methyl group degenerative transfer coordination polymerization via a living metallocene catalyst.[76] The concept showed that the frequency of methyl group transfer between active and dormant catalysts generates enantiomeric stereo-irregularity, leading atactic sequences. Furthermore, switching between active and dormant state of the catalysts enables to synthesize a discrete crystalline-amorphous-crystalline block sequences with a living polymerization character throughout the polymerization. The properties of a series of well-defined block structure polypropylenes showed fracture tensile strength over 15 MPa and greater than 1,500 % elongation. In addition to the tensile strength and elongation ratio, they reported that the chain architecture such as di-, tri-, and ter-block structure polypropylenes played a role in the fracture tensile strength.

Taking the advantage of the strategy to synthesize the discrete block architecture of polypropylene elastomers developed by Sita research group, it is valuable to investigate the structure-property relationship of the well-defined stereoblock polypropylenes and compare them with random structured stereoirregular polypropylene elastomers.

3.2. Experimental Setup

(a) General Description. All synthetic methods used in this work for stereoblock and stereoirregular PPs were described previously.[25,76] Distillation of chlorobenzene (PhCl) was performed with calcium hydride under the N_2 atmosphere. Polymer grade propene (Matheson Tri-gas, PA) was purified using sequential purification columns. The precatalyst, (η^5-C_5Me_5)$ZrMe_2$ [N(Et)C(Me)N(t-Bu)], and the methyl group transfer agent, (η^5-C_5Me_5)$ZrMe_2${N[$CH_2C(CH_3)_3$]C(Me)N(t-Bu)}, were prepared as we reported in a previous paper. For the cocatalyst, [$PhNHMe_2$][$B(C_6F_5)_4$] was purchased from Boulder Scientific and used without further purification. The synthesized polymers were characterized for molecular weight using gel permeation chromatography (GPC) using a Viscotek GPC system. Tetrahydrofuran (THF) was used as an eluent with a flow rate maintained at a 1.0 mL/min., 45 °C. Polystyrene equivalent M_w, M_n, and polydispersity index (PDI, M_w / M_n) were calibrated using Viscotek OmniSEC software and polystyrene standards (Polymer Laboratories). ^{13}C NMR spectra were obtained at 150 MHz using 30 mg of each polymer dissolved in 1,1,2,2-tetrachloroenthane-d2 as a solvent. The measurement temperature was fixed at 90 °C. The thermal analysis of each sbPP and irPP material was performed on TA Instrument Q1000 differential scanning calorimeter (DSC). All DSC samples were 5-10 mg and sealed in TA Instrument hermetic aluminum DSC pans. The samples were initially cooled down to -70 °C and then heated to 200 °C at a rate of 10 °C/min. After the initial heating was done to remove any thermal history and residual solvent effects, the cooling and heating cycle were repeated with the same manner to collect the melting and the crystallization temperatures. To obtain the

crystallinity for both sbPP and irPP materials (X_c), the heat of fusion (ΔH_f) of 100% crystalline PP is used 207 J/g from the literature.[77]

(b) Polymer Synthesis. The synthesized stereoblock and stereoirregular polypropylenes are summarized in Tables 3.1 and 3.2. The general synthetic method for both material sets are described in the previous work.[76,78] The basic concept to control the stereoregularity is the ratio of dormant state to active state of the catalyst. Previously, the Sita group has reported that the 100 % active state of the precatalyst produces a highly isotatic polypropylene using pentad analysis from ^{13}C NMR (%*mmmm*=0.71). By contrast, dormant state of the catalyst is configurationally unstable and undergoes epimerization that proceeds much faster than chain propagation. As a result, an atactic microstructure is produced from the catalyst when in the dormant state. Utilizing a rapid and reversible transfer of methyl groups between active (cationic) and dormant (neutral) catalyst, it is possible to control the number of isotatic sequence as a function of the activation level. The synthetic schemes of sbPP and irPP polypropylenes are described in Figures 3.1 and 3.2.

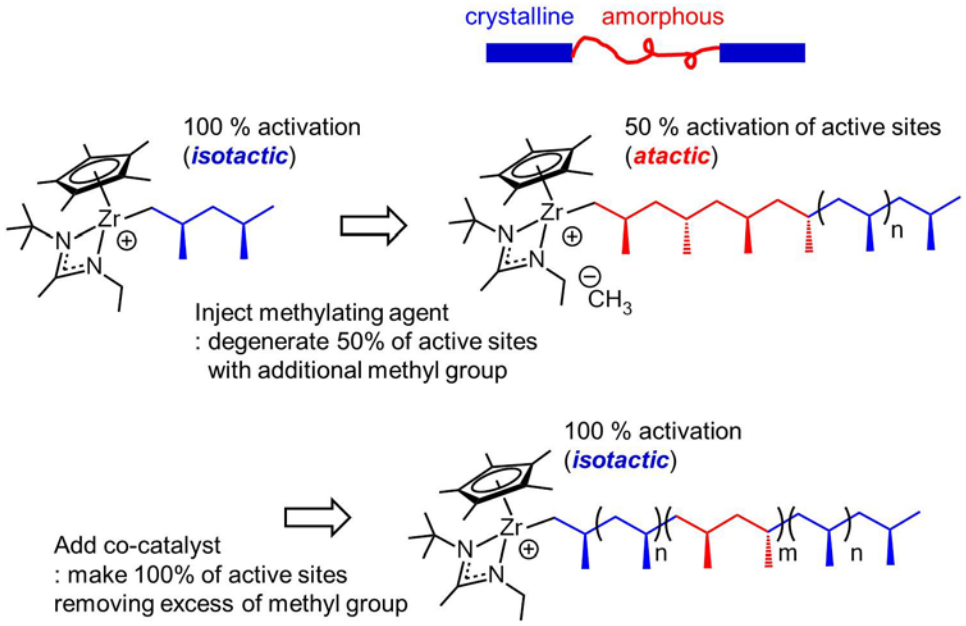

Figure 3.1 Synthetic scheme for stereoblock polypropylenes.

To obtain an *isotactic-atactic-isotactic* sbPP material, 19.9 mg (0.05 m mol) of the precatalyst, (η^5-C_5Me_5)$ZrMe_2$ [N(Et)C(Me)N(t-Bu)] was dissolved with 40.1 mg (0.05 m mol) of the cocatalyst, [$PhNHMe_2$][$B(C_6F_5)_4$], in a 250 mL Schlenk flask which contained a previously prepared 100 mL of PhCl at -10 °C. This stoichiometric amount of cocatalyst generates cationic active catalysts without any dormant species (100 % activation) resulting in an isotactic block. Subsequently, the propene was charged to 5 psi and maintained during the reaction. For sbPP-1 preparation, the first isotactic PP was synthesized for 2 hours. After 2 hours, 1 mL of aliquot solution was taken for the analysis, then, 11.0 mg (0.025 m mol) of the methyl group transfer agent, (η^5-C_5Me_5)$ZrMe_2${N[$CH_2C(CH_3)_3$]C(Me)N(t-Bu)} which was dissolved in PhCl was added into the reaction. At this point, the reaction proceeds through degenerative methyl group transfer where the dormant species undergo a metal-centered epimerization and generates stereoerrors. Thus, the resultant chain becomes atactic PP. After 20 hours for the second atactic block, 20.0 mg (0.025 m mol) of cocatalyst was added to remove the methyl

groups which were introduced by the methyl group transfer agent. In this step, the reaction was returned to 100 % activation condition. To obtain symmetric isotactic PP blocks on both chain ends, the whole reaction was quenched with acidic methanol after 2 hours. Subsequently, the reaction solution was precipitated in methanol and the polymer was dried under vacuum. During the reaction, the molecular weight for each aliquot was monitored using GPC. For other sbPP materials, the reaction times for both isotactic and atactic sequences were adjusted to control the ratio of the isotactic block and the total molecular weight.

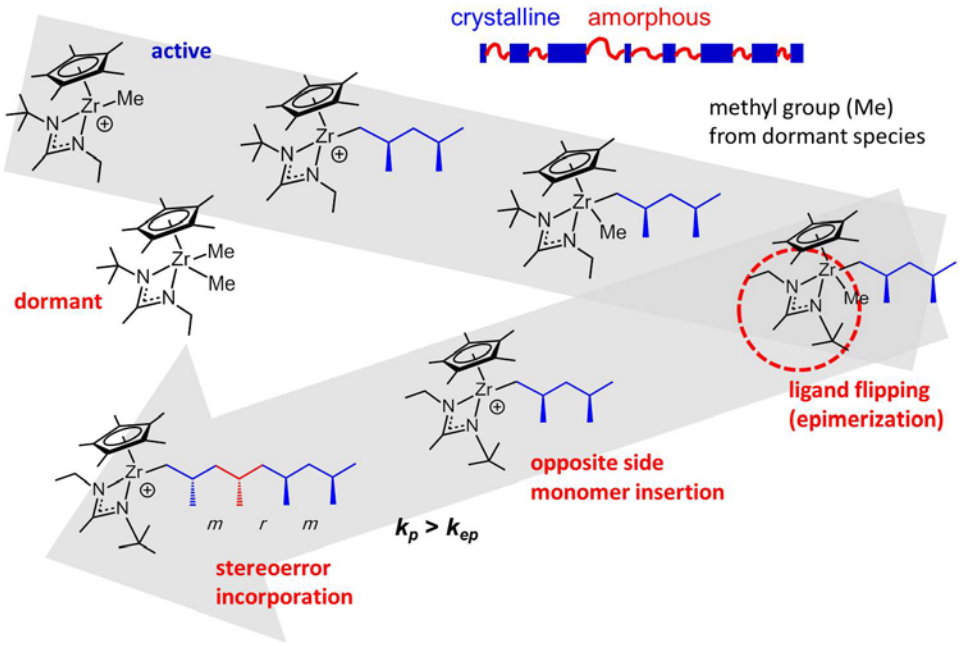

Figure 3.2 Synthetic scheme for stereoirregular polypropylenes.

To synthesize stereoirregular PP materials, the precatalyst, (η^5-C_5Me_5)$ZrMe_2$ [N(Et)C(Me)N(t-Bu)] and the cocatalyst, [$PhNHMe_2$][$B(C_6F_5)_4$] were used with a sub-stoichiometric ratios to control the activation level. For 95 % activated stereoirregular PP, 19.9 mg (0.05 m mol) of the precatalyst was dissolved in PhCl and 37.8 mg (0.047 m mol, i.e., 95 % of the amount of the precatalyst) of cocatalyst was added into 250 mL Schlenk

flask which contained a previously prepared 100 mL of PhCl at -10 °C. After the transfer of this yellow-colored catalyst mixture, the propene was charged at 5 psi and maintained during the reaction. After 60 hours, polymer solution was rapidly quenched with 1 mL of acidic methanol. To precipitate and purify the concentrated polymer solution, acidic methanol was employed. The white polymer obtained from the acidic methanol was dried under the vacuum overnight. In the same manner, 90, 85, and 80% activated stereoirregular PPs were obtained with controlled equivalent amount of the cocatalyst and reaction times.

(c) X-ray Diffraction. All the samples were measured in an as-prepared state and no further thermal annealing. 0.5 g of each irPP materials was mounted on the sample holder and the measurement was performed on Bruker D8 Advance system with LynxEye detector. The wavelength of Cu $K\alpha$ radiation was λ = 1.5418 Å and the scan angle was 5~60° with 0.05° steps. The data was collected at room temperature and the amorphous halo of each irPP materials was subtracted using amorphous PP as the background. The obtained profiles were fitted with Advanced TOPAS software. To obtain the crystallinity of irPP materials, the amorphous halo of each profile was fit and the degree of crystallinity was calculated by dividing the area of the crystalline diffraction peaks by the total area using Diffract Eva software (ver. 4.0).

(d) Mechanical Tests. All sbPP and irPP materials were prepared with a hot melt press equipment using 0.5 mm-thick mold at 100-150 °C based on the melting point from DSC. First, the polymer material was heated above the melting temperature for 30 min and then pressed with 20 K lbf for 20 min. After releasing the pressure, the sample was cooled to room temperature. The polymer film was prepared for the mechanical testing

using ASTM D638-5 dumbbell-shape cutter (sample dimension: 12.7 mm×3.175 mm×0.5 mm). Tensile test measurements were performed at room temperature (~25 °C) using an Instron 3345 tensile tester with pneumatic grips at an extension rate of 2 in/min. Recovery after break values were obtained followed the ASTM D412 protocol. For dynamic mechanical analysis (DMA), the film was cut to a rectangular shape (sample dimension : 5 mm×5.3 mm×0.5 mm) from the prepared hot melt press film and mounted in a tensile mode grip on a TA instrument Q 800 with a liquid nitrogen cooling system. The initial strain was set with 0.2 % (i.e., elastic region) and the frequency was fixed with 1 Hz having 0.01 N preload. The heating and cooling rate was set to 4 °C/min. and the each temperature point was maintained for 1 min. The obtained data was recorded at each temperature with 5 cycles from -60 °C to 100 °C. The maximum temperature was varied depending on the melting point of each material to prevent yield. The storage modulus, loss modulus, and phase lag (tan δ) were calculated using the Universal Analysis software of Q800.

3.3. Results and Discussions

The synthetic scheme for sbPP is shown in Figure 3.1. We previously reported the synthesis of crystalline-amorphous-crystalline sbPPs as a function of isotactic PP fraction.[25] As the length of isotactic PP decreases (i.e., the ratio of atactic PP increases), the overall crystallinity decreases sustaining triad distribution ratio (*%mm*) at constant in the end blocks. Even at low fraction of isotactic PP, the melting point remains the same as isotactic PP. In addition, the melting point is independent of the length of atactic PP middle block. Because the isotactic PP end blocks have constant %*mm* fraction, the

isotactic PP blocks crystallize with no discernable suppression by the atactic PP middle block. The general properties of sbPP materials are listed in Table 3.1.

Table 3.1 Characteristics of stereoblock polypropylene materials.

Sample	**wt % of *iso*PP**	**M_w / M_n (kg/mol)**	**PDI**	**% *mmmm* of *iso*PP**	**T_m (°C)**	**T_c (°C)**	**%*mm***	**%*mr***	**L_{isoPP}**	**X_c (%)**	**ΔH_f (J/g)**
sbPP – 1	12	256.0 / 200.2	1.28	0.710	-	-	0.823	0.127	14.96	-	-
sbPP – 2	24	251.3 / 206.1	1.22	“	101	-	“	“	“	0.3	0.7
sbPP – 3	36	249.6 / 195.6	1.28	“	99	39	“	“	“	3.0	6.2
sbPP – 4	50	292.6 / 220.4	1.33	“	104	52	“	“	“	7.7	16.0
sbPP – 5	14	268.5 / 205.6	1.31	“	106	-	“	“	“	0.2	0.4
sbPP – 6	23	181.2 / 140.6	1.29	“	102	47	“	“	“	1.8	3.7
sbPP – 7	24	129.9 / 117.3	1.11	“	101	45	“	“	“	2.2	4.5
sbPP – 8	44	119.8 / 102.0	1.18	“	106	57	“	“	“	7.9	16.3

By contrast, a series of irPP materials display a strong dependency of the melting point and crystallinity on the isotactic triad distribution ratio (%*mm*). The results of physical properties for a series of irPP materials are comparable to the conventional PP materials.[31] The presented synthetic scheme is shown in Figure 3.2 and the general properties of irPP materials are summarized in Table 3.2.

Table 3.2 Characteristics of stereoirregular polypropylene materials.

Sample	Activation Level (%)	M_w / M_n (kg/mol)	PDI	% *mmmm* of isoPP	T_m (°C)	T_c (°C)	*%mm*	*%mr*	L_{isoPP}	X_c (%)	ΔH_f (J/g)
irPP – 1	80	102.8 / 84.2	1.22	0.151	96	51	0.334	0.466	3.44	3.8	7.5
irPP – 2	85	160.6 / 135.8	1.18	0.488	102	59	0.668	0.252	7.33	7.6	15.7
irPP – 3	90	133.3 / 103.0	1.29	0.549	103	67	0.718	0.209	8.87	9.1	18.9
irPP – 4	95	87.8 / 64.2	1.37	0.649	105	71	0.785	0.155	12.12	17.5	36.2

The 100% activated catalyst generates 0.71 of stereoregularity (i.e., %*mmmm*), while sub-stoichiometric active catalysts undergo degenerative methyl group transfer. Due to the high rate of methyl group transfer in between active and dormant catalysts, the probability of enantiomeric stereoerror on active species changes as a function of the amount of methyl group in the system. By using degenerative methyl group transfer, the number of stereoerrors in these irPP materials can be tuned in a systematic manner. Randomly distributed stereoerror within polypropylenes reduces the consecutive isotactic sequence length, thus, the %*mmmm* varies as a function of the activation level.

In Table 3.2, the pentad analysis shows the stereoregularity of the irPP materials. As the activation level increases, the pentad ratio, the melting point, and the crystallinity increase. More importantly, the isotactic sequence length using triad analysis proves that high stereoregularity generates a longer isotatic sequence length ($<L_{isoPP}> = 2[\%mm] / [\%mr] + 2$) of up to 12 monomer units.[79] Considering the isotatic sequence length of 100 % activated isotatic PP (15 monomer units in Table 3.1), 95% activated catalyst gives a very similar isotactic sequence length in irPP-4 (12 monomer units). In addition, the melting point of irPP-4 is close to those of sbPP materials, which implies irPP-4 has very similar

properties to that of isotatic PPs. As expected, the low activation level (80 %) displays amorphous-like PP based on lower melting point and lower isotatic sequence length (ca. 3 monomer units).

Further investigation for the crystallinity of irPP materials was conducted using differential scanning calorimetry (DSC) and powder X-ray diffraction (XRD). The heat of fusion of the crystalline in irPP materials decreases as the activation level decreases. It is clear that the lower activation level generates shorter isotatic segments, which results in less crystalline polypropylene. Consequently, irPP-1 having the least amount of isotatic PP showed cold crystallization during the heating cycle in Figure 2.3. Likewise, the crystallization temperature during cooling cycle for irPP materials decreases as a function of the activation level.

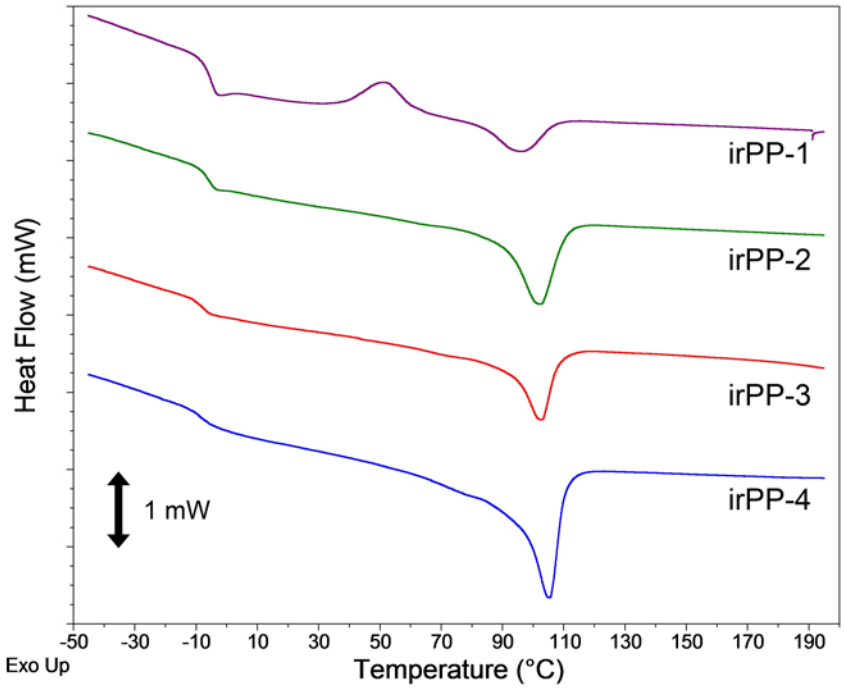

Figure 3.3 The melting point (T_m) of stereoirregular polypropylenes.

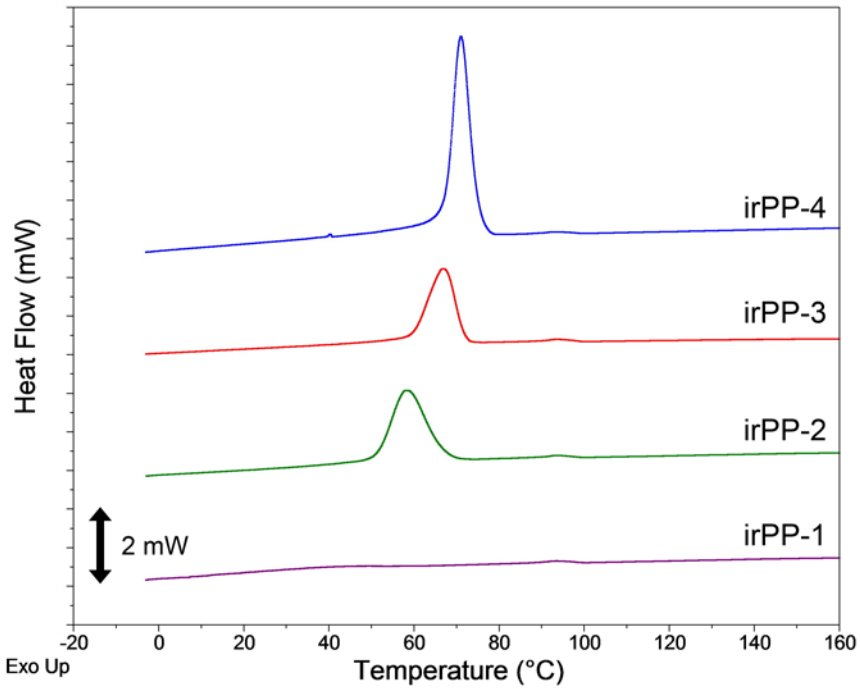

Figure 3.4 The crystallization temperature (T_c) of stereoirregular polypropylenes.

The correlation of the activation level and the crystallinity is also supported by XRD measurements. In general, polypropylenes have α and γ crystalline forms depending on the molecular weight and the microstructure. In addition, β form crystalline polypropylene is often displayed in certain temperature conditions and in strained α form crystalline polypropylenes.[31] Figure 3.5 represents the diffraction peaks of the irPP materials with different activation levels. With 95% activation irPP (irPP-4) shows 4 distinctive diffraction peaks in the range 2θ = 10-25°. The 2θ = 14.19°, 16.84° and 18.83° correspond to (110), (040) and (130) crystalline plane reflections, respectively and the fourth peak represents a mixture of (111), (131) and (041) reflections. The first 3 peaks indicate that irPP-4 crystallizes in α form. As the stereoregularity (%*mmmm*) decreases from 0.649 to 0.151, the total area of crystalline peaks and the intensity of 3 characteristic peaks decrease. Furthermore, the 2θ = 18.83° peak which arises from α form of isotactic

PP almost disappears in irPP-1. The calculated isotactic sequence length of each irPP material provides additional proof that short isotactic sequence length generates lower crystallinity. Table 3.3 summarizes the degree of crystallinity for each irPP materials obtained from DSC and XRD.

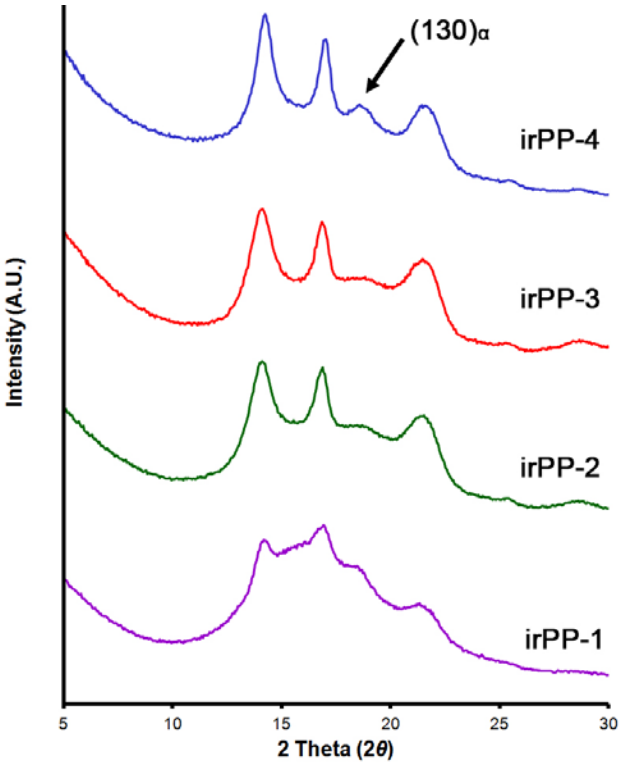

Figure 3.5 Powder X-ray Diffraction pattern of stereoirregular polypropylenes.

Table 3.3 Summary of crystallinities obtained from DSC and XRD for irPP materials.

Sample	**Activation Level (%)**	**% *mmmm* of isoPP**	**T_m (°C)**	**T_c (°C)**	***%mm***	***%mr***	**L_{isoPP}**	**X_c DSC (%)**	**X_c XRD (%)**	**ΔH_f (J/g)**
irPP – 1	80	0.151	96	51	0.334	0.466	3.44	3.8	9.8	7.5
irPP – 2	85	0.488	102	59	0.668	0.252	7.33	7.6	30.3	15.7
irPP – 3	90	0.549	103	67	0.718	0.209	8.87	9.1	35.4	18.9
irPP – 4	95	0.649	105	71	0.785	0.155	12.12	17.5	38.6	36.2

Consistent with DSC and XRD results and previous ^{13}C NMR data, it is reasonable that the higher stereoerror concentration generates more atactic sequences

along the chain and results in amorphous polypropylene having low crystallinity. Interestingly, γ form crystalline structure was not detected by XRD (2θ = 20.1°) in samples with high stereoerror level. Due to the very short isotactic sequence length, especially sample irPP-1, the material is probably amorphous rather than crystallized γ form crystals. Additionally, single peaks of T_m and T_c of irPP-1 96.0 °C and 51.4 °C in DSC indicate that the material crystallizes into α form without having a mixture of α and γ forms.

The mechanical properties of sbPP and irPP materials represent a clear contrast in stress-strain profiles. Most thermoplastic elastomers have block structures where the hard segments are on both ends and the soft segment is in the middle of the polymer chain. The hard segments provide rigidity and stiffness of elastomers and the soft segments offer flexibility. By varying the hard/soft segment ratio the mechanical properties can be tailored to a specific application. With the same analogy, sbPP materials have a discrete crystalline-amorphous-crystalline (i.e., hard-soft-hard) architecture. In comparison, irPP materials have randomized crystalline and amorphous segment sequences as a function of the activation level. To compare the structure-property relationships in sbPP and irPP materials, tensile strain measurements were conducted.

The stress-strain profiles of sbPP materials are shown in Figure 3.6. In general, most stress-strain profiles for the sbPP samples did not show a clear yield point where plastic deformation begins to occur. As the total fraction of isotactic PP increases from 12 to 44 %, the fracture tensile stress increases. Correspondingly, the fracture tensile strength increased to 15 MPa with high elongation ratio. The elongation ratios of most of sbPP materials are over 2,000 %. The Young's moduli of most of sbPP materials are

lower than 0.1 MPa. When the total isotactic PP fraction reaches 50 % (sbPP-4), however, the sbPP material exhibits a clear yield and breaks at low strain. The highest isotactic fraction sample (sbPP-4, isotactic PP 50 %) well exhibited a large Young's modulus at a short elongation and a clear yield point. Having the shortest atactic PP middle block sample sbPP-4 fractured at 500 % elongation ratio. It is reasonable that the sample with larger fractions of isotatic PP material exhibit higher stress during the elongation. When the size of isotactic PP blocks increases, the samples undergo plastic deformation after the yield with the crystalline blocks breaking and aligning along the tensile direction. In addition, the length of atactic middle block plays a role in the elongation properties. Figure 3.6 b represents the contribution of atactic middle block. When the atactic middle block increase from 56 % to 86 % (sbPP-5 through sbPP-8), the elongation ratio increases from 1,792 % to 3,438 %. By tuning the fraction of isotactic and atactic length in sbPP materials, it is possible to control the elastomeric properties. The mechanical properties of sbPP materials are summarized in Table 3.4.

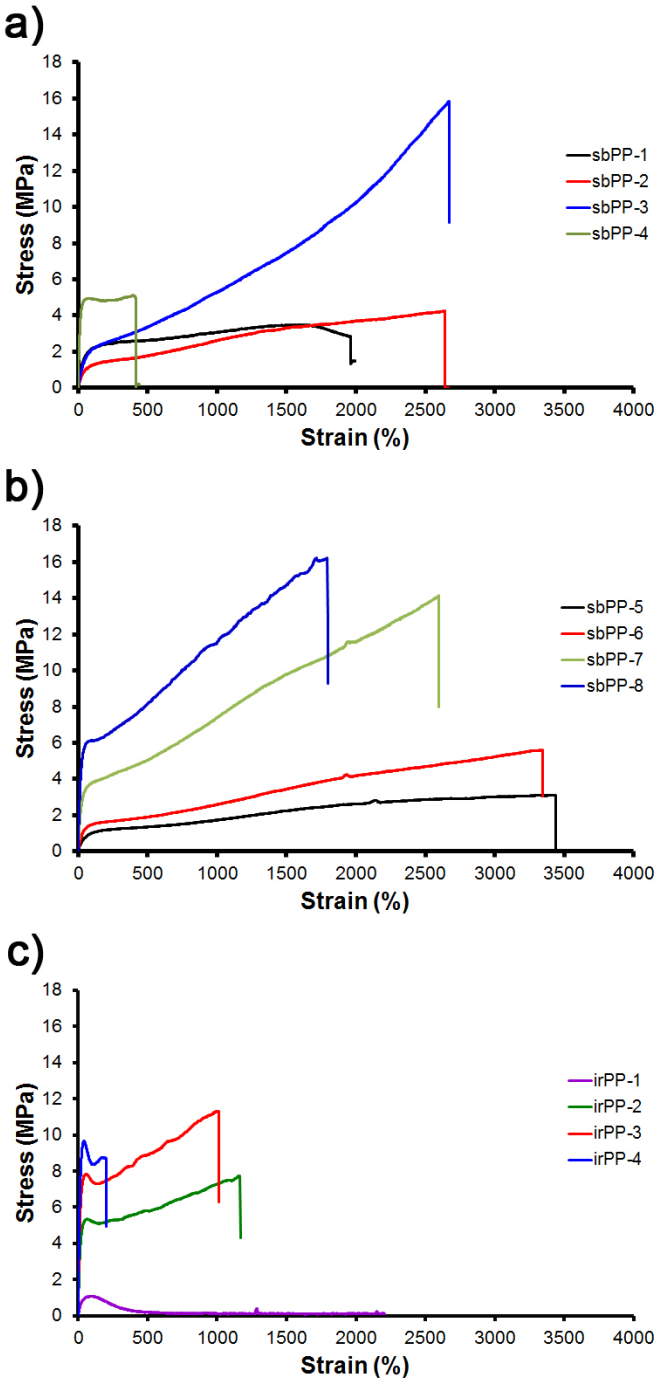

Figure 3.6 Stress-Strain curves of a) and b) sbPP and c) irPP materials listed in Table 3.1 and 3.2.

While sbPP materials represent larger fracture stress with longer elongation, irPP materials clearly exhibit yield (Figure 3.6 c) and undergo fracture at low strains. The highest fraction of crystalline isotactic PP is 15.9 % (irPP-4) synthesized with 95 %

activation level and displays a clear yield point at 50 % elongation. As the activation level decreases, the elongation at the fracture point increases. When the activation level reaches at 80 %, the amount of isotatic PP is only 3.3 % and the stress-strain curve of irPP-1 material exhibits low tensile strength and long extension. Neither a yield point nor a fracture point is observed, indicating irPP-1 is a mostly amorphous system. Previously, thermal properties of irPP-1 from DSC show a cold crystallization and low heat of fusion, which is indicative of a very low crystallinity polymer. The XRD profile of irPP-1 shows only small amount of crystalline isotactic PP. Although, irPP-1 has a small amount of crystalline isotactic PP, the material behaves largely like an amorphous system.

Measurement of recovery after the fracture illustrates clear differences between the sbPP and irPP materials. The measured value of recovery for all sbPP materials is larger than 90 %, thus, sbPP materials return to close to their initial dimensions after fracture. SbPP-1 has the lowest isotactic fraction of 12 % and exhibits the lowest fracture tensile strength as well as a tensile recovery after break of 94.6 %. As total isotactic fraction increases, the tensile recovery after the fracture point increases to 97 %. The highest value of recovery is 97.6±1.0 % from sbPP-3. As expected, sbPP-4 showing a yield point has 67.6 % of tensile recovery after fracture implying that sbPP-4 underwent plastic deformation.

While sbPP materials show excellent recovery of more than 90 % after fracture, irPP materials display significantly lower recovery of 60-70 %. IrPP-1 material with an isotactic sequence of 15 % (%*mmmm*=0.151) had the lowest tensile strength (< 2 MPa) and the lowest recovery after break (< 60 %) among the irPP materials. With increasing isotactic content, the recovery after the break increases up to 70 %. Overall, the recovery

after fracture for irPP materials is much lower than that of the sbPP materials, consistent with the observed yield point in irPP materials where crystalline domains orient during plastic deformation. Once the material undergoes plastic deformation, the initial crystallites break down and do not reassemble leading to low value of recovery.[80] Thus, irPP materials display a clear yield point and low recovery after fracture. SbPP materials, however, have long isotactic sequences at the chain ends and show higher tensile strength as well as high recovery.

Taking into account microstructure and property relationships, a well-defined long crystalline and amorphous block structure in the sbPP materials has a 'hard-soft-hard' structure and contributes stiffness and elasticity simultaneously. The cooperative effect of both long isotactic and atactic sequences in the sbPP materials increases fracture tensile strength and elongation. Even though the irPP materials have isotactic and atactic sequences, the crystalline and amorphous segments are relatively randomly distributed compared to those in the sbPP materials. Table 3.4 summarizes the mechanical properties of sbPP and irPP.

Table 3.4 Mechanical properties of sbPP and irPP.

Sample	T_m (°C)	%*mm*	%*mr*	X_c (%)	Modulus (MPa)	Yield (MPa)	Fracture Stress (MPa)	Fracture Strain (%)	Recovery after break (%)
sbPP - 1	103	0.823	0.127	-	0.070	-	2.8	1,960	92.3±1.2
sbPP - 2	100	"	"	0.3	0.061	-	4.2	2,639	96.2±1.5
sbPP - 3	106	"	"	3.0	0.097	-	15.8	2,667	97.6±1.0
sbPP - 4	118	"	"	7.7	0.511	56.9	4.9	411	67.6
sbPP - 5	106	"	"	0.2	0.043	-	3.1	3,438	96.8±0.1
sbPP - 6	102	"	"	1.8	0.063	-	5.6	3,347	97.8±0.5
sbPP - 7	101	"	"	2.2	0.487	-	14.1	2,595	98.7±1.0
sbPP - 8	106	"	"	7.9	0.510	80.9	16.2	1,792	94.4±0.5
irPP - 1	96	0.334	0.466	3.8	0.062	-	0.1	-	-
irPP - 2	102	0.488	0.668	7.6	0.460	56.0	7.7	1,161	75.1±3.8
irPP - 3	103	0.549	0.718	9.1	0.753	51.1	11.3	1,001	67.0±3.2
irPP - 4	105	0.649	0.785	17.5	0.945	39.4	8.7	196	75.4±20.0

To further understand the different stress-strain relationships in the sbPP and irPP materials, we used dynamic mechanical analysis (DMA) to explore the storage and loss modulus in both material sets. DMA can help identify crystalline and amorphous contributions as well as the glass transition temperature and also the storage and loss modulus as a function of temperature. Table 3.5 summarizes the plateau modulus at -50 °C and the glass transition temperature for sbPP and irPP materials.

Table 3.5 Summary of the plateau modulus and the glass transition temperature for sbPP and irPP materials obtained from DMA.

Sample	**T_m (°C)**	**%*mm***	**%*mr***	**X_c (%)**	**Plateau Modulus at -50 °C (MPa)**	**T_g (°C)**
sbPP - 1	103	0.823	0.127	-	1,459	10
sbPP - 2	100	"	"	0.3	1,537	10
sbPP - 3	106	"	"	3.0	1,899	10
sbPP - 5	106	"	"	0.2	813	6
sbPP - 6	102	"	"	1.8	1,884	10
sbPP - 7	101	"	"	2.2	1,790	10
sbPP - 8	106	"	"	7.9	2,618	10
irPP - 1	96	0.334	0.466	3.8	1,491	10
irPP - 2	102	0.488	0.668	7.6	1,822	6
irPP - 3	103	0.549	0.718	9.1	2,098	10
irPP - 4	105	0.649	0.785	17.5	2,185	10

Figure 3.7 displays the storage modulus as a function of temperature for the sbPP and irPP materials. Both the sbPP and irPP materials show the highest storage modulus value at -50 ˚C which is below the glass transition temperature. SbPP-3 containing 36 % isotactic sequence shows the highest storage modulus with a value of 2,000 MPa at -50 °C and the lower isotactic content sbPP-1 and sbPP-2 materials display the lower storage moduli. IrPP materials also show the decrease in the storage modulus as a function of isotactic content. The highest storage modulus is observed for irPP-4 with a value of 2,185 MPa and the lowest storage modulus is 1,500 MPa from irPP-1 at -50 °C.

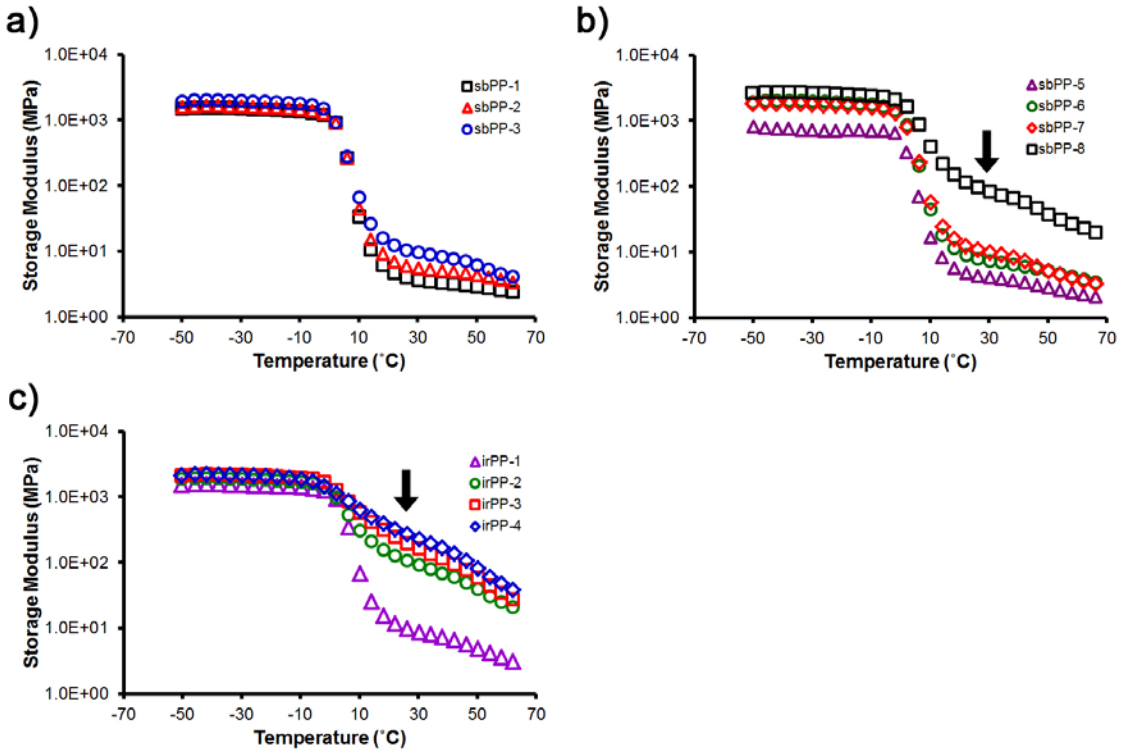

Figure 3.7 The storage modulus-temperature plots of a) and b) sbPP and c) irPP materials. The arrow in b) and c) indicates a residual storage modulus due to the crystalline domains.

As temperature increases, sbPP materials show a large drop in storage modulus of 3 orders of magnitude at about 10 ˚C at the glass transition temperature of sbPP materials. As the total weight fraction of isotactic PP increases, the storage modulus increases over the range of 10-70 ˚C. Conversely, the long amorphous segments in the middle block attributes to the lower storage modulus. For example, the lowest isotactic fraction sbPP materials (sbPP-1 and sbPP-5 with ca. 12 %) exhibit a storage modulus of less than 4 MPa. SbPP-3 and sbPP-7 with ca. 36 % have a storage modulus of about 8 MPa and finally sbPP-8 having 44 % of isotactic PP shows a storage modulus of 60 MPa in 10-70 ˚C. Moreover, sbPP-8 shows a plateau region in the storage modulus above the glass transition temperature in 30-50 °C. Presumably, the relatively large content of crystalline isotactic PP domains sustains the storage modulus at higher temperatures.

By contrast, irPP materials show a gradual loss of the storage modulus above the glass transition temperature. Similarly, the glass transition of irPP materials is also at about 10 °C where the storage modulus drops by 3 orders of magnitude. The storage moduli of irPP materials in the range of 10-70 °C is higher than the sbPP materials by about one order of magnitude (90-225 MPa), implying that the small crystalline segments contribute to the higher storage modulus under these conditions. As the overall isotactic fraction decreases, the storage modulus in 30-50 °C decreases. The irPP-1 (X_c = 3.8 %) shows the lowest storage modulus of about 8 MPa in 30-50 °C representing the similar profile with the sbPP materials.

It is expected that the storage modulus originates from immobile hard segments in the chain. Below the glass transition temperature (T_g = 10 °C), both crystalline and amorphous segments are frozen resulting in a high modulus. When the temperature is above the glass transition, but still below the melting point of the crystalline segments, only the amorphous segments are mobile, which reduces the storage modulus. Both materials sets have similar high storage moduli below the glass transition temperature. As temperature reaches the glass transition temperature for PP, the relaxed amorphous segments gain mobility and the material exhibits rubbery and flexible properties. In the case of sbPP, the discrete amorphous middle block has significant influence on the modulus decay at the glass transition. The crystalline isotactic PP blocks remain as hard blocks below the melting point, while the relatively longer amorphous block contributes to a lower storage modulus above the glass transition. As a result, the crystalline isotactic blocks serve physical cross-linking domains and the amorphous middle block provides elasticity. When the isotactic block fraction increases (i.e., atactic block fraction

decreases), sbPP materials show plastic behavior. While most sbPP materials show elastomeric behavior, the modulus behavior of sbPP-8 (44 % of isotactic PP) is similar with those of irPP materials with a 60 MPa storage modulus in at 50 °C. The modulus-temperature relationship of sbPP-8 shows a profile comparable to high isotatic fraction irPP materials. Thus, the relatively short amorphous atactic PP block in sbPP-8 is responsible for the similar storage modulus change with experimental conditions.

By contrast, irPP materials have a higher storage modulus than sbPP materials above the glass transition temperature. Due to the randomly distributed amorphous segments between the crystalline segments, the amorphous segment length in irPP materials is relatively short, resulting in low elasticity. Consequently, irPP materials still retain their stiffness and display higher storage modulus in the range of 10-70 °C.

The ratio of loss modulus to storage modulus, the phase lag (tan δ), reveals that the glass transition for both sbPP and irPP materials is observed at around 10 °C supported by the peak maximum tan δ. Likewise the storage modulus-temperature relationship, the peak maxima in the tan δ for sbPP materials correlates with the sharp storage modulus drop at 10 °C (Figure 3.8 a and b). In addition, the tan δ at 10 °C is larger than 1.0 implying that the contribution of longer amorphous atactic PP block plays a role in the larger loss modulus. The value of tan δ of sbPP materials ranges from 1.0 to 1.8 at 10 °C. Not surprisingly, sbPP-8 having 46 % of isotactic PP displays a lower value of tan δ (~0.6) at 10 °C due to the longer isotactic PP blocks.

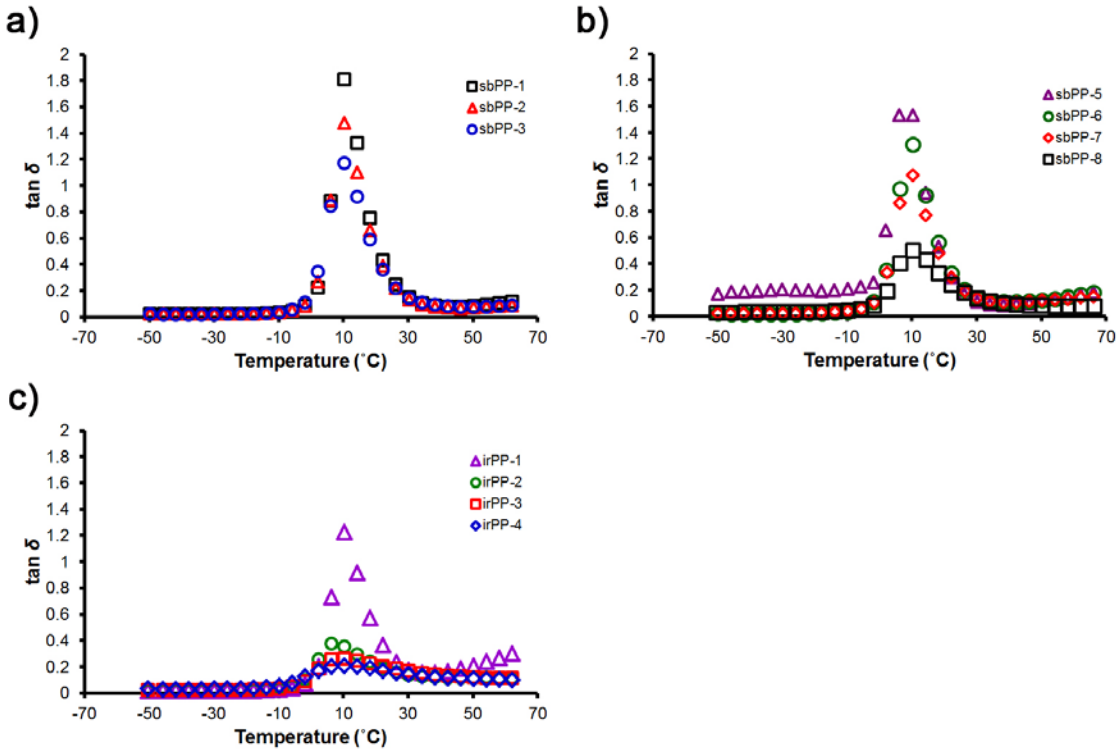

Figure 3.8 The phase lag (tan δ) for a), b) sbPP, and c) irPP.

The irPP materials show different values of the peak maxima depending on the isotactic content (Figure 3.8 c). Depending on the activation level of the catalyst, the total number of the incorporated stereoerrors generates the atactic sequences, which disrupts the isotatic PP sequences into randomly distributed small crystalline blocks. The randomly placed amorphous segments play a role in the tan δ peak maxima. IrPP-1 has very short isotactic segments and exhibits tan δ maxima of ~ 1.2 at 10 °C while irPP-4 having longer isotactic segments displays tan δ maxima of ~ 0.2 at 6.2 °C.

Since the tan δ reflects the relative chain motion as a function of temperature, it is possible to determine either elastic or viscous behavior of the materials. The storage modulus indicates elastic motion of the material and the amount of stored energy. In addition, the loss modulus represents the energy dissipation.

In a hard-soft-hard block structure, the rubbery amorphous block predominantly contributes to the energy dissipation and resulting in loss modulus. For sbPP materials, the tan δ indicates higher value of energy dissipation than the irPP materials due to the discrete long atactic middle block. In addition, the low activation level irPP (irPP-1) having large amount of atactic content shows similar behavior with that of sbPP-1 having 12 % isotactic PP. Other irPP materials have lower tan δ values, which imply a stiffer character due to the short amorphous segments. At 0.2 % elongation and 1 Hz frequency reveals that the molecular motion of irPP and sbPP materials with tan δ >1.0 exhibit viscoelastic behavior due to the large portion of atactic PP. By contrast, the irPP having tan δ <1.0 shows solid-like behavior due to the short atactic PP sequences.

Based on the results from DMA, we can differentiate the structure-property relationships for sbPP and irPP materials. The storage modulus-temperature of sbPP and irPP materials below the glass transition temperature shows very similar behavior. Above the glass transition temperature, sbPP materials exhibit a sharp decrease of storage modulus whereas irPP materials demonstrate a more gradual decrease over the temperature range 10-70 °C. The main distinction of modulus-temperature behavior for sbPP and irPP materials is the consecutive long amorphous PP sequences. For the 44 % of isotactic fraction material (sbPP-8), the modulus after the glass transition exhibits a gradual decrease, which is similar to the behavior of the irPP materials. For irPP-1 with the lowest fraction of isotactic segments, the modulus-temperature displays a similar profile with sbPP materials. The presence of long amorphous segments in both sbPP and irPP-1 materials result in a sharp decrease of the storage modulus after the glass transition temperature. The tan δ-temperature relationships also indicate that the long amorphous

segments contribute to the large loss modulus. When the fraction of isotactic block increases in sbPP materials, tan δ decreases from 1.8 to 0.6 indicating that the storage modulus from isotactic block increases relative to the loss modulus from the short atactic block at the glass transition temperature.

The phase lag (tan δ) provides a measure of the glass transition temperature as well as chain motion. The well-defined and long atactic segments in sbPP materials result in tan δ >1.0 whereas the randomly distributed short atactic segments in irPP materials result in tan δ <1.0 at the glass transition temperature. It is clear that the longer atactic segments, the larger loss modulus resulting in larger value of tan δ.

The modulus-temperature relationships from DMA are consistent with the stress-strain data from the tensile tests. When the crystalline fraction is increased, the irPP materials become rigid and undergo yield. The subsequent plastic deformation causes low recovery after deformation due to the crystalline disruption. In addition, the short elongation in irPP materials is due to the short atactic segments in the chain. The gradual decrease of the storage modulus and the low tan δ < 1.0 at the glass transition support a random structure of short amorphous segments in irPP materials restricting the flexibility of the chain. When the fraction of isotactic segments decreases, e.g. irPP-1, the modulus-temperature behavior is comparable to sbPP materials. Although the fraction of isotactic (or atactic) is the factor that can be used to tune the mechanical properties in these materials, it is not possible to obtain large tensile strengths and high value of elongation in irPP materials. By contrast, the presence of long atactic sequences between crystalline isotactic sequences in sbPP materials provides flexibility and long crystalline blocks offer both higher fracture strength and elongation. The modulus-temperature relationships from

DMA show that sbPP materials retain both stiffness and flexibility. The tan δ >1.0 at the glass transition temperature originates from the long amorphous block. The sbPP sample with a relatively short amorphous middle block (44 % isotatic fraction) shows a similar modulus-temperature behavior to the irPP materials. This result indicates that the elastomeric behavior of sbPP can be tuned using the ratio of the rubbery middle block.

Additional comparison between sbPP and irPP materials was conducted using viscoelastic property measurement near the melting point for all materials. Waymouth and coworkers reported that block structured elastomeric polypropylenes displayed better stability of crystalline hard domains than an isotactic/atactic blend system.[81] They claimed the crystalline domains in block structure can retain the segmental connectivity and provide a higher plateau modulus as a function of temperature. Thus, it is valuable to compare the flow properties of discrete block structured sbPP and random structured irPP materials as it has important applications polymer to processing methods such as extrusion, injection molding, and blow molding.

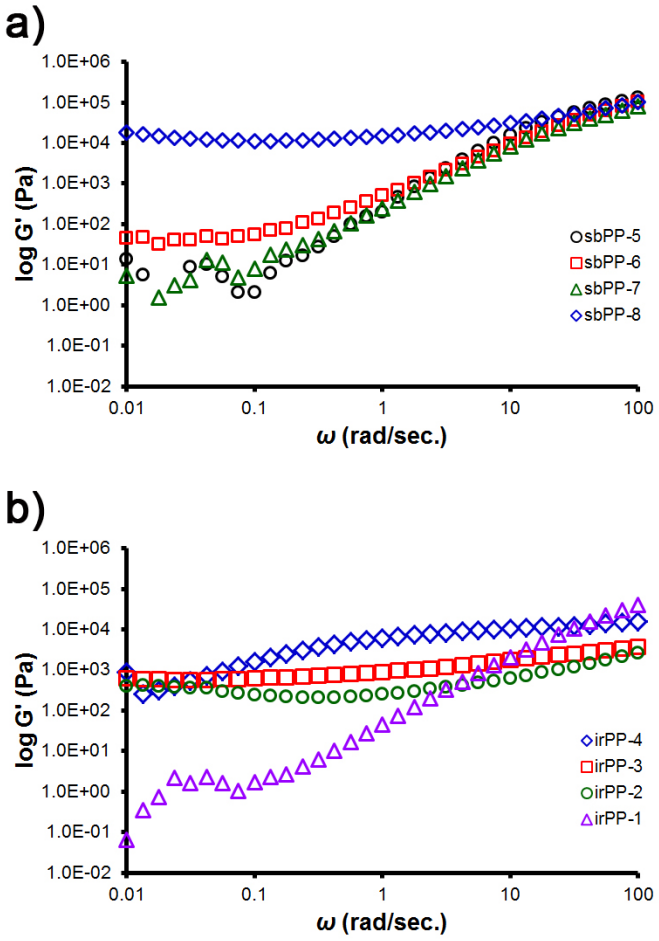

Figure 3.9 Representative viscoelastic properties of a) sbPP and b) irPP at 105 °C.

Figure 3.9 shows the shear storage modulus as a function of frequency. Materials having a higher melting point than the experiment temperature (T = 105 °C) display higher shear storage moduli regardless of chain architecture. It is known that the shear storage modulus strongly correlates with chain architecture, the molecular weight and polydispersity. Generally, larger molecular weight materials show higher storage modulus due to the larger numbers of chain entanglements. In addition, polydispersity of the polymers affects the viscoelastic properties.[82] Since both sbPP and irPP materials are linear chain with relatively similar polydispersity (~1.3), the effect of polydispersity on the viscoelasticity is negligible. Thus, the crystalline and amorphous contribution to the

shear storage and shear loss modulus can be considered. Both sbPP and irPP materials with higher isotactic fraction show higher shear storage modulus in the terminal frequency regime. Particularly, sbPP-8 with 7.9 % crystallinity shows the highest storage modulus among sbPP materials, possibly due to the contribution of the remaining crystalline segments. Similarly, irPP materials display higher storage modulus in the terminal frequency regime than irPP-1. The crystallinity of irPP-2, 3, and 4 is 7.6, 9.1, and 17.5 % respectively, which is responsible for the higher storage modulus at 105 °C.

Based on these viscoelastic measurements at 105 °C, sbPP materials with low crystallinity (<7.9 %) show low storage modulus suggesting that the sbPP materials exhibit viscous liquid behavior. IrPP materials, however, maintain the high storage modulus with the contribution of larger fraction of isotactic segments.

3.4. Conclusions

In summary, we measured the mechanical properties of the discrete block architecture stereoblock polypropylenes (sbPP) synthesized via a degenerative methyl group transfer living coordinative polymerization. For comparison, the stereoirregular polypropylenes (irPP) were synthesized by controlling the number of the activated catalyst complexes. Thanks to the living polymerization system, we were able to tune the fraction of isotactic and atactic segments in either block or random structure with narrow polydispersity.

High values of elongation ratio and fracture tensile strength are observed for sbPP materials, whereas, the irPP materials exhibit a yield point and relatively low elongation. SbPP materials with low isotactic fraction (12 and 14 %) exhibit 2.8 and 3.1 MPa fracture

strength at 2,000-3,000 % elongation. Further increase of the isotactic fraction leads to 16 MPa of facture strength at 1,800-2,700 % elongation maintaining 92-98 % recovery. By contrast, the irPP materials, analogous to commercial polypropylenes, exhibit less than 1,500 % elongation and plastic deformation. In addition, the recovery ratio of irPP materials is only in the range of 67-75 %.

The disparity in both stress-strain relationships and recovery for sbPP and irPP materials originates from the chain structure. A well-defined 'crystalline-amorphous-crystalline' block structure provides elastomeric properties with high fracture strength at high elongation. In contrast, irPP materials have randomly distributed crystalline and amorphous segments in the chain. Due to the lack of long amorphous segments, irPP materials cannot undergo long elongation and exhibit yield and plastic deformation.

DMA results for sbPP and irPP materials were measured as a function of temperature. The storage modulus of sbPP and irPP is similar at about 2,000 MPa below the glass transition temperature (T_g = 10 °C). However, sbPP and irPP exhibit different modulus-temperature behavior above T_g in the range of 10-70 °C. SbPP materials with 12-36 % of isotactic fraction display flexibility with a modulus of about 8 MPa. At an isotactic fraction of 44 %, sbPP shows more rigid properties with storage modulus of 60 MPa at 30-50 °C implying that the short amorphous block does not contribute to flexibility. For irPP materials, the storage modulus at 30-50 °C is about 90-225 MPa. This result also indicates that the lack of long amorphous segments in irPP materials is responsible for the rigid properties.

The phase lag (tan δ) further characterizes the dissimilarity of sbPP and irPP materials at the glass transition temperature (T_g = 10 °C). The long amorphous segments in sbPP materials provide flexibility resulting in a large loss modulus, which leads to a value of tan δ of about 1.0-1.8 at 10 °C. At an isotactic fraction of 44 %, the material exhibits rigid properties with tan δ of about 0.6. The peak maximum of tan δ for irPP materials is consistent with the rigid properties with a value of tan δ of about 0.2-0.4 at 10 °C. Much like sbPP materials, irPP with low isotactic fraction (irPP-1) displays tan δ of about 1.2 at 10 °C.

The well-defined crystalline-amorphous-crystalline block structure polypropylenes have advantages over random structure polypropylenes exhibiting a greater range of mechanical properties and tunability of those properties as a function of composition.

Chapter 4. Phase Behavior in Crystalline-Amorphous Block Copolymers

4.1. Background

The morphology of crystalline-amorphous block copolymers has been investigated for years due to the interaction between the two phase transitions of crystallization and microphase separation which gives rise to a structural richness at various length scales. Unlike the microdomain structures in fully amorphous state block copolymers of spheres, cylinders, double gyroid, and lamellae), crystallization of crystallizable block can generate semicrystalline lamellae [83,84], weakly-ordered crystalline lamellae [85-87], or randomly distributed lamellae. In addition, 'zig-zag' morphologies and 'wavy pattern'[17], even frustrated crystallization[88] structure have been observe in crystalline-amorphous block copolymer systems.

It is generally accepted that the final solid-state morphologies in crystalline-amorphous block copolymer systems is controlled by three key temperatures: the glass transition temperature of the amorphous block, T_g^A, the crystallization temperature of the crystalline block, T_c^C, and the order-disorder transition temperature of the block copolymer, T_{ODT}.[11,12] The strong confinement regime occurs when $T_{ODT} > T_g^A > T_c^C$, where the crystalline block is confined within the block copolymer microdomains.[15,89-94] In contrast, in the case of weak confinement, $T_{ODT} > T_c^C > T_g^A$, crystallization occurs when the amorphous block is still above T_g and a large crystalline structure is observed overriding any block copolymer microphase structure.

Theoretical models to explain the microphase separation of crystalline-amorphous block copolymer were first introduced in the early 1980s, yet, it was not demonstrated experimentally until the mid 1990s. Di Marzio *et al.*, Whitmore and Noolandi, and Vilgis and Halperin investigated the correlation between phase separation and crystallization in crystalline-amorphous block copolymer systems.[95-97] Based on these theoretical models, researchers were able to estimate the morphology. The domain periodicity D can be estimated using N_t, the total degree of polymerization of block copolymer and N_a is the degree of polymerization of the amorphous block, with the prediction that $D \sim N_t N_a^{1/3}$ for a symmetric block copolymer system.

Cohen *et al*. first showed an example in the strong-confinement regime for the phase behavior in crystalline-amorphous block copolymers with a series of polystyrene-*block*-hydrogenated polybutadiene polymers.[15] They showed a series of diblock copolymers that exhibited a variety of morphologies depending on crystallization pathways by annealing at different temperatures. Subsequently, Hamley *et al.* and Weimann *et al.* also demonstrated confined crystalline structures within well-defined microdomain structures.

Crystalline-amorphous block copolymer systems where the phase separation in the weak confinement condition ($T_{ODT} > T_c^C > T_g^A$) have been investigated with respect to crystallinity, crystallization kinetics, and crystalline orientation. Nojima *et al.* reported that the crystallization of the crystalline block is dependent on the block copolymer microdomain size.[13,98,99] In addition, a crosslink of rubbery amorphous matrix can restrict the crystalline and the crystallinity of the crystalline block. Depending on the crystallization conditions, Nojima *et al.* found that the crystalline domains confined

within the block copolymer microdomain structures exhibit lower crystallinity and lower melting point. Bates *et al.* and Register *et al.* synthesized a series of olefin-based crystalline-amorphous block copolymers, including polyethylene-poly(ethylene-*co*-propylene) (PE-PEP), polyethylene-poly(ethyl ethylene) (PE-PEE), and polyethylene-poly(3-methyl-1-butene) (PE-PMB) block copolymers.[16,34,100-102] These materials were synthesized with polydienes (e.g. 1,4-butadiene and 1,4-isoprene), then, saturated by hydrogenation. The work focused on crystallization within the confined block copolymer microdomains. They also examined that the viscoelastic behavior of molten block copolymers and how it is governed by the microdomain structure.

Further classifications of crystalline-amorphous block copolymer systems includes weak segregation[16,103-105] and strong segregation[14,99,102,106,107] depending on the segregation strength (determined by χN). When the crystalline block crystallizes in a weak segregation system in the weak confinement regime, the crystallization occurs with little confinement by the rubbery amorphous block and the block copolymer microdomain structures are largely disrupted. As a result, crystalline lamellae are the dominant observed morphology. In a strong segregation system in the weak confinement regime, the crystalline lamellae can be confined by the rubbery amorphous matrix. Register *et al.* categorized the crystalline-amorphous block copolymer system into three regimes: breakout, templated, and confined.[14] The author demonstrated three different microphase separation behaviors based on the ratio of χN at the crystallization temperature (T_c) to the order-disorder transition temperature (T_{ODT}).

Considerable effort has been made to understand the crystallization and the kinetics in crystalline-amorphous block copolymers, yet, little work has been done on the microphase separation and physical properties, especially at low molecular weight.

In this chapter, we have examined the microphase separation behavior in crystalline-amorphous olefin block copolymers that are synthesized via a combination of living coordination polymerization and living cyclopolymerization. Using a living zirconium based metallocene catalyst we have synthesized a series of poly(1-hexene)-poly(methylene-1,3-cyclopentane) (PH-PMCP) block copolymers which gives an amorphous PH block and a crystalline PMCP block. Depending on the crystalline PMCP ratio, the PH-PMCP materials demonstrate either crystallization-driven microphase separation or (normal) microphase separation. The morphology has been characterized by AFM and TEM.

4.2. Experimental Setup

a) General Description. All synthetic methods for PH-PMCP block copolymers were described previously.[108] Distillation of chlorobenzene (PhCl) was carried out over calcium hydride under the N_2 atmosphere. 1-hexene and 1,5-hexadiene monomers (Sigma Aldrich) were dried over a Na/K amalgam in gas tight storage tubes for 3-5 days. After the distillation, all monomers were transferred under vacuum with three freeze-pump-thaw degassing cycles.

The precatalyst, $(\eta^5\text{-}C_5Me_5)ZrMe_2$ [N(Et)C(Me)N(t-Bu)], was prepared as described in a previous paper.[109] For the cocatalyst, $[PhNHMe_2][B(C_6F_5)_4]$, was purchased from Boulder Scientific and used without further purification. Synthesized

polymers were characterized using gel permeation chromatography (GPC) using a Viscotek GPC system. Tetrahydrofuran (THF) was used as an eluent and the flow rate was maintained at a 1.0 mL/min. at 40 °C. M_w, M_n, and M_w/M_n were calibrated using Viscotek OmniSEC software and polystyrene standards (Polymer Laboratories). $^{13}C\{^1H\}$ NMR spectra were obtained at 150 MHz using 1,1,2,2-tetrachloroenthane-d_2 as a solvent at 110 °C. The thermal analysis for all block copolymers was performed with TA Instrument Q1000 differential scanning calorimeter (DSC). All DSC scans were taken using 5-9 mg of polymer in sealed in TA Instrument hermetic aluminum DSC pans. All samples were run using a heat-cool-heat cycle over the temperature range -70 ˚C to 200 °C at 10 °C/min. The first heat cycle was done to remove any thermal history and residual solvent, the subsequent cooling and heating cycle were done using the same conditions to measure the melting and the crystallization temperatures.

b) Polymer Synthesis. All polymerizations were carried out in a glove box. The reaction solvent, chlorobenzene (PhCl, 20 mL), was cooled to -10 °C and the precatalyst, (η^5-C_5Me_5)$ZrMe_2$ [N(Et)C(Me)N(t-Bu)], and the cocatalyst, [$PhNHMe_2$][$B(C_6F_5)_4$], were dissolved in PhCl at the ratio of 1.01 to ensure complete activation. Sequential polymer blocks were obtained by first adding 1-hexene for 2 hours followed by the addition of 1,5-hexadiene for an additional 1 hours. The molecular weight of each block was controlled by the amount of monomer present based on the kinetics of poly(1-hexene) and poly(methyl-1,3-cyclopentane). A small (<1 mL) amount of poly(1-hexene), PH, was removed and quenched for analysis immediately prior to the addition of the second monomer. Polymer samples were quenched in ca. 500 mL of acidic methanol (10 % HCl by volume). Samples were washed and filtered with MeOH and then dried under vacuum

at 25 °C until constant weight was observed. The molecular weight of each polymer was measured using gel permeation chromatography (GPC) (Viscotek TDA) equipped with a column oven. The differential refractometer detector and the four columns (T2500, T3000, T4000 and T5000) were maintained at 40 °C. Tetrahydrofuran (THF) was used as the eluent at a flow rate of 1.0 mL/min. The number-average molecular weight (M_n) and weight-average molecular weight (M_w) were obtained using Viscotek OmniSEC software.

c) Nuclear Magnetic Resonance (NMR). All samples were recorded using 30-40 mg of sample in 1,1,2,2-tetrachloroethane-d2 at 110 °C with a Bruker AVIII-600MHz NMR spectrometer operating at 150 and 600 MHz, equipped with a Bruker 5 mm C13/H1 dual probe with Z gradient. ^{13}C $\{^1H\}$ NMR spectra were collected under the following conditions: 45° pulse; without NOE; relaxation delay, 2.0 s; >9K transients.

d) Differential Scanning Calorimetry (DSC). The thermal properties of the block copolymers were obtained using a DSC Q1000 (TA Instruments). Nitrogen was used as the purge gas at 50 mL/min. The T_m, T_g, T_c and heat of fusion (ΔH) were measured using heat-cool-heat cycles at 10 °C/min. All values were taken after the first heating cycle to remove previous thermal history.

e) Powder X-ray Diffractometry (XRD). X-ray diffraction spectra of all samples were carried out with Bruker D8 Advance powder diffractometer with LynxEye detector at ambient conditions. All polymers were measured in the bulk state after thermal annealing for 12 hours. The wavelength, λ, of Cu Kα radiation was λ = 1.5418 Å and the scan angle was 5-60° with 0.05° steps. The data profiles were collected with built-in software (Advanced TOPAS).

f) Phase-Sensitive Tapping Mode Atomic Force Microscopy (ps-tm AFM). The surface morphology analysis was performed on a Multimode AFM with Nanoscope IIIa controller (Digital Instruments) in tapping mode. Both height and phase-shift data were obtained with a silicon etched tip (Nanosensors, spring constant k = 25-55 N/m, resonance frequency f = 292-377 KHz) under ambient conditions. All samples were dissolved in toluene (1 wt %) and spin-coated at 2,000 rpm onto Si substrates. Si substrates surfaces were cleaned with 7:3, H_2SO_4 : H_2O_2 "piranha" solution. Film thickness was obtained by using Gaertner ellipsometer for 3 different spots on each sample. Spin-coated film thicknesses were between 30-35 nm. All AFM samples were measured before and after annealing at 60 °C for 12 hours.

g) Transmission Electron Micrography (TEM). The cross-sectioned block copolymer thin films were sectioned with Ultramicrotome (Cryo Leica EM UC6) at -140 °C. All block copolymers were mounted on aluminum pins and annealed at 60 °C under the vacuum for 12 hours. After annealing, the mounted samples were quenched and kept in liquid nitrogen to vitrify the morphologies. The quenched polymers were quickly transferred to the cryotome when the temperature reached at -20 °C to prevent the crystallization. Cross-sectioning was carried out with diamond knife (Diatome 30°) to obtained sections with 40-60 nm thickness. All films were collected on carbon coated TEM grid and stored at -20 °C. Prior to imaging, TEM grids were warmed up to room temperature and quickly placed in the TEM grid holder. The block copolymer microdomains were examined at 100 kV on JEOL JEM 2100 LaB6 without staining.

4.3. Results and Discussions

Poly(1-hexene)-poly(methylene-1,3-cyclopentane) (PH-PMCP) di- and tri- block copolymers were synthesized using a combination of living polymerization and living cyclopolymerization as previously reported.[108] On the basis of the previous work, a series of poly(1-hexene)-poly (methylene-1,3-cyclopentane) (PH-PMCP) olefin block copolymers were synthesized as described in Figure 4.1 and the material properties are summarized in Table 4.1.

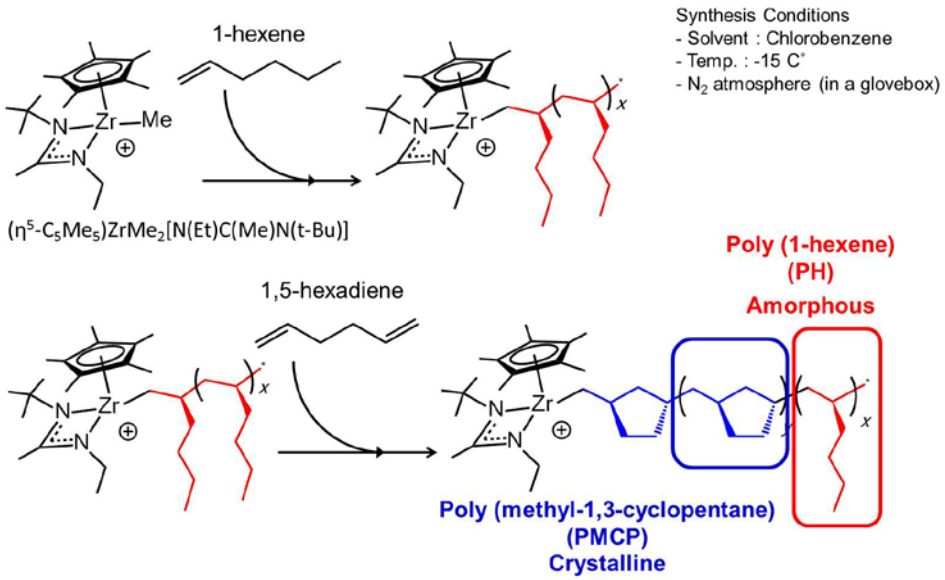

Figure 4.1 Synthetic scheme of PH-PMCP block copolymer.

All block copolymers have narrow PDI values implying that the probability of non-reacting first block is negligible. In addition, the glass transition temperature of the PH block (T_g <-40 °C) is much lower than the crystallization temperature of the PMCP block (T_m >10 °C), indicating that the PH-PMCP block copolymers fall into the weak confinement regime.

Table 4.1 Basic properties of crystalline-amorphous olefin block copolymers.

Sample	Mn of PH (kg/mol)	Mn of PMCP (kg/mol)	Mn of PH-PMCP (kg/mol)	f_{PMCP} (mole fraction)	Φ_{PMCP} (volume fraction)	PH T_g (°C)	PMCP T_m / T_c (°C)	M_w/M_n
1	21.6	10.3	31.9	0.21	0.28	-43.9	-	1.10
2	17.7	16.6	34.3	0.26	0.43	-44.9	-	1.28
3	12.6	14.5	27.1	0.41	0.48	-44.2	79.7 / 23.5	1.12
4	10.7	17.5	28.2	0.55	0.59	-45.9	73.3 / 11.3	1.18
5	11.4	4.2	15.6	0.20	0.23	-50.7	66.4 / 23.7	1.04
6	8.9	6.6	15.5	0.35	0.37	-45.4	-	1.08
7	8.0	6.3	14.3	0.37	0.39	-43.5	54.9 / 14.0	1.11

Living coordination polymerization of 1-hexene and living cyclopolymerization of 1,5-hexadiene were varied to control the total molecular weight and the block ratio. The narrow polydispersity indices (PDI) and monomodal GPC traces of all block copolymers indicate a living coordination polymerization for each monomer. Additionally, narrow PDI and monomodal GPC traces (Figure 4.2) indicate that the cyclopolymerization of 1,5-hexadiene for the second block has highly linear polymerization kinetics. Dimerization between the pendant group and the active catalyst (Figure 4.3) is negligible. Further signature of the living cyclopolymerization of 1,5-hexadiene will be discussed later in conjunction with NMR data. The thermal properties, T_g, T_m, T_c and the heat of fusion (ΔH), demonstrate that the block copolymers in this study are in the weak confinement condition (i.e., $T_{ODT} > T_c^C > T_g^A$) The matrix material, PH block, exhibits low glass transition temperature of about -40 °C. As the crystalline PMCP fraction increases to higher than 0.4, melting and crystallization temperatures for PMCP are observed using DSC. ΔH increases as the crystalline PMCP fraction increases for both high (ca. 30 kDa) and low (ca. 15 kDa) molecular weight block copolymers. In contrast, the lower PMCP fraction (<0.4) of block copolymers show no endothermic

peaks by DSC, which indicates crystallization is suppressed due to the presence of the long amorphous PH block. Crystallization suppression is verified with two homopolymer PMCP materials (6 kDa and 20 kDa) by measuring T_m and T_c. The two homopolymer PMCP materials have comparable molecular weights with those of the PMCP blocks in samples 2 and 6 (Table 4.1) and show melting points of 95 °C and 73 °C, respectively.[110,111] Based on the DSC profiles for the two PMCP homopolymers and the PH-PMCP block copolymers, a large PH fraction in the block copolymer suppresses PMCP crystallization, leading to the reduction or absence of endothermic and exothermic DSC signals.[112] Sample 4 shows T_m and T_c while sample 2 shows the absence of detectable T_m and T_c. Similar trends can be observed in samples 6 and 7.

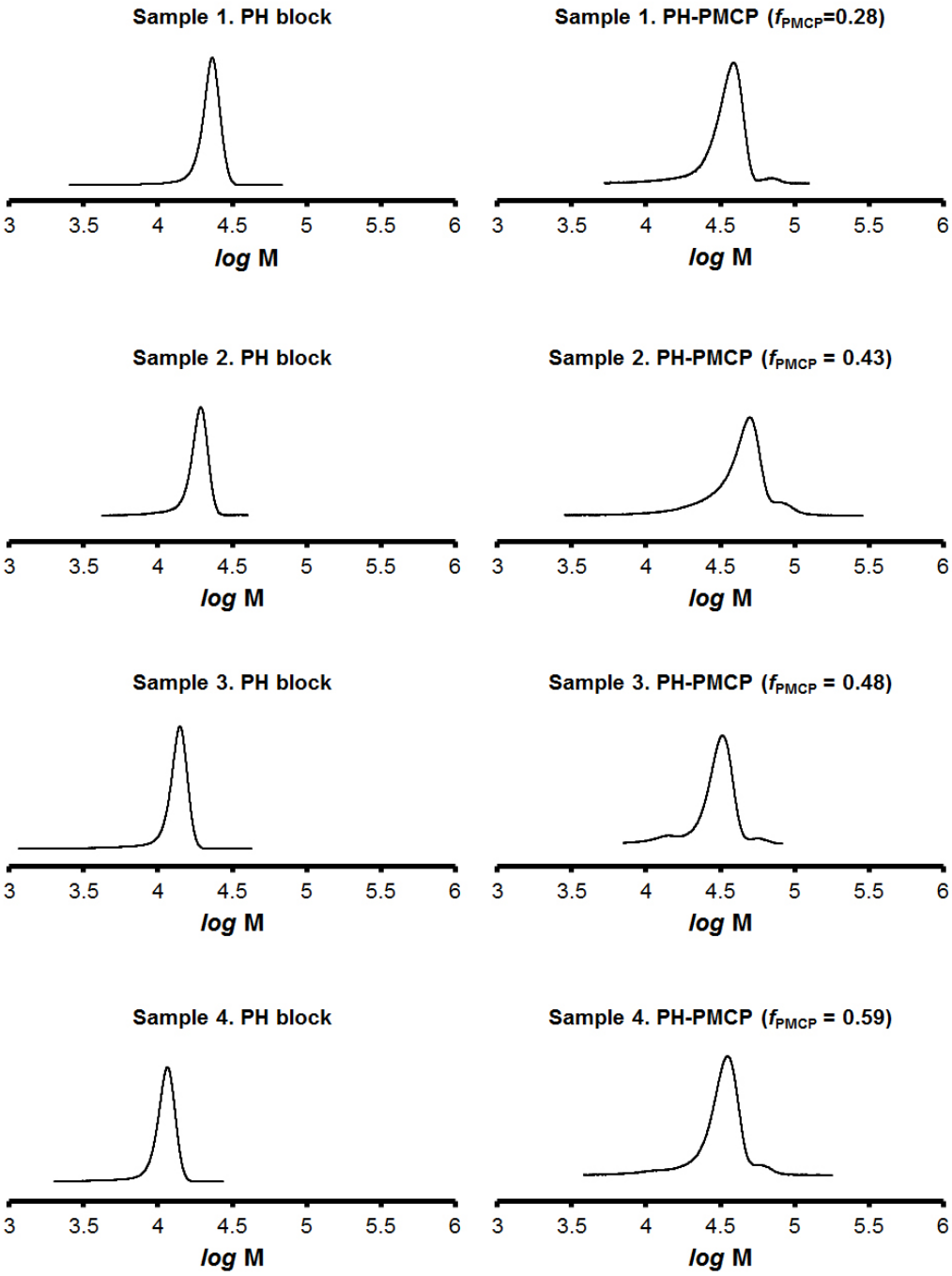
Sample 1. PH block
Sample 1. PH-PMCP (f_{PMCP}=0.28)
Sample 2. PH block
Sample 2. PH-PMCP (f_{PMCP} = 0.43)
Sample 3. PH block
Sample 3. PH-PMCP (f_{PMCP} = 0.48)
Sample 4. PH block
Sample 4. PH-PMCP (f_{PMCP} = 0.59)
3 3.5 4 4.5 5 5.5 6
log M

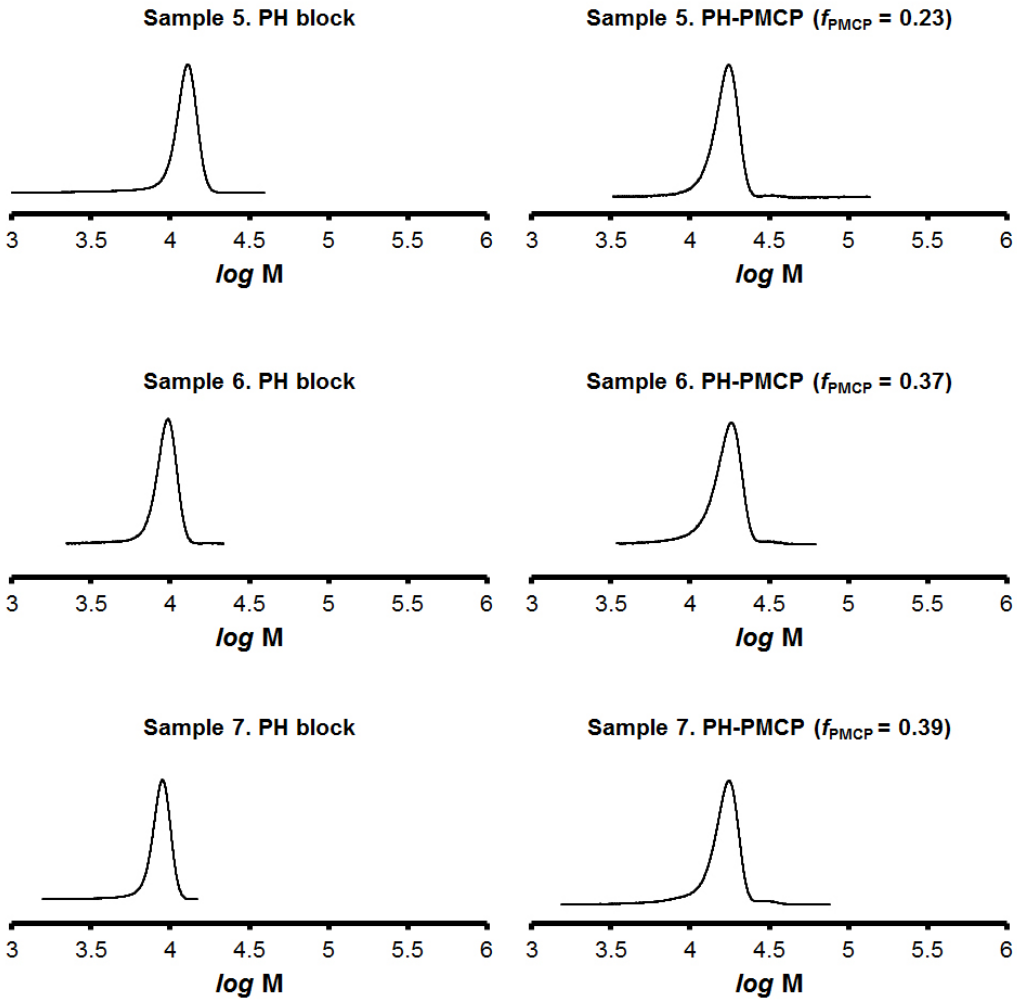

Figure 4.2 Normalized Gel Permeation Chromatography (GPC) traces of crystalline-amorphous olefin block copolymers listed in Table 4.1. All PH blocks were synthesized as a 1st block with aliquots taken after complete polymerization, subsequently, 1,5-hexadiene were added as a 2nd block.

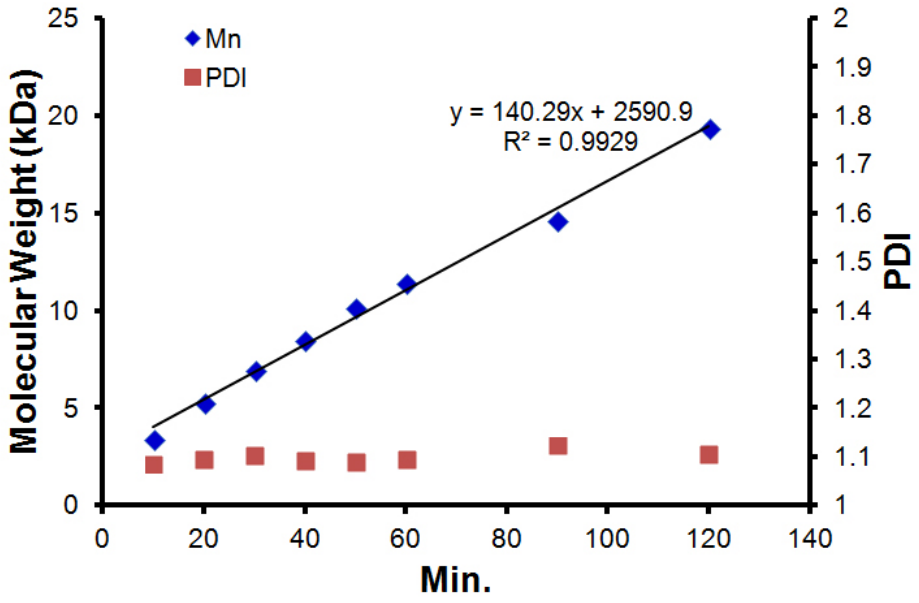

Figure 4.3 The cyclopolymerization rate of 1,5-hexadiene via living coordination.

The cyclopolymerization of 1,5-hexadiene using the homogeneous Ziegler-Natta catalyst has a rigid 5-membered ring in the main backbone, which provides an enhanced chain stiffness as well as a crystallinity[113] The zirconium-based metallocene catalyst in this study also generates a similar crystalline PMCP.[114-116] It is important to characterize the chain structure of PMCP. Based on the ^{1}H NMR of homopolymer PMCP (Figure 4.4), the mole ratio of vinyl group (4.9-5.0 and 5.5-5.7 ppm) can be calculated. Since the total number of protons from the vinyl groups and 5-memberd ring is 20 and the number of protons in the vinyl region is 3, 17 protons contribute the intensities 0.0-2.1 ppm.

$$I_{17\ protons} = 116.91 + 99.53 + 21.22 + 33.45 + 3.24 + 9.67 = 286.72$$

$$I_{1\ proton} = \frac{286.72}{17} = 16.87$$

For the intensity the region 0.0-2.1 ppm, we need to subtract the portion from the vinyl group and the intensity from the PMCP is then 168.66 (I=286.72-16.87×7). Calculating the ratio to the vinyl group,

$$\frac{2.95}{3}:\frac{168.66}{10}\ (vinyl\ group:PMCP) = 0.98:16.87$$

The fraction of vinyl group is,

$$fraction = \frac{0.98}{0.98 + 16.87} = 0.055$$

Therefore, the ratio of the vinyl group in homopolymer PMCP is 5.5%. Statistically, the vinyl group ratio varies from 2-6 % since the cyclopolymerization of 1,5-hexadiene does not undergo 100 % cyclopolymerization. In general, however, the probability of the cross-linking through the vinyl group is relatively low in block copolymerization. Figure 4.4 shows a representative ^{13}C NMR spectrum of sample 2 having 43 vol. % of crystalline PMCP. The ^{13}C NMR spectra show that the both PH and PMCP blocks have high isotactic stereoselectivity of more than 95 % (%*mmmm*) and 97 %, respectively. Moreover, NMR confirms the PH-PMCP block copolymers have a discrete block architecture due to the absence of chemical shifts in the range of 28-41 ppm.[117] The microstructure of PMCP from cyclopolymerization is found out to be 63 % of 4,5-*trans* ring structure. [114,118,119] In addition, the block ratios of all PH-PMCP materials were analyzed by GPC and ^{1}H NMR results.

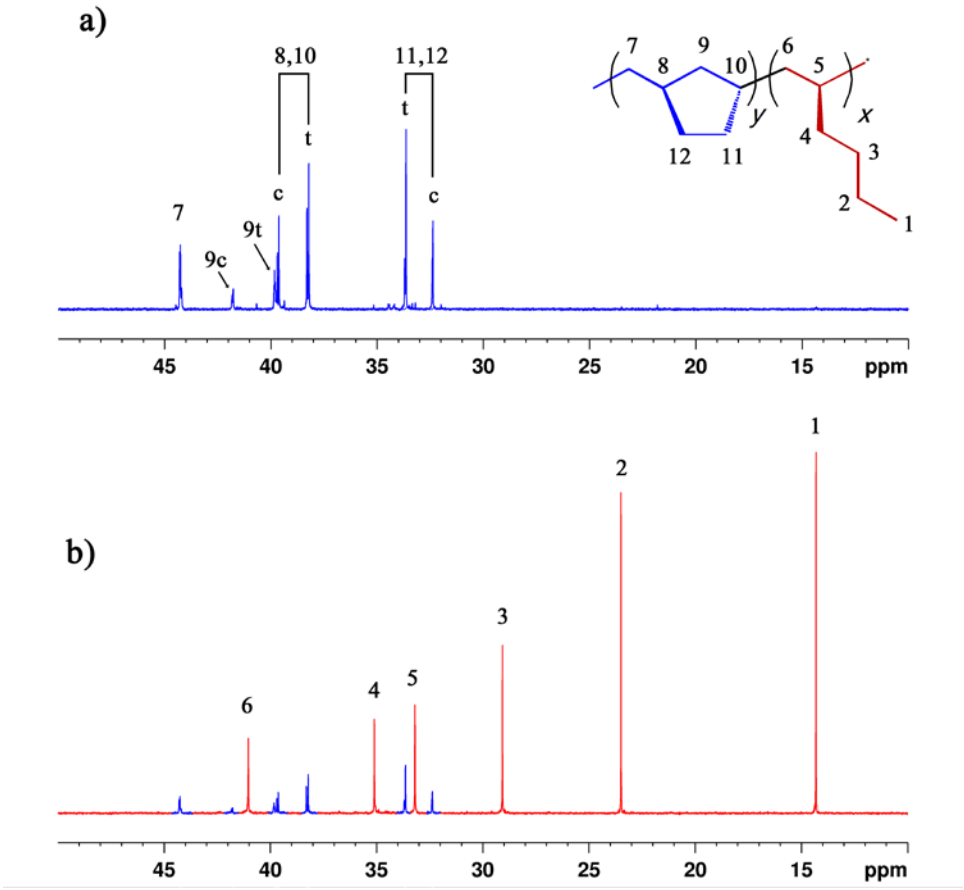

Figure 4.4 Representative ^{13}C NMR of homopolymer PMCP (20 kDa) and diblock PH-PMCP. a) Homopolymer PMCP shows 63 % of 4,5-*trans* ring structure based on the ratio between *cis*- (*c*) and *trans*-(*t*) signals in 36-38 ppm. b) PH-PMCP (sample 2, f_{PMCP} = 0.43). Blue signals indicate PMCP block.

The volume fraction of PMCP block calculated from GPC is consistent with the mole fraction from ^{1}H NMR. To obtain the mole fraction of PMCP block, ^{1}H NMR was used. The region from 1.6-2.1 ppm represents 4 protons contributed from carbon positions 4 and 5 (Figure 4.5) where the signal only comes from the PMCP block.[120] Since the region from 0.0-1.6 ppm contains 6 other protons from the PMCP block, the intensity of the 6 protons from PMCP block needs to be subtracted. For example, the ^{1}H NMR in Figure 4.6 a) is normalized by 4 protons from the PMCP block and the intensity 0.0-1.6 ppm contains other 6 protons from PMCP and 12 protons from PH.

$$I_{protons,PH} = 40.11 + 11.66 + 0.41 - 6 = 46.18$$

The ratio of PMCP is,

$$\frac{10}{10}:\frac{46.18}{12}\ (PMCP\ block:PH\ block)=1:3.85$$

$$f_{PMCP}=\frac{1}{1+3.85}=0.21$$

Therefore, the mole fraction of PMCP block is 0.21, which is consistent with the results from GPC. Using the same method, we can confirm the volume and the mole fraction of PMCP block in PH-PMCP block copolymers.

Sample 2 shows a deviation and it is due to the relatively larger PDI and possible cross-linking during polymerization.

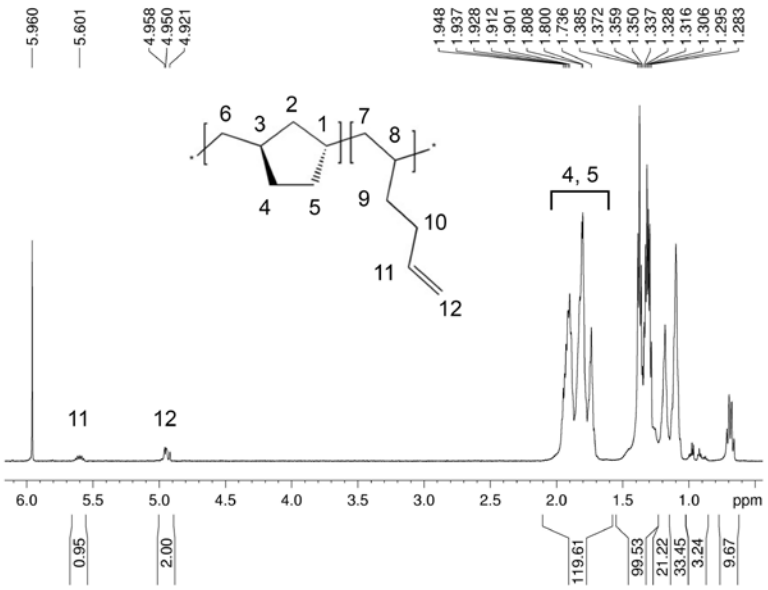

Figure 4.5 Representative ^{1}H NMR of homopolymer PMCP (20 kDa) with chemical structure. The protons from pendant group (11 and 12) and from 5-membered ring (4 and 5) are displayed with intensities.

From Figures 4.6 to 4.12, the chemical shift at 4.9-5.0 and 5.5-5.7 ppm on ^{1}H NMR indicates the presence of vinyl group of about 3% resulting from the non-cyclopolymerization of 1,5-hexadiene. When the 1,5-hexadiene does not undergo

cyclopolymerization, residual double bonds might dimerize. Based on the NMR spectra of PH-PMCP block copolymers, the discrete block structures are confirmed in both the high and low molecular weight samples.

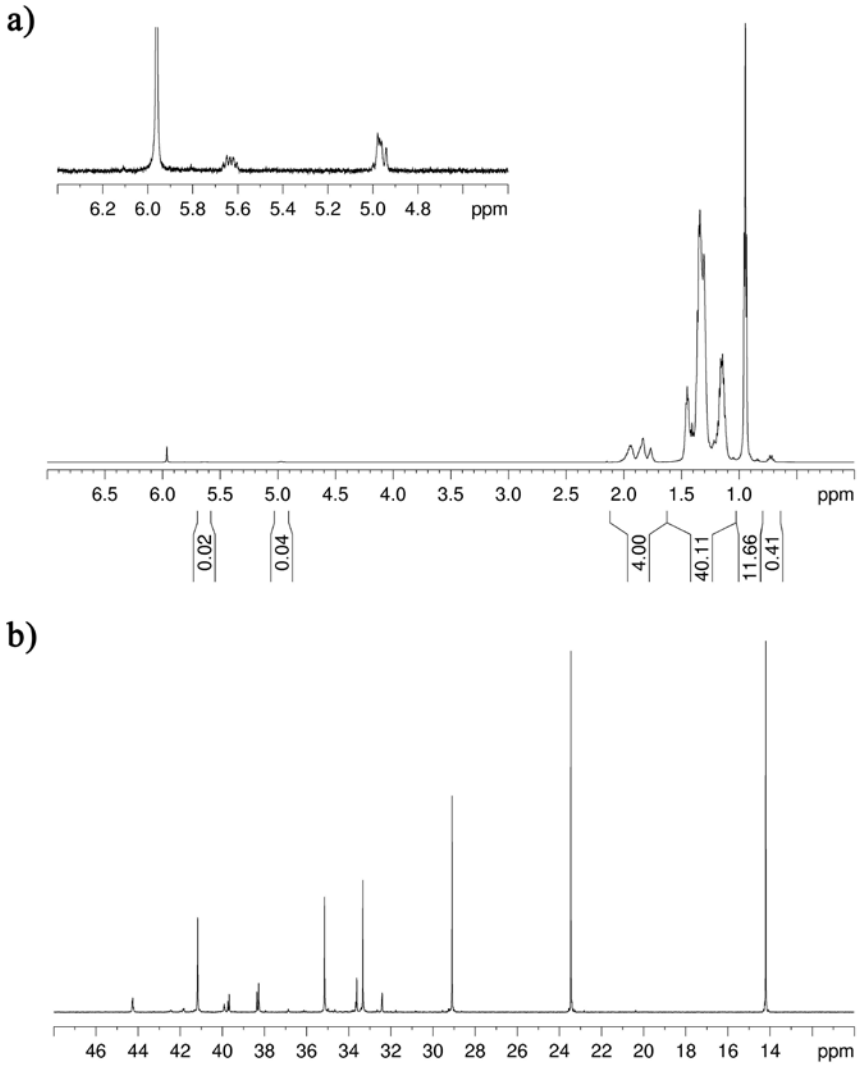

Figure 4.6 ^{1}H NMR (600 MHz, 1,1,2,2-$C_2D_2Cl_4$, 110 °C) spectra of PH-PMCP block copolymer (sample 1). Expansion shows vinyl end groups from 1,2-insertion of 1,5-hexadiene.

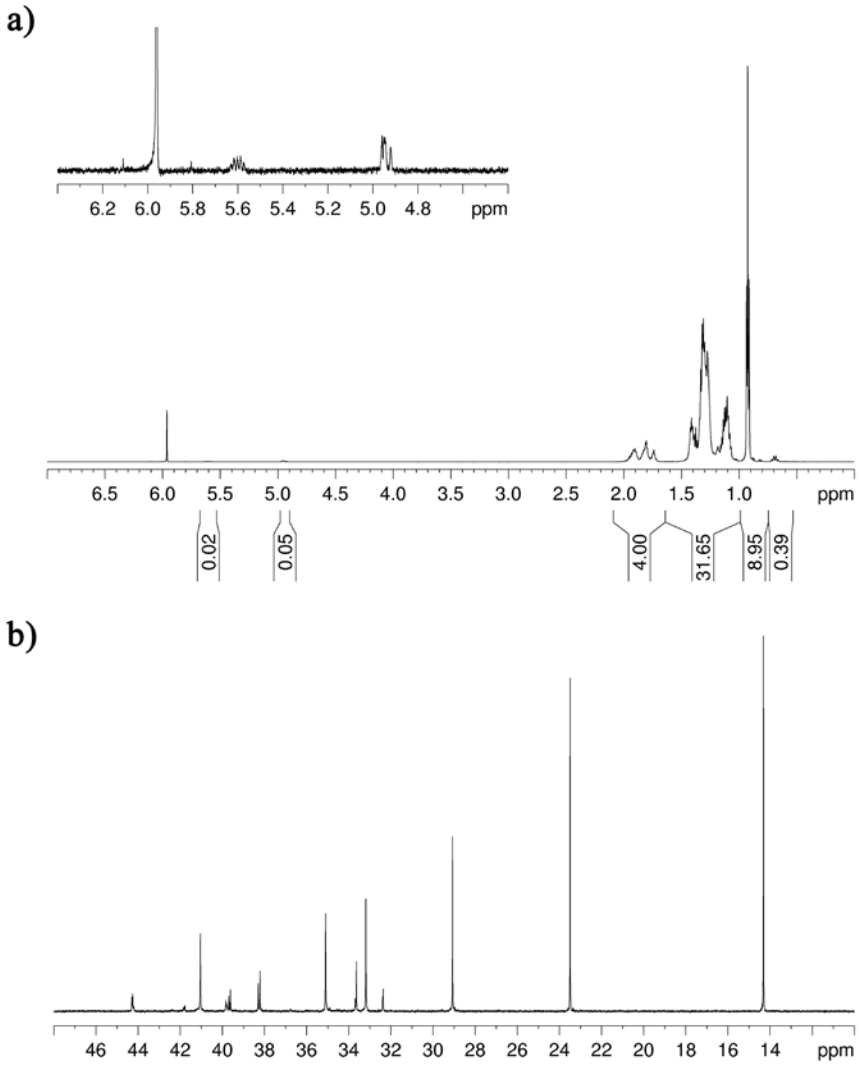

Figure 4.7 ^{1}H NMR (600 MHz, 1,1,2,2-$C_2D_2Cl_4$, 110 °C) spectra of PH-PMCP block copolymer (sample 2). Expansion shows vinyl end groups from 1,2-insertion of 1,5-hexadiene.

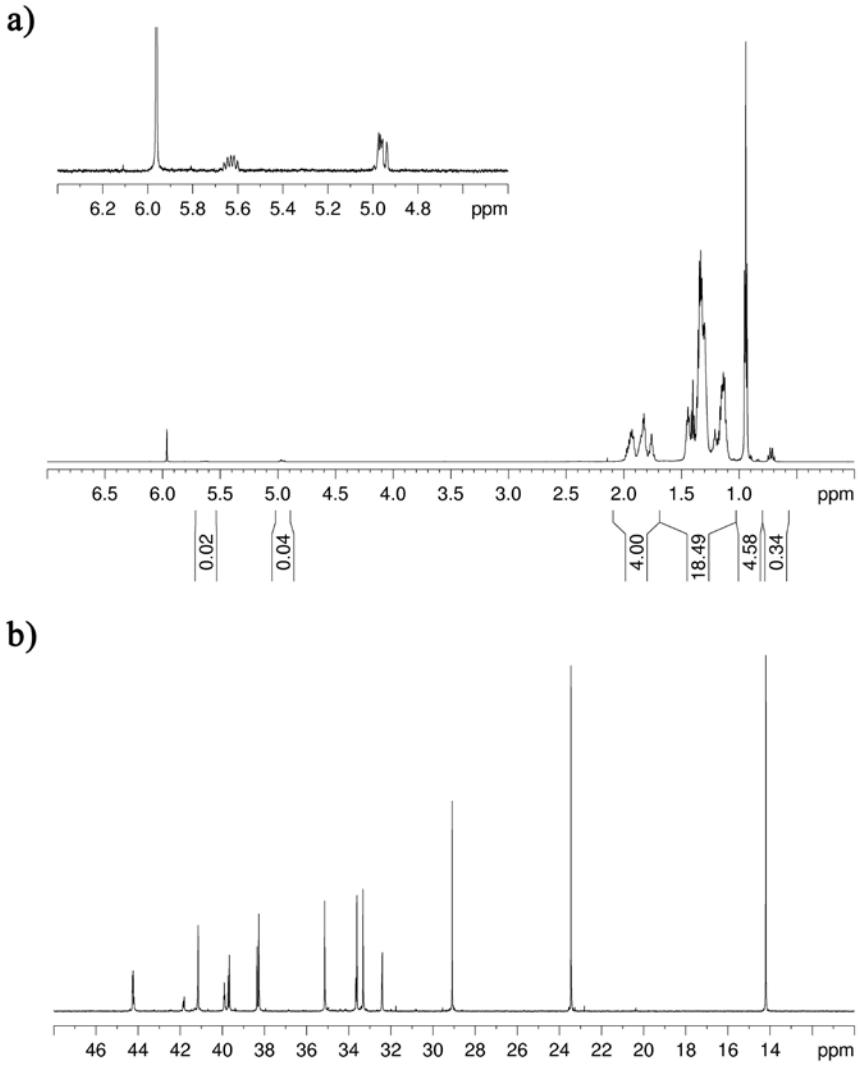

Figure 4.8 ^{1}H NMR (600 MHz, 1,1,2,2-$C_2D_2Cl_4$, 110 °C) spectra of PH-PMCP block copolymer (sample 3). Expansion shows vinyl end groups from 1,2-insertion of 1,5-hexadiene.

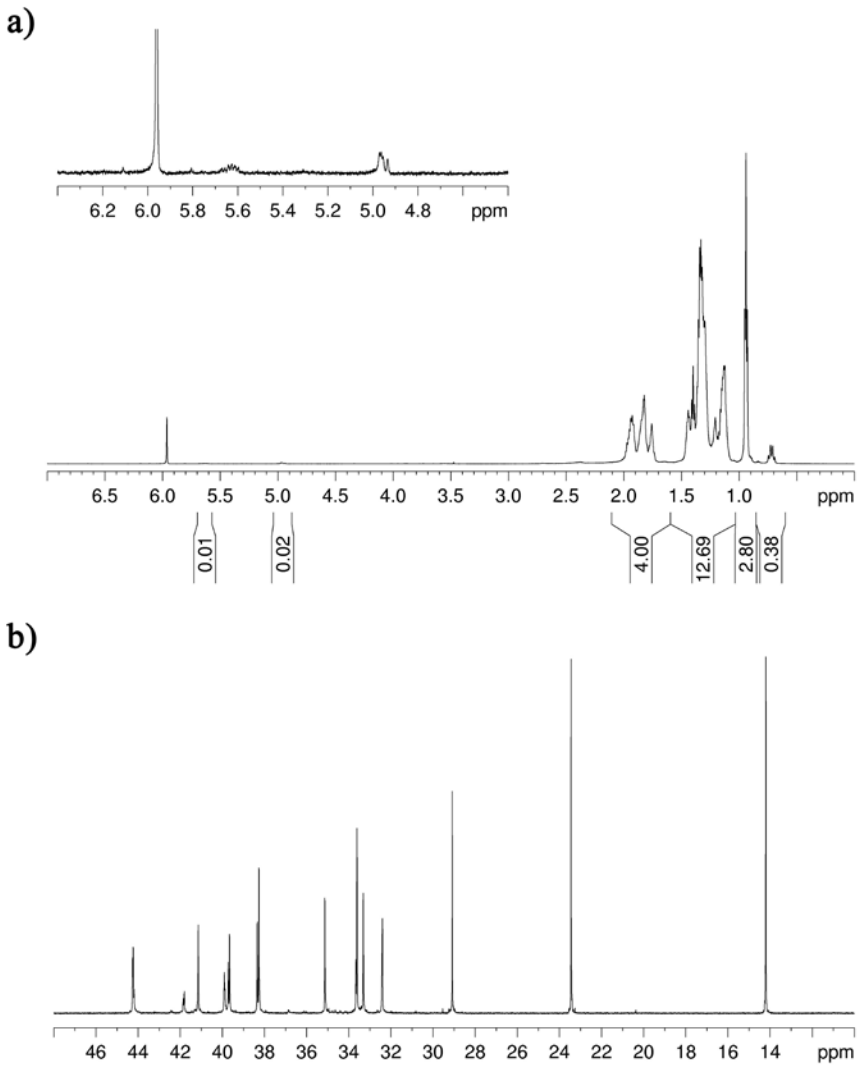

Figure 4.9 ^{1}H NMR (600 MHz, 1,1,2,2-$C_2D_2Cl_4$, 110 °C) spectra of PH-PMCP block copolymer (sample 4). Expansion shows vinyl end groups from 1,2-insertion of 1,5-hexadiene.

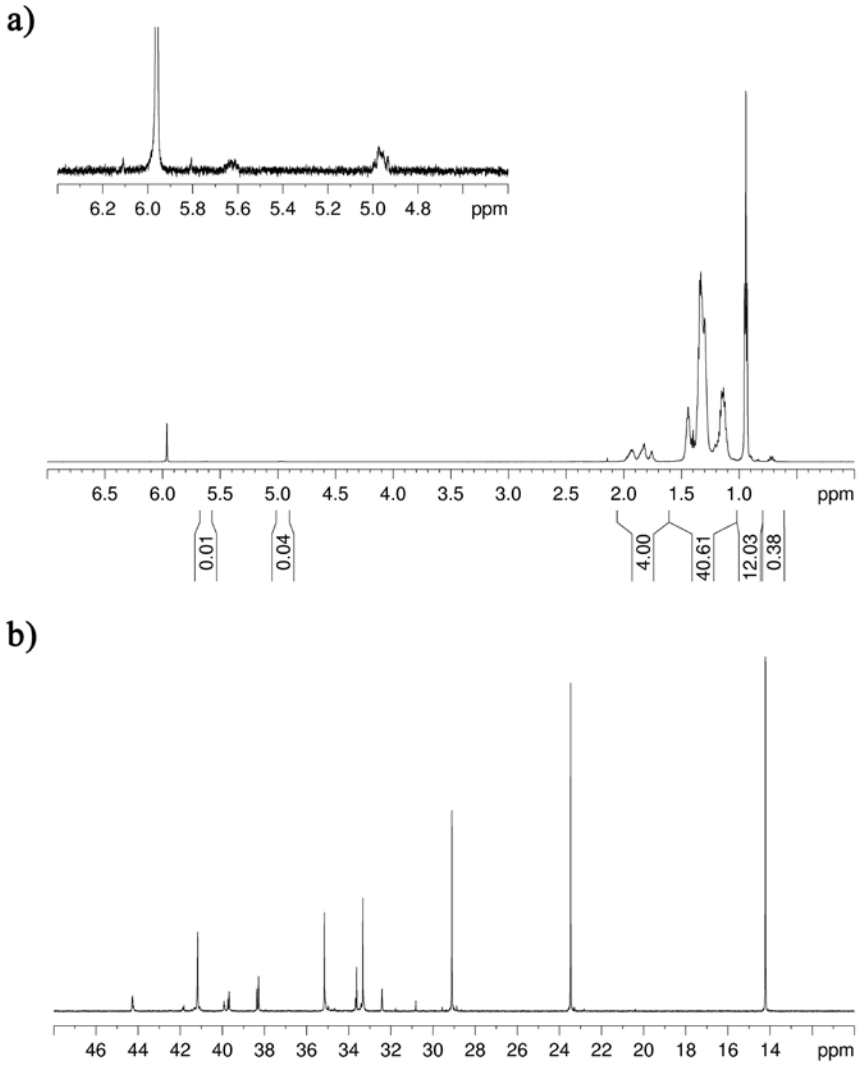

Figure 4.10 ^{1}H NMR (600 MHz, 1,1,2,2-$C_2D_2Cl_4$, 110 °C) spectra of PH-PMCP block copolymer (sample 5). Expansion shows vinyl end groups from 1,2-insertion of 1,5-hexadiene.

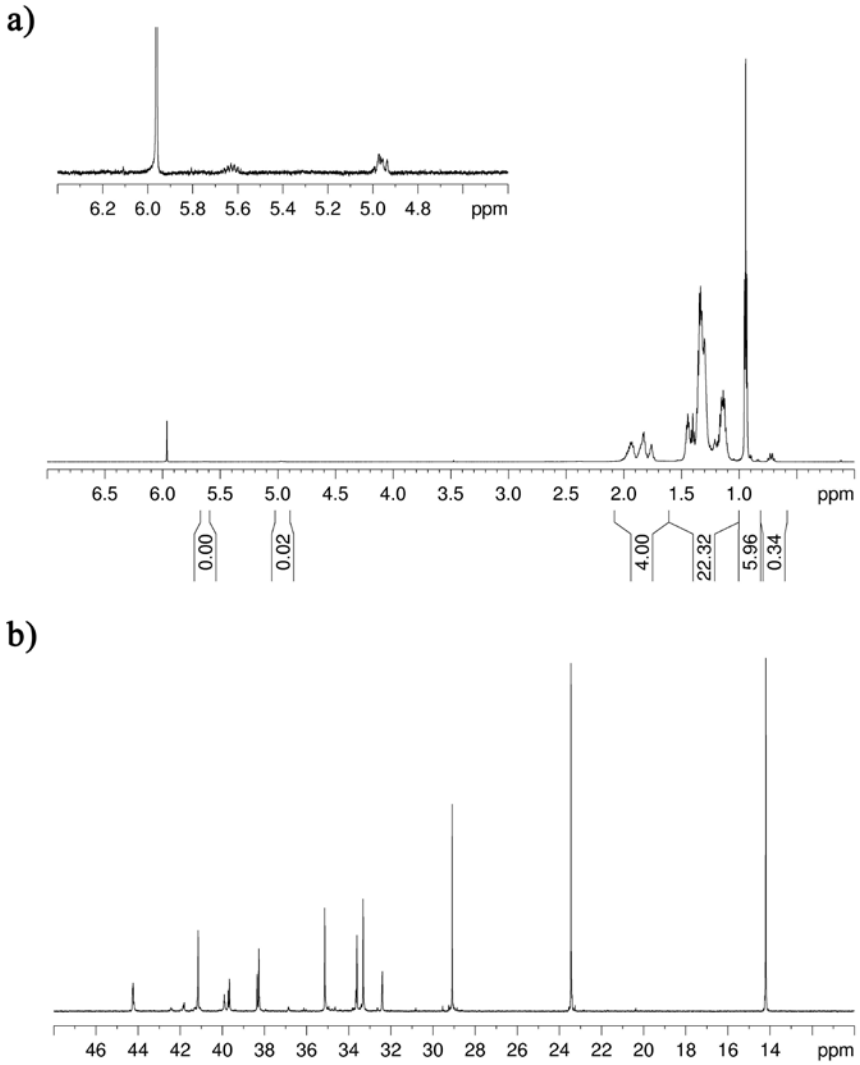

Figure 4.11 ^{1}H NMR (600 MHz, 1,1,2,2-$C_2D_2Cl_4$, 110 °C) spectra of PH-PMCP block copolymer (sample 6). Expansion shows vinyl end groups from 1,2-insertion of 1,5-hexadiene.

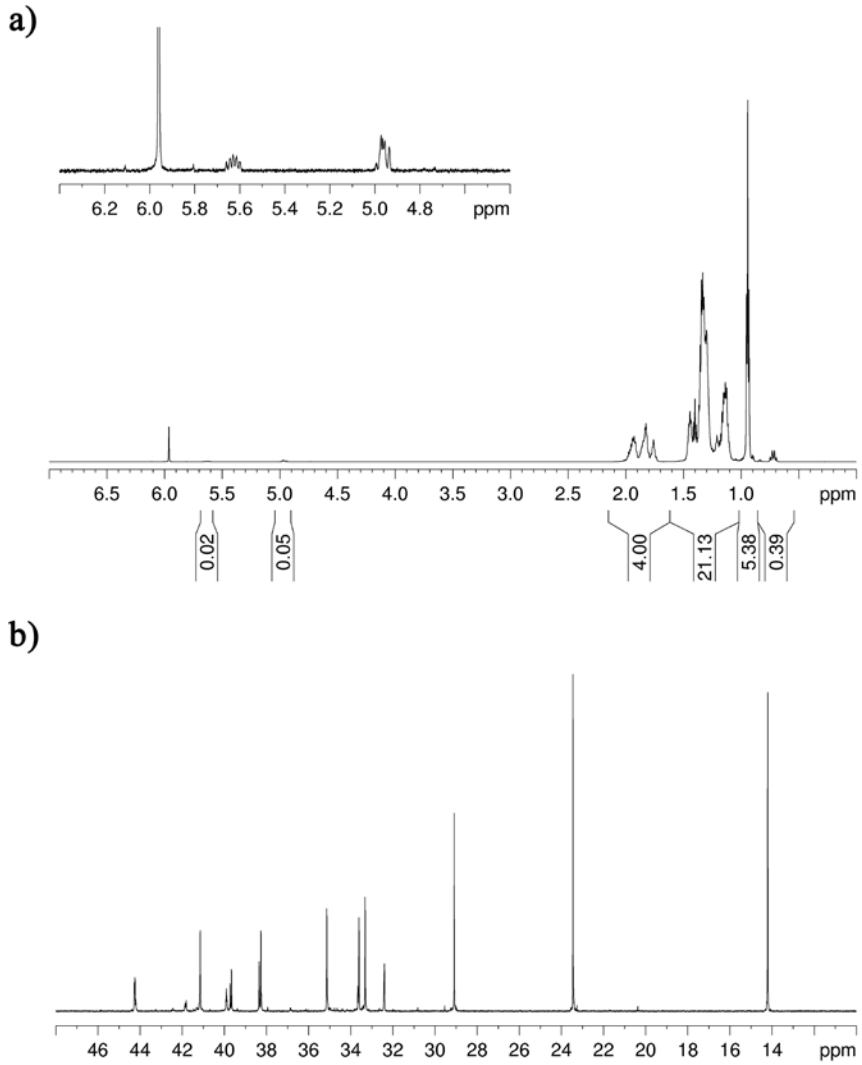

Figure 4.12 ^{1}H NMR (600 MHz, 1,1,2,2-$C_2D_2Cl_4$, 110 °C) spectra of PH-PMCP block copolymer (sample 7). Expansion shows vinyl end groups from 1,2-insertion of 1,5-hexadiene.

To characterize the crystalline structure of PMCP, powder X-ray diffraction (XRD) was carried out. Previously, Auriemma *et al*. and Naga *et al*. reported that crystalline PMCP has a hexagonally packed structure having two characteristic peaks at approximately 2θ = 18° and 32°, which correlates with d_{100} and d_{110} directions, respectively.[110,115,116] Figure 4.13 and 4.14 show a series of XRD profiles from homopolymer PMCP and block copolymers. As expected, homopolymer PMCP shows

two characteristic peaks at 2θ = 18.2 ° and 31.7 °, which correspond to the intermolecular distance of d_{100} and d_{110} directions at about 4.87 Å and 2.82 Å for each direction. The intermolecular distance d_{100} and ^{13}C NMR analysis further support that PMCP block has 63 % of 4,5-*trans* ring structure in the chain backbone.

When the crystalline PMCP content decreases in the block copolymers, the diffraction intensity of crystalline PMCP is decreased without showing peak shift. Additionally, the diffraction peaks at 2θ = 30-40 ° disappear with decreasing the crystalline PMCP content. The diffraction peak intensity for low molecular weight PH-PMCP materials (total MW =15 kDa) also decreases with increasing the amorphous PH fraction (Figure 4.14). From the XRD results, a high fraction of amorphous PH block reduces the order in the PMCP crystals.

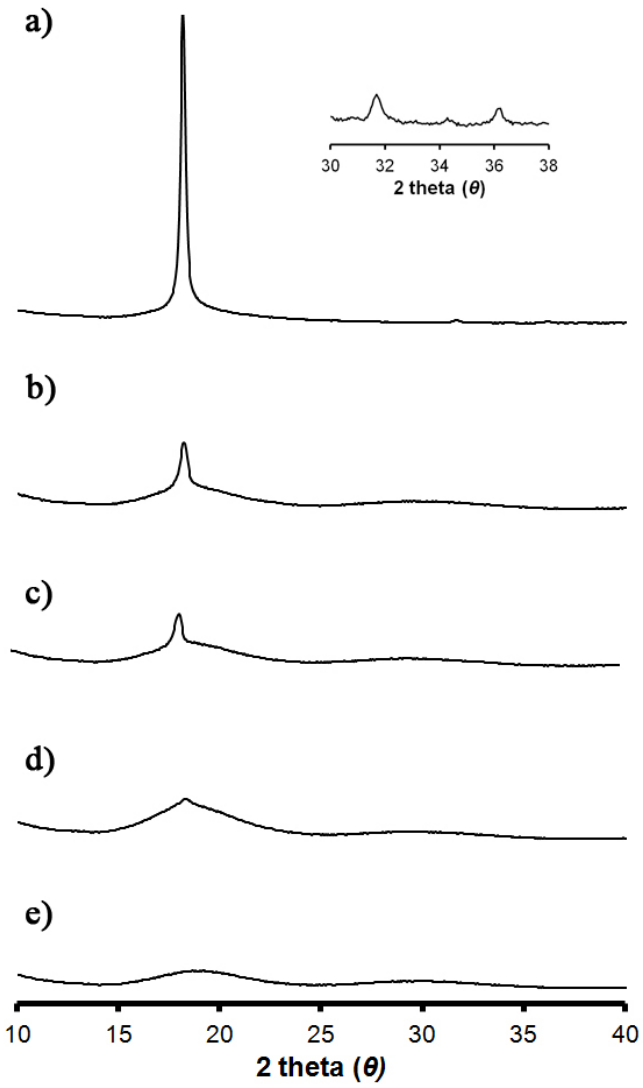

Figure 4.13 X-ray Diffraction of PMCP crystalline pattern in homopolymer PMCP and PH-PMCP block copolymers. a) homopolymer PMCP (MW=20 kDa), b) sample 4, c) sample 3, d) sample 2, and e) sample 1. The inset is the lower symmetry peaks of homopolymer PMCP.

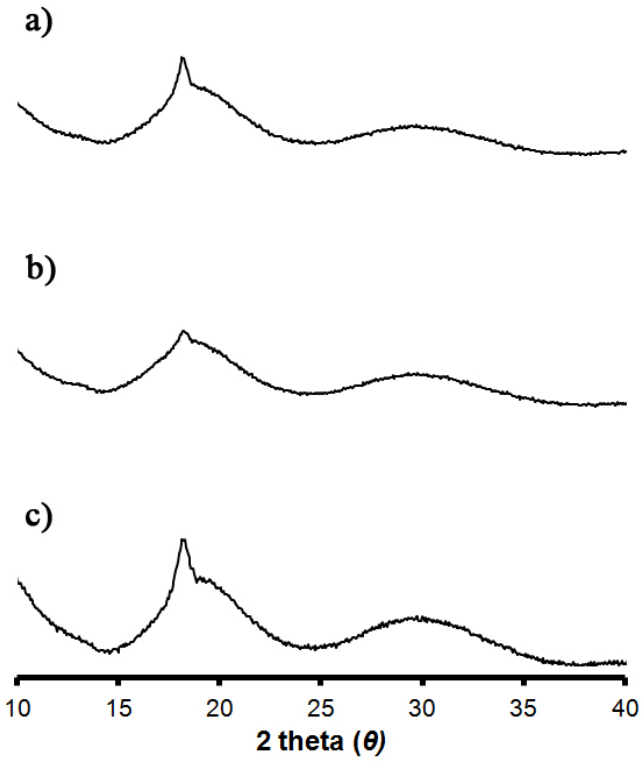

Figure 4.14 X-ray Diffraction of PMCP crystalline of PH-PMCP block copolymers. a) sample 5, b) sample 6, and c) sample 7.

An amorphous-amorphous (or coil-coil) block copolymer segregates into ordered microdomains with the structure determined by the volume fraction of each block and the Flory-Huggins interaction parameter. Crystalline-amorphous block copolymers in the weak confinement regime undergo crystallization-induced microphase separation which leads to a dominant random crystalline lamellar structure.

Prior to studying the microphase separation behavior of crystalline-amorphous PH-PMCP block copolymers, we characterized the surface topology of homopolymer PMCP in thin films using phase-sensitive tapping mode atomic force microscopy (ps-tm-AFM). In Figure 4.15, the strong contrast of phase mode shows that the width of

crystalline lamellar is 15-19 nm. The crystalline structure is needle-like with no spherulitic structure observed in the spin-coated films.

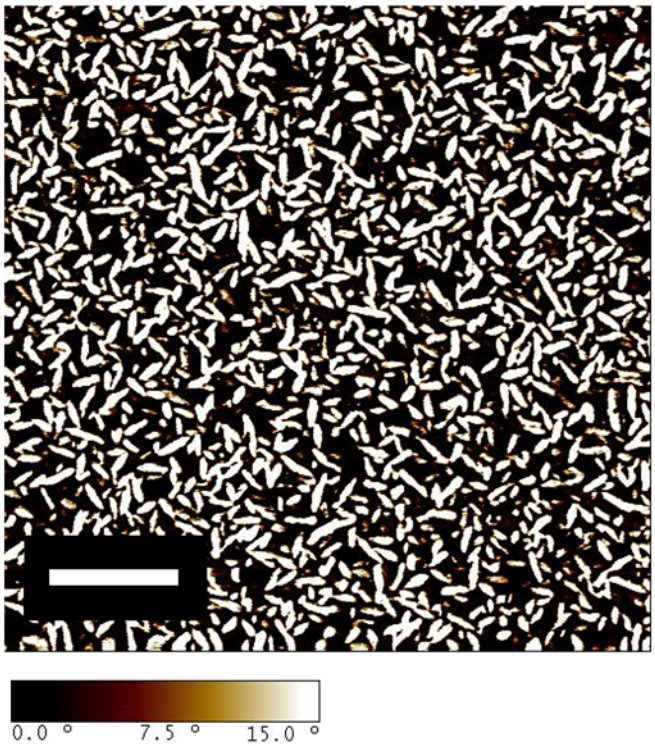

Figure 4.15 Crystalline lamellae of a homopolymer PMCP (20 kDa) thin film in phase mode AFM. The average film thickness is 30±3 nm. (scale bar : 200 nm)

Surprisingly, the surface morphologies from AFM demonstrate that PH-PMCP block copolymers give rise to well-defined and ordered microdomain structures such as spherical, cylindrical, and lamellar and a disordered crystalline lamellar phase with the increasing crystalline PMCP block ratio (Figure 4.16). At low PMCP fraction, the block copolymer shows well-ordered hexagonal packed spherical domains with a center-to-center distance is approximately 35±2 nm. As the PMCP content increases, the block copolymers show a discontinuous cylindrical phase with a center-to-center distance of 40±2 nm and the absence of macroscopic crystallization-induced phase separation. With a further the increase of the PMCP content, the domain structure begins to show

crystalline lamellar domains with short range order. The domain periodicity of crystalline lamellar phase varies in the range of 25-47 nm. When the PMCP fraction is larger than 0.4, a randomized crystalline lamellar structure becomes dominant indicating that PMCP crystals disrupt the ordered domains (Figure 4. 16 d). The bright structures in phase image correspond to the hard crystalline lamellae about 15 nm wide, which is comparable to the width observed for the homopolymer PMCP crystalline lamellar structure (15-19 nm). Similarly, Figure 4.17 shows the microphase separation of low molecular weight PH-PMCP as a function of block ratio (samples 5-7). The periodic domain spacing, *D*, decreases to 26±3nm showing the dependency on the total degree of polymerization *N* and the Flory-Huggins interaction parameter χ ($D \sim aN^{2/3} \chi^{1/6}$, where *a* is a characteristic segment length). [26] The low molecular weight block copolymers have smaller domain sizes than the high molecular weight series of block copolymers. The low PMCP fraction (f_{PMCP} = 0.23) block copolymer (sample 5) shows short domains with a low degree of ordering, however, the higher PMCP fraction (f_{PMCP} = 0.37) block copolymer (sample 6) displays a well-ordered cylindrical microdomains with the center-to-center distance of 25±2 nm. A representative transmission electron microscopy (TEM) is shown in Figure 4.18. The cylindrical microdomains are parallel and perpendicular to the cross-sectioned film. The domain spacing and the domain size are consistent with those from the AFM images. When the PMCP content increases to 0.39, the crystalline lamellar structure is the dominant phase (*d* spacing is ca. 30±3nm) with a lack of ordering.

The domain spacing *D* from two sets of AFM images support the relationship between the total degree of polymerization and periodicity, where small values of *D* correspond to the lower molecular weight and vice versa. It is reasonable that the melting

point in DSC and diffraction peaks in XRD reflect the presence of the large fraction of crystalline PMCP ($f_{PMCP} > 0.4$) in both high and low molecular weight materials (15 kDa and 30 kDa).

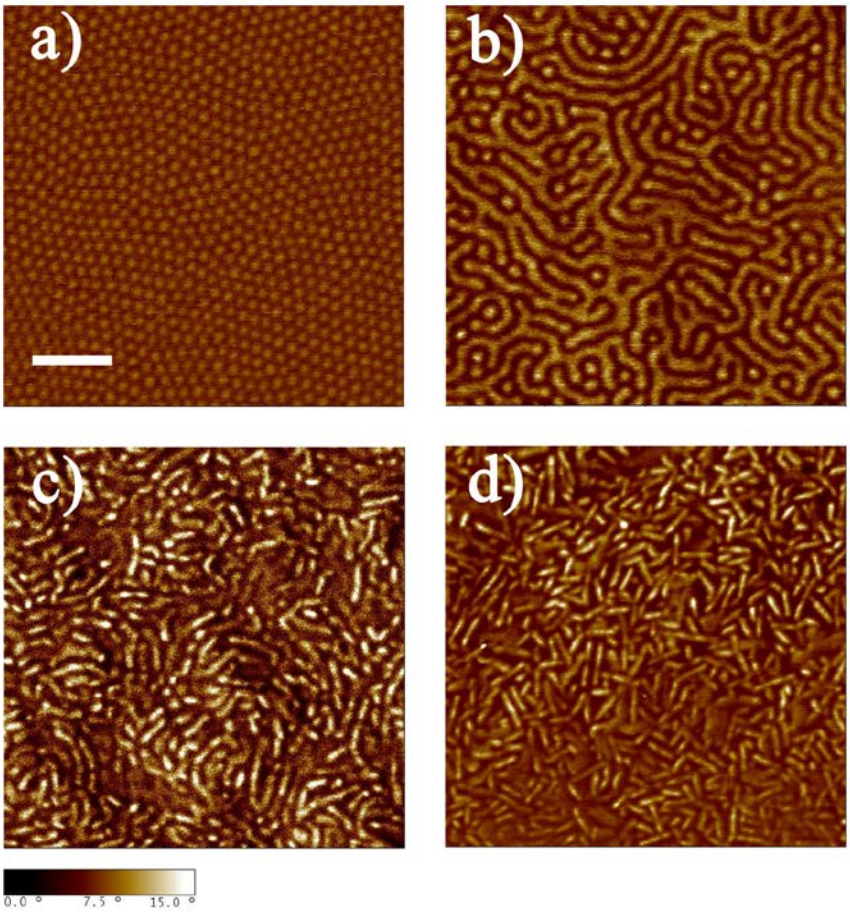

Figure 4.16 Microphase separation of PH-PMCP (samples 1-4) in phase contrast images. a) spherical, b) cylindrical, c) lamellar, and d) irregular crystalline lamellar morphologies depending on the crystalline PMCP block ratios. The average film thickness is 30±3 nm. (scale bar : 200 nm)

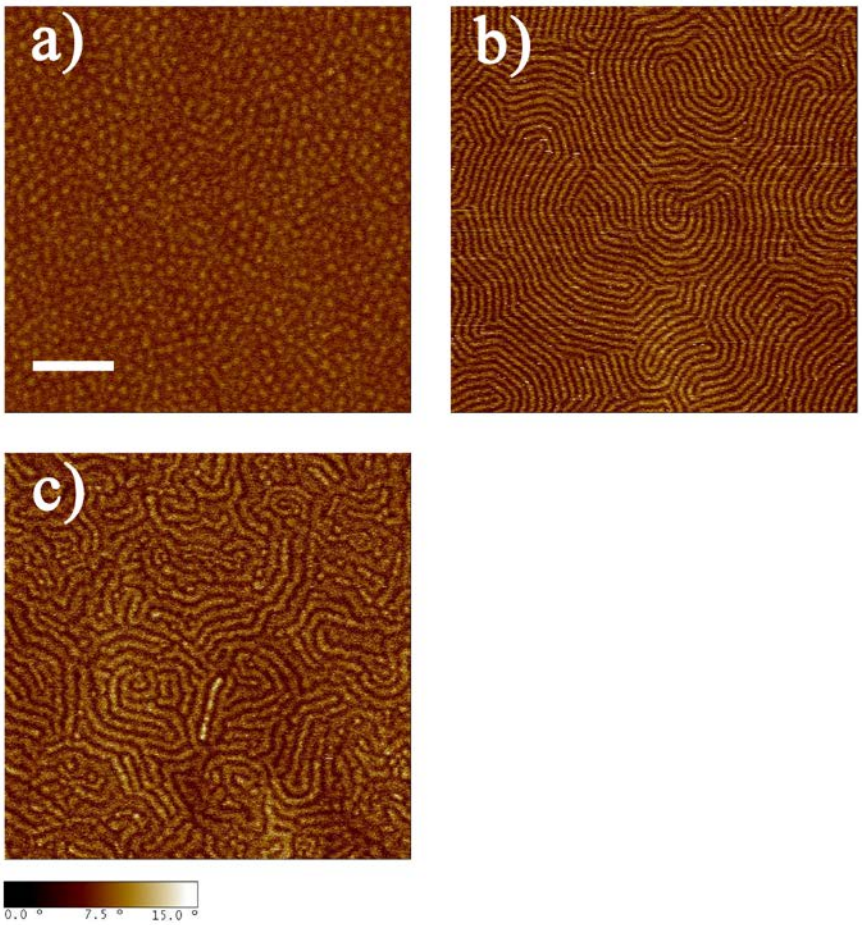

Figure 4.17 Microphase separation of PH-PMCP (samples 5-7) in phase contrast images. a) spherical, b) cylindrical, and c) lamellar morphologies depending on the crystalline PMCP block ratios. The average film thickness is 30±3 nm. (scale bar : 200 nm)

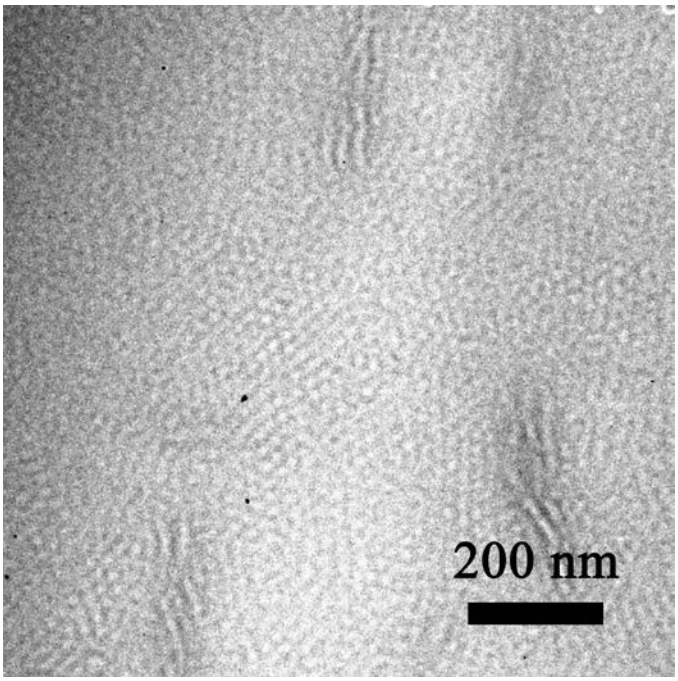

Figure 4.18 TEM micrograph of cylinder-forming PH-PMCP (sample 6) after ultramicrotomy at -140 °C. The cylindrical morphology parallel and perpendicular to the cross-sectioned film are shown. Some crystalline lamellar structures are also observed with disordered morphology.

The PH-PMCP system is expected to be in the weak confinement regime as $T_{ODT} > T_c^C > T_g^A$ based on the DSC suggesting crystallization dominant morphology. However, the phase separation behavior of PH-PMCP system exhibit PMCP crystals and microdomains in both high molecular weight series (30 kDa) and low molecular weight series (15 kDa).

One feasible explanation is that the long rubbery PH block can sufficiently restrict and isolate the crystallization of the short PMCP block to from 10-20 nm crystalline lamellae. As a result, the generated microdomains display weakly-ordered short crystalline domains with a combination of spherical domains. For cylinder-forming PH-PMCP block copolymers, larger PMCP crystals are observed in between well-defined cylinder domains. The ordered spherical and cylindrical microphase structures appear to

be the consequence of strong segregation followed by crystallization within the amorphous PH matrix.

For lamellar block copolymer phase, however, both crystalline PMCP and amorphous PH blocks show a competition between crystallization and microphase separation creating short range ordered block copolymer microdomains. When the crystalline PMCP content is sufficiently large, the crystallization-induced microphase separation causes an irregular crystalline lamellar phase. Consequently, the surface morphology displays a dominant crystalline lamellar structure from the PMCP block.

Register and coworkers suggested a classification to describe the crystallization in rubbery matrix using crystalline-amorphous block copolymers.[14] Using the ratio of χN at the crystallization temperature T_c and the order-disorder transition temperature T_{ODT}, they described the crystallization behavior as a function of the volume fraction of the crystalline block. When $((\chi N)_C)/((\chi N)_{ODT})$ >3, the crystallization will be confined in the spherical block copolymer domains. For a cylinder system, the crystallization mode is divided into three different regimes as 'confined', 'break-out', and 'templated'. Based on our observation, PH-PMCP system is located in the 'confined' regime when f_{PMCP} <0.4. Since the microdomain structures in PH-PMCP materials with f_{PMCP} <0.4 display well-defined spherical and cylindrical block copolymer domains with the absence of randomly distributed PMCP crystalline lamellar structure. When the volume fraction of PMCP is larger than 0.4, the crystallization of PMCP disrupts the block copolymer microdomain structures and generates an interconnected crystalline lamellar morphology.

To investigate the crystallization of the PMCP block as a function of the amorphous PH length, thin films of lamellar and irregular phase separated block copolymers (samples 3, f_{PMCP} = 0.41 and sample 4, f_{PMCP} = 0.55) were melted and either quenched or slow cooled, respectively.

Figure 4.19 shows the crystallization suppression depending on the thermal treatment of sample 3 (f_{PMCP} = 0.41). From the as-cast thin film, PMCP shows a crystalline lamellar structure within the amorphous matrix (Figure 4.19 a and b). The crystalline domains have a width of about 14 nm. When the sample undergoes a slow cooling from the molten state, the sample shows larger crystalline lamellae within the rubbery PH matrix (Figure 4.19 c and d). The width of crystalline lamellae is about 14-18 nm and does not show any block copolymer microdomain morphology. To try to observe the microdomain structure, we used a quenching process. Interestingly, the sample displays an amorphous morphology suggesting that the quenching process effectively suppressed the crystallization of the PMCP block (Figure 4.19 e and f).

In addition, the material with f_{PMCP} = 0.55 (sample 4) shows a similar result as sample 3 (f_{PMCP} = 0.41). The as-cast sample shows irregularly distributed PMCP crystals with a 10 nm of width (Figure 4.20 a and b). The strong phase contrast reflects the larger PMCP and the areal density of the crystalline lamellae is higher than in sample 3. When the sample was slow cooled, the PMCP crystals are noticeably more developed (Figure 4.20 c and d). The PMCP crystals of sample 4 have a width of about 14-19 nm which is similar to sample 3. Finally, the quenched sample displays some PMCP crystals within the amorphous matrix (Figure 4.20 e and f).

The series of surface morphologies demonstrate that a larger fraction of PMCP with $f_{PMCP} > 0.4$ generates crystalline lamellae instead of block copolymer microphase separation. We could not observe the microphase separation structure in either slow cooled or quenched thin film sample (samples 3 and 4). In addition, the PMCP crystals for both materials are isolated by amorphous PH blocks and have a similar width of about 14 nm, which is smaller than that of homopolymer PMCP crystals.

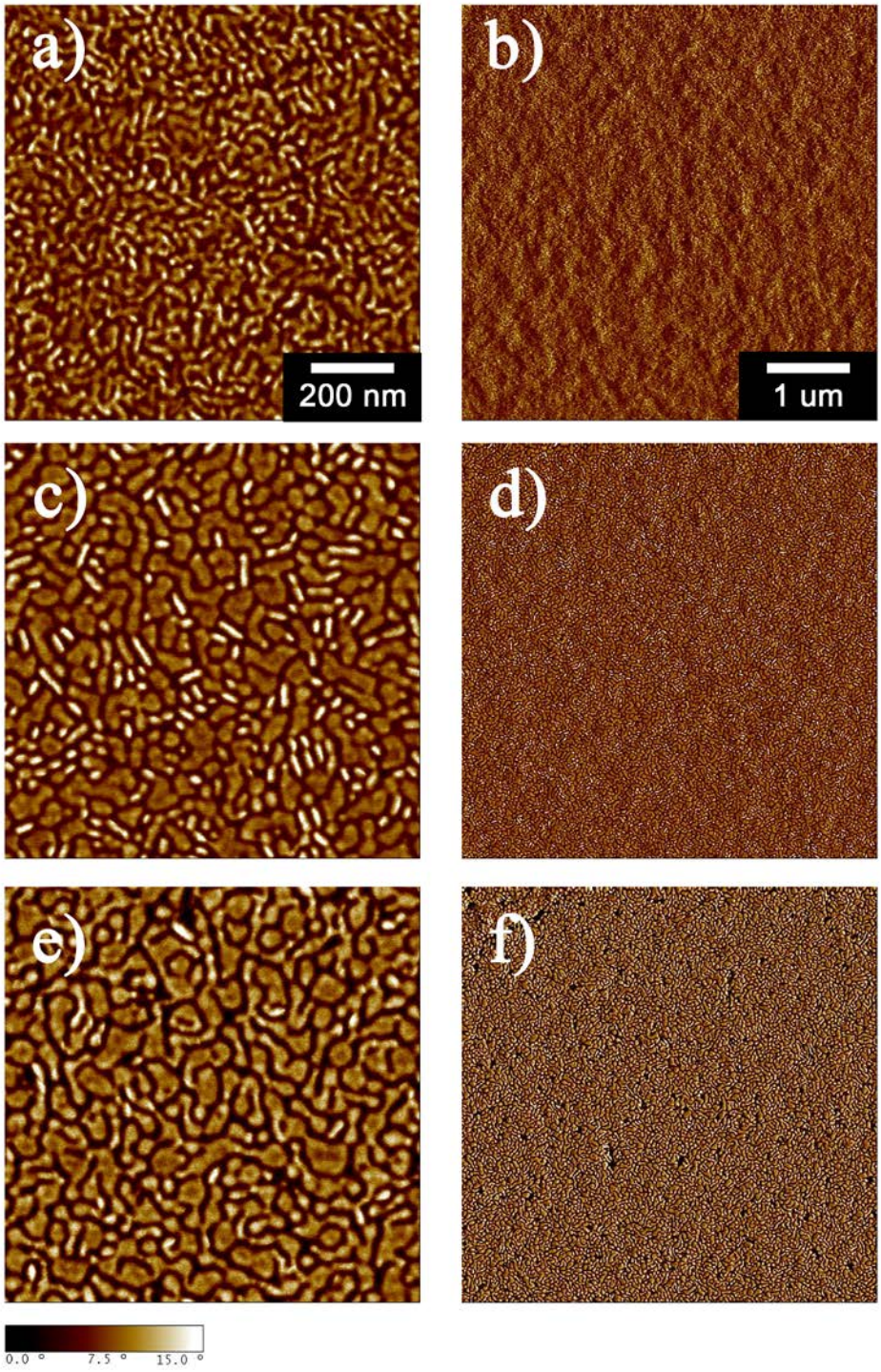

Figure 4.19 The phase images of the suppressed crystallization for sample 3. a), c), and e) are localized surface topologies (scale bar: 200 nm) and b), d), and f) are overall surface topologies (scale bar: 1 um).

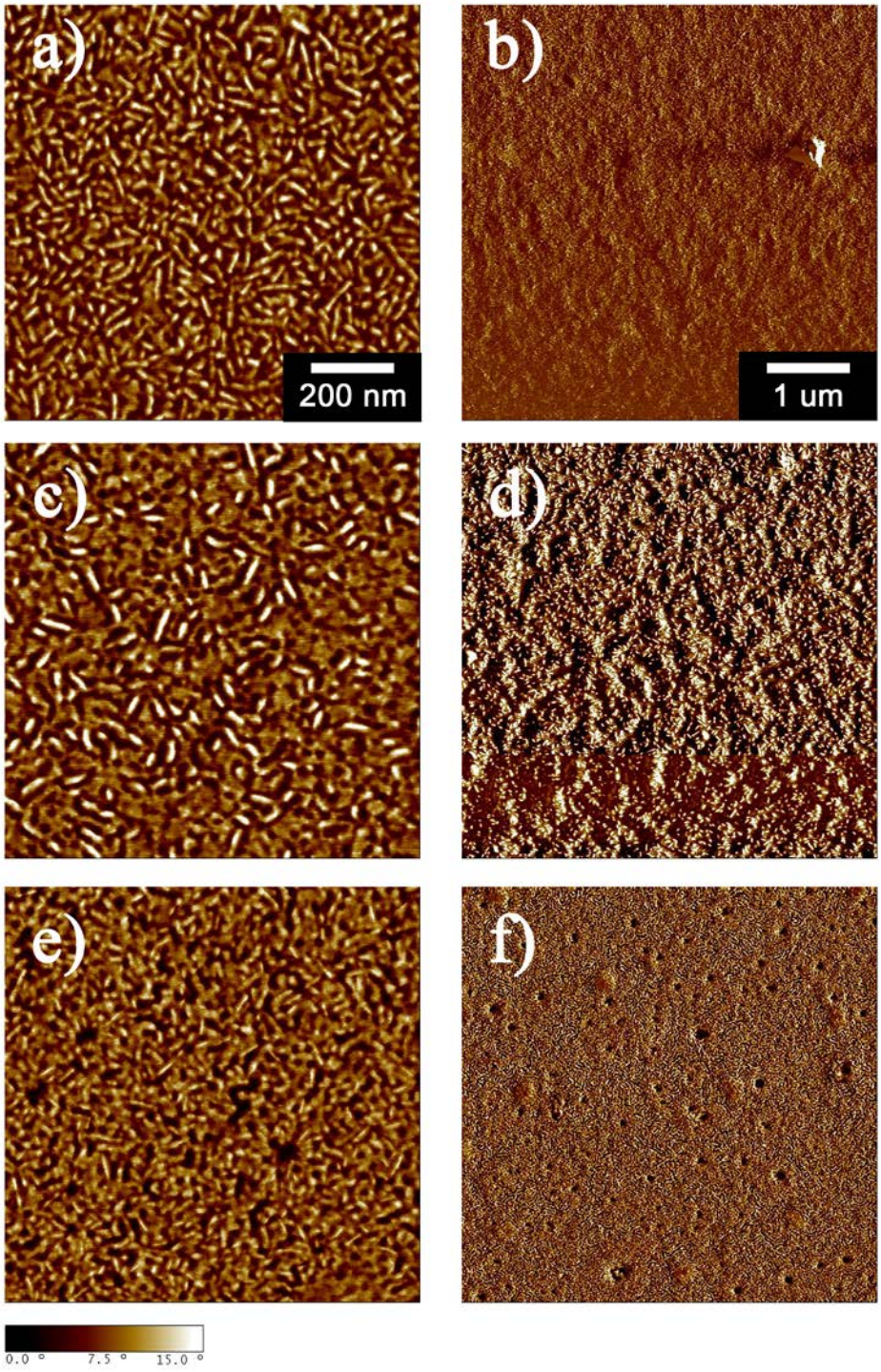

Figure 4.20 The phase images of the suppressed crystallization for sample 4. a), c), and e) are local surface topologies (scale bar: 200 nm) and b), d), and f) are overall surface topologies (scale bar: 1 um).

4.4. Conclusions

We successfully synthesized a set of crystalline-amorphous block copolymers using a combination of living coordinative olefin polymerization and living cyclopolymerization using 1-hexene and 1,5-hexadiene. Taking the advantage of the living polymerization for both monomers, a series of PH-PMCP block copolymers were systematically synthesized with the total molecular weights of M_n = 15 and 30 kDa and narrow PDI (<1.2). Interestingly, both high molecular weight (total M_n ~ 30 kDa) and low (total M_n ~ 15 kDa) PH-PMCP block copolymers demonstrated both crystallization-driven microphase separation and incompatibility-induced block copolymer microphase separation structures at ambient conditions depending on the amount of crystalline PMCP block. With increasing PMCP content to 0.4, the samples display either spherical or cylindrical block copolymer microdomain structure in AFM and TEM. The results indicate that the low T_g (-46 °C) PH matrix can confine the crystallization of the PMCP block resulting in an incompatibility-induced block copolymer microphase separation morphology. When the PMCP ratio is larger than 0.4, the morphology exhibits a crystalline lamellar structure rather than a well-defined block copolymer microdomain structure. In this case, the crystallization of the PMCP block dominates results in randomly distributed crystalline lamellae. Depending on the ratio of crystalline PMCP block, the generated microphase separation of PH-PMCP materials shows either crystallization-driven morphology or incompatibility-induced block copolymer microphase separation.

Based on the transition temperatures of PH-PMCP materials, the system is located in the weak confinement regime ($T_{ODT} > T_{PMCP}^{C} > T_{PH}^{A}$). Presumably, the large

incompatibility between PH and PMCP chain structures generate strong segregation behavior.

Chapter 5. Viscoelastic Behavior of Crystalline-Amorphous Block Copolymers: Low Molecular Weight Regime

5.1. Background

The coupling between ordered microphase structures and the mechanical response in block copolymers has been of interest due to the relevance for potential applications of these polymers as thermoplastic elastomers, blend compatibilizers, and separation membranes.[1] Important to applications is a fundamental understanding of block copolymer phase behavior and mechanical properties in order to integrate them into next generation applications. The microphase separation behavior has been investigated by both theoretical and experimental routes.

Helfand and Wasserman developed a phase separation theory (strong segregation limit, SSL), $\chi N > 100$, that describes the spatial distribution of block composition based on the probability of finding a segment in different position.[4] For the weak segregation limit (WSL) where $\chi N \sim 10$, Leibler introduced the order-disorder transition using random phase approximation which describes the behavior near the phase boundary.[5] Leibler's theory depicts the composition fluctuations near the order-disorder transition. Using the scattering function based on the composition fluctuations, Leibler predicted the critical value for the microphase separation in block copolymers, χN=10.495 when the block ratio is $f_A = f_B = 0.5$.

Dynamic linear viscoelastic measurements have been utilized to characterize the rheological response of molten block copolymers. Due to the dramatic change in elastic modulus between the ordered microphase separated state and the disordered homogenous state for block copolymer melts, viscoelastic measurements are a reliable measurement of the order-transition temperature. Chung *et al.*[121] and Gouinlock and Porter[122] reported the transition in dynamic viscoelastic modulus at the order-disorder phase boundary. Below the order-disorder transition temperature, the viscoelastic response displays unique frequency-dependent rheological properties from the microdomain structure. Above the order-disorder transition temperature, the rheological properties show properties characteristic of a homogeneous viscoelastic liquid.

Recent experiments in the weak segregation limit (WSL) where χN is close to 10.495 (at the critical value at f_A= 0.5) have shown the existence of a compositional fluctuation state and its dynamics near the order-disorder transition. Low molecular weight block copolymers (N~50) with locally segregated compositional fluctuations indicate that the fluctuation dynamics lead to a weak first-order transition for T_{ODT}.[123-127] While current research has focused on the understanding of the phase separation behavior near the order-disorder transition, the viscoelastic behavior of low molecular weight crystalline-amorphous block copolymers near the melting point has relatively little published research.

In this regard, we have designed a crystalline-amorphous block copolymer system, PH-PMCP, with extremely narrow polydispersity (<1.2) and controlled molecular weight (total M_n ~ 15 kDa). In previous chapter, a series of PH-PMCP block copolymers have demonstrated either crystallization-driven phase separation or incompatibility-induced

microphase separation at ambient conditions depending on the volume fraction of crystalline PMCP block. This result suggests that PH-PMCP is a strong segregation system with a weak confinement regime due to the large difference between the flexible PH and the rigid PMCP blocks.

Both the crystalline and amorphous blocks are composed of short PH and PMCP chains below the respective critical entanglement molecular weights (M_e, M_e of PH = 14.1 kDa, M_e of PMCP = 8.2 kDa). Interestingly, the viscoelastic behavior of their series of PH-PMCP block copolymers shows a sudden decay in the storage modulus at the PMCP melting followed by the enhancement of the storage modulus as the temperature is increased above the PMCP T_m. In particular, the sphere-forming PH-PMCP block copolymers (samples 1 and 2) exhibit a sharp drop and subsequent increase in the storage modulus during a temperatures weep through the PMCP T_m. The magnitude of the change in the modulus near the PMCP melting is approximately 2 orders. This behavior has not been observed by other researchers.

In this chapter, we examine the unusual viscoelastic behavior in a series of low molecular weight crystalline-amorphous block copolymers in terms of two thermodynamic transitions, crystallization and microphase separation.

5.2. Experimental Setup

a) General Description. All synthetic methods used for PH-PMCP block copolymers were described previously.[108] Distillation of chlorobenzene (PhCl) was carried out over calcium hydride under the N_2 atmosphere. 1-hexene and 1,5-hexadiene monomers (Sigma Aldrich) were dried over Na/K amalgam in gas tight storage tubes for

3-5 days. After the distillation, all monomers were transferred under vacuum with three freeze-pump-thaw degassing cycles.

The precatalyst, (η^5-C_5Me_5)$ZrMe_2$ [N(Et)C(Me)N(t-Bu)], was prepared as we described in previous paper.[109] For the cocatalyst, [$PhNHMe_2$][$B(C_6F_5)_4$] was purchased from Boulder Scientific and used without further purification. Synthesized polymers were characterized using gel permeation chromatography (GPC) using a Viscotek GPC system. Tetrahydrofuran (THF) was used as an eluent and the flow rate maintained at a 1.0 mL/min. at 40 °C. Polystyrene equivalent M_w, M_n, and M_w/M_n were calibrated using Viscotek OmniSEC software and polystyrene standards (Polymer Laboratories). $^{13}C\{^1H\}$ NMR spectra were obtained at 150 MHz using 1,1,2,2-tetrachloroenthane-d_2 as a solvent at 110 °C. The thermal analysis for all block copolymers was performed with TA Instrument Q1000 differential scanning calorimeter (DSC). All DSC scans were taken using 5-9 mg of polymer and sealed in TA Instrument hermetic aluminum DSC pans. All samples were run using a heat-cool-heat cycle over the temperature range -70 °C to 200 °C at 10 °C/min. The first heat cycle was done to remove any thermal history and residual solvent, the subsequent cooling and heating cycle were done using the same conditions to measure the melting and the crystallization temperatures.

b) Polymer Synthesis. All polymerizations were carried out in a glove box. The reaction solvent, PhCl (20 mL), was cooled to -10 °C and the precatalyst, (η^5-C_5Me_5)$ZrMe_2$ [N(Et)C(Me)N(t-Bu)], and the cocatalyst, [$PhNHMe_2$][$B(C_6F_5)_4$], were dissolved in PhCl at the ratio of 1.01 to ensure complete activation. Sequential polymer blocks were obtained by first adding 1-hexene for 2 hours followed by the addition of 1,5-hexadiene for an additional 1 hours. The molecular weight of each block was

controlled by the amount of monomer present based on the kinetics of poly(1-hexene) and poly(methyl-1,3-cyclopentane). A small (<1 mL) amount of poly(1-hexene), PH, was removed and quenched for analysis immediately prior to the addition of the second monomer. Polymer samples were quenched in ca. 500 mL of acidic methanol (10 % HCl by volume). Samples were washed and filtered with MeOH and then dried under vacuum at 25 °C until constant weight was observed. The molecular weights of all polymers were measured using gel permeation chromatography (GPC) (Viscotek TDA) equipped with a column oven. Differential refractometer and four columns (T2500, T3000, T4000 and T5000) were maintained at 40 °C. Tetrahydrofuran (THF) was used as the eluent at a flow rate of 1.0 mL/min. The number-average molecular weight (M_n) and weight-average molecular weight (M_w) of samples were obtained using Viscotek OmniSEC software.

c) Nuclear Magnetic Resonance (NMR). All samples were recorded using 30-40 mg of polymer in 1,1,2,2-tetrachloroethane-d2 at 110 °C with a Bruker AVIII-600MHz spectrometer operating at 150 and 600 MHz, equipped with a Bruker 5 mm C13/H1 dual probe with Z gradient. ^{13}C {^{1}H} NMR spectra were collected under the following conditions: 45° pulse; without NOE; relaxation delay, 2.0 s; >9K transients.

d) Differential Scanning Calorimetry (DSC). The thermal properties of block copolymers were obtained using a DSC Q1000 (TA Instruments). Nitrogen was used as a purge gas at 50 mL/min. The T_m, T_g, T_c and heat of fusion (ΔH) were measured using heat-cool-heat cycles at 10 °C/min. All values were taken after the first heating cycle to remove previous thermal history.

e) Powder X-ray Diffractometry (XRD). X-ray diffraction spectra of all samples were carried out with Bruker D8 Advance powder diffractometer with LynxEye

detector at ambient conditions. All polymers were measured in a bulk state after thermal annealing for 12 hours. The wavelength, λ, of Cu Kα radiation was λ = 1.5418 Å and the scan angle was 5-60° with 0.05° steps. The data profiles were collected with built-in software (Advanced TOPAS).

f) Phase-Sensitive Tapping Mode Atomic Force Microscopy (ps-tm AFM). The surface morphology analysis was performed on a Multimode AFM with Nanoscope IIIa controller (Digital Instrument) in tapping mode. Both height and phase-shift data were obtained with a silicon etched tip (Nanosensors, spring constant k = 25-55 N/m, resonance frequency f = 292-377 KHz) under ambient conditions. All samples were dissolved in toluene (1 wt %) and spin-coated at 2,000 rpm onto Si substrates. Si substrates surfaces were cleaned with 7:3, H_2SO_4 : H_2O_2 "piranha" solution. Film thickness was obtained by using Gaertner ellipsometer for 3 different spots on each sample. Spin-coated film thicknesses were between 30 to 35 nm. All AFM samples were measured before and after annealing at 60 °C for 12 hours.

g) Dynamic Mechanical Experiments. Dynamic mechanical shear modulus analysis was conducted using a RDA III Analyzer (Rheometric Scientific Inc.) with parallel plates (diameter: 7.9 mm, gap: ca. 1 mm) and an AR 2000 (TA Instruments Inc.) with parallel plates (diameter: 25 mm, gap: ca. 1 mm). Dynamic storage and loss shear moduli, *G'* and *G''*, were obtained with a shear oscillation of 0.1 rad/sec and a low strain amplitude of 0.2-2 % where the viscoelasticity was independent of the frequency. The frequency was adjusted to 10 and 100 rad/sec to detect enough mechanical response, keeping in the linear viscoelastic regime of each sample. The temperature range was 25-300 °C with 1 °C/min. ramp to obtain order-disorder transition temperatures (T_{ODT}) with

a nitrogen gas purge to prevent thermal oxidation. For the time sweep test, the temperature was held above the melting point (depending on the materials) with a constant shear oscillation (0.1 rad/sec) and constant shear amplitude (0.2-2 %) for 12 hours. After 12 hours, the temperature was increased by 1°C /min. to T_{ODT}. The storage modulus, loss modulus, and tan δ were monitored and analyzed using TA Orchestrator software version 7.2.

h) Wide and Small Angle X-ray Scattering (WAXS/SAXS). X-ray scattering experiment was conducted at X27C beamline in National Synchrotron Light Source (NSLS), Brookhaven National Laboratory (BNL). The wavelength of the beam was 1.371 Å and the beam spot diameter was 0.6 mm after three pin-hole collimation system. The scattering patterns from both wide and small angle were collected with Mar CCD (SX-165, Rayonix, LLC. Formerly, Mar USA, Inc.) which had a resolution of 1024×1024 with 0.158 mm pixel size. The heating and cooling were controlled from 25 °C to T_{ODT} with a rate of 2.5 °C/min. using a temperature-controlled sample stage. The exposure times were 10 sec. and 60 sec. for each data frame during heating and cooling processes to acquire the scattering intensity. The sample-to-detector distance for WAXS and SAXS was approximately 69.1 mm and 1,863.7 mm, respectively. For the calibration, α-Al_2O_3 crystal was used for wide angle and silver behenate (AgBe, $CH_3(CH_2)_{20}COOAg$) was for small angle as standard materials. The first two scattering peaks for each setup were chosen to calibrate the distance. For *in-situ* SAXS/WAXS experiments, Xenocs Xeuss system having Cu Kα X-ray source (λ = 1.5418 Å, GeniX3D Cu ULD, Xenocs, SA, France) was applied to obtain the microphase separation with a temperature controlled sample stage (THXS-600, Linkam Scientific Instruments Ltd.). Both heating and cooling

rates were 5 °C/min. The two-dimensional scattering data were collected with semiconductor (CMOS) detectors (Pilatus 100K and Pilatus 300K, DECTRIS, Swiss). The acquisition time was 10 min for each frame and the scattering data was collected for 10 frames for a given temperature. The sample-to-detector distance for WAXS and SAXS was approximately 206.7 mm and 2,518.7 mm, respectively using AgBe. All samples were mounted in a washer type sample holders (3 mm hole × 1 mm thick) and covered with Kapton films (ca. 0.33 mm, SPEX Industries Inc., New Jersey, USA) as a X-ray transparent window. Two dimensional spectra were integrated using the FIT2D software to obtain the scattered intensity as a function of the scattering wave vector q, which is defined as $q = \frac{4\pi}{\lambda}\sin\theta$ with 2θ being the scattering angle. All scattering signals were corrected with background scattering, air scattering, and beam intensity. For the 2-D scattering image analysis, Igor Pro software (ver. 6.3) with Irena package was used to obtain circular averaged 1-D plots of intensity versus scattering wave vector q.[128]

5.3. Results and Discussions

Poly(1-hexene)-poly(methylene-1,3-cyclopentane) (PH-PMCP) were synthesized through a combination of living polymerization and living cyclopolymerization. To characterize the viscoelastic behavior of the crystalline-amorphous block copolymers, we focused on the low molecular weight block copolymers (total M_n ~ 15 kDa) which block sizes are below the critical entanglement molecular weights (M_e of PH = 14.1 kDa, M_e of PMCP = 8.2 kDa). The higher molecular weight set of PH-PMCP block copolymers (total Mn ~ 30 kDa) did not show the order-disorder transition temperature in the experimental temperature range (25-250 °C) (Appendix S.1). However, a set of low

molecular weight PH-PMCP block copolymers (total M_n ~ 15 kDa) exhibit the order-disorder transition temperature in 25-250 °C. The properties of the low molecular weight crystalline-amorphous block copolymers are summarized in Table 5.1.

Table 5.1 Basic properties of representative low molecular weight crystalline-amorphous block copolymers.

Sample	Mn of PH (kg/mol)	Mn of PMCP (kg/mol)	Mn of PH-PMCP (kg/mol)	f_{PMCP} (mole fraction)	Φ_{PMCP} (volume fraction)	PH T_g (°C)	PMCP T_m / T_c (°C)	M_w/M_n	T_{ODT} (°C)	Morph
1	11.4	4.2	15.6	0.20	0.23	-50.7	66.4 / 23.7	1.04	109	BCC
2	10.6	3.7	14.3	0.20	0.22	-51.7	68.8 / 21.6	1.11	141	BCC
3	8.9	6.6	15.5	0.35	0.37	-45.4	-	1.08	205	HEX
4	8.6	3.7	12.3	0.30	0.26	-45.8	61.4 / -	1.05	142	HEX
5	6.5	6.5	13.0	0.50	0.46	-30.6	56.7 / -4.9	1.03	156	GYR
6	6.2	5.6	11.8	0.47	0.43	-45.5	74.7 / 29.8	1.03	142	GYR
7	5.1	6.2	11.3	0.55	0.51	-49.2	88.9 / 62.3	1.08	137	GYR
8	5.6	7.6	13.3	0.58	0.54	-48.1	92.0 / 61.0	1.08	>250	LAM
9	5.9	8.6	14.5	0.60	0.54	-40.9	94.5 / 61.9	1.11	>250	LAM
10	6.4	12.9	19.3	0.67	0.62	-38.3	93.4 / 52.5	1.20	>250	LAM

The entanglement molecular weight of homopolymer PH and homopolymer PMCP is 14.4 kDa and 8.2 kDa, respectively, calculated from the plateau modulus.[129] Thus, the synthesized block copolymers fall into the unentangled regime and the narrow PDI for all materials rules out any effects which might arise from unreacted homopolymer PH or crosslinked block copolymers.

In addition, ^{13}C NMR spectra indicate that no copolymerization occurs during polymerization as there is no mixed NMR signal between 31-42 ppm in ^{13}C NMR.[117] Clearly separated PH and PMCP NMR spectra are also consistent with the weight ratio of PH and PMCP from GPC. As described in Chapter 4, it is possible to calculate the mole

fraction of each block using ^{1}H NMR. Figure 5.1 is a representative ^{1}H and ^{13}C NMR spectra of the low molecular weight block copolymers (sample 5).

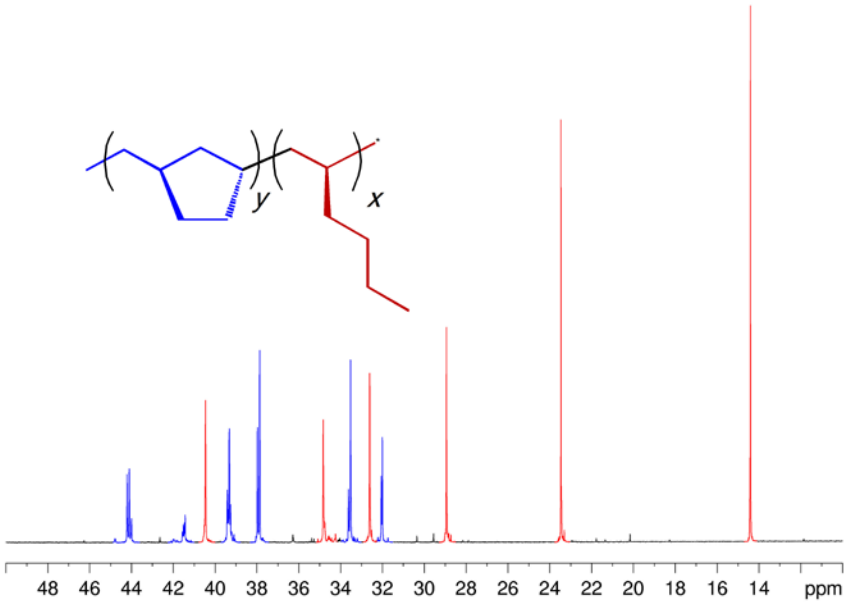

Figure 5.1 Representative ^{13}C NMR of sample 5 (CDCl at 25 °C).

To confirm the microphase separation of each block copolymer, phase sensitive tapping mode AFM was used to examine two block copolymer thin films. Figure 5.2 demonstrates a series of microdomain morphologies of these low molecular weight PH-PMCP block copolymers. As expected, weakly ordered spherical morphology is observed in the asymmetric block copolymer sample (sample 1, f_{PMCP} = 0.23). Sample 1 shows a melting point at 68 °C with short crystalline lamellae as well as spherical block copolymer microdomains due to the low fraction of crystalline PMCP. Since the crystalline domains are not confined within the spherical domains, only weakly ordered spherical domains are shown from the surface topology.[106] As the PMCP content increases to 0.3, the microdomain structure changes from spherical to cylindrical block

copolymer domains (samples 3 and 4, f_{PMCP} = 0.37 and 0.26 respectively). When the PMCP content reaches to 0.5, a crystalline lamellar morphology is dominant at ambient temperature. This result is consistent with the crystalline lamellae dominant morphologies that were observed at f_{PMCP} > 0.4 shown in Chapter 4.

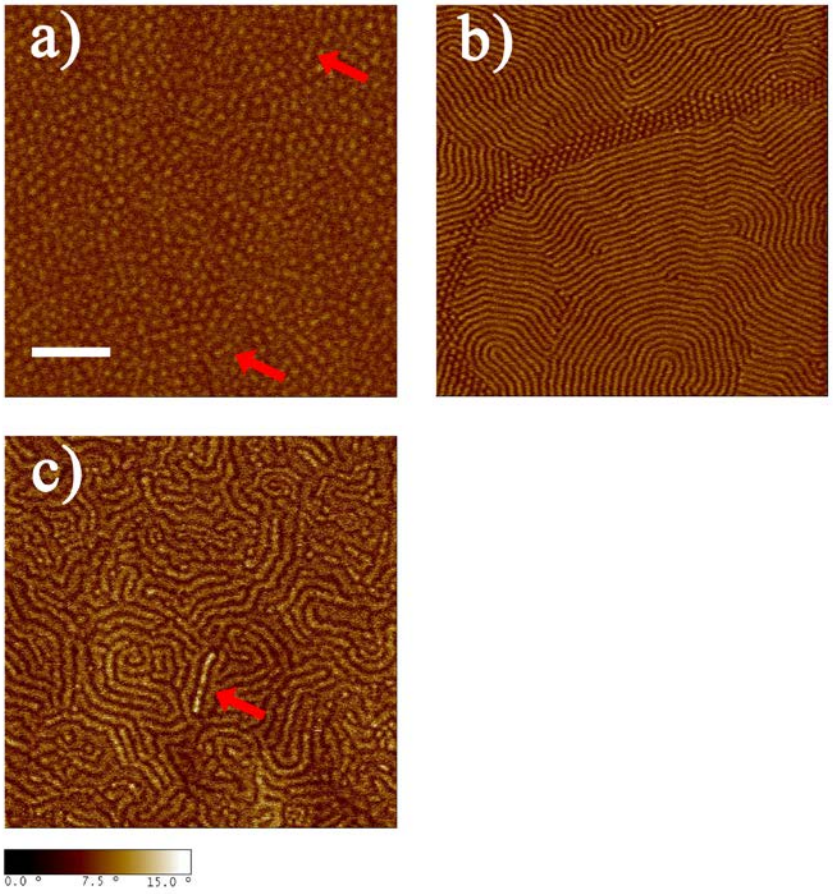

Figure 5.2 Microphase separation of PH-PMCP in phase contrast images. a) spherical (sample 1), b) cylindrical (sample 3), and c) crystalline lamellar (sample 5) morphology depending on the crystalline PMCP block ratio. The red arrows indicate PMCP crystals. The average film thickness is 30±3 nm. (scale bar : 200 nm).

The dynamic mechanical properties for the series of block copolymers were characterized using rheometry. All materials exhibit clear order-disorder transitions with sharp decrease in storage modulus (*G'*) at elevated temperature (>130 °C) except lamellar-forming PH-PMCP materials (sample 8 f_{PMCP} = 0.58, sample 9 f_{PMCP} = 0.60, and

sample 10 f_{PMCP} = 0.67). Based on the Leibler's block copolymer phase diagram, the lamellar phase is expected to have the highest order-disorder transition temperature for a given degree of polymerization, *N*. It is consistent that the T_{ODT} is increased with increasing PMCP ratio. It is likely that the lamellar samples have T_{ODT} above the experimental conditions examined in this study.

The viscoelastic behavior of sphere-forming PH-PMCP block copolymers (samples 1 and 2) is displayed in Figure 5.3. Below the PMCP melting point, there is a gradual decrease of the storage modulus implying the enhanced mobility of large fraction of amorphous PH matrix. As a result, the modulus dissipates from 9.61e+03 Pa to 6.69e+03 Pa in the range of 25-57 °C. When the temperature reaches to the melting point of PMCP crystals, there is a sudden drop in modulus at the melting temperature of PMCP crystals (T_m = 68 °C) and the modulus at the melting point is 5.91e+02 Pa.

Interestingly, the sphere-forming block copolymer samples display a sharp transition with a large drop in modulus at the melting temperature of PMCP crystals (T_m = 68 °C) followed by the enhancement of modulus above T_m. The modulus after the sharp transition is 1.73e+04 Pa. Unlike typical crystalline-amorphous block copolymer systems reported by other researchers such as polyisoprene-poly(ethylene oxide) (PI-PEO)[130] and polybutadiene-poly(ε-caprolactone) (PB-PCL)[131], the modulus of sample 1 recovers to a value about two orders higher (1.73e+04 Pa) than the value below the PMCP T_m. The recovery time from the lowest value of the modulus to the highest is 1-2 min and the magnitude of the modulus is more than at 30 times. Both samples 1 and 2 exhibit a sudden modulus drop at 109 °C and 140 °C, respectively, indicating the order-disorder transition temperature.

The sharp drop in modulus at about 68 °C is associated with the melting point of crystalline PMCP and not the order-order transition between microdomains near the phase boundary.[132-135] This behavior will be discussed further in the following chapter.

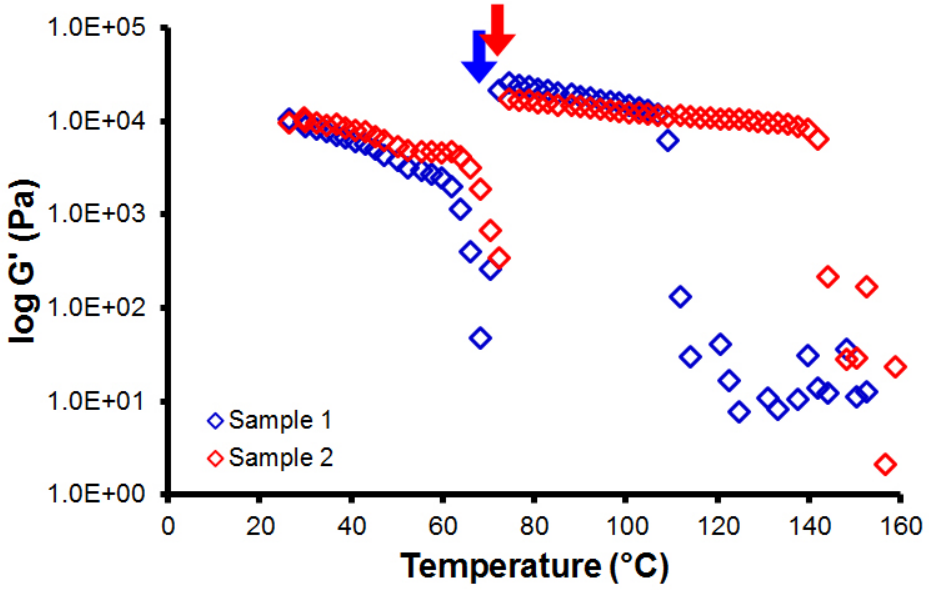

Figure 5.3 *G'*-temperature response of sphere-forming PH-PMCP block copolymers. The blue and red arrows indicate the transition point of sample 1 and 2, respectively.

Russell and co-workers studied perdeuterated polystyrene-poly(n-butylmethacrylate) (PS-PnBMA) the system and observed a lower critical ordering transition where microphase separation occurred on heating above the T_{ODT}.[136-138] The authors explained that the negative volume change with increasing temperature increases the entropy of the system resulting in microphase separation above T_{ODT}. Since a transition in modulus occurs at the PMCP melting point, it is reasonable that the modulus transition results from the melting of the crystalline PMCP block followed by improvement of the ordering of the microdomains. The modulus transition behavior will be discussed further in following chapter.

The *G'*-temperature relationships in PH-PMCP block copolymers were examined as a function of the ratio of PMCP crystals.

The *G'*-temperature responses of cylinder-forming PH-PMCP block copolymers is summarized in Figure 5.4. Interestingly, the cylinder-forming block copolymer (sample 4 f_{PMCP} = 0.30) only shows a very small modulus transition at the melting point and the storage modulus keeps decreasing as the temperature increases. The recovery in storage modulus takes for 5 min. at the PMCP melting temperature, which is slower than that in the sphere-forming samples (sample 1 and 2). The magnitude in modulus transition after PMCP T_m is only about 400 Pa. When the temperature reaches 142 °C, there is a sudden drop in modulus at the T_{ODT}. When the PMCP ratio increases, the sharp modulus increase is not observed above the PMCP melting temperature but the storage modulus decreases at the PMCP melting temperature. The viscoelastic behavior for a full set of cylinder-forming block copolymers is summarized in Appendix.

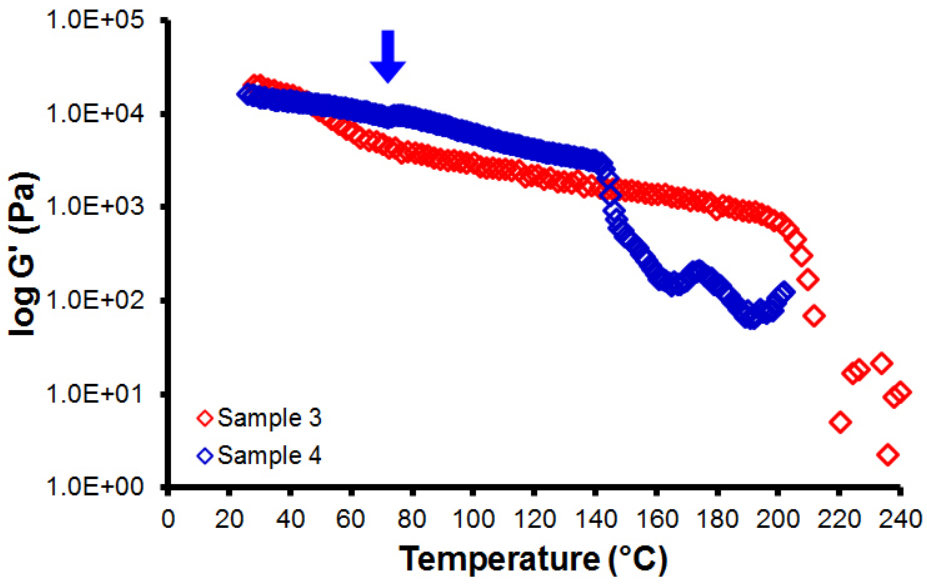

Figure 5.4 *G'*-temperature response of cylinder-forming PH-PMCP block copolymers. The blue arrow indicates the transition point for sample 4.

Samples 5-7 ($0.43 < f_{PMCP} < 0.51$) and samples 8-10 ($0.54 < f_{PMCP} < 0.62$) block copolymers show a significant decrease of the storage modulus at the melting temperature of PMCP crystals and then a gradual modulus enhancement above the melting temperature of PMCP crystals. The *G'*-temperature profiles of a series of PH-PMCP block copolymers (samples 5-7, $0.43 < f_{PMCP} < 0.51$) are summarized in Figure 5.5. For samples 5-7, the recovery time from the minimum value of the modulus at the melting point to the highest modulus value is nearly 30 min., which is much slower than those of spherical and cylindrical forming block copolymers. Due to the large fraction of crystalline PMCP ($f_{PMCP} \sim 0.53$), the initial storage modulus is close to 1.72e+05 Pa. The modulus at the transition temperature (PMCP T_m) is lower than the initial value of 5.95e+03 Pa due to the 3-dimensional network nature of the double gyroid structure. Above PMCP melting temperature, the storage modulus reaches 6.62e+03 Pa and then the order-disorder transition occurs at about 140 °C.

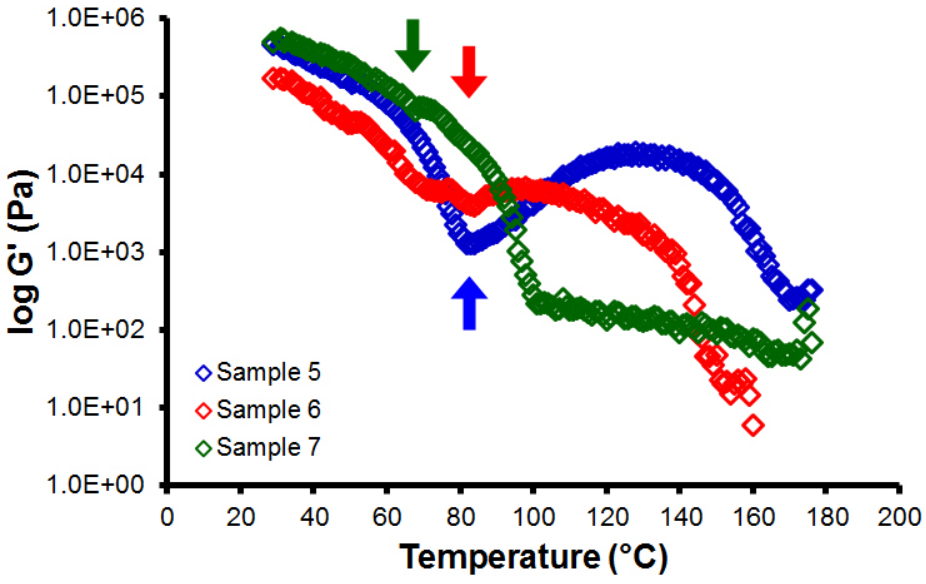

Figure 5.5 *G'*-temperature response of a series of PH-PMCP block copolymers ($0.43 < f_{PMCP} < 0.51$). The green, red, and blue arrows indicate the transition point for sample 5, 6, and 7 respectively.

Figure 5.6 displays the viscoelastic response of samples 8-10 ($0.54 < f_{PMCP} < 0.62$) as a function of temperature. Samples 8-10 also exhibit a sharp drop in the storage modulus at the PMCP melting temperature and then a modulus increase at about 180 °C. The large fraction of crystalline PMCP ($f_{PMCP} \sim 0.6$) contributes to the high storage modulus (1.92e+06 Pa) at ambient temperature and the molten PMCP block results in 3.61e+03 Pa at the melting temperature. When the temperature is increased to 250 °C, these samples do not show the order-disorder transition at higher temperature over the temperature range examined. Rather, the storage modulus increases to 1.12e+04 Pa at 179 °C. The modulus enhancement is observed at 175-180 °C for samples 8-10.

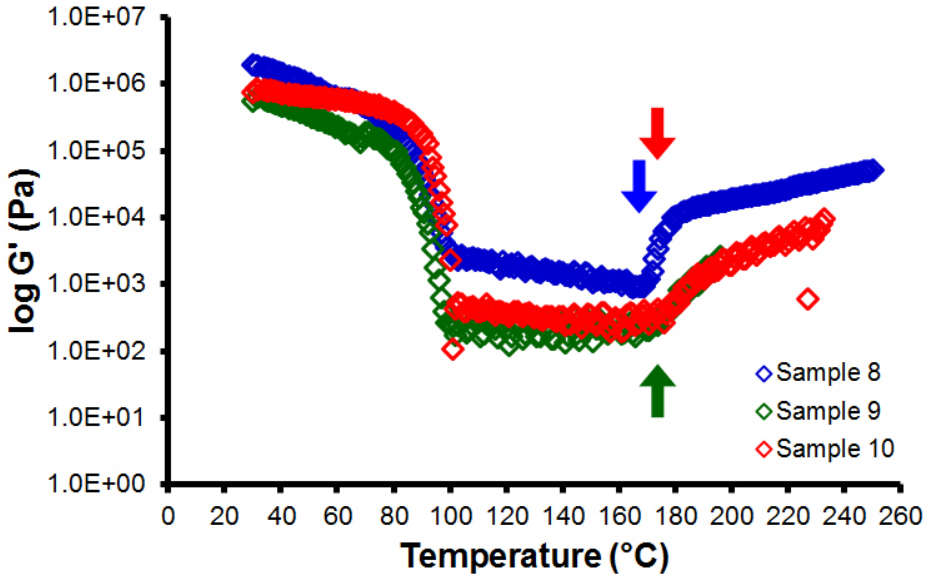

Figure 5.6 *G'*-temperature response of lamellar-forming PH-PMCP block copolymers. The blue, green, and red arrows indicate sample 8, 9, and 10 respectively.

Figure 5.7 shows representative the modulus-temperature profiles for PH-PMCP block copolymers as a function of f_{PMCP} (i.e., with different morphologies). The sharp decrease in modulus occurs at the melting temperature of PMCP crystals. As the fraction

of PMCP crystal increases in PH-PMCP block copolymers, the sudden drop temperature is also increased.

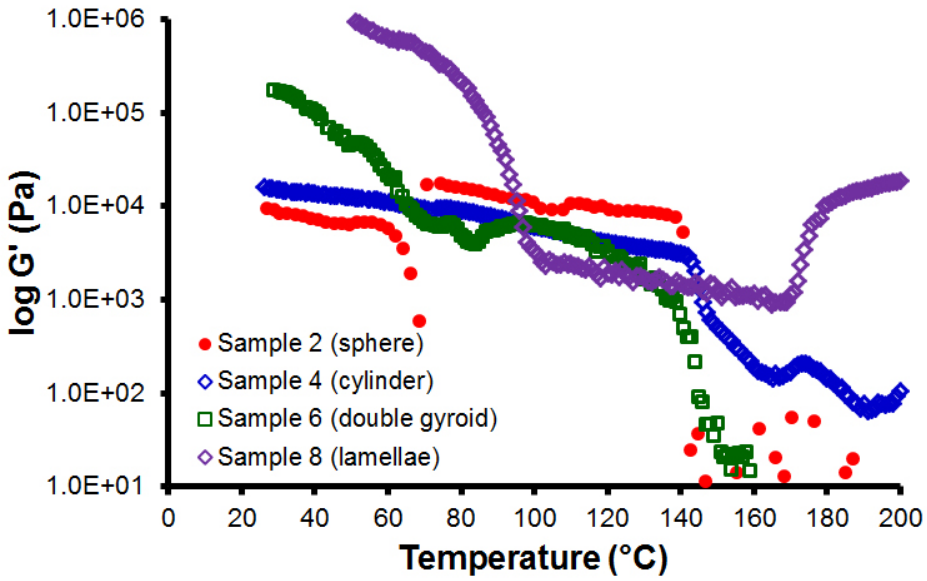

Figure 5.7 Representative sharp modulus transitions in low molecular weight PH-PMCP block copolymers.

In-situ small/wide angle X-ray scattering (SAXS/WAXS) is a powerful technique to examine the microdomain structure in block copolymers as well as the order-disorder transition. Due to the appearance of the unusual transition at about 68 °C in samples 1 and 2, it is important to examine the transition in more detail. Figure 5.8 displays *in-situ* SAXS profiles as a function of temperature. At 25 °C, crystalline diffraction is observed in the wide angle range where the scattering vector q is 1.28 $Å^{-1}$ (diffraction angle 2θ = 18.01 °). The I vs. q plot in the small angle range demonstrates a broad peak at q = 0.016 $Å^{-1}$ from the crystalline lamellae and a small peak at q = 0.028 $Å^{-1}$ from the block copolymer microdomains. This result is consistent with the surface topology measured by AFM of small crystalline PMCP lamellae as well as spherical block copolymer microdomains. As the temperature is increased, the intensity from crystalline phase diminishes in both wide and small angle regions. When the temperature is close to but

below melting point, a very faint crystalline diffraction is still observed at 2θ = 18.01 ° and a weak peak for the crystalline structure at low q. At the melting point, strong correlation scattering peaks are developed in the small angle scattering range with no crystalline diffraction signal. The correlation is well matched with a body-centered cubic structure with the scattering vector ratio of 1: √2: √3 from the primary scattering peaks q^*=0.038 Å^{-1} (d=16.8 nm). The BCC correlation is maintained up to the point where the order-disorder transition occurs at 140 °C.

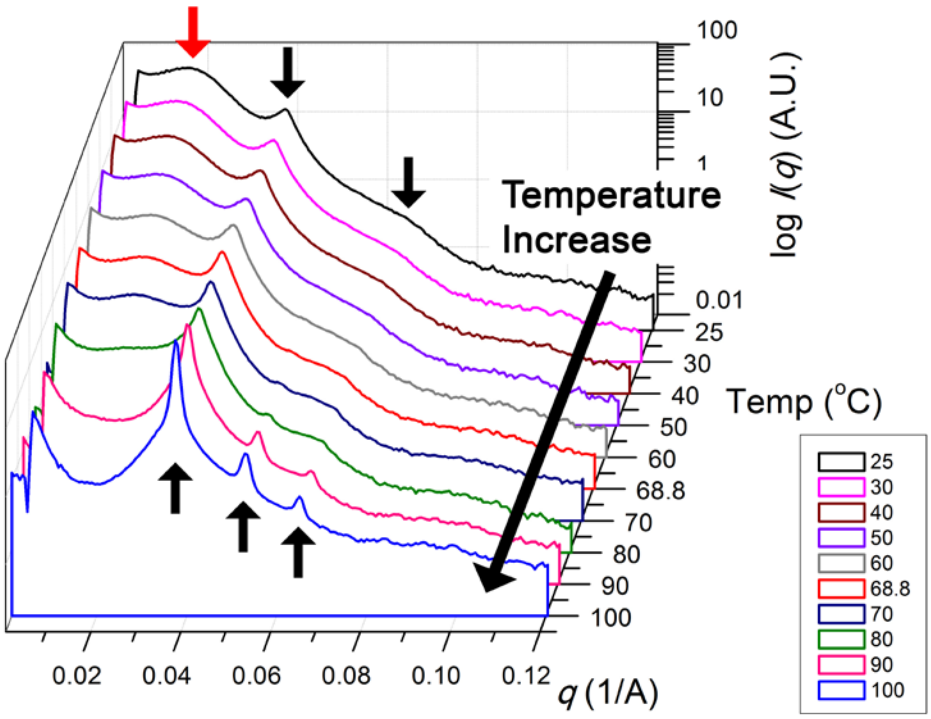

Figure 5.8 Evolution of spherical domain of sample 2 using *in-situ* SAXS. The red arrow indicates the PMCP crystals and the black arrows display the spherical microdomains.

X-ray scattering measured during cooling to ambient temperature and then reheating processes also indicates the loss of order of the spherical microdomains followed by the evolution of the PMCP crystals. The scattering peak at low q represents the evolution of crystalline lamellae as a function of time (Figure 5.9). After 12 min., the

molten PMCP block is fully crystallized with a lamellar periodicity of about 20 nm. At this stage, the high *q* scattering correlation peaks for the spherical microdomains have disappeared.

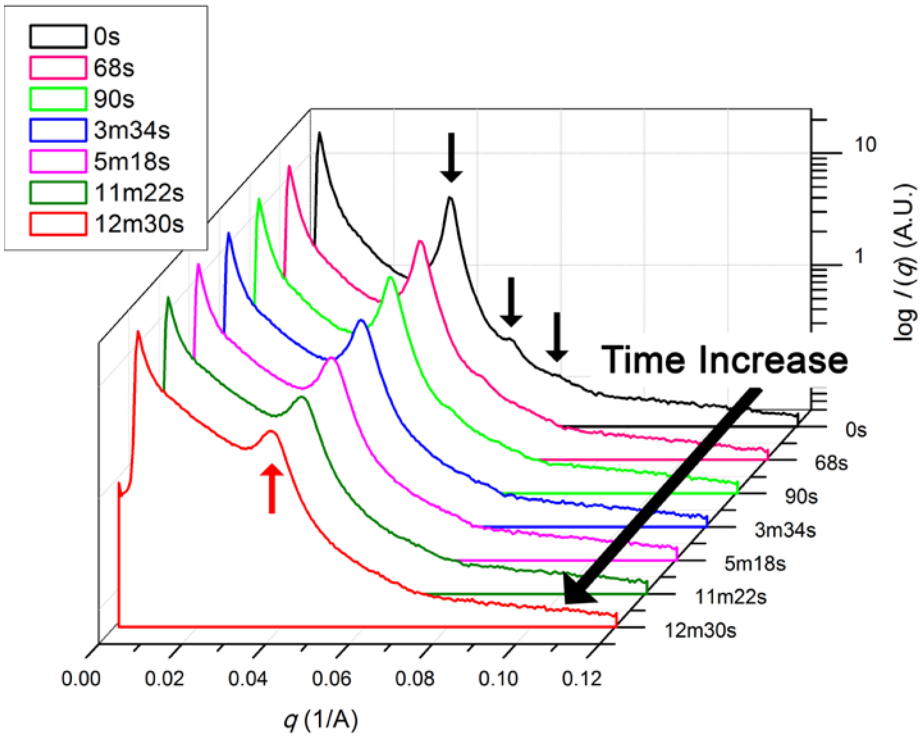

Figure 5.9 Crystallization of PMCP block in sample 2 at 20 °C. The black arrows exhibit the spherical microdomains and the red arrow indicates the PMCP crystals.

The cylinder, double gyroid, and lamellar-forming block copolymers also exhibit the crystalline domains below the melting point and well-defined block copolymer microdomain structures at temperatures higher than the PMCP melting point. Figure 5.10 displays the evolution of hexagonally-packed cylinder microdomains as a function of temperature. The cylinder-forming PH-PMCP block copolymers (samples 3 and 4) show scattering peaks from both the PMCP crystals at low *q* (q = 0.024 $Å^{-1}$) and hexagonally-packed cylinder microdomains at ambient temperature. As the temperature is increased, the scattering intensity of PMCP crystals is decreased while the scattering peak intensities

for cylindrical microdomains increase. The ratio of scattering vectors in cylinder-forming PH-PMCP is 1: √3: √4: √7 consistent with hexagonally packed cylinders with the primary scattering peak q^* =0.038 $Å^{-1}$. The domain spacing, d, is 16.5 nm. The cylindrical microdomain structure retains until T_{ODT}.

When the fraction of crystalline PMCP is larger than 0.4, the scattering from the block copolymer microdomain structures is barely observed. The larger fraction of PMCP crystals disrupt the microdomain structure and randomly distributed PMCP crystals are the major structure at ambient temperature. The scattering intensity from the PMCP crystals is dominant at low q. The strong signal at about low q = 0.024 $Å^{-1}$ indicates the presence of PMCP crystals. In addition, the diffraction peaks of d_{100} and d_{110} for the PMCP crystals are also observed by WAXS.

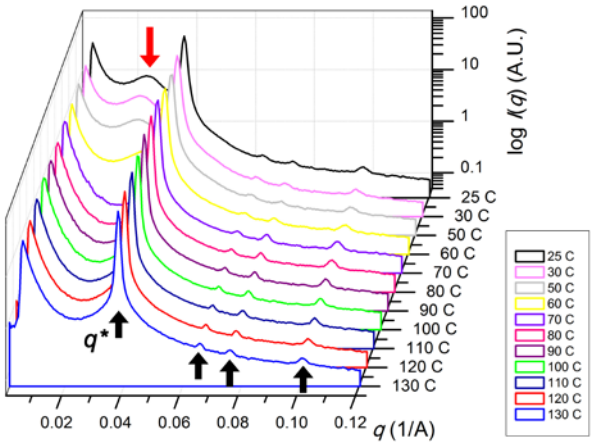

Figure 5.10 Evolution of hexagonally packed cylinder structure in sample 3 using *in-situ* SAXS. The black arrows exhibit the cylindrical microdomains and the red arrow indicates the PMCP crystals.

Figure 5.11 displays the scattering profiles as a function of temperature. At 25 °C, samples 5-7 only display a broad peak at low q (q = 0.024 $Å^{-1}$ indicative of the crystalline PMCP in samples 6-8. In addition, strong diffraction intensities d_{100} and d_{110} are observed

at 2θ = 18° and 31°, respectively. As the temperature increased, the scattering intensity at low q is decreased while the scattering from the microdomains develops. Above the PMCP melting temperature, the scattering peaks develop with ratios of √3: 2: √7: √8: √10: √11. This result is consistent with double-gyroid structure.

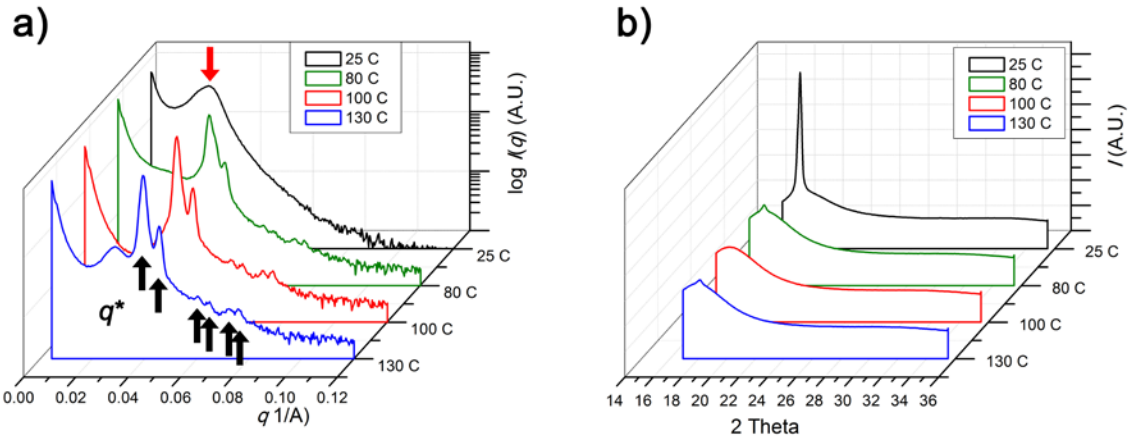

Figure 5.11 Evolution of double gyroid structure in sample 6 using *in-situ* SAXS / WAXS. a) SAXS and b) WAXS. The black arrows exhibit the double gyroid microdomains and the red arrow indicates the PMCP crystals.

Likewise, samples 8-10, lamellar-forming PH-PMCP, exhibit a broad scattering peak at low q ($q1$ = 0.018 Å^{-1}) with the strong diffraction peaks at 2θ = 18° and 31° (Figure 5.13). In addition, the large fraction of PMCP crystals exhibits a second-order scattering peak with 1: 2 ($q2$ = 0.037 Å^{-1}). As the temperature reaches the PMCP melting, the scattering peaks from the microdomains emerge. The ratio of scattering vectors of 1: 2: 3 indicates the lamellar microdomains structure with the primary scattering peak q^*= 0.040 Å^{-1} (d=15.8 nm). Due to the highly asymmetric chain stiffness in PH-PMCP block copolymers, the double gyroid and lamellar phases show up at f_{PMCP} ~ 0.51 followed by the lamellar phase at f_{PMCP} ~ 0.54.[35,139,140]

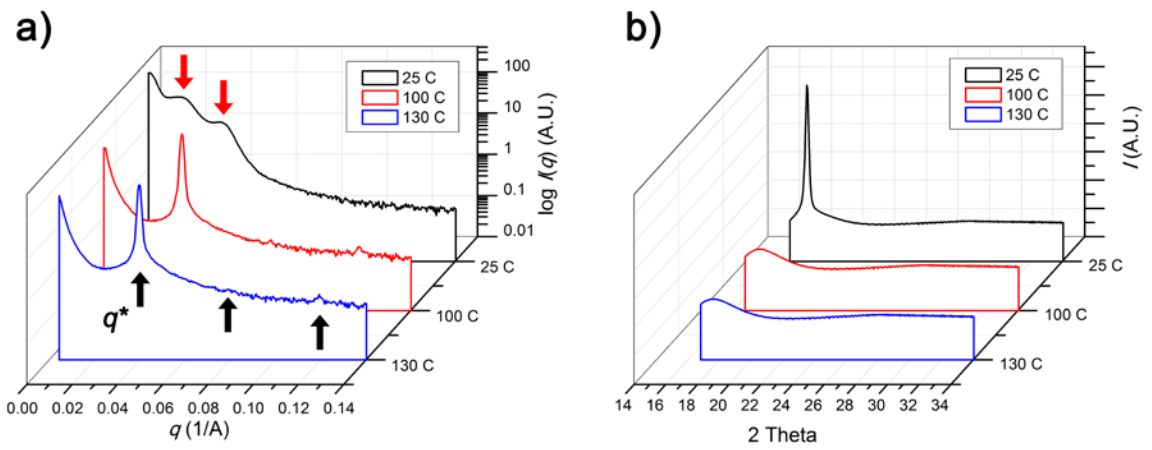

Figure 5.12 Evolution of lamellar structure in sample 8 using *in-situ* SAXS / WAXS. a) SAXS and b) WAXS. The black arrows exhibit the lamellar microdomains and the red arrows indicate the PMCP crystals.

The SAXS/WAXS data of these low molecular weight PH-PMCP block copolymers clearly demonstrates the crystalline melting of PMCP followed by the ordering of the microdomains with a concomitant during a sharp modulus transition. In the case of $f_{PMCP} < 0.4$, spherical and cylindrical block copolymer microdomains are weakly-ordered due to the presence of the small PMCP crystals at T < PMCP T_m. In addition, the scattering peak of PMCP crystals as well as the peaks of block copolymer microdomains are shown at T < PMCP T_m. When the PMCP fraction is increased ($f_{PMCP} >$ 0.4), the larger fraction of PMCP crystals disrupt the microdomain structures resulting in the scattering being dominated by the peak from the PMCP crystals at T < PMCP T_m. When the temperature is above the melting point of PMCP crystals, all samples exhibit multiple scattering peaks indicating well-ordered block copolymer microdomains until T_{ODT}.

Since the viscoelastic response in PH-PMCP system is driven by the melting and microphase separation, we have examined the reproducibility with temperature cycling. The molten PMCP blocks participated in the microphase ordering above at the PMCP

melting temperature and improve the storage modulus at T > PMCP T_m. A more detailed investigation will be discussed in Chapter 6.

To visualize the morphological changes associated with the modulus transition in samples 1 and 2 (sphere-forming PH-PMCP materials) surface topology analysis was conducted using AFM. Figure 5.13 shows the modulus transition in sample 1. We divided the modulus profile into 4 regions, I) before the melting point, II) at the melting point, III) after the melting point, and IV) after the order-disorder transition. The AFM images quenched from the different temperature regions are shown in Figure 5.14. The quenched sample below the melting point to 25 °C exhibits a mixture of weakly-ordered spherical domains and small PMCP crystals in the phase image. The distance between the domains is approximately 20 nm, which is comparable size measured by SAXS. The quenched sample from the melting point (T = 68 °C) shows well-defined spherical microdomains with no PMCP crystals. The morphology quenched from 90 °C to 25 °C also shows well-ordered spherical domains. The domain spacing for the spheres at the melting point and 90 °C are consistent with the SAXS scattering data. The quenched sample from 150 °C to ambient temperature shows no spherical microdomains indicating that above the order-disorder transition temperature the sample is disordered as expected (Figure 5.14 d).

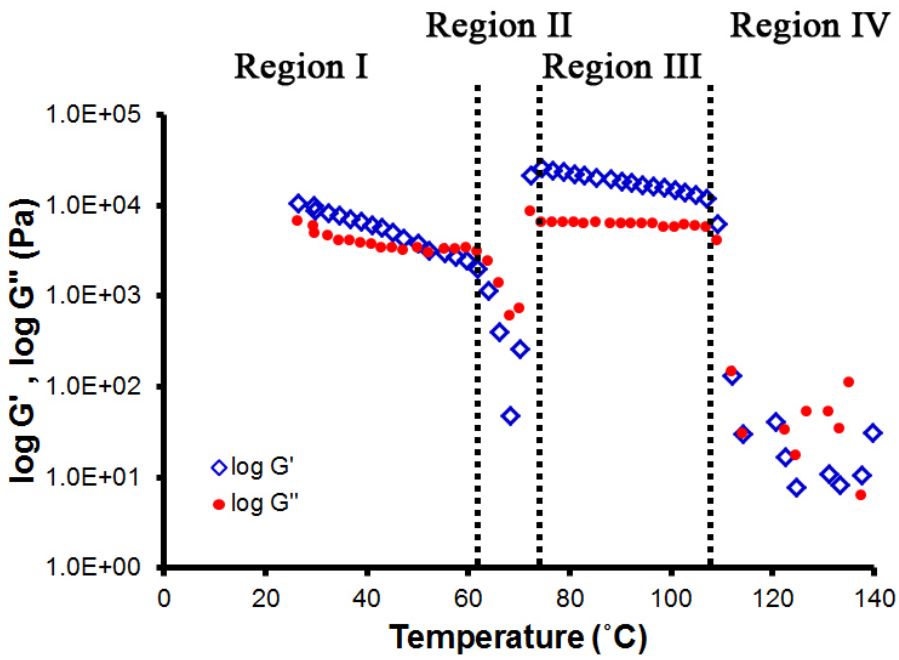

Figure 5.13 Sharp modulus transition of sphere-forming PH-PMCP (sample 1).

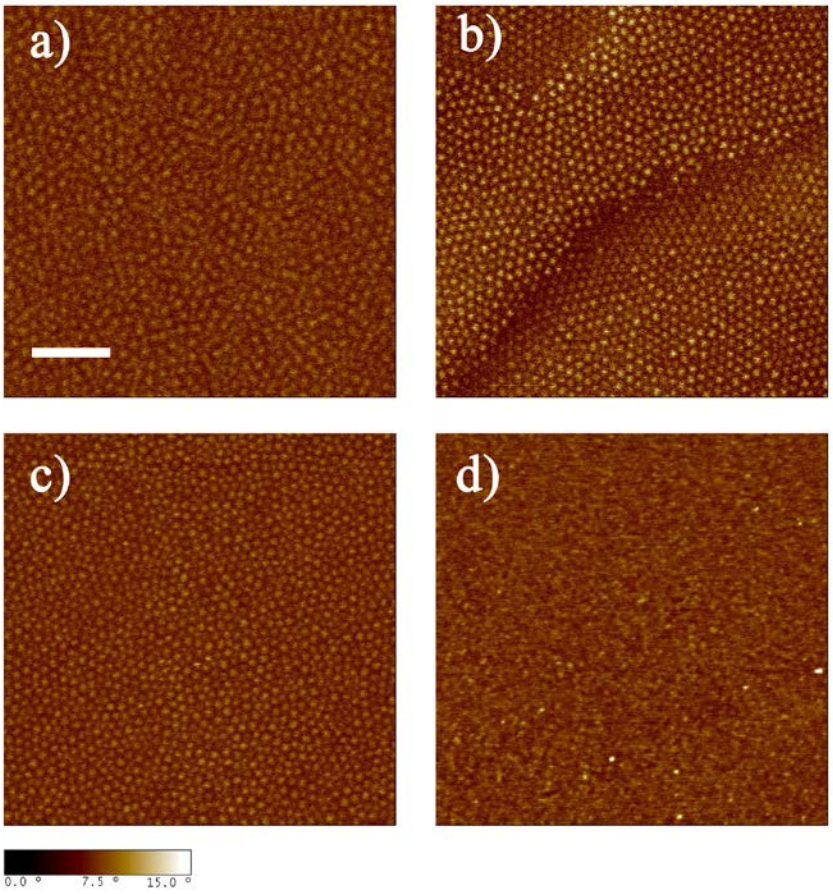

Figure 5.14 AFM images of sample 1 quenched from 4 different temperature region based on the modulus-temperature plot, a) ambient temperature (25 °C) in Region I, b) T=68 °C, Region II, c) T=90 °C, Region III, and d) T=150 °C (>T_{ODT}), Region IV. Scale bar: 200 nm.

The main driving force behind the modulus transition at 68 °C is the molecular weight of PMCP block and the size of the PMCP crystals. Small PMCP crystals are randomly distributed with dimensions of about 8-10 nm wide and 10-60 nm long. The small PMCP crystals are similar to a fringed lamellae model.[141] These small PMCP crystals provide mechanical stiffness until the melting point. The schematic of the spherical microdomain morphology before and after the transition shows this concept in Figure 5.15. Below the melting point of PMCP crystals, the small crystals are randomly distributed in the amorphous PH matrix. When the temperature increases, the crystalline block melts, and subsequently, microphase ordering improves due to the immiscibility

between the PH and PMCP blocks. We speculate that the large difference in PH and PMCP chain stiffness gives rise to a large Flory-Huggins interaction parameter facilitating a rapid microphase ordering. Additionally, the high chain mobility due to low molecular weight leads to the rapid improvement in microphase ordering. The BCC array of spherical PMCP domains increases the storage modulus after the melting point which is maintained until T_{ODT}.

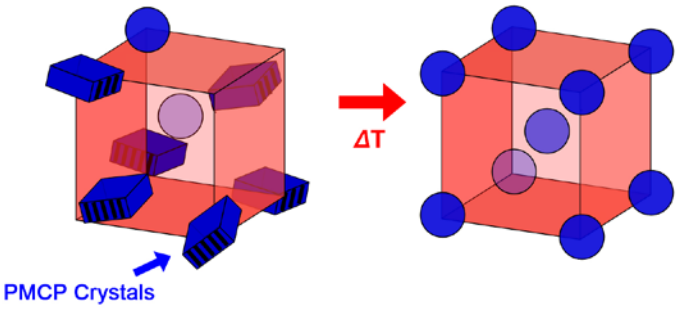

Figure 5.15 Schematics of the spherical microdomain morphology before and after the transition.

The cylinder-forming PH-PMCP block copolymers (samples 3 and 4) show the weakest modulus transition at T_m compared to among the spherical, cylindrical, double gyroid, and lamellar phases. For materials with a PMCP fraction of 0.3-0.4 by volume, the material shows both PMCP crystals and cylindrical microdomains below the PMCP melting point as previously described in Chapter 4. The cylinder-forming PH-PMCP material with a PMCP content of 0.3 shows a relatively weak scattering signal from PMCP crystals as well as hexagonally-packed cylinder microdomains (Figure 5.2 b) and *in-situ* SAXS/WAXS (Figure 5.10).

The reason for the small magnitude of the modulus transition in cylinder-forming block copolymer is that the small PMCP content (f_{PMCP} ~ 0.3) generates small PMCP crystals in the material. The small fraction of PMCP crystals results in only a very weak

modulus transition at the melting point followed, which then forms fully-developed and well-ordered cylindrical microphase. When the PMCP fraction is larger than 0.3, the PMCP crystals disturb microdomains and dominates the morphology. In this case, the larger fraction of crystalline PMCP results in a higher storage modulus at $T < T_m$. As increase in temperature, the modulus shows a lower value at $T > T_m$ without showing the increase in modulus (Appendix S.2). Figure 5.16 illustrates the phase transition before and after the PMCP melting.

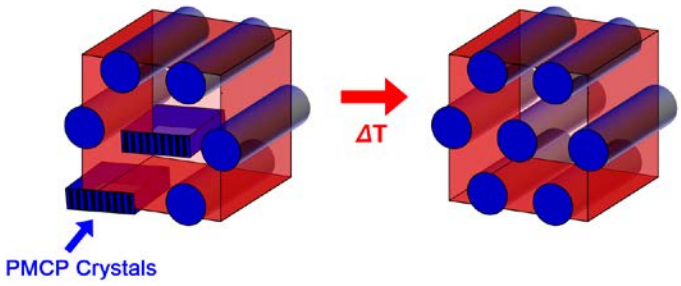

Figure 5.16 Schematics of the cylindrical microdomain morphology before and after the transition.

Samples 5-7, (double gyroid) demonstrate a similar modulus improvement at the PMCP melting point. The recovery in storage modulus takes about 15 min., which is slower than the time for sphere and cylinder forming PH-PMCP block copolymers. Both the spherical domain morphology (BCC, $Im\bar{3}m$) and the double gyroid structure (GYR, $Ia\bar{3}d$) are highly symmetric cubic phases, which give rise to a similar viscoelastic response at the terminal frequency.[33] Due to the presence of 3-dimensional translational order in cubic structures, the elastic energy for recovery exhibits the same response during oscillation. The viscoelastic behavior at the low frequency region shows the shear modulus to be independent of the frequency ($G' \sim \omega^0$).

Unlike sphere and cylinder-forming PH-PMCP, the double gyroid forming PH-PMCP block copolymers only display a broad scattering peak at low q (q = 0.02 Å^{-1}) due to the large fraction of crystalline PMCP (f_{PMCP} > 0.45) at ambient temperature. The large PMCP crystals disrupt the microdomain structure. In addition, the strong diffraction peaks in WAXS indicate that the morphology is dominated by the PMCP crystals. When the PMCP crystals melt, the molten PH-PMCP block copolymer can undergo microphase ordering to form a double gyroid microdomain structure. *In-situ* SAXS/WAXS supports the emergence of double gyroid block copolymer microdomain structure with long-range order above the PMCP T_m.[130,133,134,142-144]

The lamellar-forming PH-PMCP materials (samples 8-10) also exhibit a large decrease in modulus at the melting point. Above the melting point, the storage modulus of lamellar microdomains remains the lower magnitude with a value of 3.61e+03 Pa until 175-180 °C. Above 180 °C, a modulus enhancement occurs with no sudden drop in modulus. No thermal decomposition or cross-linking is observed after the experiment. *In-situ* SAXS/WAXS displays the presence of PMCP crystals at low q (q = 0.017 Å^{-1}) at ambient temperature. After the PMCP melting, the scattering peaks show the ratios of scattering vectors of 1: 2: 3 indicating the lamellar microdomain structure even above 180 °C. The primary scattering peak q^*= 0.040 Å^{-1} (d=15.8 nm) remains in the experimental temperature range (T_m - 250 C). Based on the in-situ SAXS/WAXS, the viscoelastic response of the lamellar-forming PH-PMCP block copolymers at T ≥ 180 °C needs to be characterized.

5.4. Conclusions

The shear modulus transition at the melting point of the crystalline PMCP block is observed in all block copolymer microdomain structures, i.e., spherical ($0.17 < f_{PMCP} < 0.25$), cylindrical ($0.29 < f_{PMCP} < 0.38$), and double gyroid ($0.43 < f_{PMCP} < 0.51$) and lamellar ($0.54 < f_{PMCP} < 0.62$) in a series of low molecular weight crystalline-amorphous PH-PMCP block copolymers (total M_n ~ 15 kDa). We have investigated the viscoelastic behavior with different block copolymer microdomain structures using rheology and *in-situ* SAXS/WAXS as a function of PMCP content. The modulus transition at the melting point varies from about 500 Pa to more than 17,000 Pa in sphere-forming PH-PMCP. In addition, the recovery time of the storage modulus after the melting of the PMCP varies from 1-2 min. in sphere- and 5 min. in cylinder-forming PH-PMCP, to about 20 min. in double gyroid-forming PH-PMCP, and 70 min. in lamellar-forming PH-PMCP.

Specifically, the change in modulus from the lowest to the highest values is about 2 orders of magnitude in spherical-forming block copolymers. A coupled effect of the melting of crystalline domains followed by the microphase ordering promotes a sharp modulus transition with a recovery time of about 1-2 min. The modulus recovery after the melting point is due to ordering of the PH-PMCP microdomain structure. Based on the results in Chapter 4, the PH-PMCP system is a strong segregation system in weak confinement regime. The Flory-Huggins interaction parameter of PH-PMCP system is expected to be large compared to many other crystalline-amorphous block copolymer systems due to the large difference in chain stiffness of these two blocks.

When the fraction of PMCP is smaller than 0.4, *in-situ* SAXS/WAXS exhibits the PMCP crystals and block copolymer microdomains at T < PMCP T_m. As the temperature is increased, only block copolymer microdomain peaks are shown in the experimental temperature range. Due to the large fraction of crystalline PMCP ($f_{PMCP} > 0.4$), the PMCP crystals are the major morphology and break the block copolymer microdomains. Consequently, *in-situ* SAXS/WAXS only display a broad scattering peak ($q = 0.02$ Å^{-1}) at T<PMCP T_m. Much like sphere and cylinder-forming PH-PMCP block copolymers, the well-ordered double gyroid and lamellar microdomains are shown at T > PMCP T_m until T_{ODT}.

This result suggests that the large difference in chain stiffness of PH-PMCP causes a sharp modulus transition at the melting point of crystalline PMCP. The improvement in storage modulus is mainly due to the rearrangement of molten PH-PMCP block copolymers resulting in well-ordered microdomains.

Chapter 6. Viscoelastic Behavior of Crystalline-Amorphous Block Copolymers: Sphere-Forming Block Copolymer

6.1. Background

The viscoelastic properties of block copolymers have been used to measure the order-disorder transition temperature (T_{ODT}). Chung *et al.* and Gouinlock and Porter have studied the dynamic mechanical properties of block copolymers as a function of temperature.[121,122] Above T_{ODT}, the single phase block copolymer displays homogeneous viscoelastic polymer behavior. Below the transition temperature, the block copolymer undergoes microphase separation and forms nanometer scale domains due to the presence of connectivity between chemically distinctive blocks. Depending on the block ratio in the copolymer, the domains can be arranged into a body-centered-cubic array of spheres (BCC), hexagonally-packed cylinders (HEX), bicontinuous double gyroid (GYR), or lamellae (LAM). Due to the characteristics of ordering of the microdomains in the block copolymers, the rheological behavior exhibits a unique viscoelastic response in the low frequency region ($T< T_{ODT}$). The viscoelastic measurement provides structural information for the block copolymer as a function of storage modulus, frequency, and temperature. A large amount research has been done to characterize the microphase separation in block copolymers using rheometry.[28,145-149]

For crystalline-amorphous block copolymer systems, the melting point of the crystalline block will influence the low-frequency dynamic viscosity measurement. It has been observed that the elastic shear modulus of a crystalline-amorphous block copolymer

decreases at the melting point.[35,37,130,135] Crystalline-amorphous block copolymers have also been examined using *in-situ* SAXS/WAXS to follow the melting of the crystalline domains as well as the order-disorder transition temperature of the block copolymer microdomains.[98,102,150,151] Only a few researches have been reported the structure-property relationships in low molecular weight crystalline-amorphous block copolymer system in the weak confinement regime.[35,152-154]

As reported in Chapter 5, the sphere-forming PH-PMCP block copolymers displayed a sharp drop in storage modulus at the PMCP melting point followed by a recovery in the modulus by 2 orders of magnitude (Figure 5.3). Based on the viscoelastic measurements and AFM images, the melting of the PMCP block triggers the sharp drop of the storage modulus followed by the microphase ordering. From DSC data, the temperature matches the melting point of crystalline PMCP block (68-69 ˚C). Moreover, no change is detected in the block copolymer microdomain morphology from AFM micrographs and *in-situ* SAXS/WAXS before and after the transition.

We have investigated the viscoelastic response in low molecular weight crystalline-amorphous sphere-forming PH-PMCP block copolymers as a function of heating rate, oscillation frequency, and oscillation time.

6.2. Experimental Setup

a) Materials. The synthesis of sphere-forming PH-PMCP materials in this study was described previously. Briefly, all syntheses were carried out at -10 °C in PhCl (20 mL) with a cocatalyst to precatalyst ratio of 1.01 to ensure the complete activation. Sequential polymer blocks were obtained by first adding 1-hexene for 2 hours followed

by the addition of 1,5-hexadiene for an additional 1 hours. The molecular weight of each block was controlled by the amount of monomer present based on the kinetics of poly(1-hexene) and poly(methyl-1,3-cyclopentane). A small (<1 mL) amount of poly(1-hexene), PH, was removed and quenched for analysis immediately prior to the addition of the second monomer. Polymer samples were quenched in ca. 500 mL of acidic methanol (10 % HCl by volume). Samples were washed and filtered with MeOH and then dried under vacuum at 25 °C until constant weight was observed. The molecular weights of all polymers were measured using gel permeation chromatography (GPC) (Viscotek TDA) equipped with a column oven. Differential refractometer and four columns (T2500, T3000, T4000 and T5000) were maintained at 40 °C. Tetrahydrofuran (THF) was used as the eluent at a flow rate of 1.0 mL/min. The number-average molecular weight (M_n) and weight-average molecular weight (M_w) of samples were obtained using Viscotek OmniSEC software.

b) Differential Scanning Calorimetry (DSC). The thermal properties of block copolymers were obtained using a DSC Q1000 (TA Instruments). Nitrogen was used as a purge gas at 50 mL/min. The T_m, T_g, T_c and heat of fusion (ΔH) were measured using heat-cool-heat cycles at 10 °C/min. All values were taken after the first heating cycle to remove previous thermal history.

c) Phase-Sensitive Tapping Mode Atomic Force Microscopy (ps-tm AFM). The surface morphology analysis was performed on a Multimode AFM with Nanoscope IIIa controller (Digital Instrument) in tapping mode. Both height and phase-shift data were obtained with a silicon etched tip (Nanosensors, spring constant k = 25-55 N/m, resonance frequency f = 292-377 KHz) under ambient conditions. All samples were

dissolved in toluene (1 wt %) and spin-coated at 2,000 rpm onto Si substrates. Si substrates surfaces were cleaned with 7:3, H_2SO_4 : H_2O_2 "piranha" solution. Film thickness was obtained by using Gaertner ellipsometer for 3 different spots on each sample. Spin-coated film thicknesses were between 30 to 35 nm. All AFM samples were measured before and after annealing at 60 °C for 12 hours.

d) Dynamic Mechanical Experiments. Dynamic mechanical shear modulus analysis was conducted using a RDA III Analyzer (Rheometric Scientific Inc.) with parallel plates (diameter: 7.9 mm, gap: ca. 1 mm) and an AR 2000 (TA Instruments Inc.) with parallel plates (diameter: 25 mm, gap: ca. 1 mm). Dynamic storage and loss shear moduli, *G'* and *G''*, were obtained with a shear oscillation of 0.1 rad/sec and a low strain amplitude of 0.2-2 % where the viscoelasticity was independent of the frequency. The frequency was adjusted to 10 and 100 rad/sec to detect enough mechanical response, keeping in the linear viscoelastic regime of each sample. The temperature range was 25-300 °C with 1 °C/min. ramp to obtain order-disorder transition temperatures (T_{ODT}) with a nitrogen gas purge to prevent thermal oxidation. For the time sweep test, the temperature was held above the melting point (depending on the materials) with a constant shear oscillation (0.1 rad/sec) and constant shear amplitude (0.2-2 %) for 12 hours. After 12 hours, the temperature was increased by 1°C /min. to T_{ODT}. The storage modulus, loss modulus, and tan δ were monitored and analyzed using TA Orchestrator software version 7.2.

6.3. Results and Discussions

The microphase separation behavior in sphere-forming PH-PMCP block copolymers is summarized in Table 6.1. In Chapter 5, we have demonstrated that the sphere-forming PH-PMCP block copolymers have short and isolated PMCP crystals as well as spherical block copolymer microdomains by *in-situ* SAXS/WAXS. Since the amount of the crystalline PMCP block is small, it is expected that the crystalline lamellae are surrounded by amorphous PH resulting in isolated crystalline domains. When the temperature increases, the crystalline PMCP lamellae melt and the spherical microdomain structure order is enhanced. This morphology is retained until T_{ODT}. The spherical block copolymer microdomain morphology is shown in Figure 6.1 as a function of temperature along with the rheological data.

Table 6.1 Characteristics of sphere-forming PH-PMCP block copolymers.

Sample	**Mn of PH (kg/mol)**	**Mn of PMCP (kg/mol)**	**Mn of PH-PMCP (kg/mol)**	f_{PMCP} **(mole fraction)**	Φ_{PMCP} **(volume fraction)**	**PH** T_g **(°C)**	**PMCP** T_m **/** T_c **(°C)**	M_w/M_n	T_{ODT} **(°C)**	**Morph**
1	11.4	4.2	15.6	0.20	0.23	-50.7	66.4 / 23.7	1.04	109	BCC
2	10.6	3.7	14.3	0.20	0.22	N/A	68.8 / 21.6	1.11	141	BCC

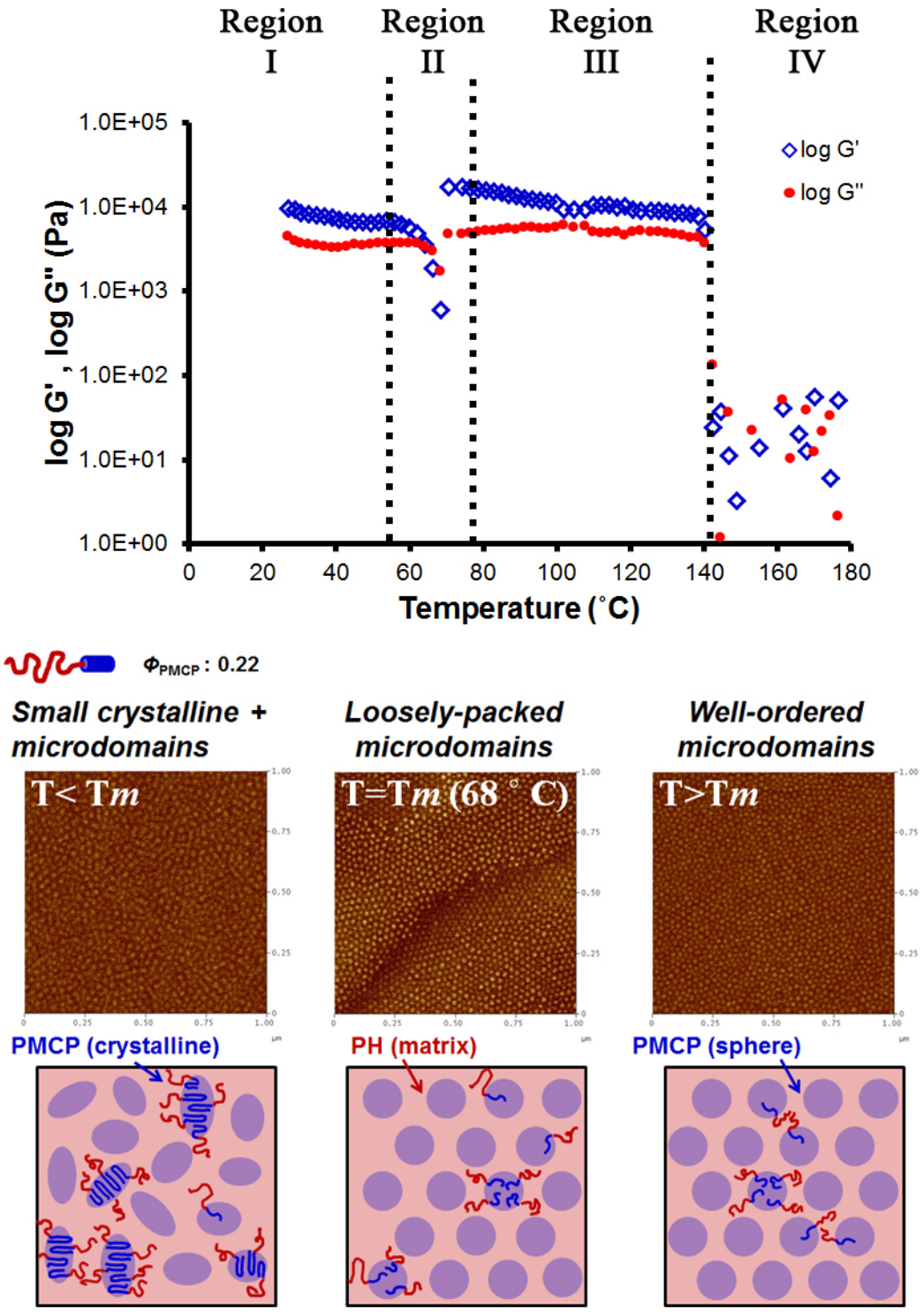

Figure 6.1 Schematic diagram of the block copolymer microdomain reorganization for different temperature zones associated with the modulus behavior.

6.3.1. Terminal frequency behavior in sphere-forming PH-PMCP

We conducted frequency sweep tests to examine the block copolymer microdomain structure in the low frequency region as a function of temperature. The viscoelastic behavior at low frequency is dependent on the ordered domain microstructures.[33] The different structures generate distinctive elastic properties in terms of G' and ω. Specifically, the viscoelastic behavior of spherical block copolymer microdomains at low frequency scale as $G' \sim \omega^0$, which indicates that the shear storage modulus is independent of the shear frequency rate.[27,155-157]

When the temperature is below the PMCP melting point, the viscoelastic response displays a power law of α=0.2 reflecting the mixture of microstructures with spherical and cylindrical morphologies (Figure 6.2 a). The irregular spherical block copolymer domains from AFM of sample 2 is consistent with the relationship of $G' \sim \omega^{0.2}$. When the temperature reaches the PMCP melting temperature (T~68 °C), the G'-ω profile dramatically changes and the modulus shows frequency-independent behavior with a power law of of α=0. This is consistent with the microstructure of the quenched sample at 68 °C, which shows well-defined spherical block copolymer domains by AFM. The terminal modulus-frequency relationship at 90 °C exhibits the same power law of α=0, suggesting a body-centered-cubic array of spherical block copolymer microdomains (Figure 6.2 c). This result is in good agreement with the AFM images from samples quenched from Region III (Figure 6.1). PH-PMCP with f_{PMCP} = 0.22 (sample 2) retains the spherical block copolymer microdomains above the PMCP melting temperature until the T_{ODT}. When the temperature decreases from 90 °C to 50 °C, the terminal viscoelastic

response maintains a power law of α=0 suggesting the continued presence of the spherical block copolymer microdomains (Figure 6.2 d).

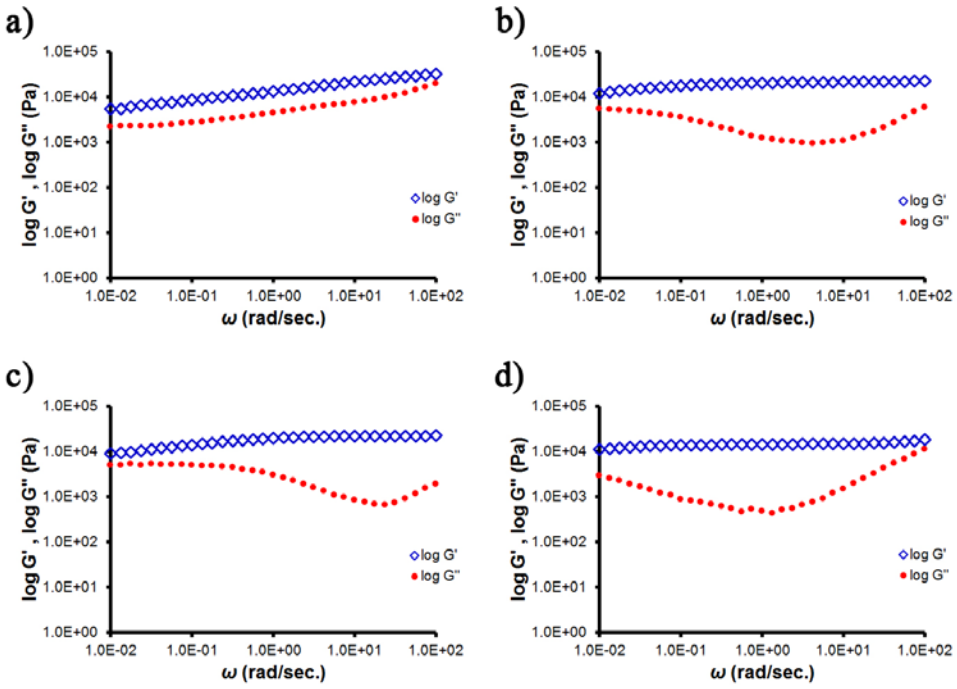

Figure 6.2 Frequency sweep of sample 2 with different temperatures. a) 50 °C, b) 68 °C, c) 90 °C and d) 50 °C after cooling from 90 °C.

To characterize the effect of rapid cooling on the modulus transition, sample 1 was cooled from 150 °C to 20 °C and the modulus measured as a function of temperature. Since the amount of PMCP crystals is responsible for the modulus transition, the rapid cooling-reheating process should suppress the crystallization of PMCP block and reduce the modulus transition. Figure 6.3 shows *G'*-temperature plots for fully-crystallized PMCP as well as quenched PMCP crystals. As expected, the rapid cooling-reheating profile shows a lower transition temperature (T = 54 °C from Figure 6.3 b) than that from the fully-crystallized condition (T = 69 °C from Figure 6.3 a). This result support that the decrease in transition temperature reflects the non-fully crystallized PMCP blocks from the homogeneous phase above T_{ODT}. In addition, the rapid cooling-reheat process

prevents the crystallization of PMCP resulting in a factor of 10 lower change in modulus during the modulus transition.

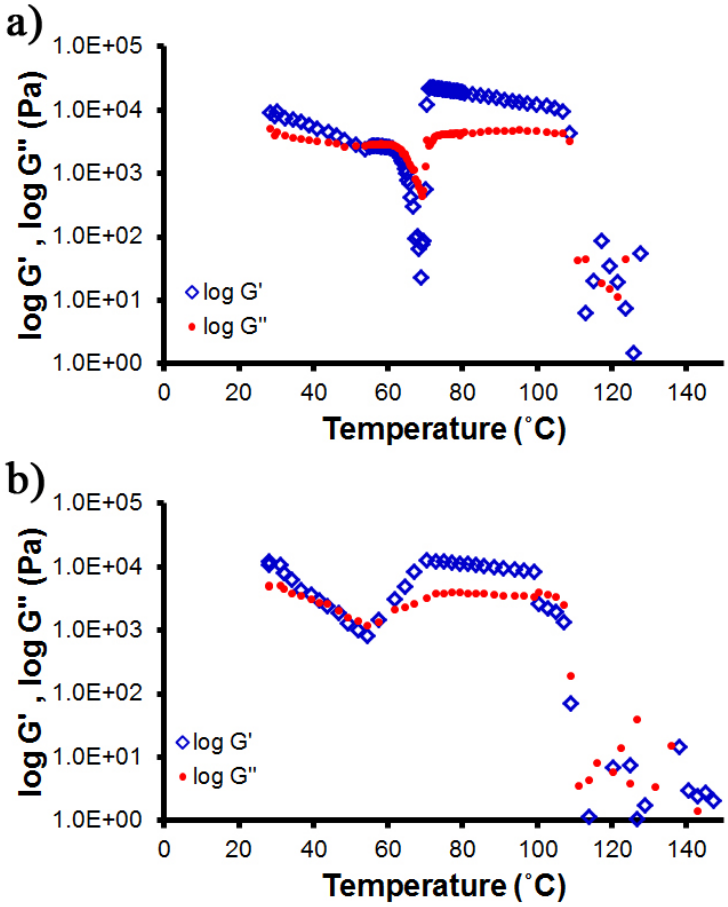

Figure 6.3 Consecutive temperature ramp for sphere-forming PH-PMCP (sample 1). a) first heating process, and b) reheating process after rapid cooling from T_{ODT}.

6.3.2. Heating rate dependence of the phase behavior in sphere-forming PH-PMCP

We investigated the heating rate-dependence of the modulus transition of the sphere-forming PH-PMCP block copolymer. Figure 6.4 displays the modulus profiles at two different heating rates, 0.5 and 1 °C/min. with a given shear rate and strain. The transition temperature (i.e., PMCP melting temperature) remains the same at the two heating rates. The trajectories of *G'* and *G''* are identical for both conditions. The results

support that the sharp modulus transition originates from the increased microdomain ordering after the melting of crystalline PMCP blocks. Consecutive runs also demonstrate the very similar temperature dependence of *G'* and *G''*. As the PMCP blocks can fully crystallize during the cooling process, the viscoelastic response of each run shows the identical behavior as a function of temperature. This supports that the modulus transition behavior is reversible with no evidence of chemical reaction during the runs (Figure 6.5).

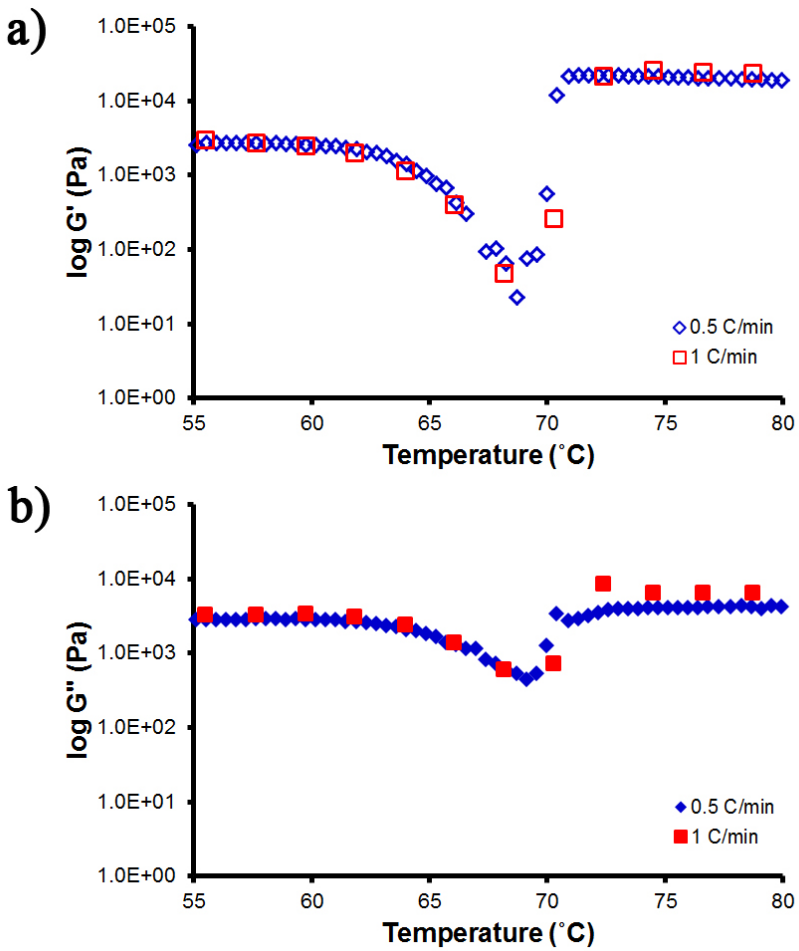

Figure 6.4 Overlayed viscoelastic profiles in sphere-forming PH-PMCP (sample 1) with different heating rates. a) *G'*-temperature and b) *G''*-temperature.

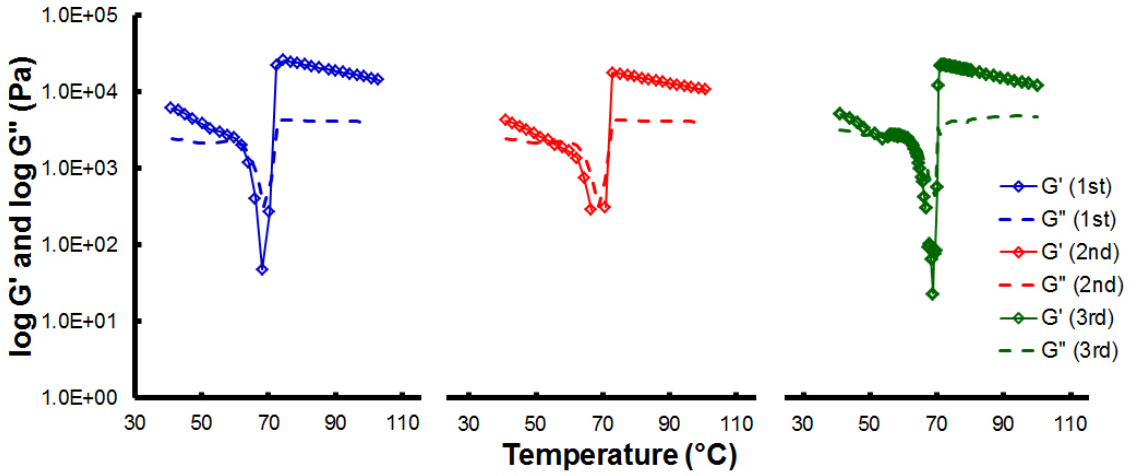

Figure 6.5 The summary of 3 consecutive modulus-temperature plots of sphere-forming PH-PMCP (sample 1).

6.3.3. Frequency dependence of the phase behavior in sphere-forming PH-PMCP

We have confirmed that the modulus transition at the PMCP melting point is independent of heating rate. Below the melting point, the weakly-ordered PMCP crystals contribute to the initial shear storage modulus. When the PMCP crystals melt, the microdomain ordering improves. The length and the large incompatibility between blocks allow the microdomain structures to rearrange within 1-2 min. after the PMCP melting.

Generally, higher oscillation frequency during rheology measurement causes a weaker signal at the order-disorder transition.[28,33] In order to understand the effect of oscillatory frequency, we examined the frequency dependence on the modulus transition. Figure 6.6 shows the frequency dependence modulus transition.

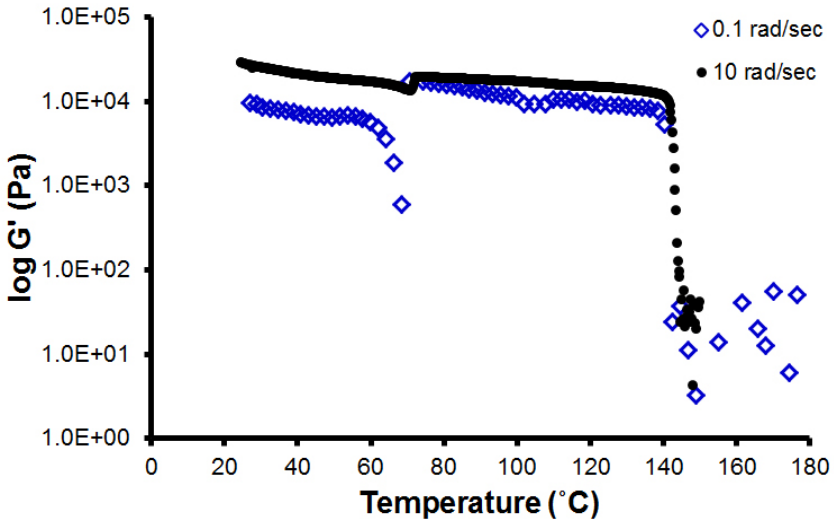

Figure 6.6 Frequency-dependent viscoelastic property of sample 2 using 0.1 and 10 rad/sec.

At low temperature, the modulus measured at10 rad/sec is larger than that measured at 0.1 rad/sec due to contribution of the amorphous PH matrix. As the PH matrix is stiffer at higher oscillation frequencies, it is reasonable that the overall modulus measured at higher frequency is larger. Interestingly, the sudden decay of the modulus at the PMCP melting temperature significantly diminishes at 10 rad/sec while the transition temperature remains approximately constant (T = 68.3 °C vs. T = 71.1 °C). At the transition point, the modulus changes from 1.32e+04 Pa to 1.92e+04 Pa at 10 rad/sec oscillation frequency. In contrast, the storage modulus changes from 0.59e+03 Pa to 1.73e+04 Pa measured at 0.1 rad/sec. In addition, the moduli for both conditions have the similar values above the PMCP melting to the T_{ODT}. Due to the high symmetry of the body-centered cubic (BCC) structure, the shear modulus-frequency relation in BCC has the same power law of 0 ($G' \sim \omega^0$) and shows a plateau for both high and low oscillation frequencies.[157,158]

We conclude that the high oscillation frequency facilitates the ordering of microphase separated spherical domains above the PMCP melting temperature. The

melting of crystalline PMCP blocks is responsible for the sharp drop in modulus. The molten PMCP reorganizes after melting to form spherical block copolymer domains more rapidly at higher oscillation frequencies. The higher oscillation frequency accelerates the evolution of microphase separation process at the melting point, which minimizes the magnitude of modulus transition.

6.3.4. Time dependence of the phase behavior in sphere-forming PH-PMCP

The sharp drop of storage modulus is due to the melting of PMCP crystals at the PMCP Tm. The subsequent increase in modulus is due to the ordering of the PMCP into spherical domains. The results of frequency sweep experiments demonstrate that sample 2 remains as a BCC structure from 68 to 140 ˚C (Region II and III in Figure 6.1). In this section, we investigated the evolution of the spherical microdomains as a function of time.

Figure 6.7 (a) displays the gradual decrease of storage modulus with increasing temperature up to 68 °C. When the temperature reaches at 68 °C, the temperature at was held at 68 °C for 1 hour under the experimental conditions (0.1 rad/sec of oscillation frequency and 2% of strain). Initially, the shear storage modulus is lower than the loss modulus since the temperature is close to the melting point of PMCP. After 25 min. (1,477 sec.), the storage modulus gradually increases and exhibits a low value of tan δ (< 1.0). Subsequently, the storage modulus increases to a value of 1.75e+04 Pa after 1 hour. Compared to the initial storage modulus of 1.17e+04 Pa at 25 °C, the final storage modulus at 68 °C after 1h is about 150 % larger. As the temperature then increases to 70 °C, the storage modulus increases to 1.94e+04 Pa. This behavior is a similar to that observed for the modulus transition in temperature ramp test (Figure 6.4). Figure 6.7 (b) clearly exhibits the increased storage modulus near 70 °C. Presumably the spherical

block copolymer microdomains at 68 °C are not fully developed and continue to order as the temperature increases to 70 °C. The *G'*-temperature plot in Figure 6.7 (c) is almost identical to the previous temperature sweep curves in Chapter 5.

The higher oscillation rate facilitates the rearrangement of the chains after the PMCP melting to improve the spherical microdomain ordering. We repeated the same experiment at a higher oscillation frequency of 10 rad/sec. Similarly, the shear modulus gradually increases for 1 h at 68 °C (Figure 6.8 a). After 1 h at 68 °C, we increased the temperature to T_{ODT}. As the temperature reaches 70 °C, the storage modulus increases from 1.91e+04 Pa to 2.03e+04 Pa (Figure 6.8 b). Overall *G'*-temperature plot in Figure 6.8 (c) is comparable to the result in Figure 6.6 with 10 rad/sec.

These results suggest that the improved ordering of the microdomains after the PMCP melts at 68 °C is incomplete after 1h and continues to improve when the temperature is subsequently increased to 70 °C.

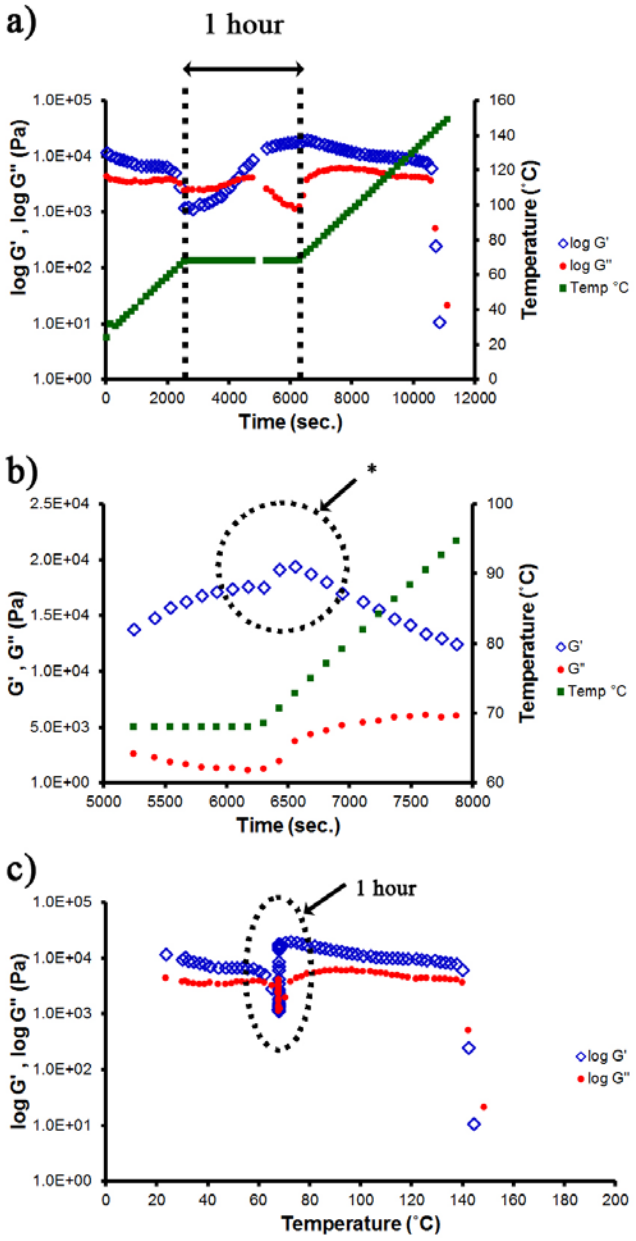

Figure 6.7 Time-dependent viscoelastic behavior of PH-PMCP block copolymers at 0.1 rad/sec. (a) Time-sweep study of the PH-PMCP block copolymer (b) Detailed modulus plot using a linear scale for clarity. * indicates the modulus transition at 70 °C. (c) Modulus-temperature plot during time dependent study.

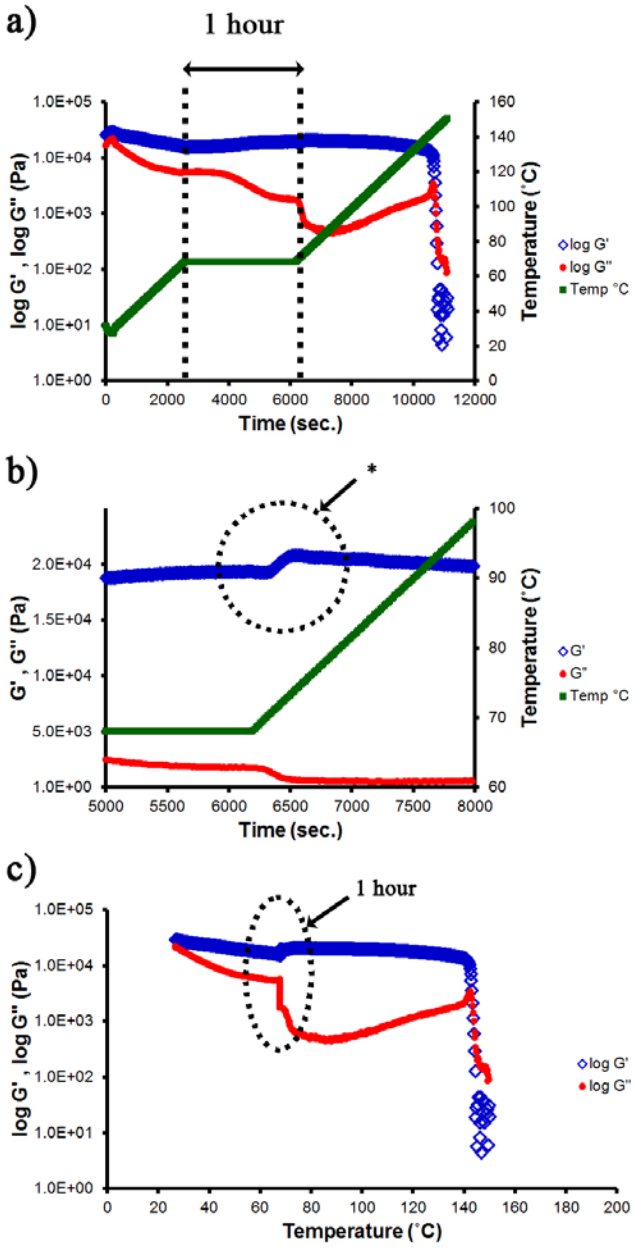

Figure 6.8 Time-dependent viscoelastic behavior of PH-PMCP block copolymers at 10 rad/sec. (a) Time-sweep study of the PH-PMCP block copolymer (b) Detailed modulus plot using a linear scale for clarity. * indicates the modulus transition at 70 °C. (c) Modulus-temperature plot during time dependent study.

We also examined the evolution of spherical block copolymer microdomains for 12 hours. We demonstrated that increased oscillation frequency can facilitate the microphase ordering process and reduce the magnitude of modulus transition at the PMCP melting temperature. In addition, the melting of PMCP followed by enhanced microphase ordering plays a key role in the observed 'modulus jump' at the melting temperature. Thus, it is useful to assess the kinetics of the microphase ordering below the melting point for these materials. With the temperature below the PMCP melting point (60 °C) to preserve the PMCP crystals, we applied the oscillatory strain for 12 hours and monitored the modulus (Figure 6.9).

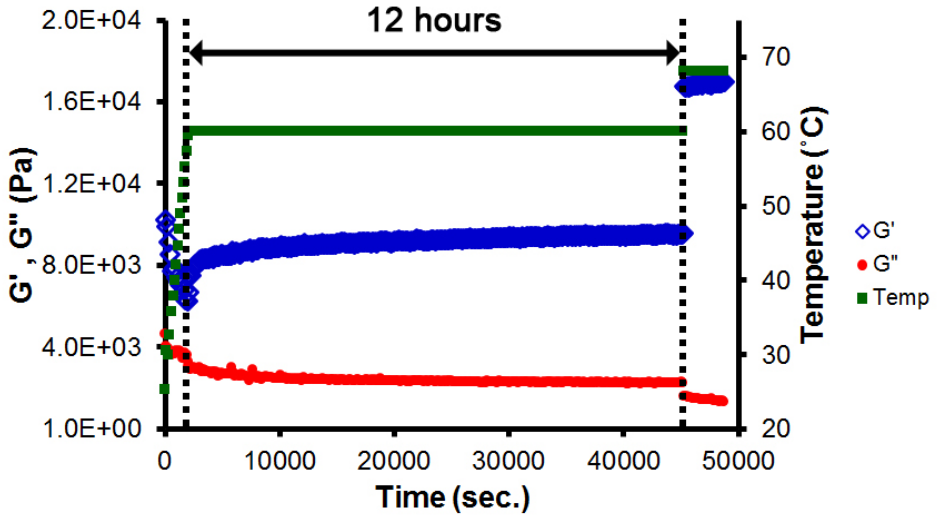

Figure 6.9 Dynamic time lapse test for sample 2.

With the temperature held at 60 °C, the shear modulus exhibits a plateau with a value of 9.1e+03 Pa over the entire 12h time period. When the temperature is then increased to 68 °C, the jump in modulus is clearly observed to a value of 1.68e+04 Pa indicating the melting and subsequent ordering of the PH-PMCP microdomains. The storage modulus jump at 68 °C is independent of oscillation time below the meting point.

Rather, the rearrangement of molten PMCP blocks into spherical block copolymer microdomains is the main factor for the sharp modulus jump above the melting point.

6.4. Conclusions

The unique viscoelastic properties of the sphere-forming PH-PMCP block copolymers have been investigated as a function of temperature, frequency, and time. The modulus transition behavior at the PMCP T_m (= 68 °C) is observed as a function of temperature. The discontinuity of the storage modulus results from the PMCP melting and subsequent improved microdomain ordering. The terminal viscoelastic behavior reveals that the block copolymer microdomain structure is spherical with a power law of α=0 above PMCP T_m.

As shown in a rapid cooling-reheating experiment, the small amount of PMCP crystals exhibit a thermal hysteresis with a lower transition temperature (T = 54 °C) and an order of magnitude decrease in the storage modulus. However, fully-crystallized PH-PMCP block copolymer displays nearly identical viscoelastic response at the transition temperature (T = 69 °C) and 2 orders of magnitude increase in modulus during the consecutive temperature ramp tests.

The storage modulus transition behavior is only governed by the melting of the PMCP block and is independent of the heating rate. As a result, both the transition temperature and the magnitude in modulus transition remain at similar values. However, the oscillation frequency plays a role in the evolution of spherical block copolymer microdomains and increased oscillation frequency reduces the magnitude of modulus

transition. This suggests that the fast oscillation facilitates the improvement of the spherical microdomains resulting in a smaller change in the storage modulus.

The improved ordering of the spherical block copolymer microdomains after PMCP melting is responsible for the higher storage modulus above ~ 70 °C. During oscillation below the PMCP melting for 1h and 12h, the spherical block copolymer microdomains are not fully developed and the storage modulus remains at 1.75e+04 Pa. When the temperature is increased above 70 °C, the storage modulus recovers to 1.94e+04 Pa.

Chapter 7. Calculation of the Flory-Huggins Interaction Parameter for Poly(1-hexene)-b-Poly(methyl-1,3-cyclopentane)

7.1. Background

The microphase separation behavior in block copolymers can be described by the volume fraction of one block f ($f_A + f_B = 1$), the degree of polymerization N (= $N_A + N_B$), the segment-segment interaction parameter (i.e., Flory-Huggins interaction parameter) χ, and the temperature T. The Flory-Huggins interaction parameter is classically used to describe the enthalpy of mixing and is as a function of temperature.[3] The segment-segment interaction that is used to describe the free energy of mixing between the components can be described by regular solution theory,

$$\chi(T) = \frac{Z}{2}\frac{1}{k_B T}(2U_{AB} - U_A - U_B) \quad (1)$$

where Z is the number of nearest neighbor monomers, k_B is the Boltzmann constant, U_{AB} is the interaction between segment A and segment B, U_A (or U_B) is the interaction between segment A (or B) with itself. The interaction energy between segment A and segment B can be estimated by the energy of vaporization.[159,160]

$$\chi(T) = \frac{v_0}{k_B T}(\delta_A - \delta_B)^2 \quad (2)$$

where v_0 is the volume per site, δ_A (or δ_B) is the solubility parameter of segment A (or B). Several experimental methods have been used to determine the Flory-Huggins interaction

parameter such as scattering[5,161], the solubility parameter approach[162-164], and differential scanning calorimetry (DSC).[165]

Scattering methods are often used to experimentally determine the Flory-Huggins interaction parameter in block copolymers as a function of temperature. As the temperature reaches to the order-disorder transition temperature, the scattering intensity decreases due to a loss of ordering in the block copolymer. When the temperature is above the order-disorder transition temperature, the scattering occurs from the compositional fluctuations in homogeneous phase. The Flory-Huggins interaction parameter can be calculated based on the degree of polymerization *N* and the order-disorder transition temperature T_{ODT} from a series of lamellar-forming block copolymers.

Depending on the physical and chemical properties of the blocks, the Flory-Huggins interaction parameter can be experimentally divided into entropic χ_S and enthalpic contributions χ_H/T.[3,166,167]

$$\chi(T) = \chi_S + \frac{\chi_H}{T} \qquad (3)$$

The enthalpic contribution in the Flory-Huggins interaction parameter results from the chemical dissimilarity between monomers in block copolymer such as dipole moment, functional group, and etc. Most polar block copolymers and amphiphilic block copolymers exhibit a larger enthalpic than entropic contributions to χ. This large difference in chemical properties is a driving force for phase separation.

By contrast, the entropic contribution, χ_S, is closely related to the physical properties of polymer chain such as chain stiffness, molecular shape, and size.[168-171]

Structural differences limit chain mixing between blocks and can lead to the phase separation in block copolymers.[139,140] The entropic contribution to χ is often more important in chemically similar block copolymers, for example in saturated carbon-based block copolymers, i.e., olefin block copolymers.[164,172]

In previous chapters, the structure-property relationships in PH-PMCP block copolymers were examined using AFM, TEM, rheometry, and in-situ SAXS/WAXS. The higher molecular weight series of PH-PMCP block copolymers (total M_n = 30 kDa) did not exhibit an observable order-disorder transition while the low molecular weight series of PH-PMCP block copolymers (M_n = 15 kDa) exhibited an experimentally accessible the order-disorder transition. It is likely the PH-PMCP system has a large difference in chain stiffness, which drives the microphase separation above the PMCP melting point. In this chapter, the Flory-Huggins interaction parameter in PH-PMCP block copolymers will be discussed using a series of lamellar-forming PH-PMCP block copolymers as a function of degree of polymerization *N*.

7.2. Experimental Setup

a) Materials. The synthesis of lamellar-forming PH-PMCP materials in this study was described previously. Briefly, all syntheses were carried out at -10 °C in PhCl (20 mL) with a cocatalyst to precatalyst ratio of 1.01 to ensure the complete activation. Sequential polymer blocks were obtained by first adding 1-hexene for 2 hours followed by the addition of 1,5-hexadiene for an additional 2 hours. The molecular weight of each block was controlled by the amount of monomer present based on the kinetics of poly(1-hexene) and poly(methyl-1,3-cyclopentane). A small (<1 mL) amount of poly(1-hexene),

PH, was removed and quenched for analysis immediately prior to the addition of the second monomer. Polymer samples were quenched in ca. 500 mL of acidic methanol (10 % HCl by volume). Samples were washed and filtered with MeOH and then dried under vacuum at 25 °C until constant weight was observed. The molecular weights of all polymers were measured using gel permeation chromatography (GPC) (Viscotek TDA) equipped with a column oven. Differential refractometer and four columns (T2500, T3000, T4000 and T5000) were maintained at 40 °C. Tetrahydrofuran (THF) was used as the eluent at a flow rate of 1.0 mL/min. The number-average molecular weight (M_n) and weight-average molecular weight (M_w) of samples were obtained using Viscotek OmniSEC software.

b) Differential Scanning Calorimetry (DSC). The thermal properties of block copolymers were obtained using a DSC Q1000 (TA Instruments). Nitrogen was used as a purge gas at 50 mL/min. The T_m, T_g, T_c and heat of fusion (ΔH) were measured using heat-cool-heat cycles at 10 °C/min. All values were taken after the first heating cycle to remove previous thermal history.

c) Dynamic Mechanical Experiments. Dynamic mechanical shear modulus analysis was conducted using an AR 2000 (TA Instruments Inc.) with parallel plates (diameter: 8 mm and 25 mm, gap: ca. 1 mm). Dynamic storage and loss shear moduli, *G'* and *G''*, were obtained with a shear oscillation of 0.1 rad/sec and a low strain amplitude of 0.2-2 % where the viscoelasticity was independent of the frequency. The temperature range was 25-250 °C with 1 °C/min. ramp to obtain order-disorder transition temperatures (T_{ODT}) with a nitrogen gas purge to prevent thermal oxidation. The storage

modulus, loss modulus, and tan δ were monitored and analyzed using Rheology Advantage Data Analysis software version 5.7.

d) Wide and Small Angle X-ray Scattering (WAXS/SAXS). *In-situ* SAXS/WAXS experiments were conducted using Xenocs Xeuss system having Cu Kα X-ray source (λ = 1.5418 Å, GeniX3D Cu ULD, Xenocs, SA, France) with a temperature controlled sample stage (THXS-600, Linkam Scientific Instruments Ltd.). Both heating and cooling rates were 5 °C/min. The two-dimensional scattering data were collected with semiconductor (CMOS) detectors (Pilatus 100K and Pilatus 300K, DECTRIS, Swiss). The acquisition time was 10 min for each frame and the scattering data was collected for 10 frames for a given temperature. To obtain the order-disorder transition temperature, the scattering data were collected with 1 °C step. The sample-to-detector distance for WAXS and SAXS was approximately 206.7 mm and 2,518.7 mm, respectively using AgBe. All samples were mounted in a washer type sample holders (3 mm hole × 1 mm thick) and covered with Kapton films (ca. 0.33 mm, SPEX Industries Inc., New Jersey, USA) as a X-ray transparent window. Two dimensional spectra were integrated using the FIT2D software to obtain the scattered intensity as a function of the scattering wave vector q, which is defined as $q = \frac{4\pi}{\lambda}\sin\theta$ with 2θ being the scattering angle. All scattering signals were corrected with background scattering, air scattering, and beam intensity. For the 2-D scattering image analysis, Igor Pro software (ver. 6.3) with Irena package was used to obtain circular averaged 1-D plots of intensity versus scattering wave vector q.[128]

7.3. Results and Discussions

Table 7.1 summarizes the characteristics of a series of lamellar-forming PH-PMCP block copolymers. All materials display relatively narrow PDI (~1.1) while the total molecular weight ranges from 9.5 kDa to 19.3 kDa. To obtain the order-disorder transition temperature, the viscoelastic response for all materials was measured as a function of temperature.

Table 7.1 Characteristics of lamellar-forming PH-PMCP materials.

Sample	Mn of PH (kg/mol)	Mn of PMCP (kg/mol)	Mn of PH-PMCP (kg/mol)	f_{PMCP} (mole fraction)	M_w/M_n	N	PMCP T_m / T_c (°C)	T_{ODT} (°C)
LAM-1	6.4	12.9	19.3	0.67	1.20	234	93.4 / 52.5	> 250
LAM-2	5.9	8.7	14.5	0.60	1.11	175	94.5 / 61.9	> 250
LAM-3	5.6	7.6	13.3	0.58	1.08	160	92.0 / 61.0	> 250
LAM-4	5.0	8.6	13.7	0.63	1.08	165	72.3 / 19.5	175
LAM-5	4.1	9.0	13.1	0.69	1.07	159	73.1 / 28.6	117
LAM-6	4.2	8.5	12.7	0.67	1.08	153	60.1 / 11.0	95
LAM-7	3.6	8.1	11.8	0.69	1.07	142	56.1 / 9.1	No microphase
LAM-8	3.9	7.9	11.8	0.67	1.10	142	67.0 / 2.3	No microphase
LAM-9	4.5	6.8	11.2	0.60	1.06	135	87.7 / 54.6	No microphase
LAM-10	3.5	5.9	9.5	0.63	1.14	114	89.0 / 63.7	No microphase

Figure 7.1 shows a representative *G'*-temperature profiles for samples (LAM-1, 2, 3, 7, and 9). As explained in Figure 5.6, no sudden drop in modulus is observed at elevated temperatures due to an T_{ODT} under the experimental conditions. A sudden modulus decrease is shown at the PMCP melting point (65-80 °C) from this set of PH-PMCP block copolymers ($0.6 < f_{PMCP} < 0.7$). The large storage modulus at ambient temperature is due to the relatively large fraction of PMCP crystals. As the temperature

reaches to the melting point of PMCP crystals, a rapid drop in modulus is shown for all samples. Above the melting point of the PMCP crystals, the storage modulus decreases with decreasing total molecular weight. Interestingly, there is a relatively sharp increase in modulus at about 180 °C with a continued gradual increase in modulus as the temperature increases above 180 °C. There is no observable T_{ODT}.

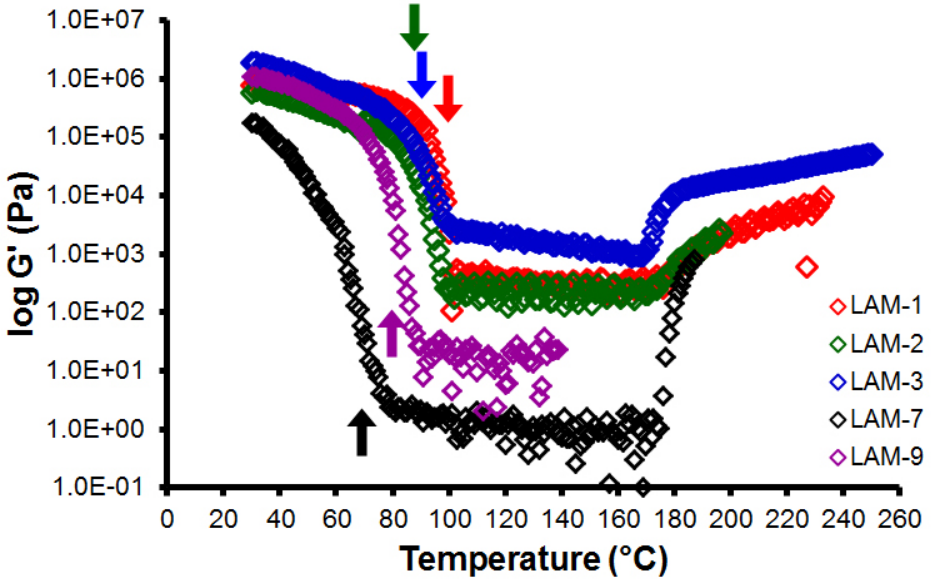

Figure 7.1 Representative temperature dependence of the dynamic shear storage modulus for the block copolymers ($0.6 < f_{PMCP} < 0.7$). The arrows indicate the melting point of PMCP crystals for each sample.

To characterize the microdomains for LAM-1 to LAM-10 samples, *in-situ* SAXS/WAXS was used as a function of temperature. Figure 7.2 shows a representative scattering plot for different temperatures for the LAM-1 sample. The broad scattering peak at 0.02 $Å^{-1}$ ($d \sim 30$ nm) indicates the presence of PMCP crystals. When the temperature increases, a series of scattering peaks arises from the lamellar microdomains with ratios of 1: 2: 3 in the experimental temperature range (25-185 °C). In addition, the scattering peaks at 185 °C indicate the presence of the lamellar microdomain structure.

The modulus enhancement at about 180 °C is not understood, however, no structural rearrangement or thermal decomposition is observed the SAXS data.

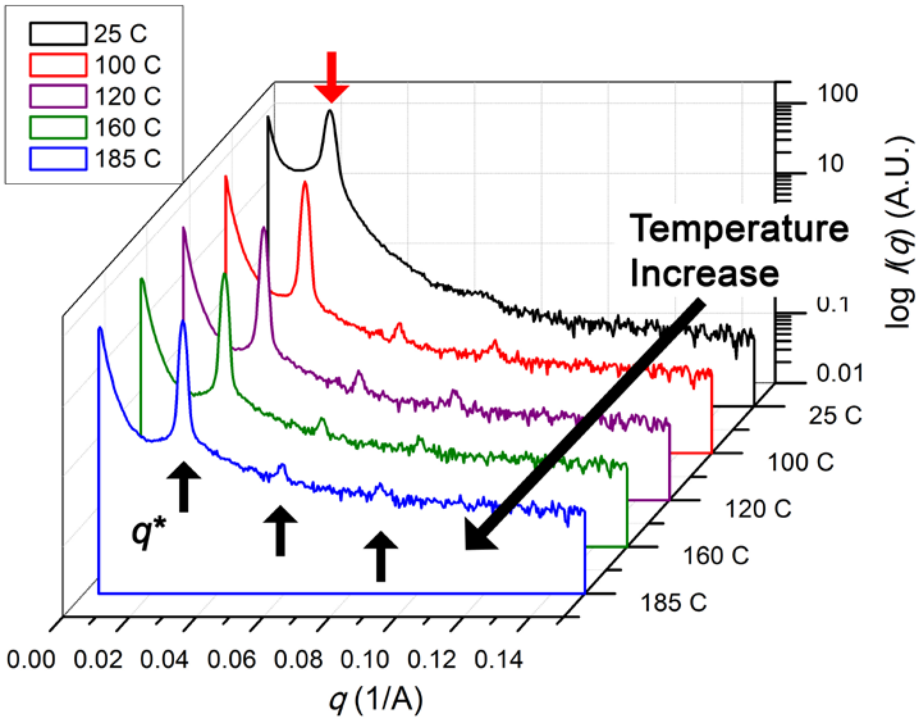

Figure 7.2 Representative scattering profiles as a function of temperature for lamellar-forming PH-PMCP (LAM-1). The red arrow indicates the PMCP crystals block and the black arrows represent lamellar block copolymer microdomains. The primary scattering vector q^*=0.029 Å^{-1}.

Due to the unobservable T_{ODT} for lamellar-forming PH-PMCP block copolymers using rheometry, the normalized scattering intensity as a function of temperature was used. In addition, when the total degree of polymerization, N, is smaller than 142, the materials did not show microphase separation above the PMCP melting temperature. In the case of N > 165, the materials maintain the microdomains with ratios of 1: 2: 3 in the experimental temperature range (25-185 °C). The lamellar-forming block copolymers with 153 < N < 165 show a T_{ODT} as measured by *in-situ* SAXS/WAXS. Figure 7.3 shows SAXS data for a series of the lamellar-forming PH-PMCP block copolymers with 153 < N < 165 (LAM-4, 5, and 6). Below T_{ODT}, the primary scattering peak from the lamellar

microdomains exhibits at q = 0.04 A^{-1} (d = 14.3 nm). When the temperature reaches to T_{ODT}, the intensity of the primary scattering peak decreases and exhibits peak broadening. As the total molecular weight decreases (i.e., the total degree of polymerization, N), the T_{ODT} decreases.

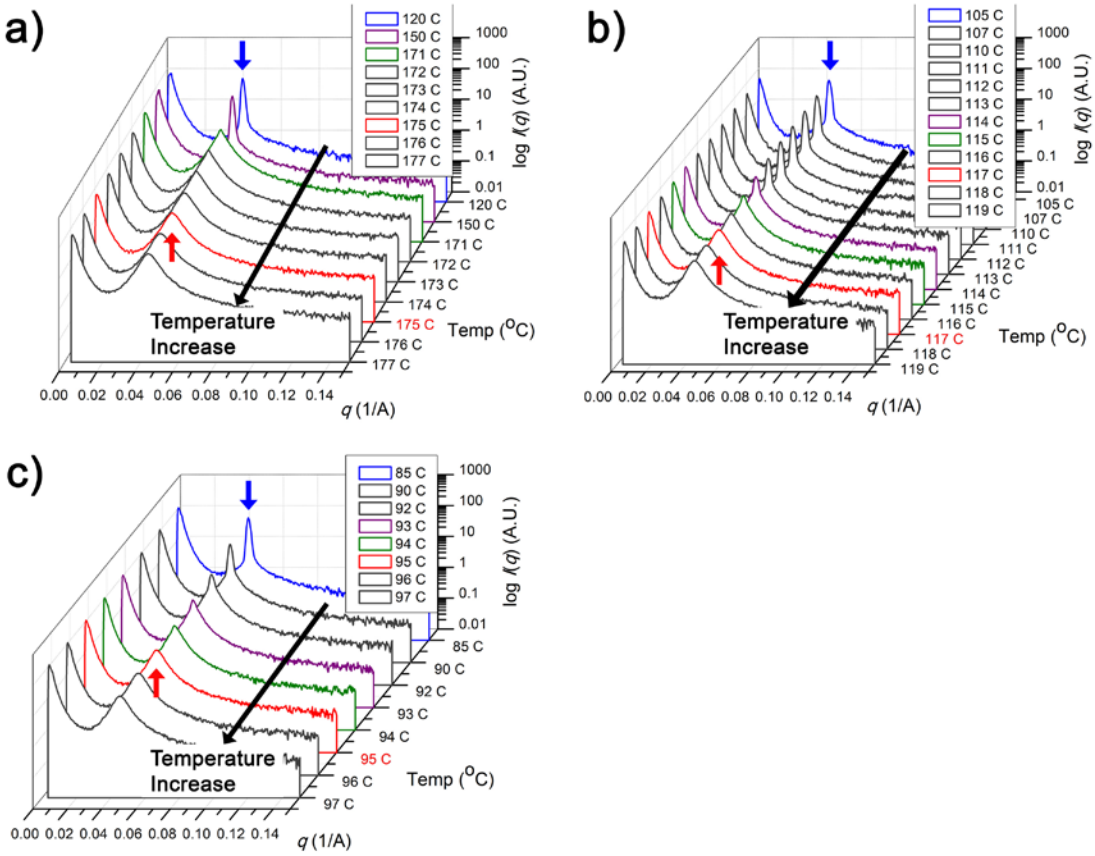

Figure 7.3 The I vs. q plots for a series of lamellar-forming PH-PMCP as a function of temperature. a) LAM-4, b) LAM-5, and c) LAM-6. The blue arrows display the scattering peaks from the lamellar microdomains and the red arrows indicate the peak from the homogeneous phase at T_{ODT}.

To observe a clear phase transition behavior at T_{ODT}, the inverse primary peak intensity, $I^{-1}(q^*)$, was plotted as a function of inverse temperature. The $I^{-1}(q^*)$ vs. T^{-1} is often used to identify the order-disorder transition temperature from a change in scattering intensity.[5,173,174]

Figure 7.4 shows a series of $I^{-1}(q^*)$ vs. T^{-1} plots for a series of the lamellar-forming block copolymers. The inverse primary peak intensity displays a gradual increase with increase of temperature and then exhibits large increase at T_{ODT}. Above T_{ODT}, the inverse primary peak intensity shows a gradual increase. LAM-4, 5, and 6 exhibit a sudden intensity change indicating the T_{ODT}. The measured T_{ODT} for LAM-4, 5, and 6 is 175 °C, 117 °C, and 95 °C respectively.

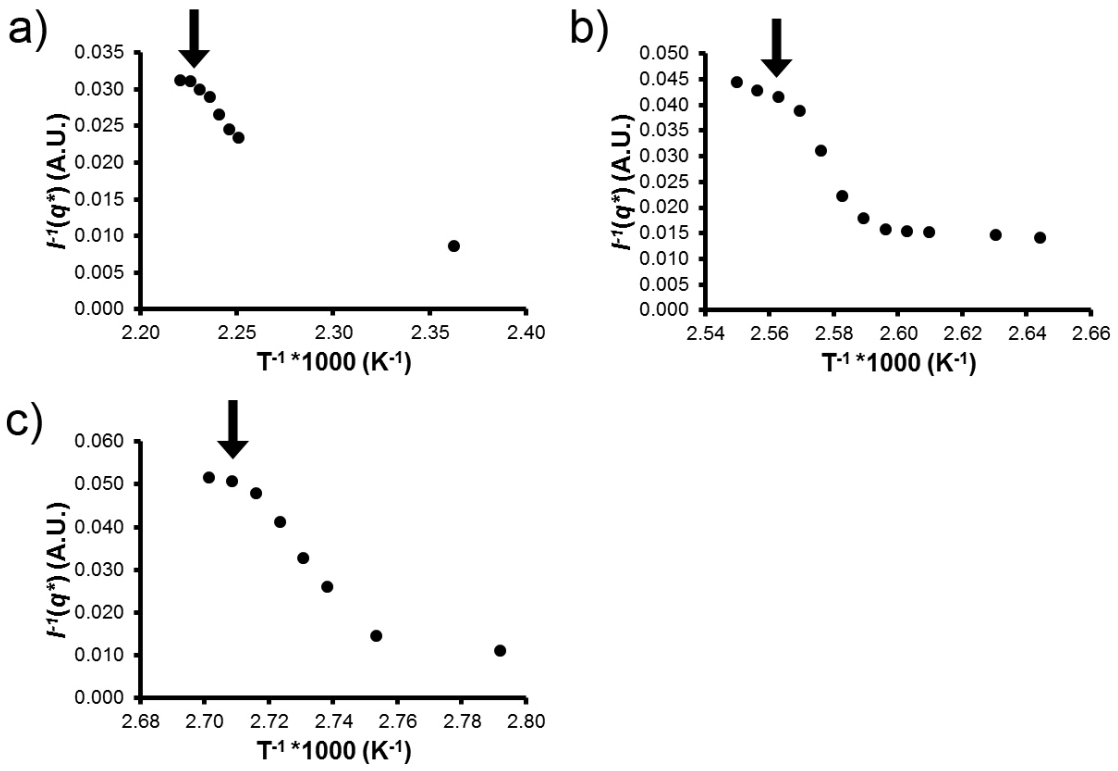

Figure 7.4 Inverse primary peak intensity, $I^{-1}(q^*)$, vs. inverse temperature, T^{-1}, for a series of lamellar-forming PH-PMCP block copolymers a) LAM-4 (N = 165), b) LAM-5 (N = 159), and c) LAM-6 (N = 153). The arrows indicate T_{ODT}.

From in-situ SAXS/WAXS, the set of PH-PMCP block copolymers, LAM-4, 5, and 6 exhibits an T_{ODT}. Using these data, it is possible to estimate the Flory-Huggins interaction parameter for the PH-PMCP block copolymer system. Based on the Leibler's block copolymer theory, the critical limit for the microphase separation in symmetric

block copolymers ($f_A = f_B = 0.5$) χN is 10.495. Table 7.2 summarizes the data for the calculation to obtain the Flory-Huggins interaction parameter.

Table 7.2 Data for the calculation of the Flory-Huggins interaction parameter.

Sample	Mn of PH (kg/mol)	Mn of PMCP (kg/mol)	Mn of PH-PMCP (kg/mol)	f_{PMCP} (mole fraction)	N	T_{ODT} (˚C)	$1/T*10^3$ (1/K)
LAM-4	5.0	8.6	13.7	0.63	165	175	2.23
LAM-5	4.1	9.0	13.1	0.69	159	117	2.56
LAM-6	4.2	8.5	12.7	0.67	153	95	2.72

Using the data in Table 7.2, the χ vs. 1/T plot is generated. Figure 7.5 shows χ for PH-PMCP block copolymers with the PMCP ratios in the range of 0.63-0.69. The equation to obtain χ is based on Leibler's theory,

$$\chi = 0.0423 + \frac{9.5}{T} \qquad (4)$$

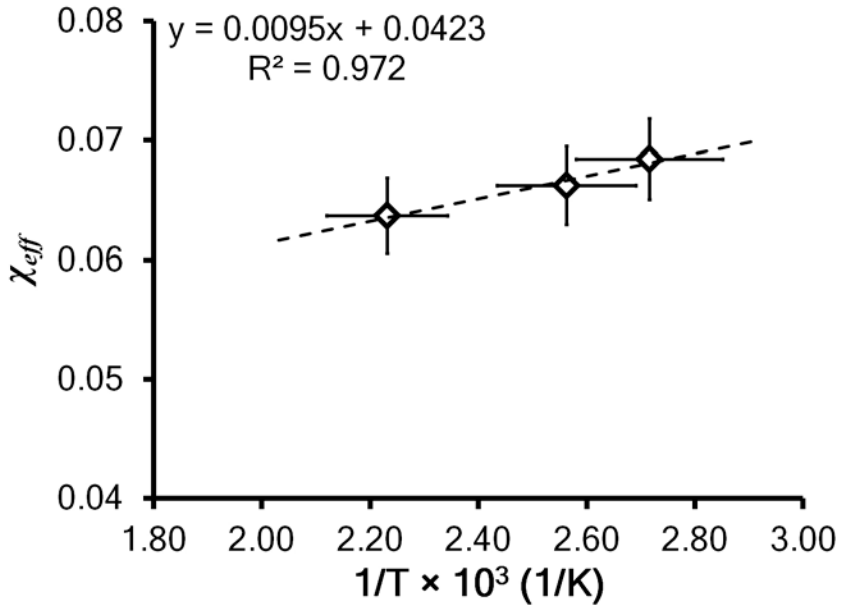

Figure 7.5 Flory-Huggins interaction parameter χ vs. 1/T for PH-PMCP block copolymers. Error bars in the plots are expected to be within 5% based on the GPC and rheology.

The Flory-Huggins interaction parameter for PH-PMCP block copolymer suggests that the entropic contribution is larger than the enthalpic contribution to χ in the range of 10-300 °C. This result suggests that the chain stiffness between flexible PH and rigid PMCP is probably the source for the large entropic contribution to χ. In addition, the large entropic contribution drives the microphase separation above the melting temperature of PMCP crystals. Due to the large entropic contribution, an T_{ODT} can only be observed over a narrow range of the total degree of polymerization N of about $153 < N < 165$.

Like other olefin block copolymer systems, PH-PMCP system has a small enthalpic contribution due to the lack of dipole moment, functional groups, or electronic properties (i.e., *sp*, *sp2* orbitals or localized π- π electrons). It is valuable to compare the Flory-Huggins interaction parameter with other block copolymer systems. Table 7.3 summarized of the Flory-Huggins interaction parameters for other block copolymers.

Table 7.3 Summary of the Flory-Huggins interaction parameter for other block copolymers.

Sample	Flory-Huggins interaction parameter	Method	Ref.
Poly(ethylene)-Poly(ethyl ethylene) (PE-PEE)	$-0.0055 + \frac{15}{T}$	Rheology	Bates *et al.*[169]
Poly(ethylene-propylene)-Polyethylethylene (PEP-PEE)	$0.0015 + \frac{4.46}{T}$	SANS Rheology	Rosedale *et al.*[175]
Poly(ethylene)-Poly(ethylene-propylene) PE-PEP	$0.019 + \frac{10.25}{T}$	SANS Rheology	"
Poly(ethylene)-Poly(cyclohexylethylene) (PE-PCHE)	$-0.0174 + \frac{29.4}{T}$	Rheology	Cochran *et al.*[176]
Poly(ethylene)-Poly(propylene) (PE-PP)	$0.00955 + \frac{1.02}{T}$	SANS	Lee *et al.*[177]
Poly(styrene)-Poly(methyl methacrylate) (PS-PMMA)	$0.0282 + \frac{4.46}{T}$	SAXS	Russell *et al.*[166] Zhao *et al.*[178]
Poly(styrene)-Poly(isoprene) (PS-PI)	$-0.0197 + \frac{34.1}{T}$	SAXS	Sakamoto *et al.*[179]
Poly(styrene)-Poly(2-vinyl pyridine) PS-P2VP	$-0.095 + \frac{91.6}{T}$	Rheology	Schulz *et al.*[180]
Poly(styrene)-Poly(ethylene oxide) (PS-PEO)	$-0.0229 + \frac{29.8}{T}$	SANS	Frielinghaus *et al.*[181]
Poly(isoprene)-Poly(ethylene oxide) (PI-PEO)	$0.125 + \frac{65}{T}$	SAXS	Floudas *et al.*[130]
Poly(ε-caprolactone)-Poly(butadiene) (PCL-PB)	$-0.0229 + \frac{71.65}{T}$	SAXS	Takagi et al.[152]
Poly(1-hexene)-Poly(methyl-1,3-cyclopentane) (PH-PMCP)	$0.0423 + \frac{9.5}{T}$	SAXS	Eq. (4)

Most polar block copolymers have high enthalpic contribution due to the chemical dissimilarity. This can allow extremely low molecular weight polar block copolymers to exhibit microphase separation. By contrast, non-polar block copolymers have relatively small entropic and enthalpic contributions resulting from the similar chain stiffness, monomer shape and size. Especially, olefin-based block copolymers tend to

have very small Flory-Huggins interaction parameters. To generate microphase separation using olefin-based block copolymers, large molecular weights are required to increase χN.

Figure 7.6 shows the Flory-Huggins interaction parameters for other block copolymer systems shown in Table 7.3. In general, polar block copolymers have larger interaction parameters than non-polar block copolymers. At high temperatures, the Flory-Huggins interaction parameter for the PH-PMCP system is relatively large compared to most block copolymers while showing only a small temperature dependence. This result explains why the order-disorder transition of PH-PMCP system is highly sensitive to the total degree of polymerization N (i.e., total molecular weight). For a small change in the degree of polymerization N, the order-disorder transition would exhibit a significant change. Based on the Flory-Huggins interaction parameter, the larger molecular weight PH-PMCP block copolymers, LAM-1 and 2 with $0.6 < f_{PMCP} < 0.7$, would exhibit an T_{ODT} = 3,452 °C and 265 °C respectively which is higher than the experimentally accessible temperature range. In addition, the T_{ODT} for the sphere and cylinder-forming PH-PMCP block copolymers display a dramatic shift relative for a small change in N.

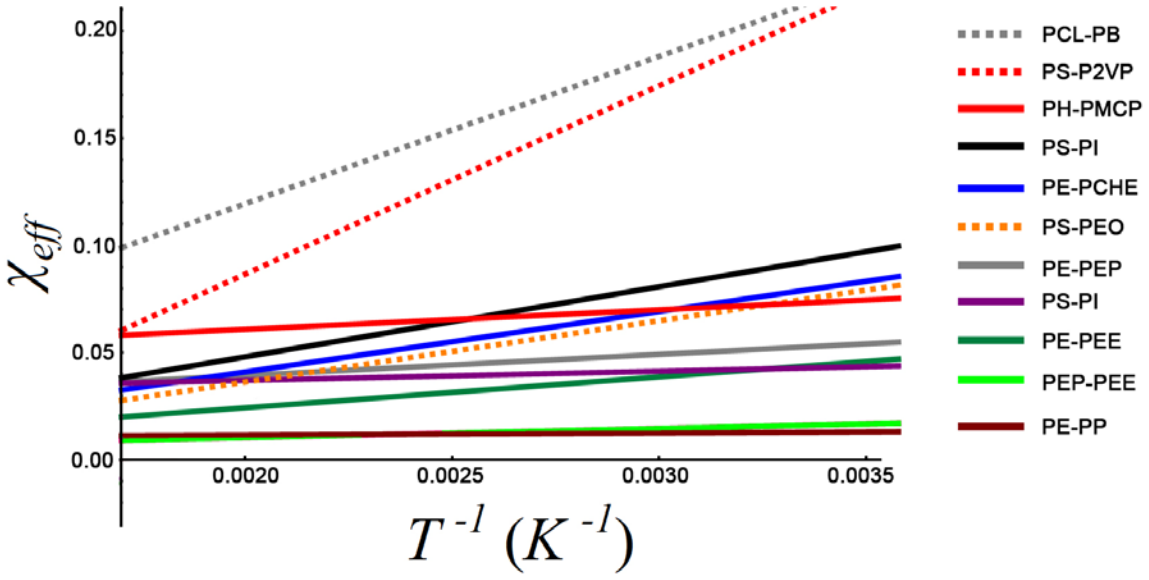

Figure 7.6 The plots of Flory-Huggins interaction parameter as a function of reciprocal temperature for represented block copolymers. Dashed lines show polar block copolymers and solid lines exhibit non-polar block copolymers.

7.4. Conclusions

The Flory-Huggins interaction parameter for the PH-PMCP block copolymer system was calculated from a series of lamellar-forming block copolymers using *in-situ* X-ray scattering. The set of lamellar-forming PH-PMCP block copolymers have similar PMCP ration ($0.63 < f_{PMCP} < 0.67$). Based on Leibler's block copolymer phase separation theory, the Flory-Huggins interaction parameter was calculated as a function of temperature. The extracted Flory-Huggins interaction parameter exhibit a large entropic contribution for the temperature ranges of 20-185 °C.

$$\chi = 0.0423 + \frac{9.5}{T}$$

Unlike other non-polar block copolymers (i.e., saturated carbon based block copolymers) with showing small entropic contribution, PH-PMCP system shows a large

entropic contribution resulting from the difference in chain stiffness between flexible PH and rigid PMCP blocks. This result can explain several features in PH-PMCP system.

1) The relatively asymmetric block ratio for lamellar-forming block copolymers with $f_{PMCP} > 0.6$ compared to the expectation on of $f_A = f_B = 0.5$.
2) Strong phase separation above T*m* due to the difference in chain stiffness between PH and PMCP blocks.
3) Large shift in T_{ODT} with relatively small changes in the total molecular weight at a given volume ratio.

Chapter 8. Conclusions

8.1. Structure-Property Relationships in Stereoblock and Stereoirregular Polypropylenes

Using degenerative methyl group transfer living coordinative polymerization, we have systematically synthesized both well-defined block and random polypropylenes. Through the stereochemical reaction we can control the microstructure of the polypropylene in a sequential manner under living polymerization conditions. The reversible change in stereochemistry allows for discrete isotactic-atactic-isotactic sequences resulting in a block architecture.

The effect of chain architecture on the mechanical properties using stereoblock and stereoirregular polypropylenes has been investigated using tensile testing, DMA, and rheometry. Discrete block polypropylenes are superior to random polypropylenes in terms of tensile strength at fracture and recovery after deformation. Stereoblock polypropylenes display 15 MPa tensile strength and more than 1,800-2,700 % elongation ratio. In addition, the recovery after the fracture is 92-98 %. However, stereoirregular polypropylenes exhibit yield at about 50 % elongation and break at about 1,500 % elongation. The recovery after break is only 67-75 % due to the presence of the yield behavior.

Due to the consecutive isotactic and atactic chains in stereoblock polypropylenes, the materials have both rigid and flexible properties which supported by DMA measurements. Both block and random polypropylenes show a similar value of storage modulus at low temperature. Above the glass transition (= 10 °C), however, the modulus-

temperature behavior differs between the block and random polypropylenes. Discrete block polypropylenes reach 60 MPa storage modulus in the range of 30-50 °C. In contrast, random polypropylenes maintain 90-225 MPa modulus over the same temperature range. The phase lag (tan δ) further characterizes the dissimilarity of block and random polypropylenes at the glass transition temperature (T_g = 10 °C). The long amorphous segments in block polypropylenes provide flexibility resulting in a large loss modulus, which leads a value of tan δ of about 1.0-1.8 at 10 °C. In contrast, the peak maximum of tan δ for random polypropylenes is 0.2-0.4 at 10 °C. Much like block polypropylenes, random polypropylene with a low isotactic fraction has a tan δ of 1.2 at 10 °C.

Propylene is the second major monomer feedstock and polypropylene has been extensively studied by many researchers. Using stereochemistry, it is possible to synthesize either isotatic polypropylene with high rigidity or atactic polypropylene with high flexibility and extensibility. To obtain both properties in single polypropylene material, generally various catalysts are used which can insert different types of stereodefects during synthesis. This conventional approach is strongly dependent on the statistical distribution of the stereodefects from each catalyst, the ability to tailor the mechanical properties is restricted for applications such as shock absorbers, adhesives, and thermoplastic elastomers. A well-defined crystalline-amorphous-crystalline block polypropylene as synthesized in this work has distinct advantages over random polypropylenes by exhibiting both rigid and flexible properties, potentially allowing for a wider range of applications coupled with good processability.

8.2. Structure-Property Relationships in PH-PMCP Block Copolymer System

Using the living polymerization and living cyclopolymerization of both 1-hexene and 1,5-hexadiene, we have successfully synthesized a series of crystalline-amorphous block copolymers and characterized their morphologies using AFM, TEM and *in-situ* SAXS/WAXS. The phase behavior of this PH-PMCP system as a function of temperature shows the competition between crystallization and microphase separation in the vicinity of the PMCP melting point.

We have focused on the microphase separation behavior and the mechanical properties of low molecular weight crystalline-amorphous block copolymers (total M_n = 15 kDa). We have synthesized low molecular weight block copolymers where the chain entanglements for both blocks are negligible (i.e., below the entanglement molecular weight). A series of low molecular weight PH-PMCP materials demonstrate a 'modulus jump' at the PMCP melting point. This modulus transition at the PMCP melting temperature is characterized by an increase in the modulus from about 600 Pa to more than 17,000 Pa in a sphere-forming PH-PMCP block copolymer. The recovery time for the modulus during the transition is 1-2 min. *In-situ* SAXS/WAXS was used to elucidate the structural changes in the crystalline lamellae and block copolymer microdomain structure at the PMCP melting temperature. In addition, we have observed similar modulus transitions in cylinder-, double gyroid-, and lamellar-forming PH-PMCP materials. The recovery time of the storage modulus after the melting of the PMCP varies from 1-2 min. in spherical morphologies- and 5 min. in cylindrical morphologies PH-PMCP, to about 20 min. in double gyroid morphologies PH-PMCP, and 70 min. in lamellar morphologies.

The main driving force for the modulus transition originates from the melting of the crystalline PMCP block followed by an increased ordering of the microdomains with the participation of the PMCP chains from the crystals that melted. Presumably, the large discrepancy in PH and PMCP chain stiffness is responsible for the strong microphase separation. The calculated Flory-Huggins interaction parameter for PH-PMCP system suggests a large entropic contribution resulting from the large difference in chain stiffness between PH and PMCP blocks.

$$\chi = 0.0423 + \frac{9.5}{T} \qquad (1)$$

A small change in the total molecular weight has significantly influence on the T_{ODT} due to the dominant entropic contribution in PH-PMCP system.

A number of theoretical studies on the microphase separation in block copolymers have been done covering the strong segregation limit (SSL), intermediate segregation region (ISR), weak segregation limit (WSL) as discussed in Chapter 1. These theories used a model system with a conformationally symmetric block copolymer where the properties of chain stiffness and the monomer volume for both blocks are the same. Based on Leibler's theory, a symmetric block copolymer at $f_A = f_B = 0.5$ exhibits lamellar phase where $\chi N = 10.495$ is the critical limit for the microphase separation for conformational symmetric block copolymer.

In a real block copolymer system, however, the phase behavior often deviates from this prediction due to the differing characteristics of the blocks. Among the many factors that influence the phase behavior, differences in chain stiffness between blocks is

one that plays a role in phase separation. The chain stiffness can be expressed through the statistical segment length (i.e., Kuhn length), *b*. Due to the differences in chain stiffness, each polymer chain occupies unequal volume which can cause shifts in microphase separation morphologies as a function of *f*.

To evaluate the phase behavior for conformationally asymmetric block copolymers, theoretical work has been carried out using different ratios of the chain stiffness for the blocks. Followed by Leibler's theory, Fredrickson and Helfand[161] and Mayes and Olvera de la Cruz[182,183] extended the microphase separation theory to include compositional fluctuation effects. The results indicate that the degree of polymerization *N* influences microphase separation near the order-disorder phase boundary although these compositional fluctuation effects are still based on a symmetric block copolymer system. Freed and coworkers[168,184] and Schweizer and coworkers[185-187] considered differences in chain segments and modified the Flory-Huggins theory. Bates and Fredrickson have pointed out that conformational asymmetry has a significant influence on the Flory-Huggins interaction parameter by increasing the entropy of mixing.[188] Several experiments have shown differences in the composition range for different microdomain morphologies compared to Leibler's prediction due to differences in the statistical segment length between blocks.[34,35,142,169,189] Whitmore and coworkers have calculated the phase diagram of a conformational asymmetric block copolymer system as a function of the ratio of the statistical segment lengths.[190-192] In their work, the ratio can be described,

$$\epsilon = \frac{\left(\frac{f_A}{f_B}\right)}{\left(\frac{R_{g,A}^2}{R_{g,B}^2}\right)} = \frac{\rho_{0,B} \times b_B^2}{\rho_{0,A} \times b_A^2} \quad (2)$$

where R_g is the radius of gyration of the block, $\rho_{0,i}$ is the density of component i, and b_i is the statistical segment length of component i. Matsen and coworkers independently studied the effect of the statistical segment length on the phase diagram using a similar relationship with Whitmore's calculation.[9,139,140,193]

$$\epsilon = \frac{a_A}{a_B} \quad (3)$$

where the statistical segment length of each block is a.

These studies show that in a conformational asymmetric block copolymer systems where the A block occupies smaller volume than B block (the chain stiffness of A is larger than that of B) the interface between blocks is concave towards the A block side of the phase diagram and stabilizes the double gyroid phase instead of the lamellar phase. Experimental confirmation has been reported with various block copolymers.[33,34,123,130,134,142,152,180,189,194-197]

Consequently, conformationally asymmetric block copolymers exhibit a distorted phase diagram. The range of the volume fraction for double gyroid structure is often used to estimate the conformation asymmetry of the block copolymer. These calculations have supported the observation that conformational asymmetry and fluctuations influence the emergence of the double gyroid phase near the order-disorder phase boundary between

the cylinder and lamellar phases. Figure 8.1 and 8.2 show two representative phase diagrams as a function of the conformation asymmetry parameter ϵ.

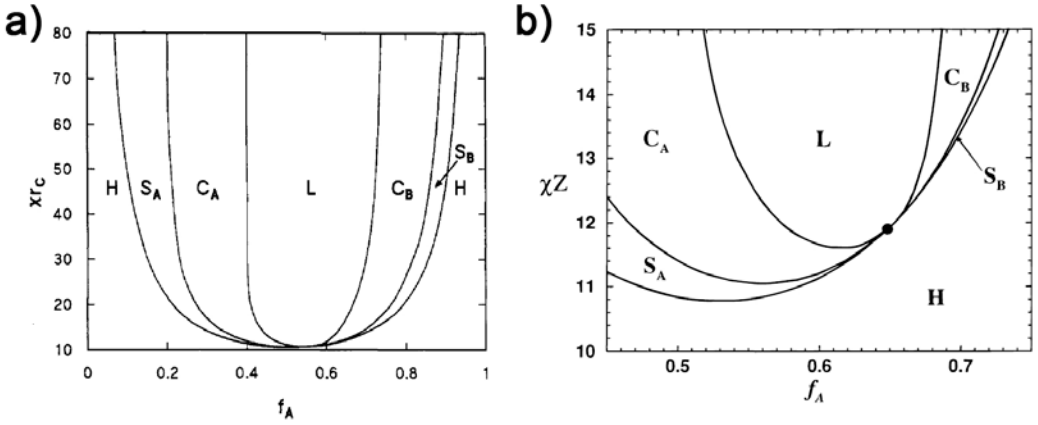

Figure 8.1 The phase diagrams of conformational asymmetric block copolymers a) $\boldsymbol{\epsilon = (\rho_{0,B} \times b_B^2)/(\rho_{0,A} \times b_A^2) = 0.6}$, and b) $\boldsymbol{\epsilon = 0.1}$.[191,192]

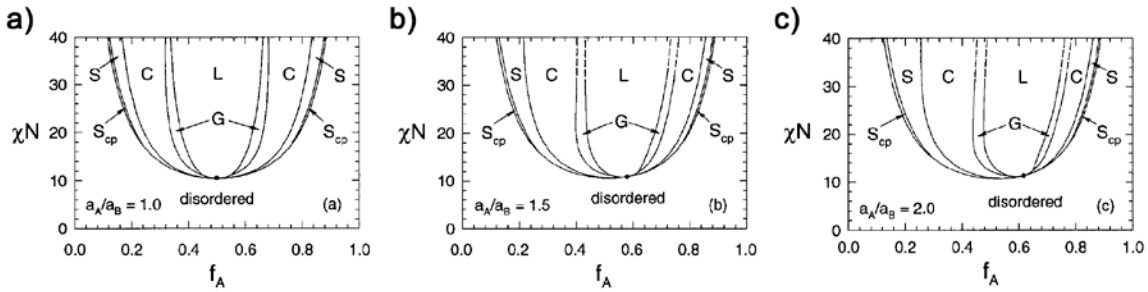

Figure 8.2 The phase diagrams of conformational asymmetric block copolymers as a function of $\boldsymbol{\epsilon}$. a) $\boldsymbol{a_A/a_B = 1.0}$, b) $\boldsymbol{a_A/a_B = 1.5}$, and c) $\boldsymbol{a_A/a_B = 2.0}$.[140]

From a thermodynamic point of view, conformational asymmetry plays a significant role in the phase behavior. A distorted phase diagram in diblock copolymer system is an indication of the presence of high conformational asymmetry.

It is generally known that the modulus in polymers decreases with increasing temperature. When the temperature is above the glass transition temperature for

amorphous polymers (T_g^A) or the melting point of crystalline polymers (T_m^C), the polymer becomes more mobile resulting in a lower modulus.[32] In block copolymers, the storage modulus-temperature relationships exhibit different responses due to the presence of ordered microdomain structures. When the temperature increases, the modulus of the block copolymer is generally observed to gradually decrease followed by a sharp decay at the order-disorder transition.

Generally, crystalline-amorphous block copolymers have higher stiffness below T_m^C. In the case of $T_m^C > T_g^A$, the crystalline block provides the stiffness of the material whereas the amorphous block offers flexibility. When the temperature is above T_m^C, the molten crystalline blocks are free to participate in the microphase separation. At this stage, the modulus-temperature behavior is expected to be the same as observed in typical amorphous-amorphous block copolymers. Most crystalline-amorphous block copolymers display a sharp decay in modulus at T_m^C due to the melting of crystalline block. Above the T_m^C, the storage modulus remains the lower than the initial modulus at $T < T_m^C$. When a phase transition occurs between different microdomain structures (for example from lamellar to double gyroid), the viscoelastic response exhibits a gradual modulus change depending on the arrangement of the microdomains. Figure 8.3 shows representative storage modulus-temperature behavior for a few different crystalline-amorphous block copolymer systems.[35,130,194,195] At about T = 55 °C in Figure 8.3 a) and b), a significant decay in modulus exhibits the melting temperature of PEO crystals. Above the melting point of PEO crystals, the microdomain structure changes from the lamellar phase (L) through the modulated lamellar (ML), the double gyroid ($Q_{Ia\bar{3}d}$) to the hexagonally packed cylinder phase (H) as a function of temperature. Due to the thermal

expansion of the blocks, stretching of chains within the microdomains occurs the phase transition as a function of temperature resulting in the observed modulus changes. A similar transition is shown in PI-PEO system (Figure 8.3 c). Above the melting point of PEO crystals, a gradual enhancement in modulus above about 420 K is exhibited due to the phase transition from the hexagonally packed cylinder phase (HEX) to the double gyroid phase (GYR).

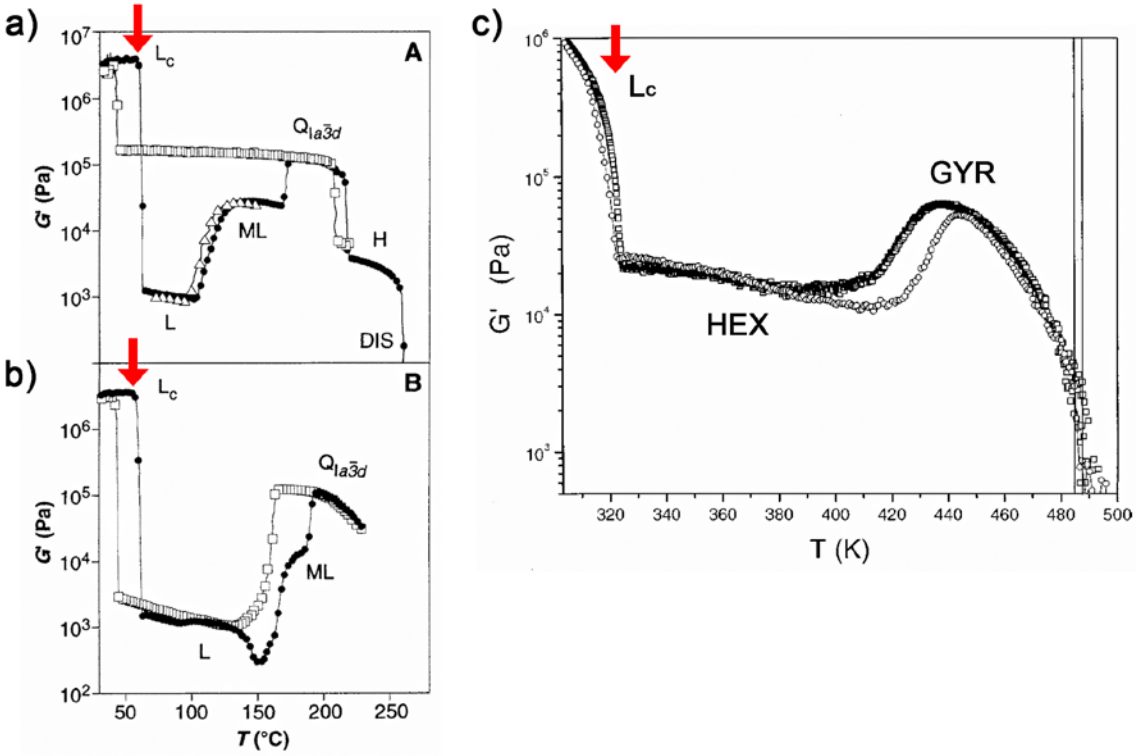

Figure 8.3 Representative storage modulus-temperature relationships in crystalline-amorphous block copolymers. a) and b) polyethylene oxide-polyethyl ethylene (PEO-PEE) (8.8 kDa and 8.4 kDa respectively with f_{PEO} ~ 0.7). The arrows indicate T_m ~ 55 °C of the PEO block[194,195], and c) polyisoprene-polyethylene oxide (PI-PEO) (9.8 kDa with f_{PEO} ~ 0.4). The arrow indicates T_m = 52 °C of the PEO block.[35,130]

It is important to emphasize that most saturated carbon based block copolymers are sensitive to conformational asymmetry. Chain stiffness is one of the factors that influence the entropic contribution to the Flory-Huggins interaction parameter. Considering the difference in chain stiffness between the blocks, most crystalline-

amorphous block copolymer systems have a range of the conformational asymmetry ratios of about $1.5 < \epsilon < 2.5$.[34,35,123,142,152,180,189,198]

Surprisingly, the PH-PMCP block copolymer system is expected to have $\epsilon > 3.0$ based on the comparison between the predicted phase diagram and the range of the double gyroid ($0.46 < f_{PMCP} < 0.51$) and lamellar phases ($0.54 < f_{PMCP} < 0.62$). Due to the presence of the consecutive cyclopentane ring structure on the main backbone, the PMCP chain has the larger chain stiffness and longer statistical segment length than the flexible PH chain. The calculated Flory-Huggins interaction parameter also supports that the PH-PMCP block copolymer system has a large difference in chain stiffness resulting in a large entropic contribution to χ.

The large difference in chain stiffness between PMCP and PH leads to an increase in modulus above the melting point of PMCP crystals with no change in the microdomain exhibiting phase morphology. In contrast to the typical crystalline-amorphous block copolymer systems having a chain conformation asymmetry of about $1.5 < \epsilon < 2.5$, the PH-PMCP system generates a modulus enhancement above the melting point of PMCP crystals. In-situ SAXS/WAXS data support that there is no microdomain transition underlying the modulus enhancement. As a result, the stiff PMCP blocks in the spherical microdomains enhance the storage modulus above the melting temperature of PMCP crystals and the body-centered cubic arrangement is sustained until the order-disorder transition.

As discussed earlier, the phase behavior in conformation asymmetric block copolymer system has been examined in both theories and experiments. The ratio of the

statistical segment lengths in block copolymer plays a significant role in the phase behavior exhibiting a distorted phase diagram. Yet, there is no study for the dynamics of crystalline-amorphous block copolymer system with a conformational asymmetry.

In this thesis, we have shown the modulus enhancement in conformational asymmetric crystalline-amorphous block copolymer system. The combination of the rigid PMCP chain and the flexible PH chain generates a high conformational asymmetry ratio. The ranges of the double gyroid ($0.46 < f_{PMCP} < 0.51$) and the lamellar phase ($0.54 < f_{PMCP} < 0.62$) support that the PH-PMCP system has high conformation asymmetry. Furthermore, the PH-PMCP block copolymer system has a large difference in chain stiffness resulting in a large entropic contribution to χ based on the calculated Flory-Huggins interaction parameter. The large difference in chain stiffness between PH and PMCP block is responsible for the microphase separation at the melting temperature of PMCP crystals. Above the melting temperature of PMCP crystals, the conformation asymmetry ratio of PH-PMCP system is the main reason to exhibit the modulus enhancement. Using this observation, it is possible to combine the dynamic mechanical response with other material properties such as electric, optic, and chemical properties.

Chapter 9. Future Work

9.1. Structure-Property Relationships in Stereoblock and Stereoirregular Polypropylenes

Based on the established synthetic route and the results, one can investigate the mechanical properties of stereogradient polypropylenes. Previously, the Sita group reported the synthesis of a series of stereogradient polypropylene materials via degenerative methyl group transfer living coordinative polymerization during the reaction. Even though there are challenges, in particular, a variable polymerization rate under the degenerative methyl group transfer process, it would be fascinating to analyze the mechanical properties of polymers with stereogradient chain architecture. In addition, it will be valuable to quantify the number of isotactic and atactic sequence lengths within such stereogradient polypropylene materials for further optimization.

One can examine tensile testing, dynamic mechanical analysis, and rheometry, as a function of environmental conditions such as temperature, humidity and atmosphere. For example, the creep test provides the mechanical stability under stress at a given temperature. When the material is subjected to the applied stress, the instrument measures the yielding time. These results can suggest specific applications based on the material performance.

9.2. Structure-Property Relationships in PH-PMCP Block Copolymer System

Given the structure-property relationships in the PH-PMCP block copolymer system, it is important to evaluate the Flory-Huggins interaction parameter of PH-PMCP block copolymer system. Both PH and PMCP chains are hydrocarbon-based polymer

chains, yet, the incompatibility triggers a unique modulus transition in 1-2 min. in sphere-forming PH-PMCP block copolymers. We speculate that the large difference in chain stiffness of PH and PMCP is responsible for the strong phase separation. Furthermore, the basic properties of the PMCP homopolymer such as thermal expansion coefficient, persistence length, and chain dimension-temperature relations still remain unknown. Combined the Flory-Huggins interaction parameters with the basic properties, it would be possible to construct the full phase diagram of the PH-PCM block copolymer system.

We have focused on the understanding of the shear modulus transition at the PMCP melting point. Additional work on the mechanical response as a function of the bulkiness of the amorphous block can be considered. By tailoring the chain structure of amorphous block with 1-octene or higher alkenes, it would be possible to study the effect of chain incompatibility on the phase behavior in additional amorphous-PMCP block copolymers.

Appendix

S.1. Viscoelastic Response of a series of PH-PMCP Block Copolymers

Table S.1 summarized the basic properties of PH-PMCP block copolymers (total M_n ~ 30 kDa). The surface morphologies of a series of PH-PMCP block copolymers were shown in Chapter 4. As the PMCP ratio increases, the materials show spheres, cylinders, weakly-ordered cylinders and crystals, and randomly distributed crystals samples 1-4 respectively.

Table S.1 Characteristics of PH-PMCP materials with total M_n = 30 kDa.

Sample	Mn of PH (kg/mol)	Mn of PMCP (kg/mol)	Mn of PH-PMCP (kg/mol)	f_{PMCP} (mole fraction)	Φ_{PMCP} (volume fraction)	PH T_g (°C)	PMCP T_m / T_c (°C)	M_w/M_n
1	21.6	10.3	31.9	0.21	0.28	-43.9	-	1.10
2	17.7	16.6	34.3	0.26	0.43	-44.9	-	1.28
3	12.6	14.5	27.1	0.41	0.48	-44.2	79.7 / 23.5	1.12
4	10.7	17.5	28.2	0.55	0.59	-45.9	73.3 / 11.3	1.18
homo PH	19.3	-	-	-	-	-48.0	-	1.05
homo PMCP	-	19.4	-	1.00	-	-	94.0 / 83.4	1.11

To obtain the order-disorder transition temperature for each block copolymer shown in Table S.1, the viscoelastic response for the samples in Table S.1 was measured. Figure S.1 shows the viscoelastic response as a function of temperature. As the PMCP ratio increases, the *G'*-temperature profiles for samples 2-4 shows a decrease in the storage modulus at the melting point of the PMCP crystals. However, all block copolymers did not show the order-disorder transition temperature in the experimental temperature range (25-250 °C). Presumably, the PH-PMCP block copolymer system has

a large incompatibility between PH and PMCP blocks due to the large difference in chain stiffness.

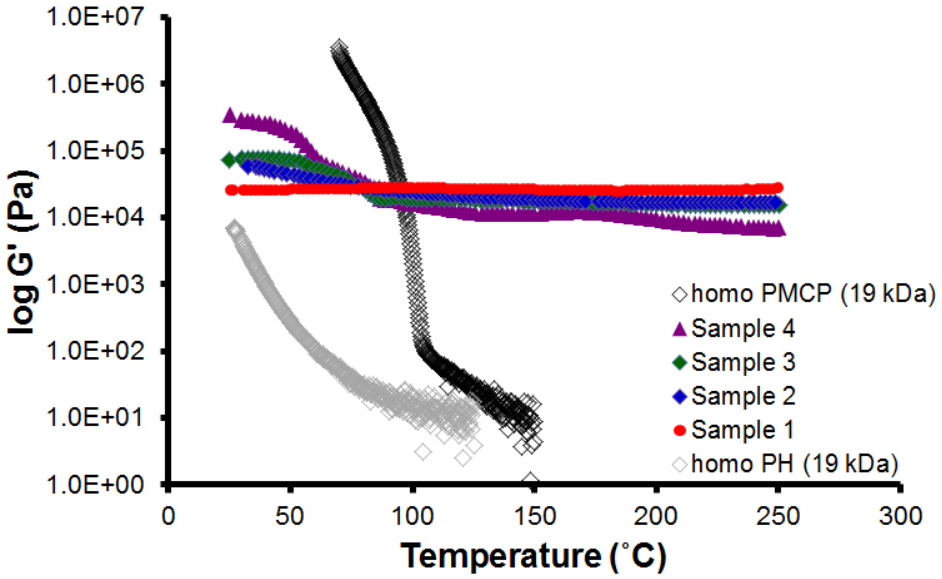

Figure S.1 The viscoelastic response of a series of PH-PMCP block copolymers (total M_n ~ 30 kDa).

S.2. Cylinder-Forming Crystalline-Amorphous PH-PMCP Block Copolymers

The unique modulus transition in cylinder-forming block copolymers has demonstrated in Chapter 5. Due to the low PMCP content, the crystalline lamellae can be confined in cylindrical block copolymer microdomains and the polymer shows a relatively small 'modulus jump' at the melting point. To prove the modulus transition-PMCP content relationships, a series of low molecular weight PH-PMCP block copolymers were synthesized with 0.26-0.39 PMCP content. Table S.2 summarizes the characteristics of cylinder-forming PH-PMCP block copolymers.

Table S.2 Characteristics of cylinder-forming PH-PMCP materials.

Sample	Mn of PH (kg/mol)	Mn of PMCP (kg/mol)	Mn of PH-PMCP (kg/mol)	f_{PMCP} (mole fraction)	PMCP T_m / T_c (°C)	M_w/M_n	T_{ODT} (°C)	Morph (AFM)
WH-1125	6.5	4.1	10.6	0.384	47.8 / 4.1	1.03	135.4	-
WH-1113	7.7	4.5	12.2	0.370	66.5 / 11.1	1.07	-	Cyl, bicon.
WH-1123	6.5	3.8	10.3	0.369	44.4 / -	1.06	117.1	Cyl, bicon.
WH-1108	7.4	4.1	11.6	0.365	53.3 / 5.7	1.03	185.5	Cyl, bicon.
WH-1146	9.0	4.7	13.8	0.344	-	1.05	-	-
WH-1126	6.6	3.2	9.8	0.330	45.5 / -	1.04	78.1	Cyl, bicon.
WH-1107	8.1	3.8	11.9	0.322	57.0 / 6.3	1.08	233.7	Cyl, bicon.
WH-1160	8.6	3.9	12.5	0.311	-	1.04	185.0	-
WH-1163	8.8	4.0	12.7	0.311	-	1.06	165.0	-
WH-1159	8.9	4.0	12.9	0.309	-	1.04	206.1	-
WH-1131	8.2	3.6	11.8	0.305	48.3 / -	1.03	158.2	-
WH-1095	8.6	3.7	12.3	0.300	- / -	1.05	144.0	Cyl, Xtal
WH-1161	9.1	3.8	12.9	0.296	- / -	1.04	186.1	-
WH-1127	7.1	3.0	10.1	0.298	- / -	1.04	53.0	Weak cont.
WH-1133	8.4	3.2	11.7	0.278	- / -	1.04	-	Cyl, bicon.
WH-1134	8.9	3.4	12.2	0.275	- / -	1.07	180.5	Cyl, bicon.
WH-1158	8.7	3.2	11.9	0.265	- / -	1.05	142.0	-
WH-1194	9.9	3.4	13.3	0.256	- / -	1.05	229.0	Cyl, bicon.

We have categorized a series of cylinder-forming PH-PMCP block copolymers by the PMCP melting point. Table S.3 displays the cylinder-forming PH-PMCP block copolymers showing a melting point. The representative materials in Table S.2 exhibit the melting point by DSC and the PMCP content is larger than 0.3. Figure S.2 depicts the modulus-temperature relations.

Table S.3 Characteristics of cylinder-forming PH-PMCP materials.

Sample	Mn of PH (kg/mol)	Mn of PMCP (kg/mol)	Mn of PH-PMCP (kg/mol)	f_{PMCP} (mole fraction)	M_w/M_n	N	PMCP T_m / T_c (°C)	T_{ODT} (°C)
WH-1107	8.1	3.8	11.9	0.322	1.03	142	57.0 / 6.3	233.7
WH-1108	7.4	4.1	11.6	0.365	1.07	139	53.3 / 5.7	185.5
WH-1125	6.5	4.1	10.6	0.384	1.06	128	47.8 / 4.1	135.4
WH-1123	6.5	3.8	10.3	0.369	1.03	123	44.4 / -	117.1
WH-1126	6.6	3.2	9.8	0.330	1.05	117	45.5 / -	78.1

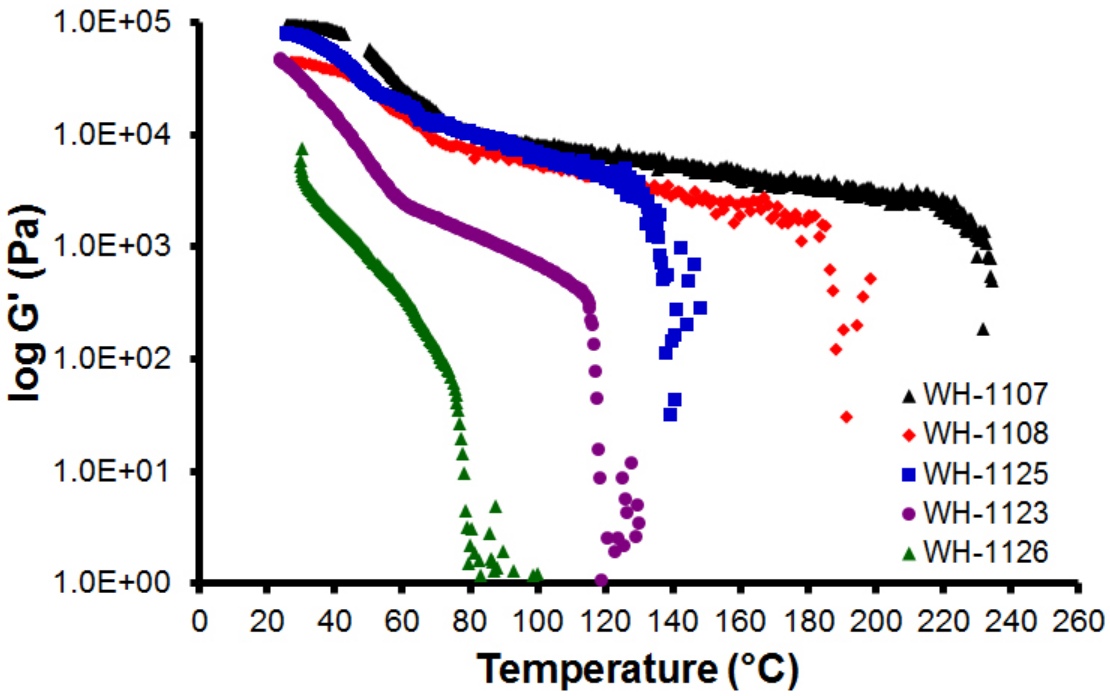

Figure S.2 Representative *G'*-temperature profiles of cylinder-forming PH-PMCP materials.

The storage moduli show sudden decrease at about the PMCP melting point (60-70 °C) and gradual decay in the modulus until the order-disorder transition temperature. Due to large PMCP content, the PMCP blocks crystallize and generate crystalline lamellae. The volume fraction of PMCP block is between 0.32-0.38 and the microdomain structure after the melting point is a cylindrical structure.

Secondly, the cylinder-forming PH-PMCP block copolymers that did not exhibit a melting point are summarized in Table S.4. The PMCP content of these materials is lower than 0.31.

Table S.4 Characteristics of cylinder-forming PH-PMCP materials.

Sample	Mn of PH (kg/mol)	Mn of PMCP (kg/mol)	Mn of PH-PMCP (kg/mol)	f_{PMCP} (mole fraction)	M_w/M_n	N	PMCP T_m / T_c (°C)	T_{ODT} (°C)
WH-1194	9.9	3.4	13.3	0.256	1.05	159	- / -	228.6
WH-1161	9.1	3.8	12.9	0.296	1.04	154	- / -	190.1
WH-1134	8.9	3.4	12.2	0.275	1.07	146	- / -	180.5
WH-1131	8.1	3.6	11.8	0.305	1.03	141	- / -	164.9
WH-1158	8.7	3.2	11.9	0.265	1.05	142	- / -	142.0

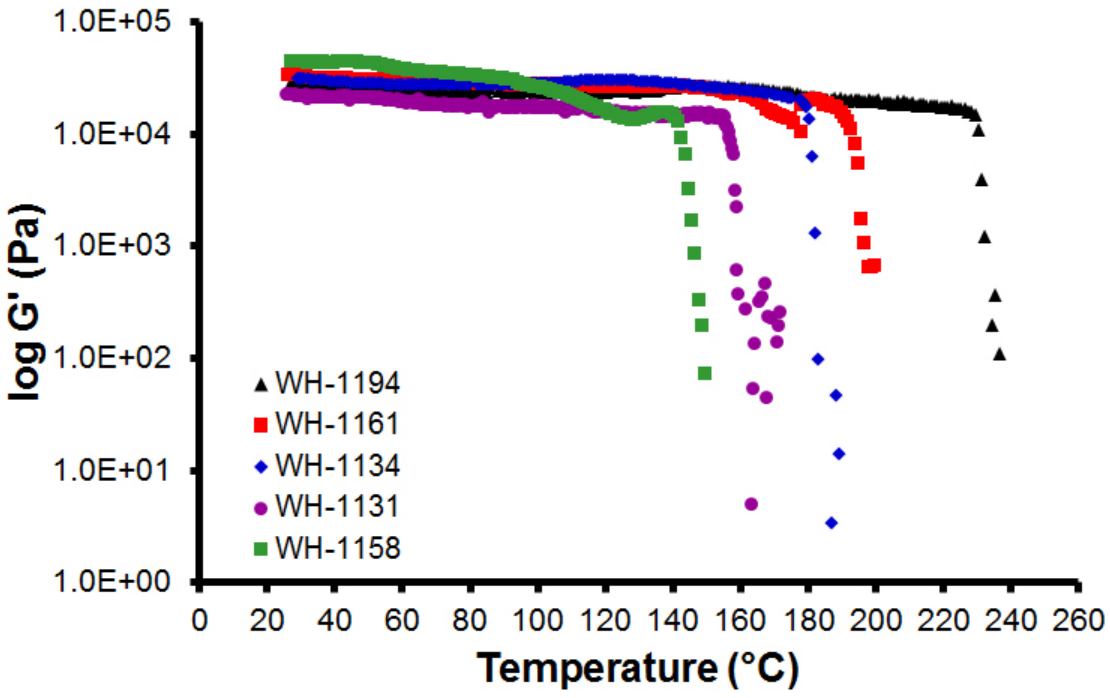

Figure S.3 Representative *G'*-temperature profiles of cylinder-forming PH-PMCP materials.

The storage moduli show gradual decay until the order-disorder transition temperature without displaying sudden decrease at about 60-70 °C. Due to the small PMCP content, the amorphous PH blocks suppress the crystallization of PMCP blocks.

The volume fraction of PMCP block is between 0.26-0.31 and the microdomain structure exhibits a cylindrical microphase structure over the entire temperature range.

S.3. Estimation of Critical Entanglement Molecular Weight of PMCP Polymer

The plateau modulus is a function of the critical entanglement molecular weight of the linear polymer chain. The plateau modulus, G_N^0, is described with the ideal gas constant, R, density of polymer chain, ρ, the entanglement molar mass of the polymer, M_e, and the temperature T.

$$G_N^0 = \frac{\rho RT}{M_e}$$

The time-temperature-superposition (TTS) curve was obtained by using rheology shown in Figure S.4. The arrow indicates the plateau modulus G_N^0 and the overlap of G' and G'' displays the cross-over frequency of the homopolymer PMCP. Based on the plateau modulus (G_N^0 = 3.97e+05 Pa), the critical entanglement molecular weight of PMCP polymer is estimated to be 8245 g/mol.

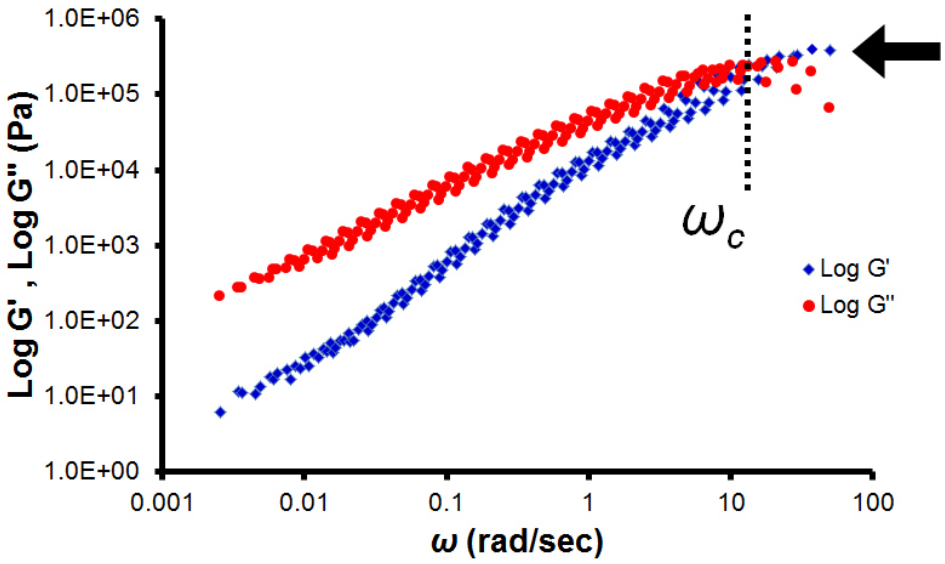

Figure S.4 Time-temperature superposition plot for homopolymer PMCP polymer. The overlap point between *G'* and *G''* displays the cross-over frequency (ω_c) of homopolymer PMCP polymer. The arrow on the right indicates the plateau modulus G_N^0 of homopolymer PMCP (total M_n = 36.5 kDa). Temperature range is from 110 to 150 °C with 10 °C steps.

References

(1) Hadjichristidis, N.; Pispas, S.; Floudas, G.: *Block Copolymers: Synthetic Strategies, Physical Properties, and Applications*; John Wiley & Sons, Inc.: Hoboken, New Jersey, 2003.

(2) Natta, G.: Properties of Isotactic, Atactic, and Stereoblock Homopolymers, Random and Block Copolymers of Alpha-Olefins. *Journal of Polymer Science* **1959**, *34*, 531-549.

(3) Flory, P. J.: *Principles of Polymer Chemistry*; Cornell University Press: Ithaca, New York, 1953.

(4) Helfand, E.: Block Copolymer Theory .3. Statistical-Mechanics of Microdomain Structure. *Macromolecules* **1975**, *8*, 552-556.

(5) Leibler, L.: Theory of Microphase Separation in Block Co-Polymers. *Macromolecules* **1980**, *13*, 1602-1617.

(6) Shull, K. R.: Mean-Field Theory of Block Copolymers - Bulk Melts, Surfaces, and Thin-Films. *Macromolecules* **1992**, *25*, 2122-2133.

(7) Mortensen, K.: *Characterization of Polymer Blends and Block Copolymers by Neutron Scattering: Miscibility and Nanoscale Morphology*; Wiley-VCH Verlag GmbH & Co. KGaA, 2015; Vol. 1.

(8) Kawakatsu, T.: *Statistical Physics of Polymers: An Introduction*; Springer-Verlag: Berlin, Germany, 2004.

(9) Matsen, M. W.; Bates, F. S.: Unifying Weak- and Strong-Segregation Block Copolymer Theories. *Macromolecules* **1996**, *29*, 1091-1098.

(10) Melenkevitz, J.; Muthukumar, M.: Density Functional Theory of Lamellar Ordering in Diblock Copolymers. *Macromolecules* **1991**, *24*, 4199-4205.

(11) Abetz, V.: *Block Copolymers II*; Springer: Berlin Heidelberg, 2005.

(12) Hamley, I. W.: *The Physics of Block Copolymers*; Oxford Science Publications: New York, New York, 1998.

(13) Nojima, S.; Kato, K.; Yamamoto, S.; Ashida, T.: Crystallization of Block Copolymers .1. Small-Angle X-Ray-Scattering Study of an Epsilon-Caprolactone Butadiene Diblock Copolymer. *Macromolecules* **1992**, *25*, 2237-2242.

(14) Loo, Y. L.; Register, R. A.; Ryan, A. J.: Modes of Crystallization in Block Copolymer Microdomains: Breakout, Templated, and Confined. *Macromolecules* **2002**, *35*, 2365-2374.

(15) Cohen, R. E.; Cheng, P. L.; Douzinas, K.; Kofinas, P.; Berney, C. V.: Path-Dependent Morphologies of a Diblock Copolymer of Polystyrene Hydrogenated Polybutadiene. *Macromolecules* **1990**, *23*, 324-327.

(16) Quiram, D. J.; Register, R. A.; Marchand, G. R.: Crystallization of Asymmetric Diblock Copolymers from Microphase-Separated Melts. *Macromolecules* **1997**, *30*, 4551-4558.

(17) Chen, J. T.; Thomas, E. L.; Ober, C. K.; Mao, G.: Self-Assembled Smectic Phases in Rod-Coil Block Copolymers. *Science* **1996**, *273*, 343-346.

(18) Ho, R. M.; Lin, F. H.; Tsai, C. C.; Lin, C. C.; Ko, B. T.; Hsiao, B. S.; Sics, I.: Crystallization-Induced Undulated Morphology in Polystyrene-b-Poly(L-lactide) Block Copolymer. *Macromolecules* **2004**, *37*, 5985-5994.

(19) Menard, K. P.: *Dynamic Mechanical Analysis: A Practical Introduction*; CRC Press: Boca Raton, Florida, 1999.

(20) Randall, J. C.: Modeling Asymmetric and Symmetric Chains and the Structures of Stereo-Defects in Isotactic Polypropylenes. *Macromolecules* **1997**, *30*, 803-816.

(21) Bruce, M. D.; Waymouth, R. M.: Statistical Analysis and Simulation of Pentad Distributions of Stereoblock Polypropylenes. *Macromolecules* **1998**, *31*, 2707-2715.

(22) Cheng, S. Z. D.; Janimak, J. J.; Zhang, A. Q.; Hsieh, E. T.: Isotacticity Effect on Crystallization and Melting in Polypropylene Fractions .1. Crystalline-Structures and Thermodynamic Property Changes. *Polymer* **1991**, *32*, 648-655.

(23) Coates, G. W.; Waymouth, R. M.: Oscillating Stereocontrol: A Strategy for the Synthesis of Thermoplastic Elastomeric Polypropylene. *Science* **1995**, *267*, 217-219.

(24) De Rosa, C.; Auriemma, F.; Di Capua, A.; Resconi, L.; Guidotti, S.; Camurati, I.; Nifant'ev, I. E.; Laishevtsev, I. P.: Structure-Property Correlations in Polypropylene from Metallocene Catalysts: Stereodefective, Regioregular Isotactic Polypropylene. *Journal of the American Chemical Society* **2004**, *126*, 17040-17049.

(25) Giller, C.; Gururajan, G.; Wei, J.; Zhang, W.; Hwang, W.; Chase, D. B.; Rabolt, J. F.; Sita, L. R.: Synthesis, Characterization, and Electrospinning of Architecturally-Discrete Isotactic-Atactic-Isotactic Triblock Stereoblock Polypropene Elastomers. *Macromolecules* **2011**, *44*, 471-482.

(26) Bates, F. S.; Fredrickson, G. H.: Block Copolymer Thermodynamics: Theory and Experiment. *Annual Review of Physical Chemistry* **1990**, *41*, 525-57.

(27) Fredrickson, G. H.; Bates, F. S.: Dynamics of Block Copolymers: Theory and Experiment. *Annual Review of Materials Science* **1996**, *26*, 501-550.

(28) Bates, F. S.: Block Copolymers near the Microphase Separation Transition .2. Linear Dynamic Mechanical-Properties. *Macromolecules* **1984**, *17*, 2607-2613.

(29) Tyler, C. A.; Morse, D. C.: Orthorhombic Fddd Network in Triblock and Diblock Copolymer Melts. *Physical Review Letters* **2005**, *94*, 208302-208305.

(30) Lee, S.; Bluemle, M. J.; Bates, F. S.: Discovery of a Frank-Kasper Sigma Phase in Sphere-Forming Block Copolymer Melts. *Science* **2010**, *330*, 349-353.

(31) Pasquini, N.: *Polypropylene Handbook*; Hanser Publications: New York, New York, 2005.

(32) Ferry, J. D.: *Viscoelastic Properties of Polymers*; John Wiley & Sons, Inc.: New York, New York, 1961.

(33) Kossuth, M. B.; Morse, D. C.; Bates, F. S.: Viscoelastic Behavior of Cubic Phases in Block Copolymer Melts. *Journal of Rheology* **1999**, *43*, 167-196.

(34) Zhao, J.; Majumdar, B.; Schulz, M. F.; Bates, F. S.; Almdal, K.; Mortensen, K.; Hajduk, D. A.; Gruner, S. M.: Phase Behavior of Pure Diblocks and Binary Diblock Blends of Poly(ethylene)-Poly(ethylethylene). *Macromolecules* **1996**, *29*, 1204-1215.

(35) Floudas, G.; Vazaiou, B.; Schipper, F.; Ulrich, R.; Wiesner, U.; Iatrou, H.; Hadjichristidis, N.: Poly(ethylene oxide-b-isoprene) Diblock Copolymer Phase Diagram. *Macromolecules* **2001**, *34*, 2947-2957.

(36) Gopalan, P.; Zhang, Y. M.; Li, X. F.; Wiesner, U.; Ober, C. K.: Liquid Crystalline Rod-Coil Block Copolymers by Stable Free Radical Polymerization: Synthesis, Morphology, and Rheology. *Macromolecules* **2003**, *36*, 3357-3364.

(37) Olsen, B. D.; Teclemariam, N. P.; Muller, S. J.; Segalman, R. A.: Rheological Properties and the Mechanical Signatures of Phase Transitions in Weakly-Segregated Rod-Coil Block Copolymers. *Soft Matter* **2009**, *5*, 2453-2462.

(38) Guinier, A.; Fournet, G.: *Small Angle Scattering of X-Rays*; John Wiley & Sons, Inc.: New York, 1955.

(39) Glatter, O.; Kratky, O.: *Small Angle X-Ray Scattering*; Academic Press: New York, New York, 1982.

(40) Roe, R.-J.: *Methods of X-Ray and Neutron Scattering in Polymer Science*; Oxford University Press: New York, New York, 2000.

(41) Cullity, B. D.: *Elements of X-ray Diffraction*; Addison-Wesley Publishing Company, Inc.: Reading, Massachusetts, USA, 1956.

(42) Burger, C.; Zhou, S.; Chu, B.: *Nanostructures of Polyelectrolyte-Surfactant Complexes and Their Applications*; American Scientific Publishers: Stevenson Rance, California, USA, 2002; Vol. 3.

(43) Sawyer, L. C.; Grubb, D. T.; Meyers, G. F.: *Polymer Microscopy*; Springer: New York, New York, 2008.

(44) Legge, N. R.; Holden, G.; Schroeder, H. E.: *Thermoplastic Elastomers: A Comprehensive Review*; Hanser Gardner Publications: New York, New York, 1987.

(45) White, J. L.; Choi, D. D.: *Polyolefins: Processing, Structure Development, and Properties*; Hanser Gardner Publications: Cincinnati, Ohio, 2004.

(46) Kennedy, M. A.; Peacock, A. J.; Failla, M. D.; Lucas, J. C.; Mandelkern, L.: Tensile Properties of Crystalline Polymers - Random Copolymers of Ethylene. *Macromolecules* **1995**, *28*, 1407-1421.

(47) Muller, G.; Rieger, B.: Propene Based Thermoplastic Elastomers by Early and Late Transition Metal Catalysis. *Progress in Polymer Science* **2002**, *27*, 815-851.

(48) Cobzaru, C.; Hild, S.; Boger, A.; Troll, C.; Rieger, B.: "Dual-side" Catalysts for High and Ultrahigh Molecular Weight Homopolypropylene Elastomers and Plastomers. *Coordination Chemistry Reviews* **2006**, *250*, 189-211.

(49) Bu, H. S.; Cheng, S. Z. D.; Wunderlich, B.: Addendum to the Thermal-Properties of Polypropylene. *Makromolekulare Chemie-Rapid Communications* **1988**, *9*, 75-77.

(50) Ichikawa, M.; Sugimoto, M.; Hatada, K.; Tanaka, T.: Effect of Tacticity on Toughness of Polyproylene. *Kobunshi Ronbunshu* **1995**, *52*, 134-140.

(51) Dunlap, M. S.; Nicholas, K. M.: Catalyst Structural Effects in Titanocene-Catalyzed Pinacol Coupling: Activity, Stereo Selectivity and Mechanistic Implications. *Journal of Organometallic Chemistry* **2001**, *630*, 125-131.

(52) Miller, S. A.; Bercaw, J. E.: Isotactic-Hemiisotactic Polypropylene from C-1 Symmetric Ansa-Metallocene Catalysts: A New Strategy for the Synthesis of Elastomeric Polypropylene. *Organometallics* **2002**, *21*, 934-945.

(53) Baugh, L. S.; Canich, J. A. M.: *Stereoselective Polymerization with Single-Site Catalysts*; CRC Press: Boca Raton, Florida, 2007.

(54) Lin, S.; Waymouth, R. M.: 2-Arylindene Metallocenes: Conformationally Dynamic Catalysts to Control the Structure and Properties of Polypropylenes. *Accounts of Chemical Research* **2002**, *35*, 765-773.

(55) Schonherr, H.; Wiyatno, W.; Pople, J.; Frank, C. W.; Fuller, G. G.; Gast, A. P.; Waymouth, R. M.: Morphology of Thermoplastic Elastomers: Elastomeric Polypropylene. *Macromolecules* **2002**, *35*, 2654-2666.

(56) Collette, J. W.; Ovenall, D. W.; Buck, W. H.; Ferguson, R. C.: Elastomeric Polypropylenes from Alumina-Supported Tetraalkyl Group-Ivb Catalysts .2. Chain Microstructure, Crystallinity, and Morphology. *Macromolecules* **1989**, *22*, 3858-3866.

(57) Collette, J. W.; Tullock, C. W.; Macdonald, R. N.; Buck, W. H.; Su, A. C. L.; Harrell, J. R.; Mulhaupt, R.; Anderson, B. C.: Elastomeric Polypropylenes from Alumina-Supported Tetraalkyl Group-IVB Catalysts .1. Synthesis and Properties of High Molecular-Weight Stereoblock Homopolymers. *Macromolecules* **1989**, *22*, 3851-3858.

(58) Xu, J. T.; Feng, L. X.; Yang, S. L.: Formation Mechanism of Stereoblocks in Polypropylene Produced by Supported Ziegler-Natta Catalysts. *Macromolecules* **1997**, *30*, 2539-2541.

(59) De Rosa, C.; Auriemma, F.; Perretta, C.: Structure and Properties of Elastomeric Polypropylene from C-2 and C-2v Symmetric Zirconocenes. The Origin of Crystallinity and Elastic Properties in Poorly Isotactic Polypropylene. *Macromolecules* **2004**, *37*, 6843-6855.

(60) Resconi, L.; Cavallo, L.; Fait, A.; Piemontesi, F.: Selectivity in Propene Polymerization with Metallocene Catalysts. *Chemical Reviews* **2000**, *100*, 1253-1346.

(61) Brintzinger, H. H.; Fischer, D.; Mulhaupt, R.; Rieger, B.; Waymouth, R. M.: Stereospecific Olefin Polymerization with Chiral Metallocene Catalysts. *Angewandte Chemie-International Edition* **1995**, *34*, 1143-1170.

(62) Chien, J. C. W.; Llinas, G. H.; Rausch, M. D.; Lin, Y. G.; Winter, H. H.; Atwood, J. L.; Bott, S. G.: Metallocene Catalysts for Olefin Polymerizations .24. Stereoblock Propylene Polymerization Catalyzed by Rac-[Anti-Ethylidene(1-Eta-5-Tetramethylcyclopentadienyl) (1-Eta-5-Indenyl)Dimethyltitanium - a 2-State Propagation. *Journal of Polymer Science Part a-Polymer Chemistry* **1992**, *30*, 2601-2617.

(63) Llinas, G. H.; Dong, S. H.; Mallin, D. T.; Rausch, M. D.; Lin, Y. G.; Winter, H. H.; Chien, J. C. W.: Crystalline Amorphous Block Polypropylene and Nonsymmetric Ansa-Metallocene Catalyzed Polymerization. *Macromolecules* **1992**, *25*, 1242-1253.

(64) Kravchenko, R.; Masood, A.; Waymouth, R. M.; Myers, C. L.: Strategies for Synthesis of Elastomeric Polypropylene: Fluxional Metallocenes with C-1 Symmetry. *Journal of the American Chemical Society* **1998**, *120*, 2039-2046.

(65) Madkour, T. M.; Mark, J. E.: Modelling of Crystallization in Stereoblock Polypropylene. Idealized Structures Showing the Effects of Isotactic Block Lengths and Their Polydispersity. *Polymer* **1998**, *39*, 6085-6091.

(66) Madkour, T. M.; Azzam, R. A.; Mark, J. E.: Recent Advances in the Modeling and Simulation of Metallocene Catalysis, Sequence Distribution, Chain Conformations, and Crystallization of Polymers. *Journal of Polymer Science Part B-Polymer Physics* **2006**, *44*, 2524-2541.

(67) Madkour, T. M.; Mark, J. E.: Mesoscopic Modeling of the Polymerization, Morphology, and Crystallization of Stereoblock and Stereoregular Polypropylenes. *Journal of Polymer Science Part B-Polymer Physics* **2002**, *40*, 840-853.

(68) Cheng, H. N.; Kasehagen, L. J.: Tacticity Distribution and Simulation. *Macromolecules* **1993**, *26*, 4774-4782.

(69) Coates, G. W.: Precise Control of Polyolefin Stereochemistry Using Single-Site Metal Catalysts. *Chemical Reviews* **2000**, *100*, 1223-1252.

(70) Coates, G. W.; Hustad, P. D.; Reinartz, S.: Catalysts for the Living Insertion Polymerization of Alkenes: Access to New Polyolefin Architectures using Ziegler-Natta Chemistry. *Angewandte Chemie-International Edition* **2002**, *41*, 2236-2257.

(71) De Rosa, C.; Auriemma, F.; Spera, C.: Comparison between Polymorphic Behaviors of Ziegler-Natta and Metallocene-Made Isotactic Polypropylene: The Role of the Chain Microstructure. *Macromolecular Symposia* **2001**, *169*, 113-124.

(72) De Rosa, C.; Auriemma, F.; Spera, C.; Talarico, G.; Gahleitner, M.: Crystallization Properties of Elastomeric Polypropylene from Alumina-Supported Tetraalkyl Zirconium Catalysts. *Polymer* **2004**, *45*, 5875-5888.

(73) De Rosa, C.; Auriemma, F.; De Lucia, G.; Resconi, L.: From Stiff Plastic to Elastic Polypropylene: Polymorphic Transformations During Plastic Deformation of Metallocene-Made Isotactic Polypropylene. *Polymer* **2005**, *46*, 9461-9475.

(74) De Rosa, C.; Auriemma, F.; Paolillo, M.; Resconi, L.; Camurati, I.: Crystallization Behavior and Mechanical Properties of Regiodefective, Highly Stereoregular Isotactic Polypropylene: Effect of Regiodefects versus Stereodefects and Influence of the Molecular Mass. *Macromolecules* **2005**, *38*, 9143-9154.

(75) De Rosa, C.; Auriemma, F.: Structural-Mechanical Phase Diagram of Isotactic Polypropylene. *Journal of the American Chemical Society* **2006**, *128*, 11024-11025.

(76) Harney, M. B.; Zhang, Y.; Sita, L. R.: Discrete, Multiblock Isotactic-Atactic Stereoblock Polypropene Microstructures of Differing Block Architectures through Programmable Stereomodulated Living Ziegler-Natta Polymerization. *Angewandte Chemie-International Edition* **2006**, *45*, 2400-2404.

(77) van der Wal, A.; Mulder, J. J.; Gaymans, R. J.: Fracture of polypropylene: 2. The effect of crystallinity. *Polymer* **1998**, *39*, 5477-5481.

(78) Harney, M. B.; Zhang, Y.; Sita, L. R.: Bimolecular Control over Polypropene Stereochemical Microstructure in a Well-Defined Two-State System and a New Fundamental Form: Stereogradient Polypropene. *Angewandte Chemie-International Edition* **2006**, *45*, 6140-6144.

(79) De Rosa, C.; Auriemma, F.; Circelli, T.; Waymouth, R. M.: Crystallization of the alpha and gamma forms of isotactic polypropylene as a tool to test the degree of segregation of defects in the polymer chains. *Macromolecules* **2002**, *35*, 3622-3629.

(80) Ward, I. M.; Sweeney, J.: *An Introduction to The Mechanical Properties of Solid Polymers*; John Wiley & Sons Inc.: Hoboken, New Jersey, 2004.

(81) Carlson, E. D.; Krejchi, M. T.; Shah, C. D.; Terakawa, T.; Waymouth, R. M.; Fuller, G. G.: Rheological and Thermal Properties of Elastomeric Polypropylene. *Macromolecules* **1998**, *31*, 5343-5351.

(82) Han, C. D.: *Rheology and Processing of Polymeric Materials*; Oxford University Press Inc.: New York, New York, 2007; Vol. 1.

(83) Hong, S.; MacKnight, W. J.; Russell, T. P.; Gido, S. P.: Structural evolution of multilayered, crystalline-amorphous diblock copolymer thin films. *Macromolecules* **2001**, *34*, 2876-2883.

(84) Hong, S.; Yang, L. Z.; MacKnight, W. J.; Gido, S. P.: Morphology of a crystalline/amorphous diblock copolymer: Poly((ethylene oxide)-b-butadiene). *Macromolecules* **2001**, *34*, 7009-7016.

(85) Nojima, S.; Hashizume, K.; Rohadi, A.; Sasaki, S.: Crystallization of epsilon-caprolactone blocks within a crosslinked microdomain structure of poly(epsilon-caprolactone)-block-polybutadiene. *Polymer* **1997**, *38*, 2711-2718.

(86) Huang, Y. H.; Yang, C. H.; Chen, H. L.; Chiu, F. C.; Lin, T. L.; Liou, W.: Crystallization-Induced Microdomain Coalescence in Sphere-Forming Crystalline-Amorphous Diblock Copolymer Systems: Neat Diblock versus the Corresponding Blends. *Macromolecules* **2004**, *37*, 486-493.

(87) Tsai, J. C.; Kuo, J. C.; Ho, R. M.; Chung, T. M.: Syntheses of stereoregular amorphous-crystalline diblock copolymers and their self-assembly studies. *Macromolecules* **2006**, *39*, 7520-7526.

(88) Park, J. W.; Thomas, E. L.: Frustrated crystallization of a rod-coil block copolymer from its liquid crystalline state. *Macromolecules* **2006**, *39*, 4650-4653.

(89) Hamley, I. W.; Fairclough, J. P. A.; Ryan, A. J.; Bates, F. S.; TownsAndrews, E.: Crystallization of nanoscale-confined diblock copolymer chains. *Polymer* **1996**, *37*, 4425-4429.

(90) Weimann, P. A.; Hajduk, D. A.; Chu, C.; Chaffin, K. A.; Brodil, J. C.; Bates, F. S.: Crystallization of tethered polyethylene in confined geometries. *Journal of Polymer Science Part B-Polymer Physics* **1999**, *37*, 2053-2068.

(91) Loo, Y. L.; Register, R. A.; Adamson, D. H.: Direct imaging of polyethylene crystallites within block copolymer microdomains. *Journal of Polymer Science Part B-Polymer Physics* **2000**, *38*, 2564-2570.

(92) Zhu, L.; Calhoun, B. H.; Ge, Q.; Quirk, R. P.; Cheng, S. Z. D.; Thomas, E. L.; Hsiao, B. S.; Yeh, F.; Liu, L. Z.; Lotz, B.: Initial-stage growth controlled crystal orientations in nanoconfined lamellae of a self-assembled crystalline-amorphous diblock copolymer. *Macromolecules* **2001**, *34*, 1244-1251.

(93) Zhu, L.; Cheng, S. Z. D.; Calhoun, B. H.; Ge, Q.; Quirk, R. P.; Thomas, E. L.; Hsiao, B. S.; Yeh, F.; Lotz, B.: Phase structures and morphologies determined by self-organization, vitrification, and crystallization: confined crystallization in an ordered lamellar phase of PEO-b-PS diblock copolymer. *Polymer* **2001**, *42*, 5829-5839.

(94) Loo, Y. L.; Register, R. A.; Ryan, A. J.; Dee, G. T.: Polymer Crystallization Confined in One, Two, or Three Dimensions. *Macromolecules* **2001**, *34*, 8968-8977.

(95) Dimarzio, E. A.; Guttman, C. M.; Hoffman, J. D.: Calculation of Lamellar Thickness in a Diblock Copolymer, One of Whose Components Is Crystalline. *Macromolecules* **1980**, *13*, 1194-1198.

(96) Whitmore, M. D.; Noolandi, J.: Theory of Crystallizable Block Copolymer Blends. *Macromolecules* **1988**, *21*, 1482-1496.

(97) Vilgis, T.; Halperin, A.: Aggregation of Coil Crystalline Block Copolymers - Equilibrium Crystallization. *Macromolecules* **1991**, *24*, 2090-2095.

(98) Rohadi, A.; Endo, R.; Tanimoto, S.; Sasaki, S.; Nojima, S.: Effects of Molecular Weight and Crystallization Temperature on the Morphology Formation in Asymmetric Diblock Copolymers with a Highly Crystalline Block. *Polymer Journal* **2000**, *32*, 602-609.

(99) Nojima, S.; Toei, M.; Hara, S.; Tanimoto, S.; Sasaki, S.: Size dependence of crystallization within spherical microdomain structures. *Polymer* **2002**, *43*, 4087-4090.

(100) Rangarajan, P.; Register, R. A.; Fetters, L. J.: Morphology of Semicrystalline Block-Copolymers of Ethylene-(Ethylene-Alt-Propylene). *Macromolecules* **1993**, *26*, 4640-4645.

(101) Quiram, D. J.; Register, R. A.; Marchand, G. R.; Ryan, A. J.: Dynamics of Structure Formation and Crystallization in Asymmetric Diblock Copolymers. *Macromolecules* **1997**, *30*, 8338-8343.

(102) Quiram, D. J.; Register, R. A.; Marchand, G. R.; Adamson, D. H.: Chain Orientation in Block Copolymers Exhibiting Cylindrically Confined Crystallization. *Macromolecules* **1998**, *31*, 4891-4898.

(103) Rangarajan, P.; Register, R. A.; Fetters, L. J.; Bras, W.; Naylor, S.; Ryan, A. J.: Crystallization of a Weakly Segregated Polyolefin Diblock Copolymer. *Macromolecules* **1995**, *28*, 4932-4938.

(104) Hamley, I. W.; Fairclough, J. P. A.; Terrill, N. J.; Ryan, A. J.; Lipic, P. M.; Bates, F. S.; TownsAndrews, E.: Crystallization in oriented semicrystalline diblock copolymers. *Macromolecules* **1996**, *29*, 8835-8843.

(105) Hobbs, J. K.; Register, R. A.: Imaging block copolymer crystallization in real time with the atomic force microscope. *Macromolecules* **2006**, *39*, 703-710.

(106) Reiter, G.; Castelein, G.; Sommer, J. U.; Rottele, A.; Thurn-Albrecht, T.: Direct Visualization of Random Crystallization and Melting in Arrays of Nanometer-Size Polymer Crystals. *Physical Review Letters* **2001**, *87*, 226101-226104.

(107) Ueda, M.; Sakurai, K.; Okamoto, S.; Lohse, D. J.; MacKnight, W. J.; Shinkai, S.; Sakurai, S.; Nomura, S.: Spherulite formation from microphase-separated lamellae in semi-crystalline diblock copolymer comprising polyethylene and atactic polypropylene blocks. *Polymer* **2003**, *44*, 6995-7005.

(108) Jayaratne, K. C.; Keaton, R. J.; Henningsen, D. A.; Sita, L. R.: Living Ziegler-Natta Cyclopolymerization of Nonconjugated Dienes: New Classes of Microphase-Separated Polyolefin Block Copolymers via a Tandem Polymerization/Cyclopolymerization Strategy. *Journal of the American Chemical Society* **2000**, *122*, 10490-10491.

(109) Jayaratne, K. C.; Sita, L. R.: Stereospecific Living Ziegler-Natta Polymerization of 1-Hexene. *Journal of the American Chemical Society* **2000**, *122*, 958-959.

(110) Naga, N.; Yabe, T.; Sawaguchi, A.; Sone, M.; Noguchi, K.; Murase, S.: Liquid Crystalline Features in a Polyolefin of Poly(methylene-1,3-cyclopentane). *Macromolecules* **2008**, *41*, 7448-7452.

(111) Naga, N.; Shimura, H.; Sone, M.: Liquid Crystalline Features of Optically Active Poly(methylene-1,3-cyclopentane). *Macromolecules* **2009**, *42*, 7631-7633.

(112) Chen, H. L.; Hsiao, S. C.; Lin, T. L.; Yamauchi, K.; Hasegawa, H.; Hashimoto, T.: Microdomain-Tailored Crystallization Kinetics of Block Copolymers. *Macromolecules* **2001**, *34*, 671-674.

(113) Makowski, H. S.; Wilchinsky, Z. W.; Shim, B. K. C.: 1,5-Hexadiene Polymers .1. Structure-Properties of Poly-1,5-Hexadiene. *Journal of Polymer Science Part a-General Papers* **1964**, *2*, 1549-1566.

(114) Coates, G. W.; Waymouth, R. M.: Enantioselective Cyclopolymerization of 1,5-Hexadiene Catalyzed by Chiral Zirconocenes - A Novel Strategy for the Synthesis of Optically-Active Polymers with Chirality in the Main Chain. *Journal of the American Chemical Society* **1993**, *115*, 91-98.

(115) Deballesteros, O. R.; Cavallo, L.; Auriemma, F.; Guerra, G.: Conformational-Analysis of Poly(Methylene-1,3-Cyclopentane) and Chain Conformation in the Crystalline Phase. *Macromolecules* **1995**, *28*, 7355-7362.

(116) Deballesteros, O. R.; Venditto, V.; Auriemma, F.; Guerra, G.; Resconi, L.; Waymouth, R.; Mogstad, A. L.: Thermal and Structural Characterization of Poly(Methylene-1,3-Cyclopentane) Samples of Different Microstructures. *Macromolecules* **1995**, *28*, 2383-2388.

(117) Pan, Y.; Xu, T. Q.; Ge, Y. S.; Lu, X. B.: N-heterocyclic Carbene Scandium Complexes: Synthesis, Structure, and Catalytic Performance for alpha-Olefin Polymerization and Copolymerization with 1,5-Hexadiene. *Organometallics* **2011**, *30*, 5687-5694.

(118) Cheng, H. N.; Khasat, N. P.: C-13-NMR Characterization of Poly(1,5-Hexadiene). *Journal of Applied Polymer Science* **1988**, *35*, 825-829.

(119) Coates, G. W.; Waymouth, R. M.: Enantioselective Cyclopolymerization - Optically-Active Poly(Methylene-1,3-Cyclopentane). *Journal of the American Chemical Society* **1991**, *113*, 6270-6271.

(120) Guo, F.; Nishiura, M.; Koshino, H.; Hou, Z. M.: Scandium-Catalyzed Cyclocopolymerization of 1,5-Hexadiene with Styrene and Ethylene: Efficient Synthesis of Cyclopolyolefins Containing Syndiotactic Styrene-Styrene Sequences and Methylene-1,3-cyclopentane Units. *Macromolecules* **2011**, *44*, 6335-6344.

(121) Chung, C. I.; Lin, M. I.: Nature of Melt Rheological Transition in a Styrene-Butadiene-Styrene Block Copolymer. *Journal of Polymer Science Part B-Polymer Physics* **1978**, *16*, 545-553.

(122) Gouinlock, E. V.; Porter, R. S.: Linear Dynamic Mechanical-Properties of an SBS Block Copolymer. *Polymer Engineering and Science* **1977**, *17*, 535-543.

(123) Almdal, K.; Mortensen, K.; Ryan, A. J.; Bates, F. S.: Order, disorder, and composition fluctuation effects in low molar mass hydrocarbon-poly(dimethylsiloxane) diblock copolymers. *Macromolecules* **1996**, *29*, 5940-5947.

(124) Kennemur, J. G.; Hillmyer, M. A.; Bates, F. S.: Rheological Evidence of Composition Fluctuations in an Unentangled Diblock Copolymer Melt near the Order-Disorder Transition. *Acs Macro Letters* **2013**, *2*, 496-500.

(125) Lee, S.; Gillard, T. M.; Bates, F. S.: Fluctuations, Order, and Disorder in Short Diblock Copolymers. *Aiche Journal* **2013**, *59*, 3502-3513.

(126) Gillard, T. M.; Medapuram, P.; Morse, D. C.; Bates, F. S.: Fluctuations, Phase Transitions, and Latent Heat in Short Diblock Copolymers: Comparison of Experiment, Simulation, and Theory. *Macromolecules* **2015**, *48*, 2801-2811.

(127) Hickey, R. J.; Gillard, T. M.; Lodge, T. P.; Bates, F. S.: Influence of Composition Fluctuations on the Linear Viscoelastic Properties of Symmetric Diblock Copolymers near the Order-Disorder Transition. *Acs Macro Letters* **2015**, *4*, 260-265.

(128) Ilavsky, J.; Jemian, P. R.: Irena: tool suite for modeling and analysis of small-angle scattering. *Journal of Applied Crystallography* **2009**, *42*, 347-353.

(129) Fetters, L. J.; Lohse, D. J.; Garcia-Franco, C. A.; Brant, P.; Richter, D.: Prediction of Melt State Poly(alpha-olefin) Rheological Properties: The Unsuspected Role of the Average Molecular Weight Per Backbone Bond. *Macromolecules* **2002**, *35*, 10096-10101.

(130) Floudas, G.; Ulrich, R.; Wiesner, U.: Microphase Separation in Poly(isoprene-b-ethylene oxide) Diblock Copolymer Melts. I. Phase State and Kinetics of the Order-to-Order Transitions. *Journal of Chemical Physics* **1999**, *110*, 652-663.

(131) Nojima, S.; Inokawa, D.; Kawamura, T.; Nitta, K.: Dynamic Mechanical Study of Block Copolymer Crystallization Confined within Spherical Nanodomains. *Polymer Journal* **2008**, *40*, 986-991.

(132) Ryu, C. Y.; Lee, M. S.; Hajduk, D. A.; Lodge, T. P.: Structure and Viscoelasticity of Matched Asymmetric Diblock and Triblock Copolymers in the Cylinder and Sphere Microstructures. *Journal of Polymer Science Part B-Polymer Physics* **1997**, *35*, 2811-2823.

(133) Schulz, M. F.; Bates, F. S.; Almdal, K.; Mortensen, K.: Epitaxial Relationship for Hexagonal-to-Cubic Phase Transition in a Block Copolymer Mixture. *Physical Review Letters* **1994**, *73*, 86-89.

(134) Forster, S.; Khandpur, A. K.; Zhao, J.; Bates, F. S.; Hamley, I. W.; Ryan, A. J.; Bras, W.: Complex Phase-Behavior of Polyisoprene-Polystyrene Diblock Copolymers near the Order-Disorder Transition. *Macromolecules* **1994**, *27*, 6922-6935.

(135) Hamley, I. W.; Castelletto, V.; Floudas, G.; Schipper, F.: Templated Crystallization from Oriented Gyroid and Hexagonal Melt Phases in a Diblock Copolymer. *Macromolecules* **2002**, *35*, 8839-8845.

(136) Russell, T. P.; Karis, T. E.; Gallot, Y.; Mayes, A. M.: A Lower Critical Ordering Transition in a Diblock Copolymer Melt. *Nature* **1994**, *368*, 729-731.

(137) Karis, T. E.; Russell, T. P.; Gallot, Y.; Mayes, A. M.: Rheology of the Lower Critical Ordering Transition. *Macromolecules* **1995**, *28*, 1129-1134.

(138) Ryu, D. Y.; Jeong, U.; Kim, J. K.; Russell, T. R.: Closed-loop phase behaviour in block copolymers. *Nature Materials* **2002**, *1*, 114-117.

(139) Matsen, M. W.; Schick, M.: Stable and Unstable Phases of a Linear Multiblock Copolymer Melt. *Macromolecules* **1994**, *27*, 7157-7163.

(140) Matsen, M. W.; Bates, F. S.: Conformationally asymmetric block copolymers. *Journal of Polymer Science Part B-Polymer Physics* **1997**, *35*, 945-952.

(141) Sperling, L. H.: *Introduction to Physical Polymer Science*; John Wiley & Sons, Inc.: New York, New York, 1992.

(142) Khandpur, A. K.; Forster, S.; Bates, F. S.; Hamley, I. W.; Ryan, A. J.; Bras, W.; Almdal, K.; Mortensen, K.: Polyisoprene-polystyrene diblock copolymer phase diagram near the order-disorder transition. *Macromolecules* **1995**, *28*, 8796-8806.

(143) Hajduk, D. A.; Takenouchi, H.; Hillmyer, M. A.; Bates, F. S.; Vigild, M. E.; Almdal, K.: Stability of the perforated layer (PL) phase in diblock copolymer melts. *Macromolecules* **1997**, *30*, 3788-3795.

(144) Kim, J. K.; Lee, H. H.; Gu, Q. J.; Chang, T. H.; Jeong, Y. H.: Determination of order-order and order-disorder transition temperatures of SIS block copolymers by differential scanning calorimetry and rheology. *Macromolecules* **1998**, *31*, 4045-4048.

(145) Almdal, K.; Bates, F. S.; Mortensen, K.: Order, Disorder, and Fluctuation Effects in an Asymmetric Poly(Ethylene-Propylene)-Poly(Ethylethylene) Diblock Copolymer. *Journal of Chemical Physics* **1992**, *96*, 9122-9132.

(146) Colby, R. H.: Block copolymer dynamics. *Current Opinion in Colloid & Interface Science* **1996**, *1*, 454-465.

(147) Doi, M.; Harden, J. L.; Ohta, T.: Anomalous Rheological Behavior of Ordered Phases of Block-Copolymers .2. *Macromolecules* **1993**, *26*, 4935-4944.

(148) Larson, R. G.; Winey, K. I.; Patel, S. S.; Watanabe, H.; Bruinsma, R.: The Rheology of Layered Liquids - Lamellar Block-Copolymers and Smectic Liquid-Crystals. *Rheologica Acta* **1993**, *32*, 245-253.

(149) Ohta, T.; Enomoto, Y.; Harden, J. L.; Doi, M.: Anomalous Rheological Behavior of Ordered Phases of Block-Copolymers .1. *Macromolecules* **1993**, *26*, 4928-4934.

(150) Li, L. B.; Serero, Y.; Koch, M. H. J.; de Jeu, W. H.: Microphase Separation and Crystallization in an Asymmetric Diblock Copolymer: Coupling and Competition. *Macromolecules* **2003**, *36*, 529-532.

(151) Ryan, A. J.; Fairclough, J. P. A.; Hamley, I. W.; Mai, S. M.; Booth, C.: Chain Folding in Crystallizable Block Copolymers. *Macromolecules* **1997**, *30*, 1723-1727.

(152) Takagi, H.; Yamamoto, K.; Okamoto, S.; Sakurai, S.: A Study on the Phase Behavior of Poly(epsilon-caprolactone)-Poly(butadiene) Diblock Copolymers: The Influence of Relatively Low-Molecular-Weight Block Copolymers on the Order-Disorder Transition Behavior. *Polymer* **2015**, *67*, 20-27.

(153) Takagi, H.; Sugino, Y.; Hara, S.; Yamamoto, K.; Shimada, S.: Non-Equilibrium Disordered Micelles Observed after Melting of Crystalline-Amorphous Alternating Lamellar Structure in Crystalline-Amorphous Block Copolymers Forming Spherical Morphology. *Colloid and Polymer Science* **2016**, *294*, 993-999.

(154) Ryan, A. J.; Mai, S. M.; Fairclough, J. P. A.; Hamley, I. W.; Booth, C.: Ordered melts of block copolymers of ethylene oxide and 1,2-butylene oxide. *Physical Chemistry Chemical Physics* **2001**, *3*, 2961-2971.

(155) Jones, J. L.; Mcleish, T. C. B.: Rheological Response of Surfactant Cubic Phases. *Langmuir* **1995**, *11*, 785-792.

(156) Watanabe, H.; Kanaya, T.; Takahashi, Y.: Equilibrium Elasticity of Diblock Copolymer Micellar Lattice. *Macromolecules* **2001**, *34*, 662-665.

(157) Sebastian, J. M.; Lai, C.; Graessley, W. W.; Register, R. A.: Steady-Shear Rheology of Block Copolymer Melts and Concentrated Solutions: Disordering Stress in Body-Centered-Cubic Systems. *Macromolecules* **2002**, *35*, 2707-2713.

(158) Tyler, C. A.; Morse, D. C.: Linear Elasticity of Cubic Phases in Block Copolymer Melts by Self-Consistent Field Theory. *Macromolecules* **2003**, *36*, 3764-3774.

(159) Hildebrand, J. H.: *Regular Solutions*; Prentice-Hall: New York, 1962.

(160) Mark, J. E.: *Physical Properties of Polymers Handbook*; 2nd ed.; Springer: New York, 2007.

(161) Fredrickson, G. H.; Helfand, E.: Fluctuation Effects in the Theory of Microphase Separation in Block Copolymers. *Journal of Chemical Physics* **1987**, *87*, 697-705.

(162) Krevelen, D. W. v.; Nijenhuis, K. t.: *Properties of Polymers*; Elsevier: Oxford, UK, 2009.

(163) Callaghan, T. A.; Paul, D. R.: Interaction Energies for Blends of Poly(Methyl Methacrylate), Polystyrene, and Poly(Alpha-Methylstyrene) by the Critical Molecular-Weight Method. *Macromolecules* **1993**, *26*, 2439-2450.

(164) Krishnamoorti, R.; Graessley, W. W.; Balsara, N. P.; Lohse, D. J.: Structural Origin of Thermodynamic Interactions in Blends of Saturated-Hydrocarbon Polymers. *Macromolecules* **1994**, *27*, 3073-3081.

(165) Nishi, T.; Wang, T. T.: Melting-Point Depression and Kinetic Effects of Cooling on Crystallization in Poly(Vinylidene Fluoride) Poly(Methyl Methacrylate) Mixtures. *Macromolecules* **1975**, *8*, 909-915.

(166) Russell, T. P.; Hjelm, R. P.; Seeger, P. A.: Temperature-Dependence of the Interaction Parameter of Polystyrene and Poly(Methyl Methacrylate). *Macromolecules* **1990**, *23*, 890-893.

(167) Bates, F. S.: Polymer-Polymer Phase-Behavior. *Science* **1991**, *251*, 898-905.

(168) Dudowicz, J.; Freed, K. F.; Madden, W. G.: Role of Molecular-Structure on the Thermodynamic Properties of Melts, Blends, and Concentrated Polymer-Solutions - Comparison of Monte-Carlo Simulations with the Cluster Theory for the Lattice Model. *Macromolecules* **1990**, *23*, 4803-4819.

(169) Bates, F. S.; Schulz, M. F.; Rosedale, J. H.; Almdal, K.: Correlation of Binary Polyolefin Phase-Behavior with Statistical Segment Length Asymmetry. *Macromolecules* **1992**, *25*, 5547-5550.

(170) Milner, S. T.: Chain Architecture and Asymmetry in Copolymer Microphases. *Macromolecules* **1994**, *27*, 2333-2335.

(171) Kozuch, D. J.; Zhang, W. L.; Milner, S. T.: Predicting the Flory-Huggins Parameter for Polymers with Stiffness Mismatch from Molecular Dynamics Simulations. *Polymers* **2016**, *8*, 241-257.

(172) Fredrickson, G. H.; Liu, A. J.; Bates, F. S.: Entropic Corrections to the Flory-Huggins Theory of Polymer Blends - Architectural and Conformational Effects. *Macromolecules* **1994**, *27*, 2503-2511.

(173) Bates, F. S.; Rosedale, J. H.; Fredrickson, G. H.; Glinka, C. J.: Fluctuation-Induced 1st-Order Transition of an Isotropic System to a Periodic State. *Physical Review Letters* **1988**, *61*, 2229-2232.

(174) Bates, F. S.; Rosedale, J. H.; Fredrickson, G. H.: Fluctuation Effects in a Symmetric Diblock Copolymer near the Order-Disorder Transition. *Journal of Chemical Physics* **1990**, *92*, 6255-6270.

(175) Rosedale, J.; Bates, F. S.; Almdal, K.; Mortensen, K.; Wignall, G. D.: Order and Disorder in Symmetrical Diblock Copolymer Melts. *Macromolecules* **1995**, *28*, 1429-1443.

(176) Cochran, E. W.; Bates, F. S.: Thermodynamic behavior of poly(cyclohexylethylene) in polyolefin diblock copolymers. *Macromolecules* **2002**, *35*, 7368-7374.

(177) Lee, J. H.; Balsara, N. P.; Chakraborty, A. K.; Krishnamoorti, R.; Hammouda, B.: Thermodynamics and phase behavior of block copolymer/homopolymer blends with attractive and repulsive interactions. *Macromolecules* **2002**, *35*, 7748-7757.

(178) Zhao, Y.; Sivaniah, E.; Hashimoto, T.: SAXS Analysis of the Order-Disorder Transition and the Interaction Parameter of Polystyrene-block-poly(methyl methacrylate). *Macromolecules* **2008**, *41*, 9948-9951.

(179) Sakamoto, N.; Hashimoto, T.: Order-Disorder Transition of Low-Molecular-Weight Polystyrene-Block-Polyisoprene .1. Saxs Analysis of 2 Characteristic Temperatures. *Macromolecules* **1995**, *28*, 6825-6834.

(180) Schulz, M. F.; Khandpur, A. K.; Bates, F. S.; Almdal, K.; Mortensen, K.; Hajduk, D. A.; Gruner, S. M.: Phase behavior of polystyrene-poly(2-vinylpyridine) diblock copolymers. *Macromolecules* **1996**, *29*, 2857-2867.

(181) Frielinghaus, H.; Hermsdorf, N.; Almdal, K.; Mortensen, K.; Messe, L.; Corvazier, L.; Fairclough, J. P. A.; Ryan, A. J.; Olmsted, P. D.; Hamley, I. W.: Micro- vs. macro-phase separation in binary blends of poly(styrene)-poly(isoprene) and poly(isoprene)-poly(ethylene oxide) diblock copolymers. *Europhysics Letters* **2001**, *53*, 680-686.

(182) Mayes, A. M.; Delacruz, M. O.: Concentration Fluctuation Effects on Disorder-Order Transitions in Block Copolymer Melts. *Journal of Chemical Physics* **1991**, *95*, 4670-4677.

(183) Mayes, A. M.; Delacruz, M. O.: Equilibrium Domain Spacing in Weakly Segregated Block Copolymers. *Macromolecules* **1991**, *24*, 3975-3976.

(184) Tang, H.; Freed, K. F.: Static Structure Factors of Compressible Polymer Blends and Diblock Copolymer Melts .2. Constraints on Density-Fluctuations. *Macromolecules* **1991**, *24*, 958-966.

(185) Curro, J. G.; Schweizer, K. S.: An Integral-Equation Theory of Polymer Blends - Athermal Mixtures. *Macromolecules* **1990**, *23*, 1402-1411.

(186) David, E. F.; Schweizer, K. S.: Influence of Conformational Asymmetries on Local Packing and Small-Angle Scattering in Athermal Diblock Copolymer Melts. *Macromolecules* **1995**, *28*, 3980-3994.

(187) Yethiraj, A.; Kumar, S.; Hariharan, A.; Schweizer, K. S.: Surface Segregation in Polymer Blends Due to Stiffness Disparity. *Journal of Chemical Physics* **1994**, *100*, 4691-4694.

(188) Bates, F. S.; Fredrickson, G. H.: Conformational Asymmetry and Polymer-Polymer Thermodynamics. *Macromolecules* **1994**, *27*, 1065-1067.

(189) Bates, F. S.; Schulz, M. F.; Khandpur, A. K.; Forster, S.; Rosedale, J. H.; Almdal, K.; Mortensen, K.: Fluctuations, Conformational Asymmetry and Block-Copolymer Phase-Behavior. *Faraday Discussions* **1994**, *98*, 7-18.

(190) Vavasour, J. D.; Whitmore, M. D.: Self-Consistent Mean Field-Theory of the Microphases of Diblock Copolymers. *Macromolecules* **1992**, *25*, 5477-5486.

(191) Vavasour, J. D.; Whitmore, M. D.: Self-Consistent-Field Theory of Block-Copolymers with Conformational Asymmetry. *Macromolecules* **1993**, *26*, 7070-7075.

(192) Vavasour, J. D.; Whitmore, M. D.: Self-consistent theory of block copolymers with conformational asymmetry (vol 26, pg 7070, 1993). *Macromolecules* **1996**, *29*, 5244-5244.

(193) Matsen, M. W.; Schick, M.: Microphases of a Diblock Copolymer with Conformational Asymmetry. *Macromolecules* **1994**, *27*, 4014-4015.

(194) Hillmyer, M. A.; Bates, F. S.; Almdal, K.; Mortensen, K.; Ryan, A. J.; Fairclough, J. P. A.: Complex phase behavior in solvent-free nonionic surfactants. *Science* **1996**, *271*, 976-978.

(195) Hillmyer, M. A.; Bates, F. S.: Synthesis and characterization of model polyalkane-poly(ethylene oxide) block copolymers. *Macromolecules* **1996**, *29*, 6994-7002.

(196) Mai, S. M.; Fairclough, J. P. A.; Terrill, N. J.; Turner, S. C.; Hamley, I. W.; Matsen, M. W.; Ryan, A. J.; Booth, C.: Microphase separation in poly(oxyethylene)-poly(oxybutylene) diblock copolymers. *Macromolecules* **1998**, *31*, 8110-8116.

(197) Zalusky, A. S.; Olayo-Valles, R.; Wolf, J. H.; Hillmyer, M. A.: Ordered nanoporous polymers from polystyrene-polylactide block copolymers. *Journal of the American Chemical Society* **2002**, *124*, 12761-12773.

(198) Hamley, I. W.; Castelletto, V.; Yang, Z.; Price, C.; Booth, C.: Melt phase behavior of poly(oxyethylene)-poly(oxypropylene) diblock copolymers. *Macromolecules* **2001**, *34*, 4079-4081.

Contributions

1. Publications

1. Unusual Modulus Enhancement in Conformationally Asymmetric Crystalline-Amorphous Block Copolymers. (*In Preparation*)

2. Structure-Property Relationships in Low Molecular Weight Crystalline-Amorphous Block Copolymers. (*In Preparation*)

3. The Effect of Chain Architecture on the Mechanical Response in Polypropylenes. (*In Preparation*)

4. Dynamic Sub-10 nm Nanostructured Ultrathin Films of Sugar-Polyolefin Conjugates Thermoresponsive at Physiological Temperatures. Nowak, S. R.; **Hwang, W.**; Sita, L. R. *J. Am. Chem. Soc.* **2017**, ASAP

5. End-Group Functionalized Poly(α-olefinates) (x-PAOs) as Non-Polar Building Blocks: Self-Assembly of Sugar-Polyolefin Hybrid Conjugates. Thomas, T. S.; **Hwang W.**; Sita, L. R. *Angew. Chem. Int. Ed.* **2016**, *55*, 4683-4687.

6. Superabsorbent Hydrogels that are Strong and Highly Stretchable. Cipriano, B. H.; Banik, S. J.; Sharma, R.; Rumore, D.; **Hwang, W.**; Briber, R. M.; Raghavan, S. R. *Macromolecules* **2014**, *47*, 4445-4452.

7. Dinuclear Bis-Propagators for the Stereoselective Living Coordinative Chain Transfer Polymerization of Propene. Wei, J.; **Hwang, W.**; Zhang, W.; Sita, L. R. *J. Am. Chem. Soc.* **2013**, *135*, 2132-2135.

8. Synthesis, Characterization, and Electrospinning of Architecturally-Discrete Isotactic-Atactic-Isotactic Triblock Stereoblock Polypropene Elastomers. Giller, C.; Gururajan, G.; Wei, J.; Zhang, W.; **Hwang, W.**; Chase, D. B.; Rabolt, J. F.; Sita, L. R. *Macromolecules* **2011**, *44*, 471-482.

9. Surface Induced Nanofiber Growth by Self-Assembly of a Silk-Elastin-Like Protein Polymer. **Hwang, W.**; Kim, B. H.; Dandu, R.; Cappello, J.; Ghandehari, H.; Seog, J. *Langmuir* **2009**, *25*, 12682-12686.

2. Presentations

1. Microphase Separation in Low Molecular Weight Crystalline-Amorphous Block Copolymers. *MASM* **2015**

2. Iso-Polypropylene / a-Polypropylene Block Copolymer Blends with Low Molecular Weight Functionalized iso-Polypropylene Homopolymer. *MASM* **2013**

3. Synthesis and Characterization of Stereoblock and Stereorandom Polypropylenes. *ACS Fall Meeting* **2012**

4. Structure-Property Relationships of Semicrystalline Polyolefins. *MASM* **2012**

5. Synthesis and Characterization of Stereoblock and Stereorandom Polypropylenes. *MARM* **2011**